This electronic thesis or dissertation has been downloaded from Explore Bristol Research, http://research-information.bristol.ac.uk

Author:
Abu El Magd, Noha

Title:
Biocrystals

General rights
Access to the thesis is subject to the Creative Commons Attribution - NonCommercial-No Derivatives 4.0 International Public License. A copy of this may be found at https://creativecommons.org/licenses/by-nc-nd/4.0/legalcode This license sets out your rights and the restrictions that apply to your access to the thesis so it is important you read this before proceeding.

Take down policy
Some pages of this thesis may have been removed for copyright restrictions prior to having it been deposited in Explore Bristol Research. However, if you have discovered material within the thesis that you consider to be unlawful e.g. breaches of copyright (either yours or that of a third party) or any other law, including but not limited to those relating to patent, trademark, confidentiality, data protection, obscenity, defamation, libel, then please contact collections-metadata@bristol.ac.uk and include the following information in your message:

- Your contact details
- Bibliographic details for the item, including a URL
- An outline nature of the complaint

Your claim will be investigated and, where appropriate, the item in question will be removed from public view as soon as possible.

Biocrystals; Growth, Synthesis and Materials

By

Noha Abu El Magd

Department of Chemistry

University of Bristol

A dissertation submitted to the University of Bristol in accordance with the requirements of the degree of DOCTOR OF PHILOSOPHY in the Faculty of Science.

June 2019

Word count: 47367

Abstract

The central theme of this thesis is to exploit the concepts of biomimetic, biokleptic and bio-inspired design, utilising biocrystals as precursors for the fabrication of novel functional materials. As an inherently multi-disciplinary field of research, the work presented in this thesis bridges bio-synthetic techniques such as compartmentalisation, top-down and bottom-up synthesis, and non-contact manipulation. A comprehensive report of three experimental chapters that employ these themes is presented with the aim to enhance our understanding of existing processes such as protein crystallisation, advance our ability to tailor materials for specific functions and present reasonable alternatives and opportunities for the development of materials technology for a more sustainable future. A novel, cheap and facile protein crystallisation technique was designed, in which colloidosomes (Pickering emulsions) were successfully used as microcompartment reaction vessels for the growth of protein crystals. The results obtained were investigated in an effort to optimise the crystallisation conditions and refine the technique. Conventional synthetic routes of carbon dots (fluorescent nanoparticles) were applied to create hybrid top-down and bottom up synthesis mechanism of N-doped and N, S-doped carbon dots (CDs) using cellulose nanocrystals was developed. This cheap, facile and energetically efficient technique was highly reproducible, and the CDs synthesised were extensively characterised to better understand their resultant properties and elucidate the underlying photoluminescence mechanism. The work of these two projects was then built on to explore the potential applications and enhancement of the properties of CDs synthesised by the aforementioned mechanism using compartmentalisation and non-contact acoustic manipulation. The photostability, cytotoxicity and fluorescence decay of CDs in solution and CDs encapsulated in colloidosomes and coacervates (acoustically patterned) were investigated to explore their potential for bio-imaging and photo-sensing applications.

Dedication and Acknowledgements

All praise to the all high. All gratitude and praise due to God, this journey would not have been possible without the mercy, blessings and guidance of God alhamdolilAh.

I have been privileged to be afforded the opportunity to complete my doctorate and develop my skills and knowledge, as a researcher, critical thinker and philosopher. The value that the past 5 years has added to my life is invaluable and cannot be put to words. It has been one of the most difficult undertakings of my life and has tested me in every means imaginable and even ways I did not think it could. This PhD has taken me around the world, taught me so much about the universe and myself and taken me to some extreme highs and lows. However, I believe I am better for it.

I have had the honour and privilege to work alongside a brilliant group of scientists and academics, who have taught me so much and made my experience so worthwhile. I am honoured to call them colleagues and friends. I would first like to thank Dr Terry McMaster and Dr Annela Seddon for accepting me into the BCFN programme and believing in my potential. Dr Annela Seddon, I want to thank you for being there for me every step of the way. You are my role model and I am grateful to have known you and had your influence in my life as a student and a woman. I would not have been able to do this without you and probably would have quit were it not for your consistent encouragement and for believing in me when I did not believe in myself. I would also like to thank the administrative team of the BCFN who are the backbone of the centre, Joanna Bird and Becky Drinkwater and the team of academics particularly Dr Simon Hall, Prof Charl Faul and Dr Sean Davis.

I would like to thank my supervisory team Dr Avinash patil and Dr Ross Anderson for their direction, guidance and scientific discussions throughout this project. Thank you for your support and understanding and for always pushing me to do better, aim higher and fulfil my potential. I would like to thank Prof Stephen Mann for the opportunity to undertake my PhD in such an excellent and prestigious research group and for his support and guidance throughout the project.

Thank you to the EPSRC for my finding and to everyone at the School of Chemistry EMU, XRD facility and Diamond Light Source particularly Helena Mikolajek for all their help, training and support.

My journey would have been impossible if it were not for the gracious and supportive community, I found in the Mann group. Thank you to the members of the Mann group for all the support, training, scientific discussion, socials, coffee breaks and Christmas dinners. I would like to thank in particular Sam Briggs, Matthew Mulvee, Johnny Fruze, Laura Rodriguez Arco, Joanna Sparks, Mary Jenkinson-Finch, Maddy Nichols, Angela Suriyakumaran, Liangfei Tian, Nicolas Martin and Pierangelo Gobbo. Thank you for your support and friendship and for keeping me sane. Thank you for making work less daunting and for listening to me problems and frustrations and for offering your advice and help where you could and your sympathy where you couldn’t. I would like to thank my collaborators Monika Jakimowicz and Diego Garcia Hernandez for their work on the cell studies. I would also like to thank Dr Alice Parnell for her assistance, support and patience with the Diamond light Source experiments and Dr Omar Gomez Rojas for his help with XRD and for being an excellent supportive and encouraging friend.

None of this would have been possible without the support, patience and prayers of my family and friends. Thank you to my grandparents, parents, sister and brother for everything. To my friends who know who they are, thanks for continuing to let me be a miserable grump and for sticking. Y me through thick and thin. Thank you especially to Sadiyah Sheikh and Thomas Richardson (DJ Tem) for being kind, generous and excellent friends and for keeping me sane for the last hurdle.

The proofreading of this thesis was no small task as I write very fast and by the end of it forgot how to read so thank you to Dr Imke Sittel and Sean O'Neill for helping it all come together nicely.

I would also like to thank the following online platforms Netflix, Amazon Prime, Spotify Premium student subscription and the 2DopeQueens podcast for getting me through. I would also like to thank the NUS, for helping me realise that despite the difficulty of doing a PhD there are much worse things in life.

Author’s Declaration

I declare that the work in this dissertation was carried out in accordance with the requirements of the University’s Regulations and Code of Practice for Research Degree Programmes and that it has not been submitted for any other academic award. Except where indicated by specific reference in the text, the work is the candidate’s own work. Work done in collaboration with, or with the assistance of, others, is indicated as such. Any views expressed in the dissertation are those of the author.

Signed…………………………………………………………Date……………………………….

Table of Contents

Table of Tables

Table of Figures

Table of Schemes

Chapter 1: Introduction

1.1. Introduction and Thesis Outline

The scientific community has long strived to develop technological approaches that put less strain on the planet's natural resources, minimise energy consumption, generate less waste and pave a less destructive path for future generations to come. In these efforts, it has become apparent that nature itself provides the best source of inspiration to achieve this vision. Biological materials and processes generally are much more environmentally friendly than those used and obtained by synthetic ones. Millions of years of evolution have resulted in optimised material architectures, properties and behaviours for their desired function. Additionally, biological processes tend to self-regulate, occur under mild "reaction conditions" and exploit the lowest energetic pathways available. [1,2] This field has often been termed bio-mimetics, in which scientists effectively mimic or copy the example of nature to incorporate its advantageous features and properties into innovative systems and materials design. It can be defined as "the study and development of synthetic systems that mimic the formation, function or structure of bio-logically produced substances and materials and biological mechanisms and processes."[1] The field itself is inherently multi-disciplinary and is dependent on the collaboration between the fields of chemistry, physics, biology, engineering, materials science and biotechnology, and as we are starting to see with nanoscale biomaterials in the field of quantum technologies as well.

The field can be further divided into three main categories as described by Galloway et al. (2013): bioinspired ("advances, components or systems inspired by nature"), biokleptic ("using components form nature within artificial systems") and biomimetic ("mimicking a natural component or method in the system").[2] These strategies often encompass the following three objectives: to gain a better understanding of biology and its processes through reverse engineering and artificial reconstruction, to enhance our ability to tailor materials for specific functions, and to develop materials technology for a sustainable future. [1,2]

Proto-cellular research is an excellent example of the use of bio-mimetics and bio-inspired design to develop our understanding of natural processes and systems, specifically the origin of life. Protocells have been defined under various terms and can be described as ranging from a "a plausible representation of a hypothetical precursor to the first biological cell" to "a synthetic cell-like entity that contains non-biologically relevant components" ascribed to the presence of life.[3,4]

Mann et al. have utilised compartmentalisation in organic membranes and vesicles of artificial proto-cells to investigate the precursors for basic evolutionary viability and autonomy of living cells in terms of: component self-organisation, physio-chemical environment and basic chemical processes or reactions. These models have served to contribute to the understanding of evolution as well as the design of artificial protocells and protocell systems for applications in biotechnology.[3,5–7]

Biokleptic research into template-directed synthesis of nanoparticles using porous protein crystals (PPC) via host-guest complexation is an example of where the field has been used to enhance our ability to tailor materials for specific functions. The larger 'host' molecule (in this case PPC) assembles into a lattice that incorporates the smaller 'guest' molecule forming a host-guest system. The host structure may be a porous ordered material which incorporates the 'guest' species into voids or ordered channels within the structure, a covalently synthesised macromolecule which forms a complex with smaller 'guest' molecules, or a self-assembled aggregate which forms spontaneously in solution with the guest material. PPC combine the 'softness' of a dynamic, structurally transformative framework with the rigidity and regularity of a crystalline structure and a regular array of solvent channels which are able to incorporate guest species and provide a unique chiral environment for site-specific reactions.[8,9] PPC have been used for the template-directed synthesis of Ag and Ag nanoparticles, inorganic nanoparticles, and polymer films and have been used to create novel biohybrid materials with unique properties which can be tailored for applications in catalysis, separation, drug delivery and storage.[9–12]

The areas in which biomimetics are being employed to develop materials technology for a more sustainable future are numerous. This is possibly the most prevalent area of the research objectives. These endeavours range from biomimetic photosynthesis, engineering biological enzymes to convert organic matter into fuels, and engineering biomolecular motors which harness chemical and solar energy. [13]

The work presented in this thesis draws on the concepts of biokleptic, biomimetic and bioinspired design to enhance existing processes and synthesise functional materials with unique properties for a diverse range of technological applications. The themes of the field are described as they relate to the experimental features of the work in the objectives, design of the research and the outcomes.

Chapter 2 discusses the development of a novel, cheap and facile protein crystallisation technique. Amphiphilic silica particles were used to stabilise a water-in-oil Pickering emulsions (colloidosmes) to generate a confined micro-compartment reaction vessel for growth of protein crystals. This approach is biokleptic in its use of protein molecules, which exist naturally in abundance. It is bio-inspired by the compartmentalisation measures which occur in nature such as the evolution of large enzyme complexes and distinct cellular organelles.[14] It is also biomimetic as the process is somewhat analogous to the biomineralization process which occurs in magnetotactic bacteria to produce uniform crystals inside lipid vesicle magnetosomes.[1]

The size, shape, and location of these crystals within the colloidosome spheres was characterised. This novel approach to protein crystallisation combines concepts of droplet confinement and diffusion gradients across a membrane in an attempt to better understand and control protein crystallisation. The size, morphology, and location of crystals within the spherical colloidosomes were investigated in an effort to optimise crystallisation conditions. The newly developed technique was highly robust and reproducible crystallisation of lysozyme and ferritin was obtained. Furthermore, promising results with mCherry and bovine liver catalase were also observed. In addition to crystallisation of native proteins, colloidosome encapsulation was also used to successfully functionalise lysozyme crystals *in situ* with metallic gold nanoparticles as well as fluorescent carbon nanoparticles.

Chapter 3 outlines a novel hybrid synthetic mechanism for the synthesis of N-doped as well as N- and S-doped carbon dots (CDs). CDs are carbon-based fluorescent nanoparticles, which can be manufactured by a variety of ‘top-down’ and ‘bottom-up’ synthetic techniques.

Utilising a variety of readily available organic precursors, these CDs can be functionalised with a variety of chemical moieties. Heteroatom doping of CDs during the synthesis is used to enhance the photoluminescence (PL) of these particles and improve their quantum yield. N-CDs and N,S-CDs were synthesised by a novel hybrid approach which draws on the principles of both top-down and bottom-up synthetic techniques. Cellulose nanocrystals, obtained from the acid dehydration of cellulose pulp, was used as a novel organic precursor for the facile, cheap and time-efficient synthesis via microwave-assisted pyrolysis. The major theories surrounding PL in CDs include the radiative recombination in the carbon core and the formation of emissive traps at the surface, although the exact mechanism involved still remains to be fully understood. The CDs were characterised to examine their size, morphology, optical properties, crystalline structure, quantum yield, photostability and biocompatibility. This characterisation served to elucidate the PL mechanism of CDs and identify factors affecting and contributing to the PL behaviour. The CDs were characterised by HRTEM, XRD, FTIR, XPS, and their PL properties as well as quantum yields were determined. The biokleptic aspect involves the use of cellulose (the most abundant natural polymer) as the precursor for a hybrid synthetic process which is biomimetic of metabolic processes (top-down: catabolic and bottom-up: anabolic) to create bio-inspired fluorescent CDs.

Chapter 4 builds on the work carried out in chapter 3 by exploring the potential of CDs synthesised for application in bio-imaging and photo-sensing by investigating their cytotoxicity, photostability and fluorescence decay. Encapsulation of the CDs within colloidosomes and coacervates was carried out to explore the potential enhancement of their photostability. Acoustic trapping of CDs in coacervates was employed to aid the manipulation and characterisation of CDs and serve as a model for spatial separation of CDs in 2D.

Each chapter includes a dedicated introduction, theory background and literature review. The experimental methods and materials used, and the conclusions derived from this work and suggestions for future work are outlined.

1.2. References

1. Rawlings, A. E., Bramble, J. P. & Staniland, S. S. Innovation through imitation: Biomimetic, bioinspired and biokleptic research. *Soft Matter* **8**, 6675–6679 (2012).

2. Galloway, J. M., Bramble, J. P. & Staniland, S. S. Biomimetic synthesis of materials for technology. *Chem. - A Eur. J.* **19**, 8710–8725 (2013).

3. Dzieciol, A. J. & Mann, S. Designs for life: Protocell models in the laboratory. *Chem. Soc. Rev.* **41**, 79–85 (2012).

4. Mann, S. The origins of life: old problems, new chemistries. *Angew. Chem. Int. Ed. Engl.* **52**, 155–62 (2013).

5. Li, M., Green, D. C., Anderson, J. L. R., Binks, B. P. & Mann, S. In vitro gene expression and enzyme catalysis in bio-inorganic protocells. *Chem. Sci.* **2**, 1739 (2011).

6. Li, M., Huang, X., Tang, T.-Y. D. & Mann, S. Synthetic cellularity based on non-lipid micro-compartments and protocell models. *Curr. Opin. Chem. Biol.* **22**, 1–11 (2014).

7. Mann, S. Systems of creation: The emergence of life from nonliving matter. *Acc. Chem. Res.* **45**, 2131–2141 (2012).

8. Vilenchik, L. Z., Griffith, J. P., St. Clair, N., Navia, M. A. & Margolin, A. L. Protein crystals as novel microporous materials. *J. Am. Chem. Soc.* **120**, 4290–4294 (1998).

9. Horike, S., Shimomura, S. & Kitagawa, S. Soft porous crystals. *Nat. Chem.* **1**, 695–704 (2009).

10. England, M. W., Patil, A. J. & Mann, S. Synthesis and confinement of carbon dots in lysozyme single crystals produces ordered hybrid materials with tuneable luminescence. *Chemistry* **21**, 9008–13 (2015).

11. Muskens, O. L., England, M. W., Danos, L., Li, M. & Mann, S. Plasmonic response of Ag- and Au-infiltrated cross-linked lysozyme crystals. *Adv. Funct. Mater.* **23**, 281–290 (2013).

12. England, M. W. *et al.* Fabrication of polypyrrole nano-arrays in lysozyme single crystals. *Nanoscale* **4**, 6710 (2012).

13. Inspired by Biology: From Molecules to Materials to Machines. Washington (DC): National Academies Press (US). *Advanced Functional Materials* 3 (2008). Available at: https://www.ncbi.nlm.nih.gov/books/NBK214499/.

14. Chen, A. H. & Silver, P. A. Designing biological compartmentalization. *Trends Cell Biol.* **22**, 662–670 (2012).

Chapter 2: Porous Protein Crystals; Growth and Engineering

2.1. Aims of the Work

The aim of the work presented in this chapter was to develop a novel protein crystallization mechanism utilising silica nanoparticle-stabilised Pickering (water in oil) emulsions called colloidosomes. The colloidosomes offer a small-volume confined environment for the crystallization process, and the permeability of the colloidosome membrane creates a diffusion gradient which aides the crystallization process and allows for cross-linking of protein molecules within the micro-compartments post-crystallisation. Lysozyme from hen egg white was the main protein crystal investigated. The mechanism was also successful for the crystallisation of Ferritin from equine spleen. Crystals grown inside colloidosomes were investigated to identify the ideal conditions of size, concentration, crystallisation system and temperature towards enhanced control of the crystallisation process as compared to traditional crystallisation techniques of hanging drop vapour diffusion and batch crystallisation. Colloidosomes were also used as reaction vessels for the growth of functionalised lysozyme crystals. Lysozyme crystals were grown in the presence of gold nanoparticles, N-doped carbon dots (N-CDs) and N- and S-doped carbon dots (N-S-CDs); the synthesis and characterisation of these CDs is covered in Chapter 3. The results of these investigations were used to develop the theory of protein crystallisation in colloidosomes alongside existing theories which are most synonymous with the work presented in this chapter, namely confined volume batch crystallisation. To my knowledge, this work is first in kind and may be of great benefit to the field of protein crystallisation as it presents a facile, cheap and highly reproducible non-contact technique for functionalised and non-functionalised protein crystallisation.

2.2. Introduction

2.2.1. Porous Protein Crystals

Protein crystal structures possess 3D nanoporous architectures, held together by non-covalent forces.[7] Their crystalline structures contain a well-ordered network of solvent channels (d = 0.5 – 10 nm), which make up 30-60% of the total volume.[2,11] Protein crystals are comparable to porous materials in their high porosity and specific surface area. They possess a wide range of pore sizes (20 – 100 Å) and large pore surface areas (800 – 2000 m^2g^{-1})

Solvent channels also present a confined, chiral environment of protein molecules that can be exploited as reaction vessels and organised molecular templates for the synthesis of many materials. The size and morphology of the solvent channels depend on the crystallisation conditions and surface characteristics of the protein.[1,7] The crystals are however quite fragile and prone to dissolution in their native state in comparison to other porous materials. Chemical cross-linking has emerged as a means to improve the mechanical stability of protein crystals. Protein crystals also possess a regular arrangement of functional groups from amino acid residues along the protein crystal lattice, which can be additionally functionalised. The porous space inside crystals contains the capacity to incorporate guest molecules through chemical modification and coordination in a periodic arrangement.[7]

These crystals can be utilised as porous biomaterials for separation, drug delivery and heterogeneous enzymatic catalysis.[12] The incorporation of guest molecules within the crystal lattice, such as metal complexes and inorganic nanoparticles, creates novel biohybrid materials with unique characteristics. The capacity to design and impart unique properties enables these materials to be tailored for specific functions such as in optics and catalysis.[7]

2.2.2. Protein crystallisation

Protein crystallisation has been instrumental for the elucidation of the three-dimensional molecular structures, and thereby function, of a variety of biomolecules through x-ray diffraction. As well as developing into an extensive research field in its own right, protein crystallography has fed into many other fields from protein engineering to rational drug design.[13] A protein crystal consists of a 3D ordered array of protein molecules, held together by non-covalent molecular interactions such as hydrogen bonding and van der Waals forces, with solvent and other chemical molecules filling the array voids.[14]

The crystallisation of proteins is a complex process. Compared to other inorganic molecules, most proteins are difficult to crystallise. Proteins are large, complex molecules which are physically and chemically relatively unstable and have dynamic molecular properties varying in different solvent environments. Crystallisation parameters must be adjusted in such a way to ensure the protein molecule interacts correctly both within the protein and with its solution environment. The diversity of chemical groups involved in the interaction means that even slight changes in pH, ionic strength, temperature, concentration of the protein molecule, auxiliary ion, and so on, impact the proteins ability to crystallise in solution. Individual parameters can also simultaneously influence several elements of the crystallisation experiment tor example, temperature affects the solubility of the protein in solution and thereby influences the nucleation and growth rates of the protein crystal. It is therefore quite challenging to isolate individual parameters and their effects and interpret experimental results accordingly. Additionally, every protein molecule is unique and thus conclusions from one protein crystallisation experiment cannot considerably apply to others. [15] Table 2.1 demonstrates some of the parameters that may influence protein crystallisation and growth in solution.

Table 2.1: Adjustable parameters influencing protein crystallisation[15].

Physical Factors	**Chemical Factors**	**Biochemical Factors**
Temperature	Precipitant type	Sample source & history
Methodology	Precipitant concentration	Aggregation
Time/pressure	Ionic strength	Ligands, co-factors & inhibitors
Magnetic/electric fields	pH & Buffer	Chemical modifications
Volume	Sample concentration	Sample PI
Viscosity & equilibration rate	Sample source & purity	Purification method
Gravity, convection & sedimentation rates	Redox environment	Microbial contamination

There are, however, general principles to the thermodynamics of protein crystallisation that can be applied in order to fine-tune conditions appropriately. Protein crystallisation occurs when there are insufficient water molecules available to maintain the full solvation of protein molecules in an aqueous environment. In these conditions, an energy minimum exists whereby the molecules aggregate into an amorphous state or crystallise.[16] Although crystallisation is a complex process that involves multiple equilibrium states, the thermodynamic process of crystallisation takes place via the following three main stages: [13]

1. Nucleation – whereby sufficient molecules associate together to form a thermodynamically stable nucleus

2. Crystal growth – this occurs by various mechanisms as the nuclei provide suitable surfaces for crystal growth
3. Cessation of growth – crystal growth comes to an end as the solution is depleted of protein material, or the growing crystal face is poisoned by impurities, or due to deformation-induced strain which destabilises the crystal lattice.

These stages occur preferentially in different phases of supersaturation. Figure 2.1 shows the phase diagram for crystal nucleation and growth. The supersolubility curve divides the phase spaces into regions of 'supersaturation' where crystal growth is supported and 'undersaturation' where crystals will dissolve. Adjustable parameters include the concentrations of different macromolecules present in the crystallising solution. The supersaturation region is further divided into areas of higher (the metastable zone) and lower (the labile zone) supersaturation. Growth and nucleation occur in the 'labile' region of higher supersaturation and only growth occurs in the 'metastable' region of lower supersaturation. [13] The crystallisation process requires that the system be guided from a region of undersaturation into a region of supersaturation by decreasing the solubility of protein molecules in solution. However, solubility must be decreased very slowly so as to avoid the formation of amorphous precipitates or many low-quality small crystals in the event that nucleation and growth rates are similar. Ideally, nucleation should be induced at the lowest possible supersaturation level ('labile' region). As solute is excluded from the solution, the system gradually moves into a state of lower supersaturation, entering the 'metastable' region where select crystals will grow without additional nucleation or precipitation to form large, good quality crystals. [13,16]

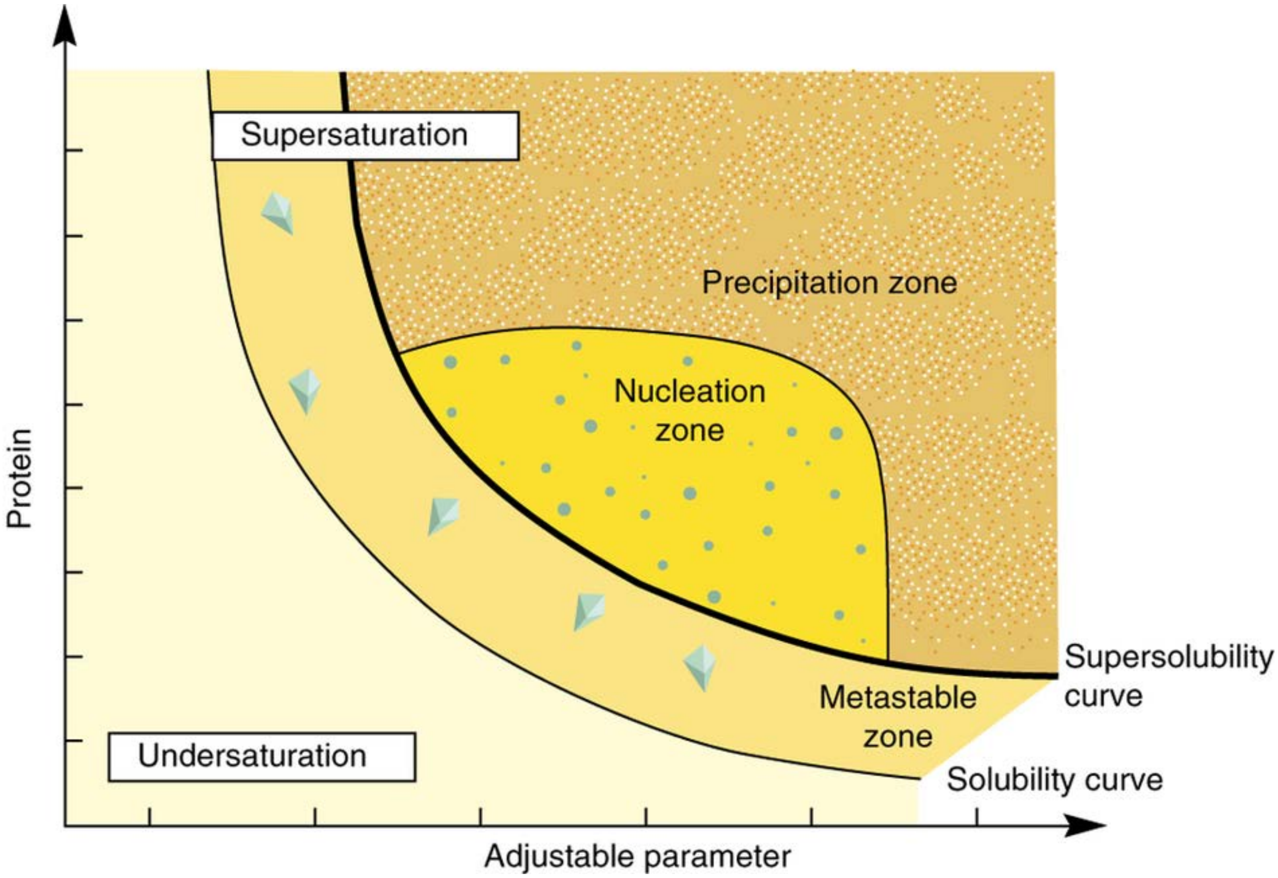

Figure 2.1: Phase Diagram of Protein Crystallisation (y axis: protein concentration).[16]

2.2.3. Protein Cross-Linking

As mentioned, protein crystals are highly fragile and prone to dissolution in their native state. Chemical cross-linking has been utilised to increase the mechanical and thermal stability of protein crystals. Cross-linked protein crystals (CLPCs) are mechanically and thermally highly stable, insoluble in most solvents and retain their crystal lattice structure. They remain chemically active and can be recycled for multiple use.[1] As a result, they have been utilised for a variety of applications including heterogeneous catalysis, separation processes and drug delivery.[2] Cross-linked *Candida rugose* lipase crystals have been used by Margolin et al. as porous materials for separating molecules[3] and the enantioselective hydrolysis of chiral esters.[4] Glutaraldehyde is one of the most common chemical cross-linking agents. Glutaraldehyde is a saturated dialdehyde consisting of a straight chain of 5 carbon atoms, the structure of which is shown below in Figure 2.2. It is a highly versatile, and efficient cross-linker, soluble in water and organic solvents chloroform and ethanol. The mechanism of cross-linking is still not fully understood. However, it has been extensively investigated, and has been seen to take place as two main stages. This is outlined in Scheme 2.1[1].

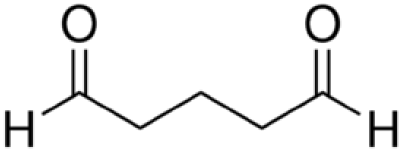

Figure 2.2: Chemical structure of glutraldehyde molecule.

The first stage involves self-polymerisation of glutaraldehyde. The two aldehyde groups are highly reactive in aqueous media and hence glutaraldehyde possesses a high capacity for self-polymerisation. This process is highly pH and concentration dependent, with a higher rate of polymerisation observed at higher pH and glutaraldehyde concentration. Under alkaline conditions, glutaraldehyde undergoes polymerisation into saturated polymers of different lengths via a series of aldol condensations. This results in a large degree of variation and uncertainty in the lengths and position of cross-links formed.

The second stage is the cross-linking step, whereby the predominant mechanism involves the reaction of aldehyde groups with the ε-amino groups of lysine residues. Cross-links formed can be both inter- and intra-molecular. Temperature, pH, crystal structure, concentration and polymerisation state of glutaraldehyde all affect the successful cross-linking of protein crystals. Additionally, due to the discrepancy of accessibility to aldehyde groups of molecules on the exterior compared to those in the interior of the protein crystal, the cross-linking is inhomogeneous. This can affect the mechanical stability of CLPCs, leading to cracks from internal stress in the event of inhomogeneous heat expansion and cold contraction. The cross-linking produces CLPCs of high purity, high stability, and high activity in a variety of solvents. [1]

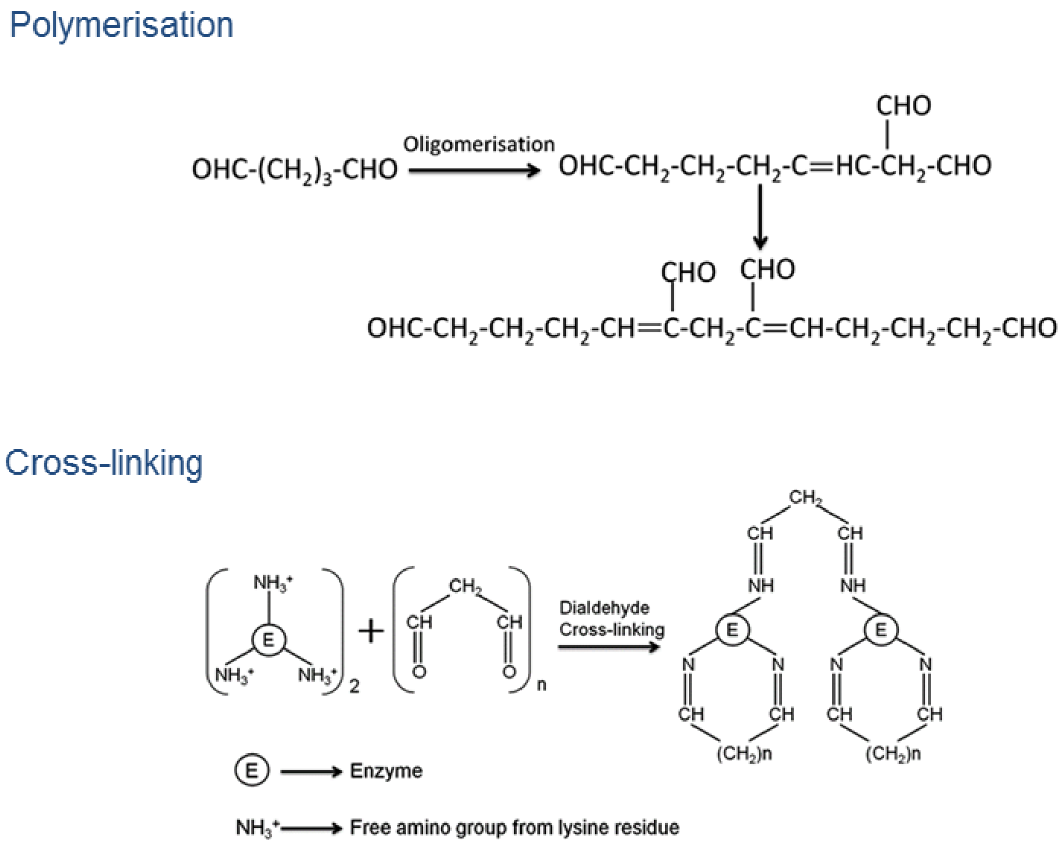

Scheme 2.1: Two-stage cross-linking process of glutaraldehyde. Adapted from Yan et al 2015[1].

2.2.4. Protein Crystallisation Methods

The ability to decipher the structures of protein crystals and the associated biotechnology, materials and rational drug design applications requires the availability of high-quality crystals.[5] The challenges to appropriate manipulation and control of the protein crystallisation process are many. The complexity of the crystallisation process and multitude of influencing parameters mean that it is difficult to reproduce the process and predict outcomes with the variation of a single parameter. Many methods have been developed towards the automation of protein crystallisation, and to improve the understanding and control over the process and the parameters influencing it.[5–13] The principles of these methods have been driven with the common concepts of diffusion, mass transport and precipitation in confined geometries.[13] The most common and successful methods of protein crystallisation are batch crystallisation and vapour diffusion. Batch crystallisation is one of the most common and reproducible methods for producing protein crystals (Figure 2.3). All components are combined into a single super-saturated solution. The initial solution is in the labile region and moves towards the metastable region as solute is depleted from the system during crystal growth. This requires supersaturation levels for nucleation to be achieved upon mixing. Therefore, where crystal growth is successful, the conditions required for crystallisation can be precisely identified.

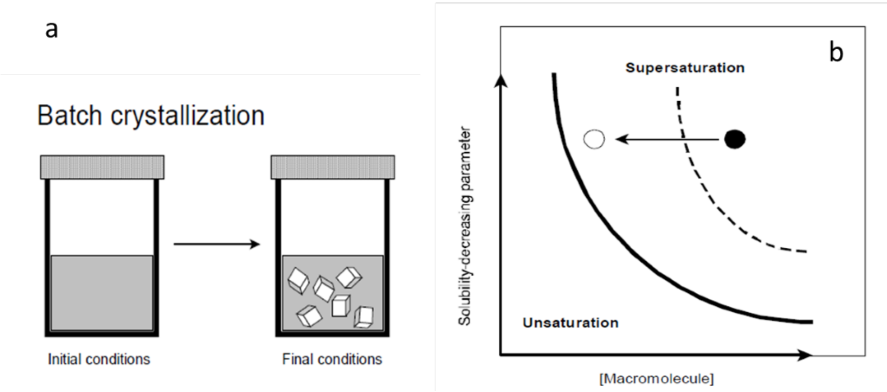

Figure 2.3: a) Batch crystallisation set up, b) Phase diagram of protein crystallisation.

Vapour diffusion is carried out by suspending a mixture of unsaturated protein solution and precipitant (either sitting or suspended) over a reservoir of precipitant solution in an enclosed chamber (Figure 2.4). The difference in precipitate concentration between the solution in the droplet and the reservoir drives a reduction in the droplet volume. Through vapour equilibration of the droplet and reservoir solution, the droplet solution reaches a level of supersaturation that allows nucleation and initial crystal growth. The phase diagram of this process is illustrated in Figure 2.4b.[13,14]

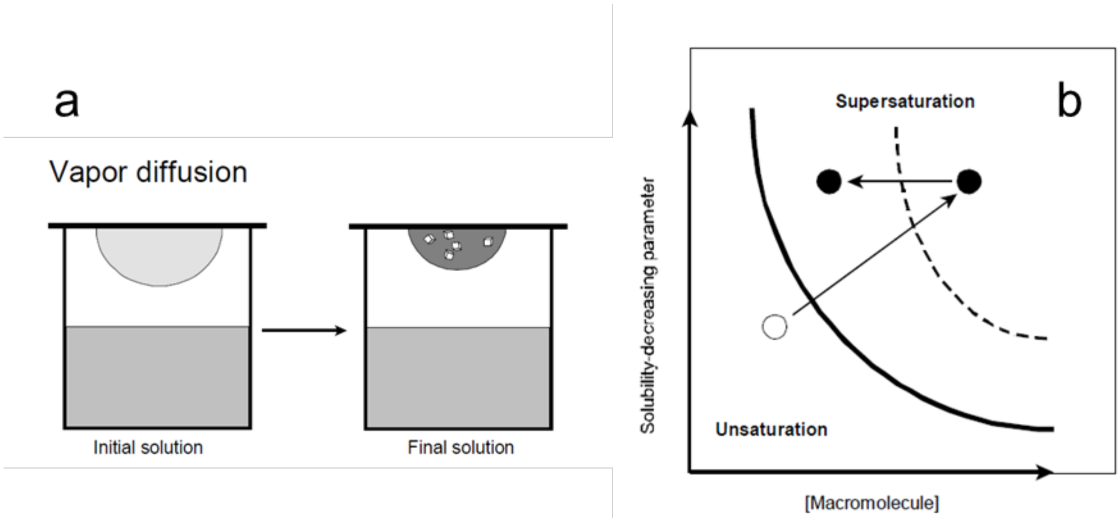

Figure 2.4: Vapour diffusion crystallisation method instrumental set-up, b) Phase diagram of vapour diffusion protein crystallisation.[14]

Counter diffusion crystallisation in capillaries has been used to prepare samples suitable for immediate x-ray diffraction (XRD) analysis. The technique involves the arrangement of volumes of protein solution and precipitant solution adjacent to each other inside an XRD capillary. The two solutions diffuse against each other which results in a spatial-temporal diffusion gradient along the length of the capillary (Figure 2.5a). The conditions leading to crystallisation can therefore be controlled within the capillary directly, and crystals grow selectively in response to different conditions of supersaturation.[13]

Microfluidic systems have been developed for enhanced automation and control of protein crystallisation. These systems have been employed to separate the nucleation and growth stages[11], create multi-dimensional concentration gradients to screen multiple parameters for protein crystallisation[15] and investigate the effects of mixing,[10] multiple phase flow,[6] and protein molecular diffusion[7] on protein crystallisation as well as conduct *in situ* data collection of crystals grown in micro-capillaries.[16] These methods have been extremely advantageous towards large-scale screening of conditions, and investigating their influence on protein crystallisation in isolation. However, despite the combination of droplet-based microfluidics and automated robotics, and the elucidation of critical droplet sizes for crystal growth, the current literature has not advanced protein crystallisation to sizes below the macrometer scale.[12]

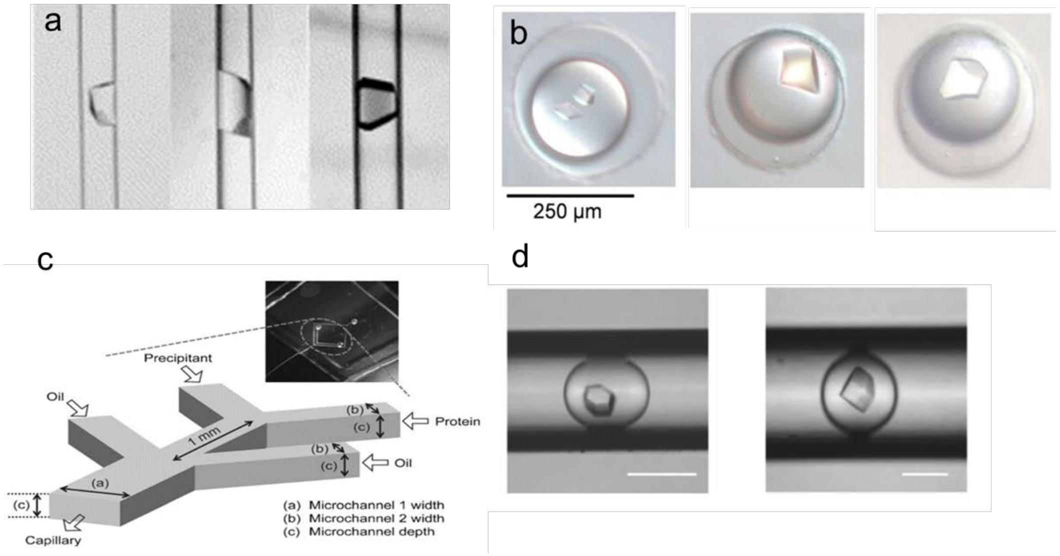

Figure 2.5: Protein crystallisation techniques a) Crystals grown by counter-diffusion in capillaries, from left to right: insulin, thaumatin, and lysozyme,[13] b) Crystals grown by microfluidic droplet robot, from left to right: thaumatin, trypsin and isomerase; scale bar = 250 µm,[12] c) Diagram illustrating the microfluidic channels within a PDMS chip used to grow lysozyme crystals, d) Lysozyme crystallisation inside microfluidic droplets; scale bar = 200 µm.[7]

2.2.5. Compartmentalisation in Pickering Emulsions (Colloidosomes)

Colloidosomes are selectively permeable, microscale compartments. They are formed by the self-assembly of colloidal nanoparticles on the interface of a biphasic system of two immiscible liquids. [17,18] Colloidosomes behave much like Pickering emulsifiers, whereby the solid colloidal particles stabilise the system by minimising the total surface energy of the system.[19,20] This results in the formation of hollow, porous microcapsules of which the permeability, elasticity and size can be precisely controlled.[17,21]

A variety of colloidal particles and stimuli-responsive particle emulsifiers have been used to fabricate colloidosomes in a wide range of systems, demonstrated in Figure 2.6, generating an avenue for microencapsulation that is highly selective, robust and responds to changes in pH and temperature.[18] This has led to multiple avenues of research into the use of colloidosomes as microcompartments for molecular transport and storage, catalysis, drug delivery and protocell research.[22–27]

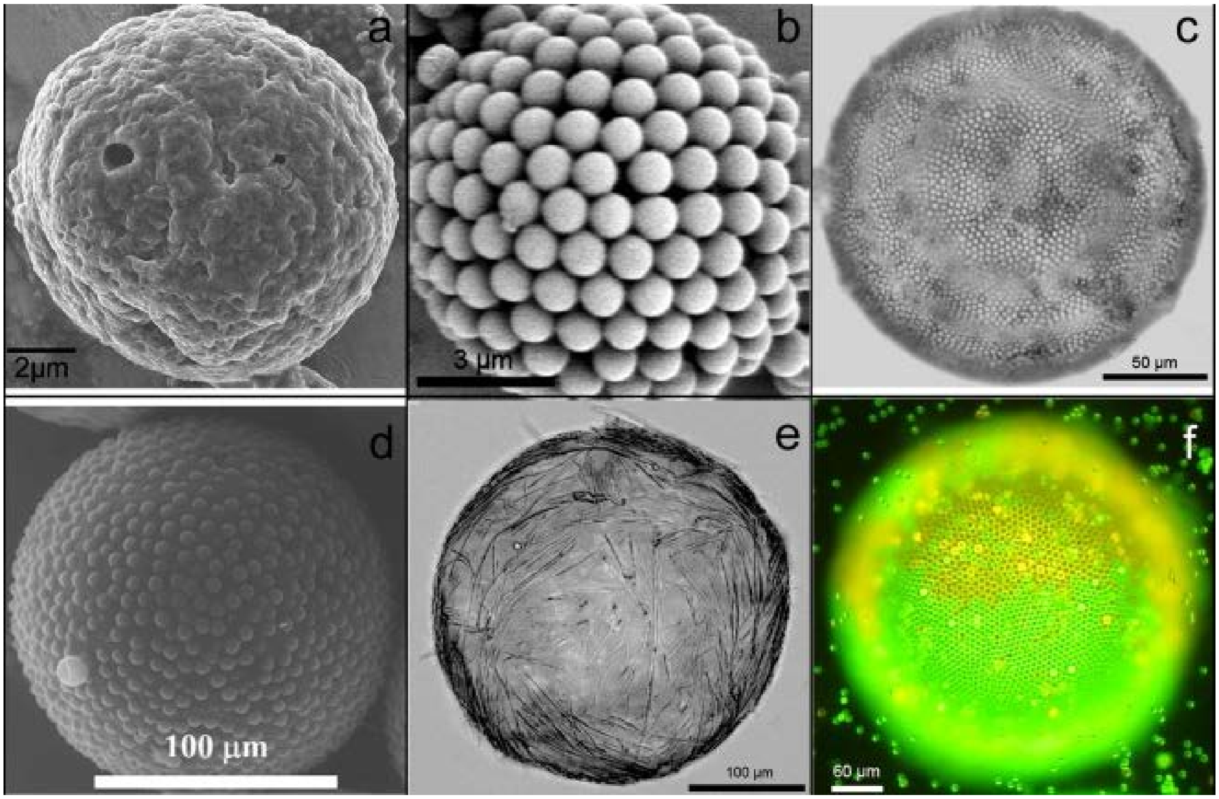

Figure 2.6: Variety of particle emulsifiers and emulsion systems used to fabricate colloidosomes by soft-template method (a) polystyrene/melamine-formaldehyde composite assembled on an oil-in-water droplet, (b) Polystyrene particles assembled on a vegetable oil/toluene-in-water emulsion, (c) Amine polystyrene particles assembled on a water-in sunflower oil droplet, (d) Poly (DVB-55) porous particles on a *p*-xylene-in-water droplet, (e) Polymeric microrods on an agarose gel bead in tricaprylin, (f) Polystyrene particles assembled in a Janus particle arrangement (a-c = 4.9 µm, d-f = 4.0 µm particles). [21]

There are many potential advantages of using colloidosomes as efficient encapsulation structures. The permeability, size, mechanical strength and elasticity as well as surface functionalisation and therefore compatibility in different environments, can be easily manipulated for a variety of functions.[19] Control of the size enables selectivity of the material encapsulated, with the permeability allowing for selective, time-dependent and activated release of the encapsulated material. Precise control of these features leads to the potential for their use as compartmentalisation and delivery vehicles for different biomolecules.[19] A major limitation of colloidosomes, however, lies in the poor yield of their production and their fragility when transferred across different media (particularly from oil to water).[19]

Colloidosomes have been successfully used to sequester many biomolecules including proteins, enzymes and living cells across a variety solvent, pH and temperature conditions, whilst retaining the ability to undergo chemical reactions within the compartment, e.g. cell-free gene expression (Figure 2.7), enzyme catalysis and in vitro protein synthesis.[17,26,28]

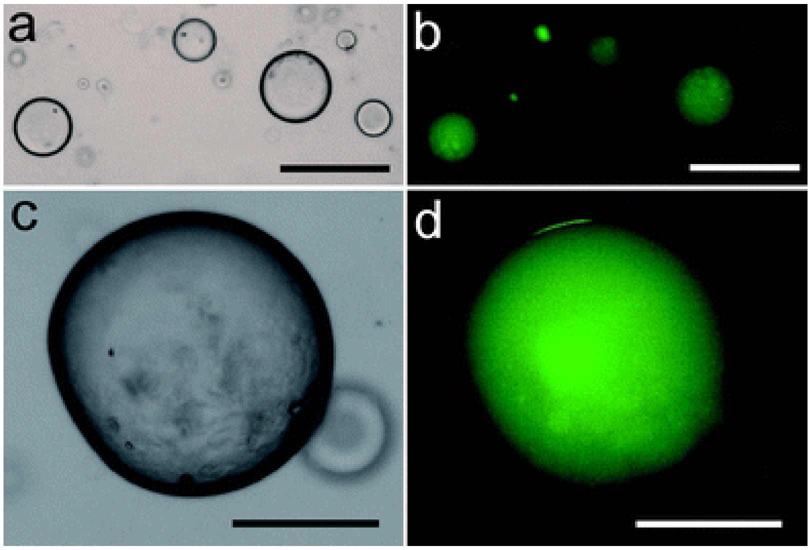

Figure 2.7: In vitro gene expression of fluorescent eGFP by plasmid pEXP5-NT/eGFP inside silica colloidosomes. Scale bars: (a, b) 50 mm, (c, d) 100 mm.[29]

The ability to encapsulate materials such as proteins without denaturation has led to investigations into the use of colloidosomes as micro-compartments for protein crystallisation, as a means of enhancing the control of the crystallisation process. Silica nanoparticles were used as particle emulsifiers to prepare water-in-oil emulsion-based colloidosomes, also known as Pickering emulsions. The closely packed silica nanoparticles were used to stabilise aqueous microdroplets of protein and precipitant solution (analogous to batch crystallisation) and serve as semi-permeable reaction vessels for protein crystallisation.[30]

2.2.6. Interfacial assembly of solid particles and formation of colloidosomes

Pickering emulsions are emulsions stabilised by the adsorption of solid colloidal particles at the water/oil interface. The emulsions are prepared by the dispersion of solid colloidal particles in the continuous phase of an emulsion. According to the partial wettability of the particles in each phase they will adsorb onto the interface and stabilise emulsified droplets by forming an effective steric and electrostatically stable shell around them. Pickering emulsions are classified based on the type of emulsion formed, such as oil-in-water, or water-in-oil etc. This depends on the preferential wettability of the particle phases, and forms emulsified droplets in the order of micrometres. The particle wettability (described by the hydrophilic-lipophilic parameter) is analogous to the three-phase contact angle of a solid particle on a planar fluid-water interface. The contact angle is measured at the water phase (θ_w), and given by Young's equation (Equation 2.1). Where $\gamma_{\frac{s}{o}}$, $\gamma_{\frac{s}{w}}$ and $\gamma_{\frac{o}{w}}$ are the interfacial energies at the solid/oil, solid/water and oil/water interfaces, respectively. For more lipophilic particles θ_w >90˚ and most particles are wetted by the oil phase. The opposite is true for hydrophilic particles where θ_w <90˚ and most particles are wetted by the water phase. Particles wetted by both phases result in θ_w ≈90˚, where the oil/water interface is planar (Figure 2.8).[22,31,32]

$$Cos\theta_{w} = \frac{\gamma_{\frac{s}{o}} - \gamma_{\frac{s}{w}}}{\gamma_{\frac{o}{w}}} \tag{2.1}$$

Young's equation.

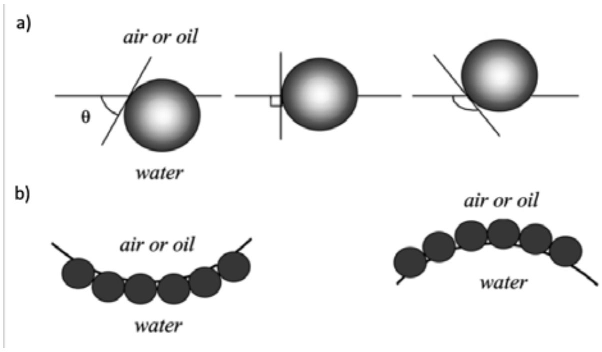

Figure 2.8: a) position of solid spherical particle on the air or oil and water interfaceθ_w <90˚ (left), $\theta_w \approx$ 90˚ (centre) and θ_w >90˚ (right), b) Possible positions of particles at a curved fluid-water interface corresponding to their contact angle θ_w .[22]

Optimum stability is reached when θ_w approaches 90˚ whilst retaining preferential wettability in different phases. For solid particles smaller than 2 µm in size, the gravitational effect can be ignored, and the energy ΔE required to remove a solid spherical particle from the oil water interface can be calculated by equation 2.2,[22] where r is the radius of the particle.[22,31]

$$\Delta E = \pi r^2 \gamma_{\frac{o}{w}} (1 \pm cos\theta_w)^2 \qquad (2.2)$$

The energy of adsorption of a particle to the water/oil interface is always greater than its thermal energy, and therefore once attached to the interface the solid particle can be considered irreversibly adsorbed. Pickering emulsions possess many of the same basic principles of other emulsifiers, and when compared to surfactants would be expected to exhibit much higher stability due to the relatively fast adsorption and desorption rates of surfactants from the interface. In addition to the contact angle, the stability of Pickering emulsions is also influenced by the particle size, shape, concentration, ionic strength and composition of the system as well as the ratio of water to oil phase.[22,33,34] Silica colloidosome assembly is carried out by the established method used by Mann et al. which is described in the Materials and Methods section of this chapter.

2.2.7. Colloidosome Cross-Linking

Cross-linking of colloidosomes is important to allow the transfer of the colloidosomes and the encapsulated species into aqueous medium. Tetramethylorthosilicate (TMOS) was used as a cross-linking agent for the silica nanoparticles. A series of hydrolysis and condensation reactions take place at the water droplet/oil interface (Figure 2.9). The hydrolysis of TMOS (Equation 2.3 – 2.5) produces methanol as a by-product. During the reaction, partially hydrolysed TMOS might be present where n proceeds from 1 to 3. Through a complete hydrolysis reaction mono-silica monomers dimerise.[35] Partially hydrolysed TMOS also dimerises and generates a 3D silica network. This cross-links the colloidosome shell, leaving pores of 3–5 nm in size.[26,30] Cross-linking of the membrane and resultant pore-diameters are dependent on many variables including pH, ionic strength, the buffer in use, and the molar ratio between TMOS and water.[35]

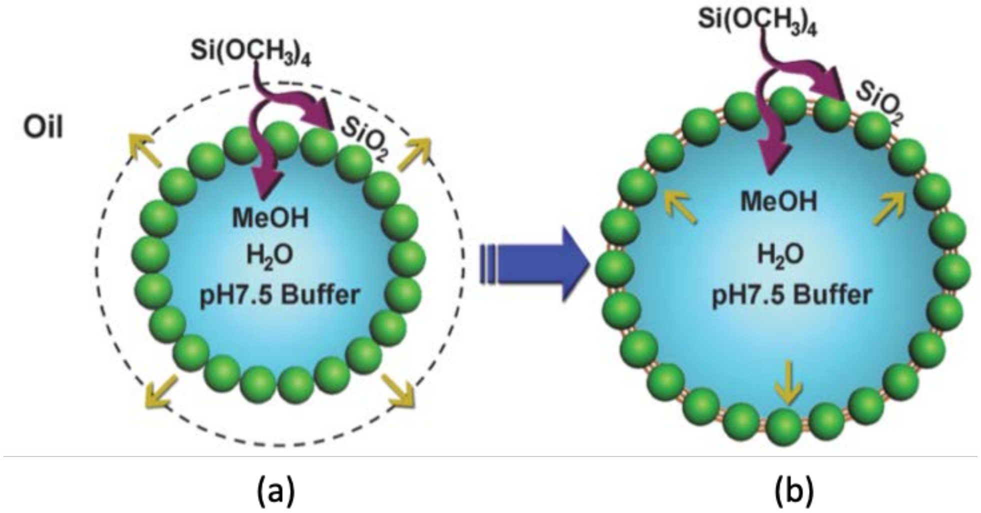

Figure 2.9:Cross-linking of silica nanoparticle membrane of colloidosomes by TMOS[26] (a) The oil phase contains silica collloidosomes formed by self-assembly. The addition of TMOS to the oil phase causes the formation of silica oligomers at the oil/water interface and the production of methanol which diffuses into the interior of the colloidosomes causing an expansion in size, (b) The nanoparticle membrane cross-links with the silica oligomers which stabilises the internal compartment as the volume expands and internal pressure increases.

$$Si(OCH_3)_4 + 4H_2O \rightarrow Si(OH)_4 + 4CH_3OH \quad (2.3)$$

$$Si(OCH_3)_4 + nH_2O \rightarrow (H_3CO)_{4-n}Si(OH)_n + nCH_3OH \qquad (n = 1 – 3) \quad (2.4)$$

$$Si(OH)_4 + Si(OH)_4 \rightarrow (HO)_3Si\text{-}O\text{-}Si(OH)_3 + H_2O \quad (2.5)$$

2.2.8. Proteins

2.2.8.1. Lysozyme

Lysozyme is a relatively small protein, with a single polypeptide chain consisting of 129 amino acids (M_w = 14600 Da).[36,37] Figure 2.10a demonstrates the structure of lysozyme obtained by pulsed liquid droplet and x-ray free electron laser.[38] Lysozyme is also stable over a wide range of pH and temperature ranges, with 10-12 positive charges at pH 4.5 and can be crystallised to a variety of polymorphs including tetragonal, monoclinic and triclinic (Figure 2.11).[39–41] The most common tetragonal polymorph (space group $P4_32_12$) contains distinct uni-directional solvent-channels, aligned parallel to the crystallographic c-axis which are 1-2.5 nm in diameter. Each solvent channel is positioned in the centre of the unit cell and surrounded by four protein molecules.[37,42] Figure 2.10b demonstrates the location of major solvent channels in a tetragonal lysozyme crystal lattice, generated from XRD data.[42,43]

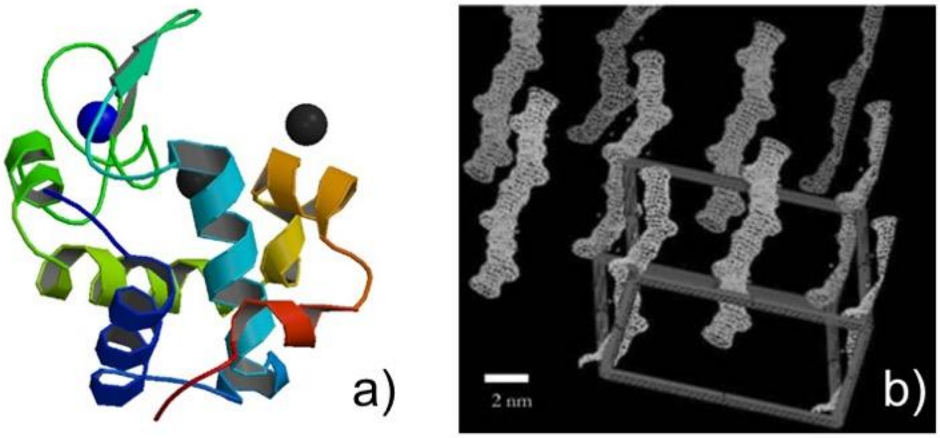

Figure 2.10: a) Structure of hen egg-white lysozyme obtained by pulsed liquid droplet by Mafune et al.,[38] b) Solvent channels within tetragonal lysozyme crystals generated from XRD data.[42]

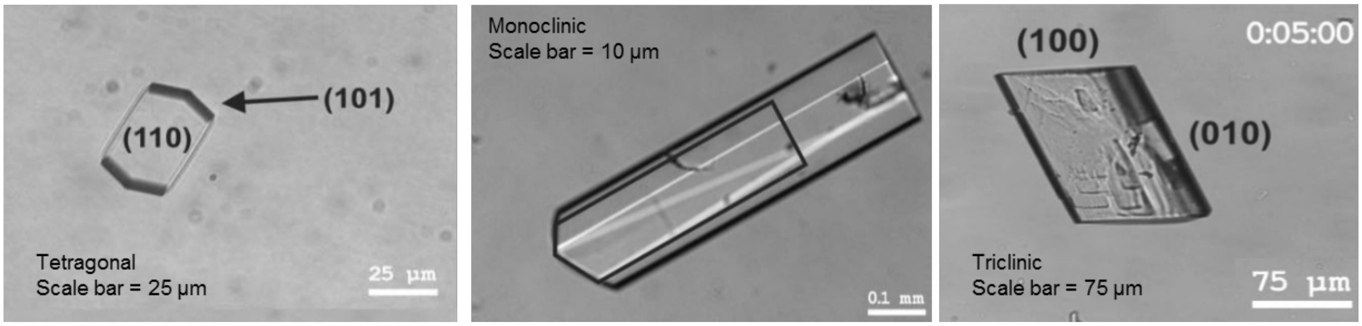

Figure 2.11: Polymorphs of lysozyme adapted from Heijna et al 2007;[41] from left to right: tetragonal, monoclinic, and triclinic.

2.2.8.2. Ferritin

Ferritin is a large, hollow 450 kDa globular protein consisting of 24 identical 174 residue long subunits arranged in an octahedral complex. Produced by almost all living organisms it is the primary intracellular iron-storage protein. Ferritin was selected as it is amongst one of the most readily crystallised proteins, crystallising almost immediately in the presence of Cd^{2+} ions. Equine spleen ferritin was used in the investigations, the biological assembly of which is shown in Figure 2.12.

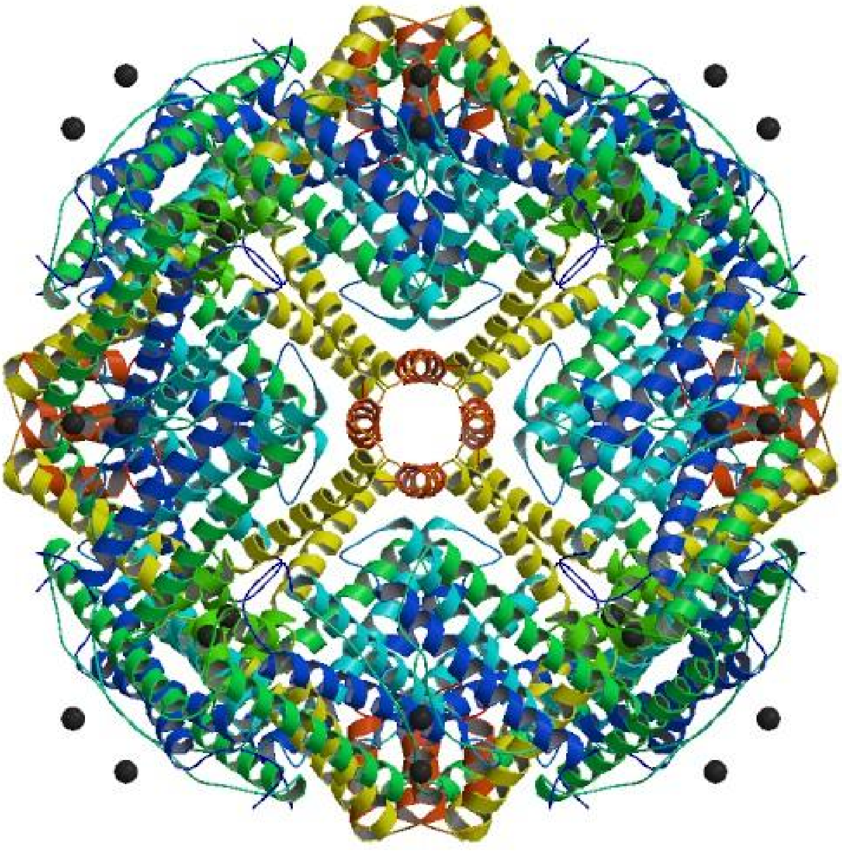

Figure 2.12: Biological assembly of equine spleen ferritin.[44] The ferritin shell is comprised of 24 protein subunits (apoferritin) and a core of Fe^{3+} ions.

2.3. Materials and Methods

2.3.1. Protein Crystallisation and Cross-Linking in Bulk

Investigations were carried out using optical microscopy as the primary tool. Samples were prepared by pipetting aliquots of the samples onto a glass slide and imaged using a Leica DMI3000B Fluorescence Optical Microscope. Lysozyme protein crystallisation and cross-linking in bulk is illustrated in Scheme 2.2.[1] Protein crystallisation was carried out using the batch crystallisation method described previously. A 10 mL protein crystallisation solution comprising of 60 mgL^{-1} NaCl, 8.2 mgL^{-1} NaOAc, and 17–20 mgL^{-1} of hen egg white lysozyme was prepared and adjusted to ~ pH 4 using 50% (v/v) of acetic acid. The crystallisation solution was filtered through a 0.45 µm syringe filter into a glass vial containing 10 mL of dichloromethane (DCM) and incubated at room temperature for 24–48 hours until the appearance of macroscopic crystals at the water/DCM surface. The aqueous and DCM supernatant were then removed, 10 mL of cross-linking solution was added (1-3 % glutaraldehyde, 60 mgL^{-1} NaCl, 8.2 mgL^{-1} NaOAc, adjusted to pH ~ 4.0 with 50% (v/v) acetic acid). The crystals were incubated in the cross-linking solution at room temperature for 24- 48 hours until the crystals turned pale yellow in colour. The crystals were then washed with deionised water several times and dried under vacuum for three hours at 40°C.

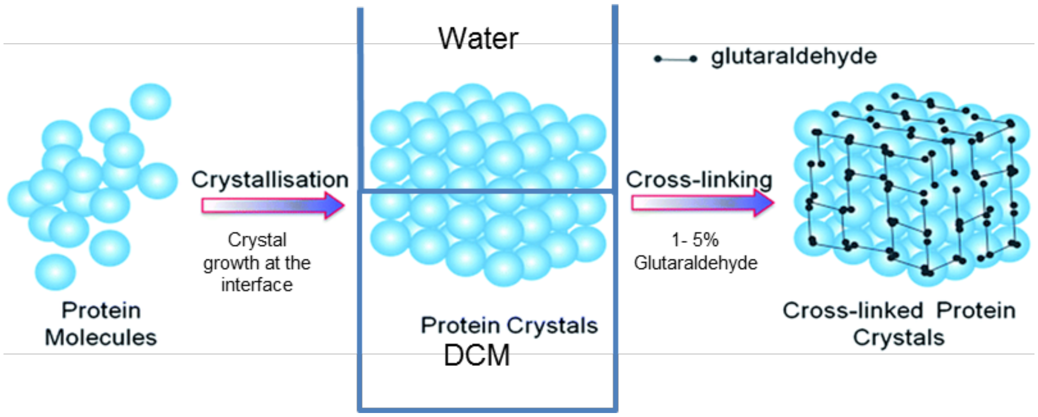

Scheme 2.2: Protein crystallisation at water/DCM interface and cross-linking with 1-5% glutaraldehyde. Adapted from Yan et al 2015.[1]

2.3.2. Assembly of the Colloidosomes

20 mg of silica nanoparticles were added to 2 mL of dodecane anhydrate (purchased from Honeywell Research Chemicals) and homogenised at 10,000 rpm for 30-60 s. 100 µL of protein crystallisation solution was then added and the solution was shaken by hand for 30-60 s (Scheme 2.3). The protein crystals in colloidosome (PCC) systems were then incubated at the appropriate temperatures and left undisturbed for different periods of time, which are mentioned in the 'Results and Discussion' sections of this thesis.

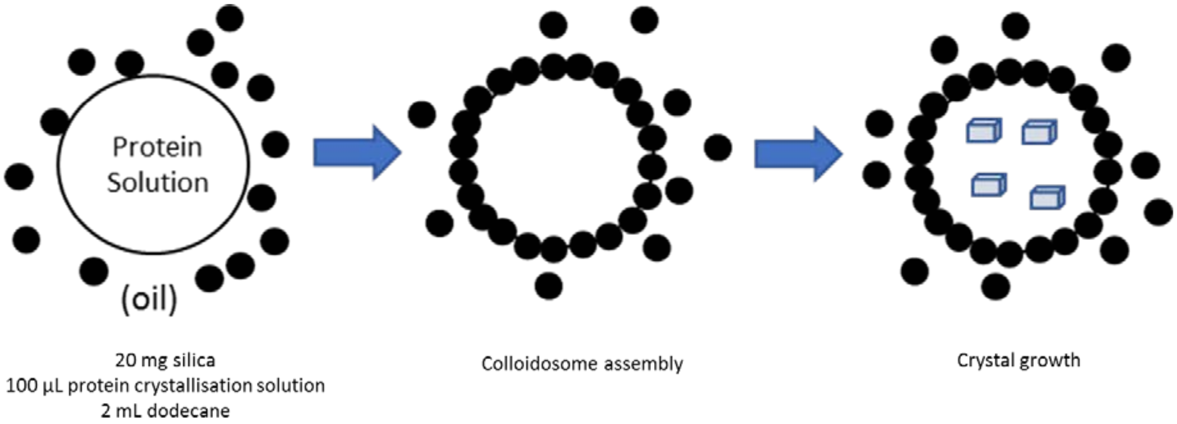

Scheme 2.3: Assembly of protein crystallisation solution in colloidosomes.

2.3.3. Cross-Linking of Colloidosomes

Colloidosomes were cross-linked using TMOS (purchased from Sigma). 15 uL of TMOS was added to 2 mL of PCC in dodecane. The lysozyme-colloidosome cross-linking was carried out at room temperature for 18 hours and then 36 hours. The ferritin-colloidosome system cross-linking was carried out at ~ 4˚C in the fridge for 42 hours and 4 days. Samples were left undisturbed throughout the cross-linking process.

2.3.4. Extraction of colloidosomes from oil into water

Extraction of colloidosomes was carried out after cross-linking with TMOS was completed. The point of complete cross-linking was determined by an increase in the roughness of the colloidosomes' shell and subsequent contraction of the colloidosome size and spherical shape, which was observed under optical microscope. Extraction into water was carried out by a multi-step centrifugation process. The colloidal dispersion was diluted with a non-aqueous phase (ethanol) and water with stepwise increase in the proportion of water to ethanol, with centrifugation carried out between each step. 200 µl of the colloidosome dispersion in dodecane was pipetted into an Eppendorf tube, with 1 mL of 7:3 ethanol to water solution. The mixture was centrifuged at 3000 rpm for 5 min, and the resulting layers of dodecane and supernatant were removed by careful pipetting. 1 mL of 1:1 ethanol to water solution was added and the centrifugation and removal of supernatant steps were repeated. 1 mL of water was then added, and the centrifugation and removal of supernatant were repeated under the same conditions. The colloidosomes were finally suspended in 1 mL of crystallisation buffer solution.

2.3.5. Lysozyme crystal growth in the presence of Au NPs and CDs

2.3.5.1. Synthesis of Gold Nanoparticles

The synthesis of these gold nanoparticles (Au NPs) was carried out using the Turkevich-Frens method by Ella Carter (BCFN) to prepare Au NPs which were 15-20 nm in diameter. All glassware was washed with concentrated hydrochloric acid followed by MilliQ water before use. 10 mg (0.025 mol) gold (III) chloride trihydrate were dissolved in 95 mL water in a conical flask. 1 % w/v solution of sodium citrate dihydrate solution (0.1 g in 10 mL Milli Q) was prepared. 5 mL 1% sodium citrate solution was quickly added to the gold (III) chloride trihydrate solution. The solution was heated for 15 min. Once cooled the solution was transferred to vials and stored in the dark at 4°C.

The synthesised Au NPs were 18.3 ± 1.7 nm in diameter as measured by TEM (Figure 2.13). The average hydrodynamic radius of the Au NPs was 28.88 ± 0.35 nm and zeta potential were measured to be -28.9 ± -4.9 mV.

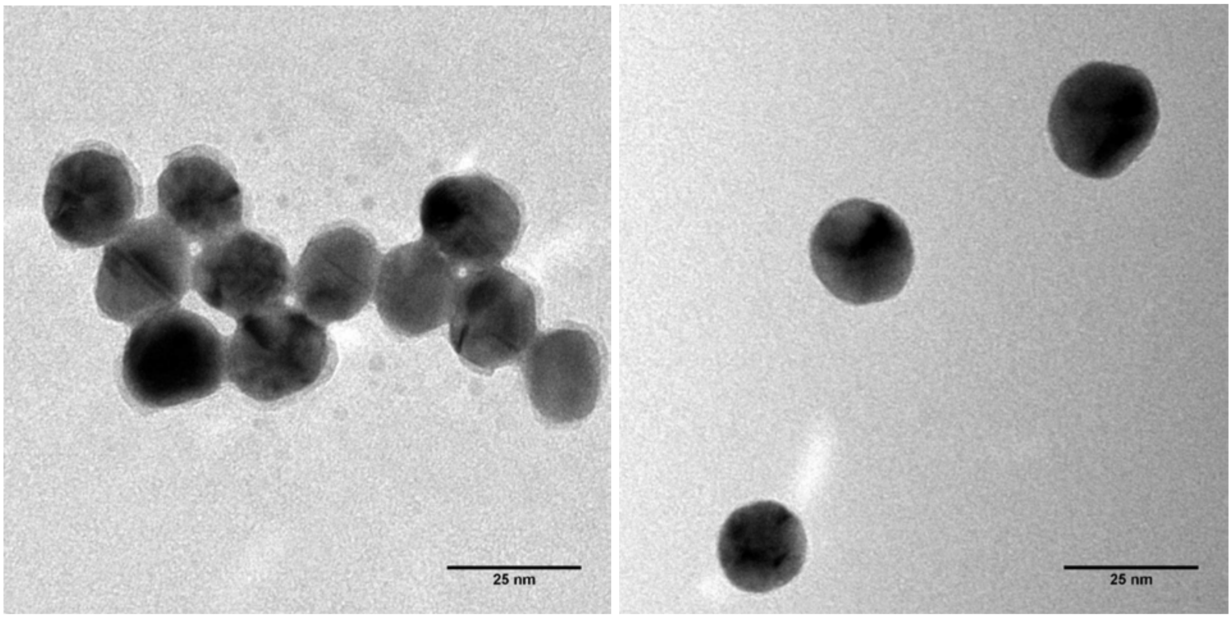

Figure 2.13: TEM images of gold nanoparticles synthesised using the Turkevich-Frens method by Ella Carter; scale bar = 25 nm.

2.3.5.2. Synthesis of Carbon Dots

Chapter 3 of this thesis summarises the synthesis method and characterisation techniques used to synthesise N-doped carbon dots (N CDs) and N- and S-doped carbon dots (NS CDs).

2.3.5.3. Ferritin Crystallisation

Ferritin crystal growth was investigated using two discrete crystallisation systems S1 (20 mg/ml Ferritin, 60 mg/ml $CdSO_4$, 0.8 M $(NH_4)_2SO_4$, 0.1 M Tris, pH 7.5) and S2 (50 mg/ml Ferritin in 150 mM NaCl with 60 mg/ml $CdSO_4$, 0.1M NaOAc in 0.1 M HEPES buffer at pH 7.5). Vapor diffusion hanging drop (VDHD) crystallisation of ferritin was set up as the control experiment. Ferritin growth inside colloidosomes was carried out using 100 ⌠m of the protein crystallisation solutions S1 and S2 as the aqueous phase to assemble colloidosomes by the method described in section 2.2.

Other proteins which were investigated for crystallisation inside colloidosomes included bovine liver catalase (BLC) and mCherry. The crystallisation system used for BLC was 0.05 M sodium phosphate pH 6.8, 12% PEG4000. The crystallisation system used for mCherry was 100 mM NaOAc, 100 mM Tris pH 8.5, 30% PEG4000.

2.3.5.4. Confined Growth of Lysozyme Crystals in the Presence of Au NPs and CDs

The lysozyme protein crystallisation solution was added to the silica dodecane suspension and shaken by hand for 30-60 s to assemble colloidosomes as described in section 2.2 ‘Assembly of the colloidosomes’. 100 µL of lysozyme crystallisation solution (20 mg mL^{-1} lysozyme, 60 mg mL^{-1} NaCl and 8.2 mg mL^{-1} NaOAc buffer at pH 4.08) were added to 2 mL of silica-dodecane suspension (10 mg mL^{-1}). The volumes of gold nanoparticle solution, N CDs and NS CDs solution added are summarised in Table 2.2. All samples were stored at room temperature and batch crystallisation samples of lysozyme were prepared as described in section 2.1 ‘Protein crystallisation and cross-linking’, as a control with the addition of volumes of CDs and Au NPs recorded in Table 2.2.

Table 2.2: Preparation of functionalised lysozyme crystals inside colloidosomes.

Sample	***Sample name***	***Sample Number***			
		1	2	3	4
		Volume of sample added [µL]			
Au NPs (Batch)	A	20	40	60	80
Au NPs (Colloidosomes)	B	10	20	30	40
N CDs (Batch)	C	20	40	60	80
N CDs (Colloidosomes)	D	10	20	30	40
N S CDs (Batch)	E	20	40	60	80
NS CDs (Colloidosomes)	F	10	20	30	40

2.4. Results and Discussion: Colloidosomes as Reaction Vessels for Protein Crystal Growth

2.4.1. Influence of Crystallisation Conditions on Lysozyme Crystal Growth

Lysozyme crystallisation inside colloidosomes was carried out, with the method used analogous to reduced volume batch crystallisation. The method was highly reproducible, with protein crystal growth observed within 12 hours of incubation of the protein crystallisation solution inside the colloidosomes. Samples were stable for up to 8 months (Figure 2.14). Crystallisation inside the colloidosomes was investigated at different temperatures, and concentrations against a control of batch crystallisation of lysozyme crystal on a water/dichloromethane (DCM) interface. The size, shape and location of crystals grown inside colloidosomes were investigated. Investigations were carried out using optical microscopy as the primary tool.

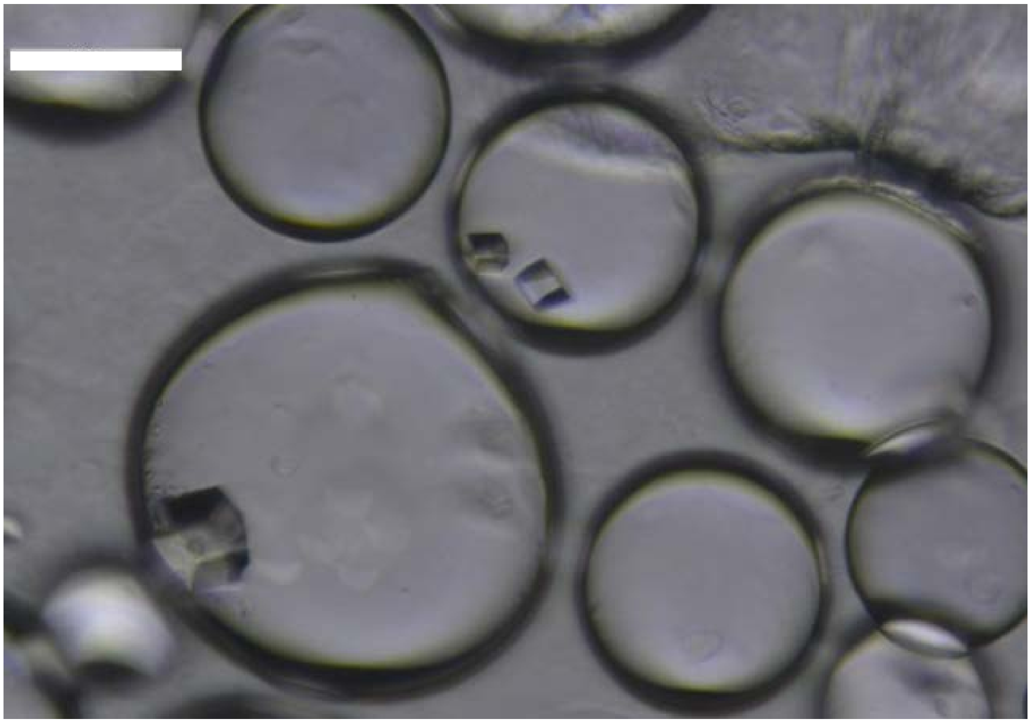

Figure 2.14: Optical microscopy image of lysozyme crystal growth observed inside colloidosomes. Scale bar = 100 µm.

2.4.1.1. Temperature

Lysozyme crystallisation was carried out inside silica colloidosomes and at the interface between water and DCM (control) at room temperature and at 4˚C. Optical micrographs of the lysozyme crystals grown under these conditions are shown in Figure 2.15, following 48 hours of incubation. At room temperature, crystals grown inside colloidosomes were stable for up to four weeks. Crystals grown on the water/DCM interface were also stable for up to four weeks but were very fragile and broke upon contact. Crystals grown inside colloidosomes at 4˚C displayed morphologies akin to 'sea urchin' morphologies[45] and were stable for up to four weeks of incubation time. The sea urchin morphology has been observed in investigations using different heterogenous nucleation sites to investigate the nucleation and growth of lysozyme crystals.[45] The sea urchin structures demonstrated potential crystallinity and uniformity in the direction of growth from a central nucleus. Crystals grown at the interface of water/DCM were subjected to Ostwald ripening and dissolution within 48 hours of incubation.

The transition of tetragonal lysozyme crystals to sea urchin-like particles made of crystalline needles has been observed by Lorber et al. in 1996.[46] This effect was observed when an increase in hydrostatic pressure was applied, which caused an increase in protein solubility and a decline in the number of tetragonal lysozyme crystals in favour of the crystalline needles. The changes in solubility and consequent crystallisation are attributed to minor reversible changes in the protein caused by changes in pressure.[46]

Temperature influences the solubility of the protein in solution, as observed with increased Ostwald ripening at 4˚C compared to room temperature in the control crystallisation experiment (water/DCM interface). The decrease in temperature from room temperature to 4˚C caused an increase in the hydrostatic pressure, due to the increase in density of water. The change in hydrostatic pressure is more significant in colloidosomes due to the small size of the liquid droplets containing the crystallisation solution, therefore resulting in the formation of crystalline needles. To corroborate this theory, further investigation into the changes to hydrostatic pressure against changes in temperature of the aqueous droplets inside colloidosomes is required.

In addition to the effect of hydrostatic pressure, the presence of these sea urchin needle-like crystals is due to the formation of a single crystal nucleus on a surface (evidently the silica nanoparticles, indicated by the proximity of the needle-like crystals to the silica membrane) by heterogenous epitaxy. This forms an active crystal which is deficient of nutrients for crystal growth on the face of attachment to the substrate. Other faces of the crystal are able to expand and grow, which creates significant strain on the crystal lattice causing it to ‘splinter’ and grow multiple separate crystals in different directions, giving rise to the ‘sea-urchin’ morphology observed. A suggested method to overcome this effect would be to introduce seeds of previously formed crystals where the strain induced on the crystal lattice due to surface attachment is not present. This may allow the isolation of these two effects to better determine the effect of temperature on crystal growth within colloidosomes more effectively. However, it is important to consider that seeding also introduces a new set of issues and variables relating to seeding and micro-seeding effects which must be considered. These issues are not discussed in detail as they are beyond the scope of this work.[47] In addition to the temperature-dependent effects observed, the size of lysozyme crystals grown inside colloidosomes were observed to be 10-20 times smaller than those grown by batch crystallisation on the surface of water/DCM. This effect is highly significant as a means towards controlled and predictable protein crystallisation and further emphasises the value of this technique as a novel crystallisation technique.

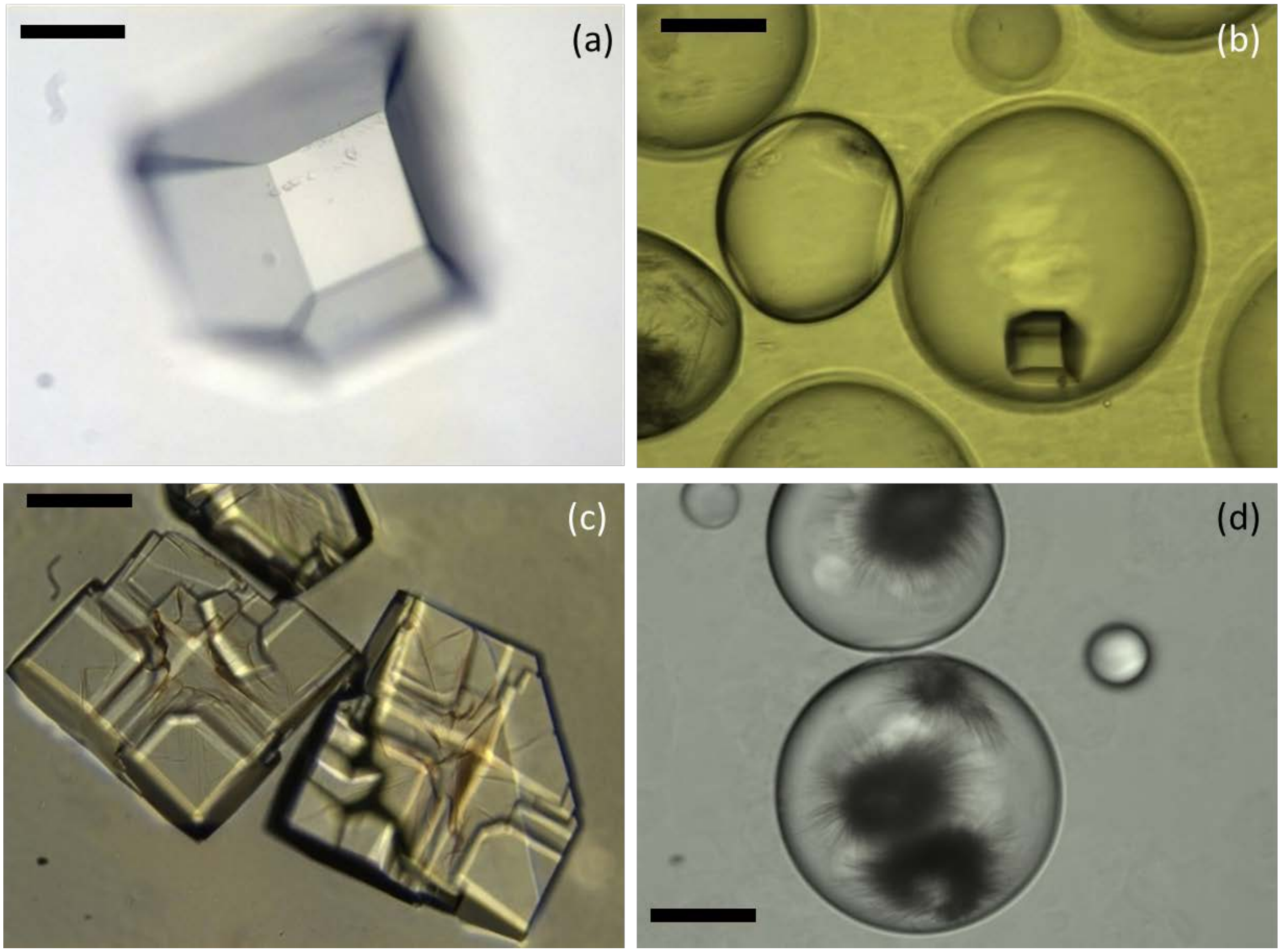

Figure 2.15: Optical microscopy images of lysozyme crystallisation. Images taken 48 hours after incubation. (a) batch crystallisation on water/DCM interface at room temperature. (b) crystallisation inside colloidosomes at room temperature; (c) batch crystallisation at water/DCM interface at 4˚C . (d) crystallisation inside colloidosomes at 4˚C . Scale bar = 100 μm.

2.4.1.2. Lysozyme Concentration

In addition to temperature, the concentration of protein and availability of protein molecules affects the diffusion and solubility gradient, therefor having a significant effect on the protein crystallisation. The effect of protein concentration on the growth of lysozyme crystals inside colloidosomes was investigated (Figure 2.17). The increase in protein concentration was observed to cause a change in crystal morphology. This is due to the concentration-dependence of crystal growth rates for different crystallographic faces. The crystalline faces are illustrated in Figure 2.16.[46,48]

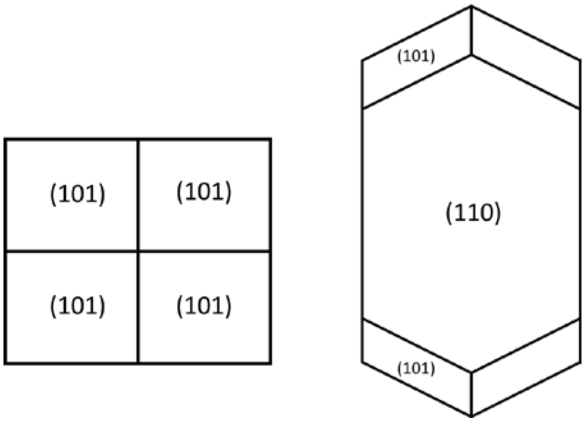

Figure 2.16: Crystalline faces of lysozyme crystals.

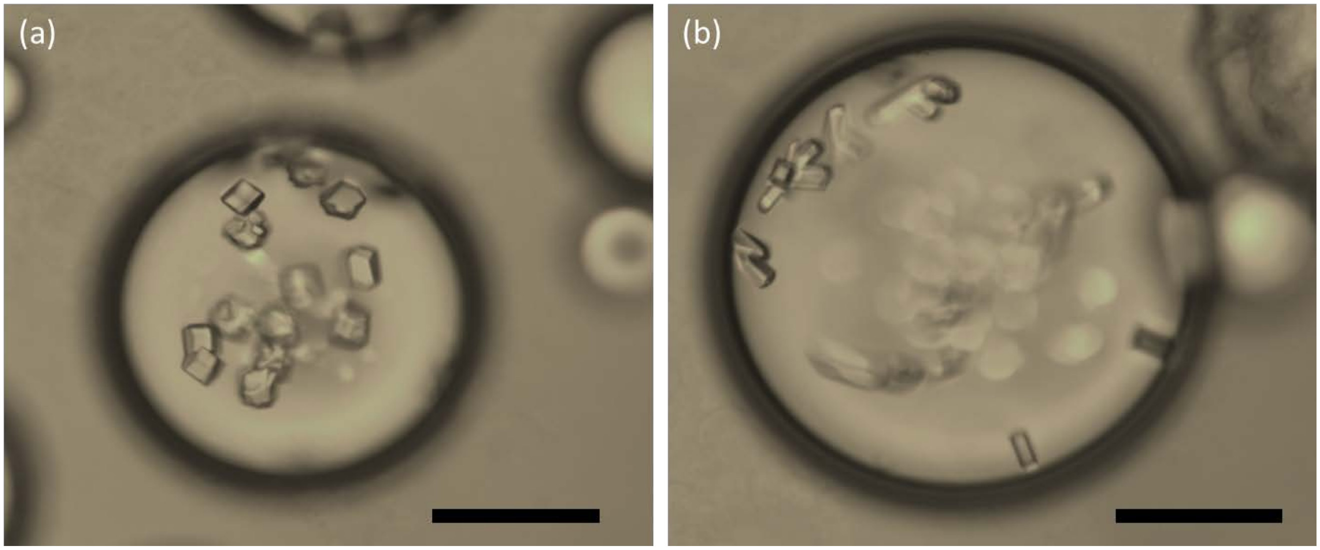

Figure 2.17: Lysozyme crystallisation in colloidosomes with varying concentrations of lysozyme. (a) 0.17 mg/mL; (b) 0.21 mg/mL. Images taken after 4 days of incubation. Scale bar = 100 µm.

The increase in protein concentration is observed to favour the growth of the (110) face over that of the (101) face, resulting in elongated crystals as observed in Figure 2.17. This result was not observed in batch crystallisation as the concentration of lysozyme added was varied from 0.17-0.22 mg/mL. Further investigation is required to determine the ratio of growth of these two phases in response to changes in protein concentration, as well as changes in salt concentration and pressure.

2.4.1.3. Nucleation and crystallisation phase

In order to investigate the effect of the interface on crystal growth, particularly the nucleation stage, an experiment was designed whereby aliquots of a protein crystallisation solution on the surface of water/dodecane (t_s) were isolated at hourly intervals. The aliquots taken at these intervals were used to assemble colloidosomes with the aliquot acting as the aqueous phase and dodecane as the oil phase. The experimental set up is illustrated in Scheme 2.4. The aliquots taken at the dodecane/water interface were used to mimic the biphasic system present in colloidosomes in the absence of silica particle emulsifiers. The t_s solution was used to prepare two samples of protein crystals in colloidosomes. The first sample (t_0) was prepared with t_s immediately. The second sample (t_n) was prepared 5 hours from the start of incubation to model crystal growth between the labile and metastable phase (post-nucleation). Colloidosomes containing the lysozyme crystallisation solution using aliquots from t_s were assembled using the method previously described. All three samples were incubated at room temperature in a sealed glass vial and left undisturbed. Experiments were carried out whereby t_n was maintained at room temperature and only disturbed between 0-5 hours at 1-hour intervals to take aliquots of the protein crystallisation solution at the interface. Aliquots taken between t = 1–5 hours yielded similar results to those observed at t_0 and are not presented.

This investigation was carried out to investigate the possibility of isolating the stages of nucleation and growth during the protein crystallisation process inside colloidosomes.

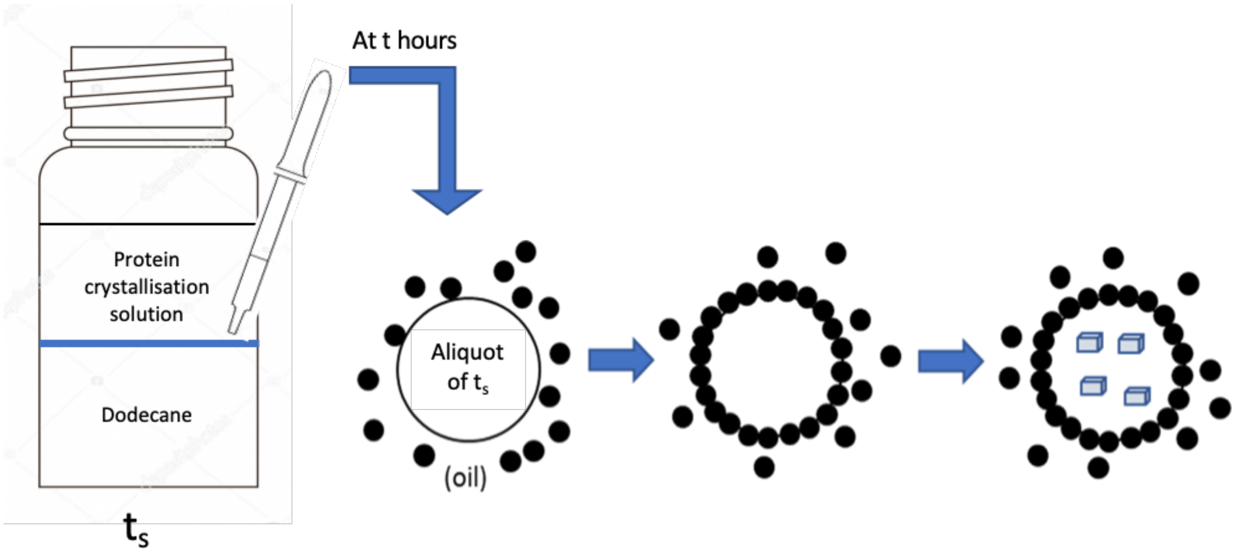

Scheme 2.4: Experimental set-up to investigate the effect of nucleation and crystallisation phase on the protein crystal growth of lysozyme inside colloidosomes.

The protein crystallisation solution prepared at the water/dodecane interface showed the two phases to be completely separated with dodecane settling at the top layer, and the aqueous phase settling at the bottom. Protein crystallisation occurred only in the aqueous phase, with crystals forming along the sides and at the bottom of the glass vial. The experiments were investigated by optical microscopy (Figures 2.18, 2.19, 2.20) with images taken after 14 days of incubation. On comparing experiments t_0 and t_n, it appeared that crystals grown inside colloidosomes after 5 hours of incubation had a much higher aspect ratio of growth, with more occurrences of single crystal growth per colloidosome than in experiment t_0. This might imply that crystal growth inside the colloidosomes moves more rapidly between the labile and metastable regions, resulting in a larger number of smaller crystals forming. Crystal growth induced in colloidosomes after a certain point in time produced fewer, larger crystals. This would indicate that crystal growth inside the colloidosomes is perhaps taking place in the metastable region of the crystallisation phase diagram, with no additional nucleation taking place. The isolation of the protein solution into a confined volume post-nucleation reduces the volume of protein crystallisation solution and limits the amount of solute available, therefore isolating crystal growth at a particular point of the phase diagram for a longer time. This would mean that protein crystallisation solute material is favourably targeted towards crystal growth rather than the generation of additional nuclei; smaller crystals or precipitates present in the solution are sacrificed towards the growth of the larger, existing crystals (Ostwald ripening). The shape of crystals formed in t_s had lower aspect ratios than those grown inside colloidosomes, indicating that the encapsulation of the protein crystallisation solution within colloidosomes affects the rate of growth of crystal faces differentially, resulting in different crystal morphologies. These morphologies appear to be tetragonal in t_s, elongated tetragonal in t_0 and monoclinic in t_n to the closest approximation, however, further investigation and resolution of the crystallographic structure is required to confirm this.

These results support the theory that perhaps some of the lysozyme in the crystallisation solution which passes through dodecane during the process of colloidosome assembly becomes denatured. The denatures lysozyme then serves as a homogenous nucleation site for the growth of the lysozyme crystals. However, it is not possible to isolate the influence of potentially denatured lysozyme from the silica colloidosome membrane which may additionally serve as a heterogenous nucleation site for lysozyme crystal growth. Further investigation utilising the principles of this experiment is required to gain a better understanding of crystal growth inside colloidosomes. In addition, investigations are needed into the effect of isolating stages of protein crystallisation and 'seeding' using denatured lysozyme crystals at different points during the crystallisation process to control the size and morphology of crystals grown. The isolation of the stages of protein crystal growth to better understand the crystallisation process is very complex and requires a high degree of control and advanced monitoring at very high resolution without disrupting the experimental set-up. This was unfortunately not possible to develop within the time-frame of this project, and so is beyond the primary scope of this work.

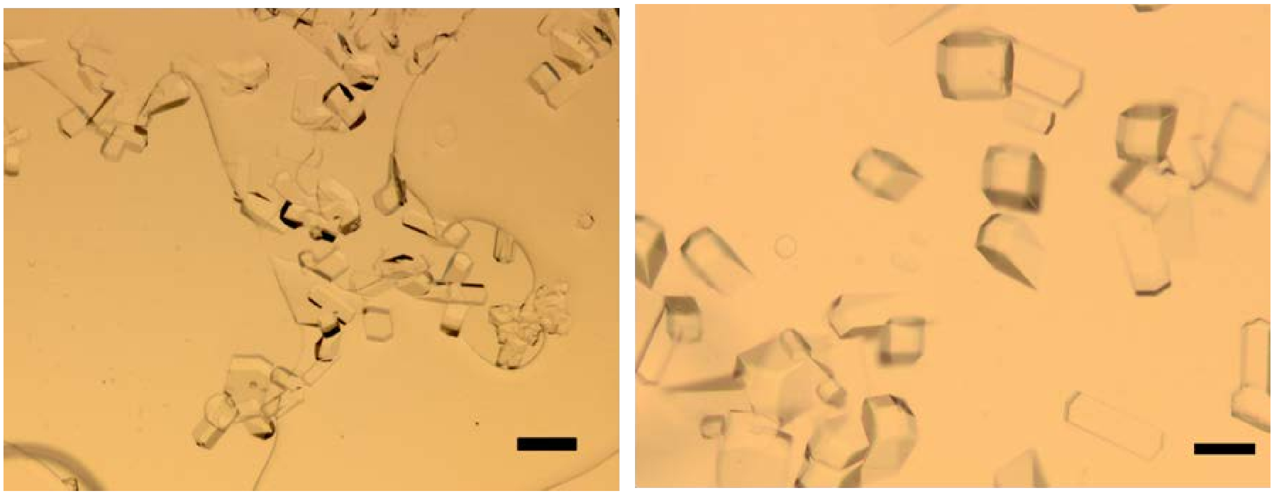

Figure 2.18: Optical microscopy image of native lysozyme crystals grown in the aqueous phase of a biphasic system of dodecane and water (containing protein crystallisation solution). Left image (x4 magnification, scale bar = 100 µm). Right image (x10 magnification, scale bar = 50 µm).

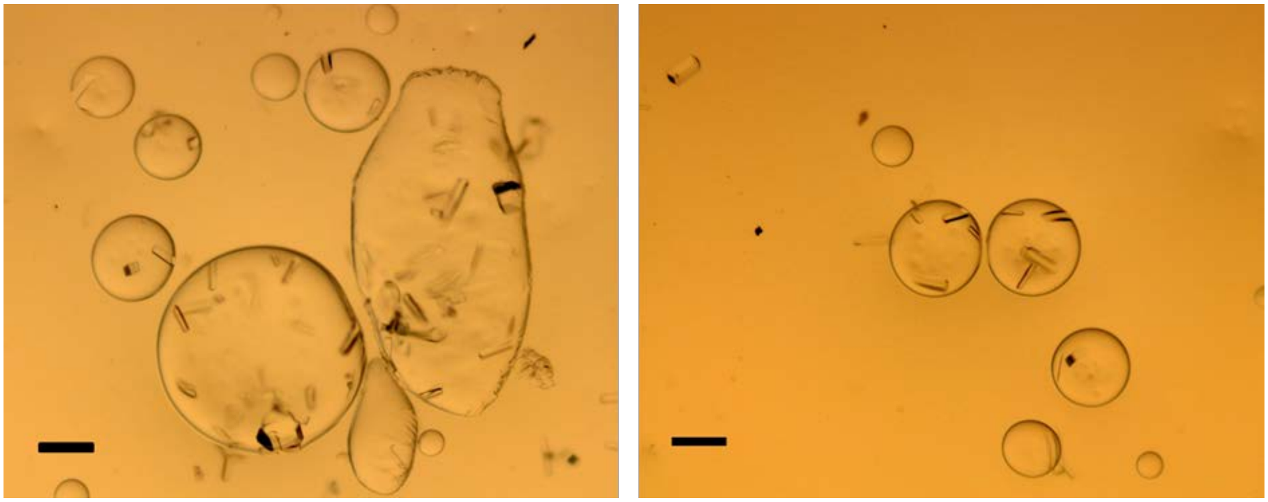

Figure 2.19: Optical microscopy image of t_0 experiment. Scale bar = 100 µm.

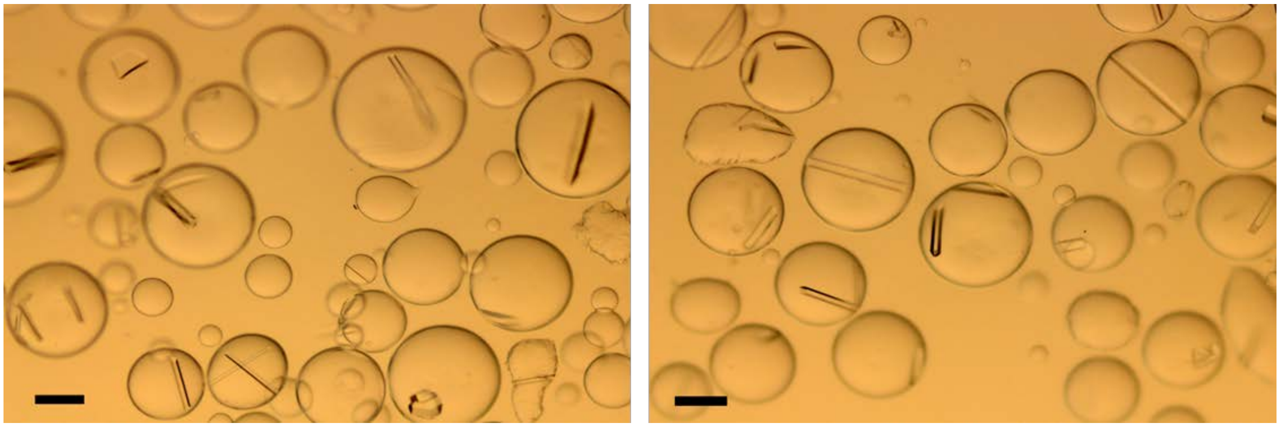

Figure 2.20: Optical microscopy images of t_n experiment. Scale bar = 100 µm.

2.4.1.4. Size, Shape and Location

Crystals grown inside colloidosomes were further characterised by statistical analysis of the number of crystals grown inside colloidosomes, their size, their shape, and their location within the colloidosomes. The analysis was carried out on a single sample of lysozyme crystals grown inside colloidosomes to obtain an idea of the size distribution, shape and location of the crystals. Images were taken following 21 days of incubation. Statistical analysis of the crystals was obtained with 14 samples of lysozyme crystals grown inside the colloidosomes with 240 images taken using an optical microscope to obtain these results.

The number of crystals was plotted against the diameter of colloidosomes in which they were grown to get an idea of the minimum size (from the diameter) of colloidosome required for crystal growth, as well as to investigate the correlation between the diameter of colloidosomes and the number of crystals formed. This information would be useful for standardisation of the crystallisation process inside colloidosomes, through identifying a size range that is most suitable for protein crystal formation. It was observed that colloidosomes within the size range of ~100–200 µm contained 1–3 crystals on average. Colloidosomes of diameters between ~ 250-450 µm contained up to 9 crystals on average (Figure 2.21). This may indicate a critical droplet size required for protein crystallisation, where crystal growth was not observed in colloidosomes smaller than 100 µm. However, the absence of crystal growth in some colloidosomes larger than 100 µm in size indicates that the size of the colloidosome does not guarantee crystal growth in the encapsulated solution. A weak correlation between the average diameter of the colloidosome and the number of lysozyme crystals was observed. This may be simply due to the increased volume of protein crystallisation solution encapsulated in larger colloidosomes.

Further analysis of the critical colloidosome size for protein growth and whether there is a conclusive correlation between the size of colloidosomes and the formation of crystals is required, in addition to investigating the composition of droplets where crystallisation has occurred.

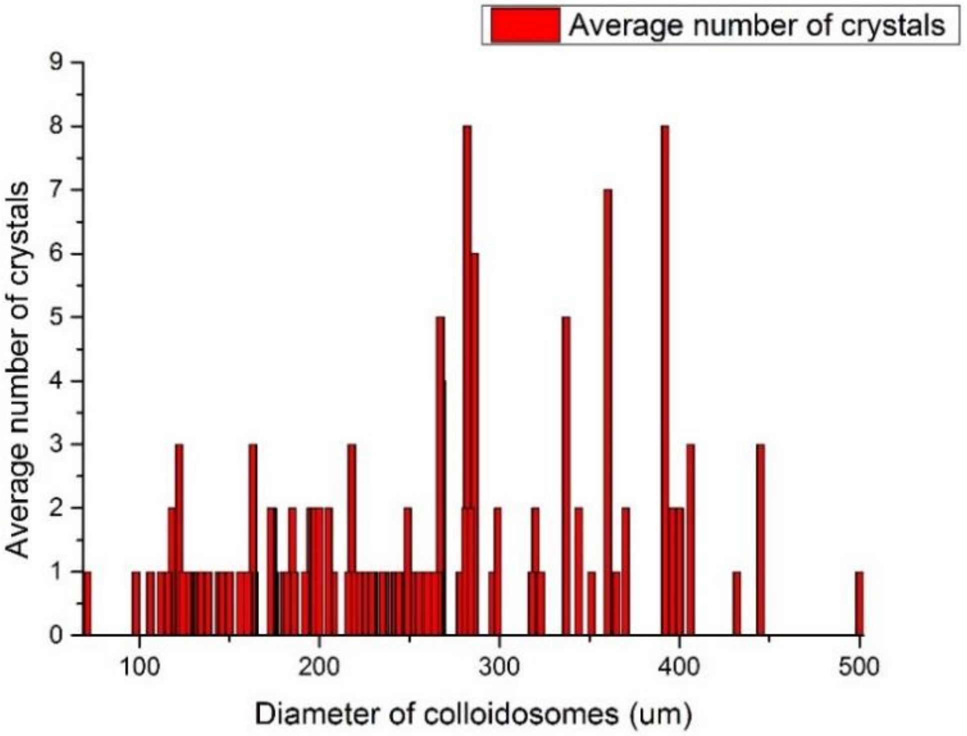

Figure 2.21: The average number of crystals grown was plotted against the diameter of the colloidosomes (µm) in which they were formed to demonstrate the probability of crystal formation in colloidosomes of different diameters.

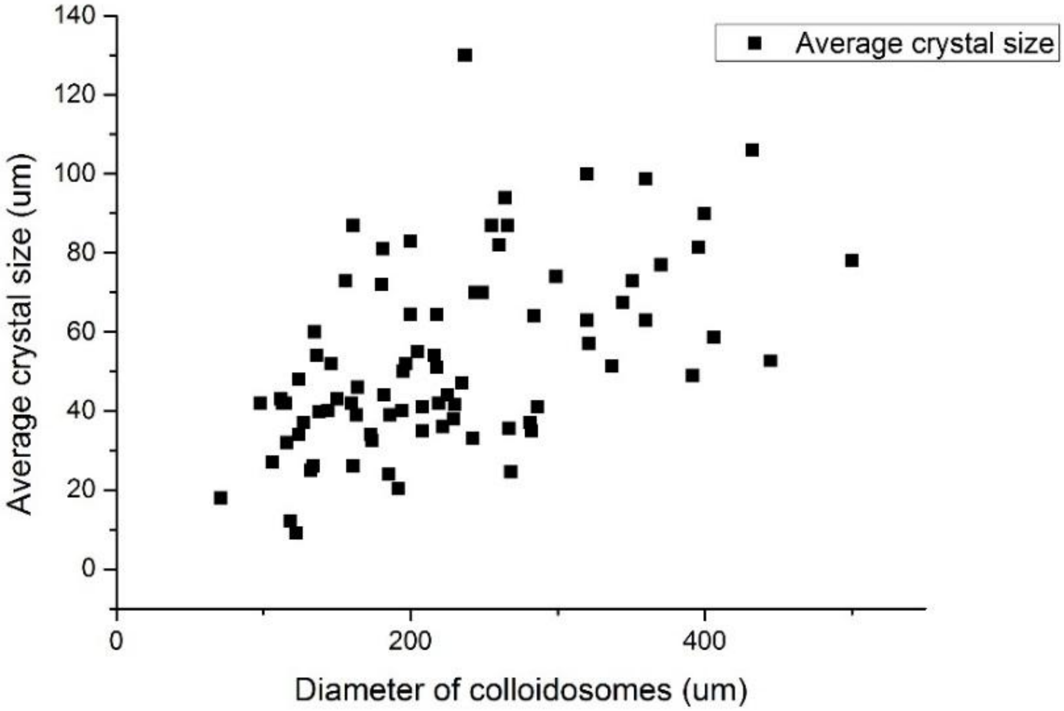

Figure 2.22: Average number of crystals formed plotted against the diameter of the colloidosomes to demonstrate any correlation between the size of the colloidosomes and the number of crystals formed.

Statistical analysis of the shape of crystals grown inside colloidosomes was carried out using optical microscopy images of the crystals. The shapes were classified as 'tetragonal', 'semi-tetragonal' in which (110) of the tetragonal crystal is elongated, 'plates/needles', referring to a combination of orthogonal plates and 'sea urchin' crystalline needles, and 'tetragonal pyramidal', which refers to elongated tetragonal morphologies where the (101) face is also elongated. Examples of crystals classified as such are demonstrated in Figure 2.23. Colloidosomes which did not exhibit crystal growth inside the microcapsule were excluded from this study. Analysis of the number of crystal shapes on average (Figure 2.24) and in total (Figure 2.25) was carried out for a sample size of 150 colloidosomes. The shapes were classified according to estimations in comparison to known crystal structures, however, 3D reconstruction modelling and/or XRD is required for accurate phase identification.

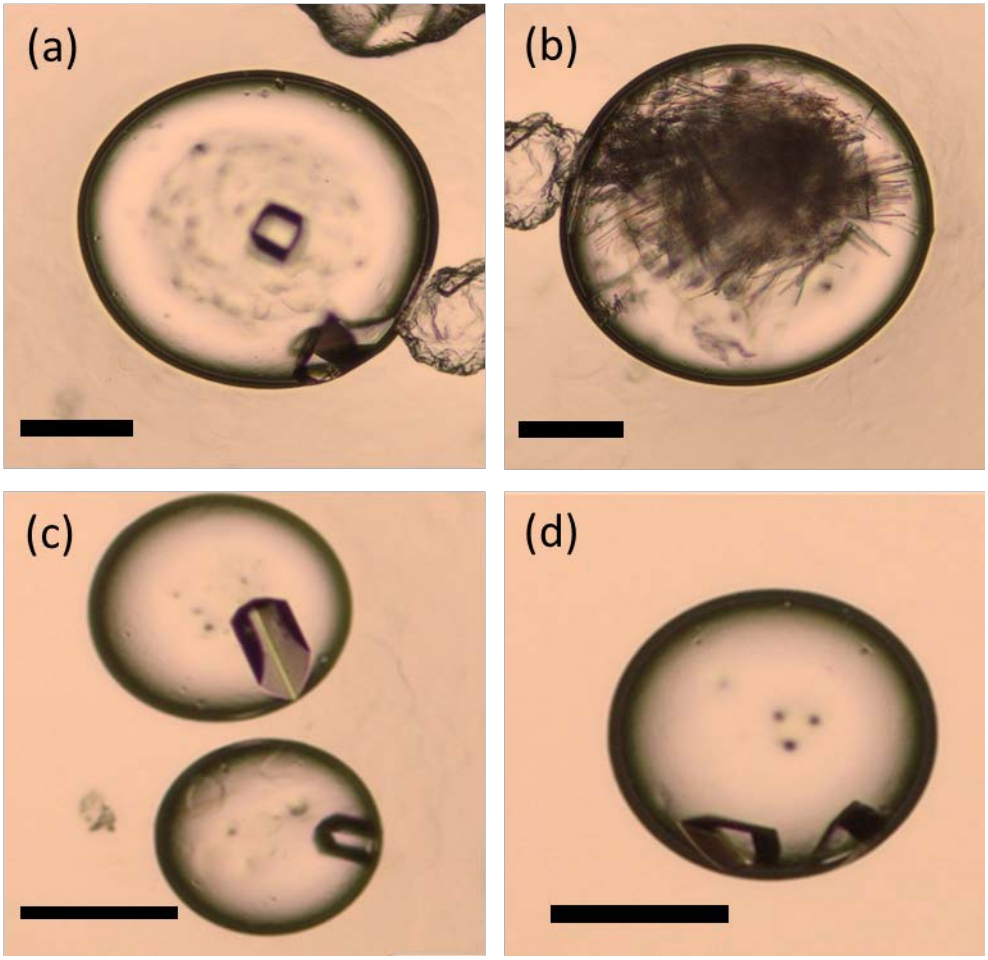

Figure 2.23: Examples of crystal shapes used in the shape classification to the best estimation in comparison to known crystal structures: (a) tetragonal; (b) plates and needles; (c) semi-tetragonal; (d) tetragonal pyramidal. Scale bar = 100 µm.

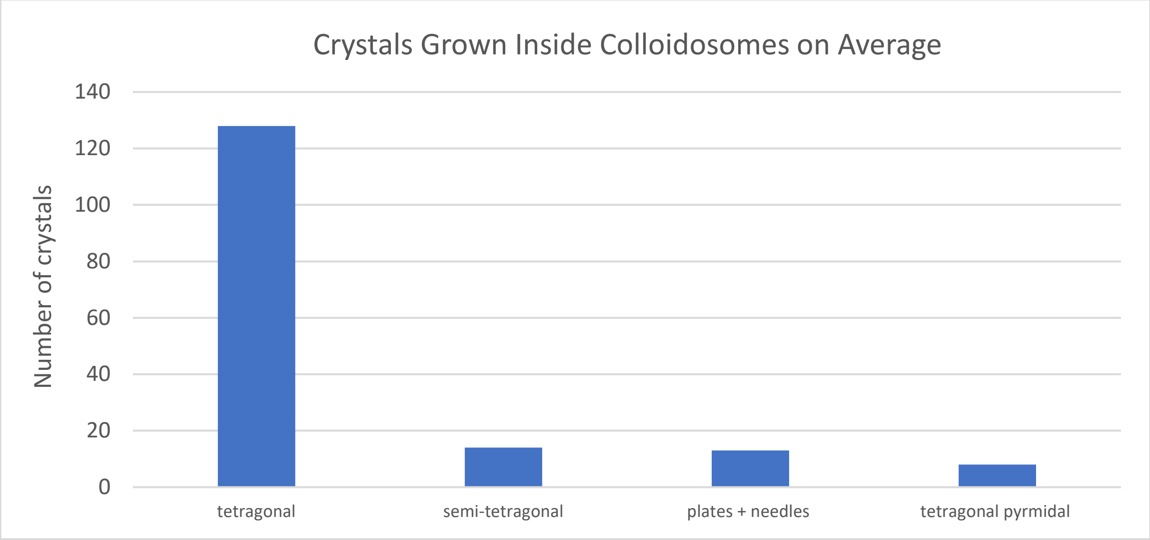

Figure 2.24: Number of crystals of classified shapes on average.

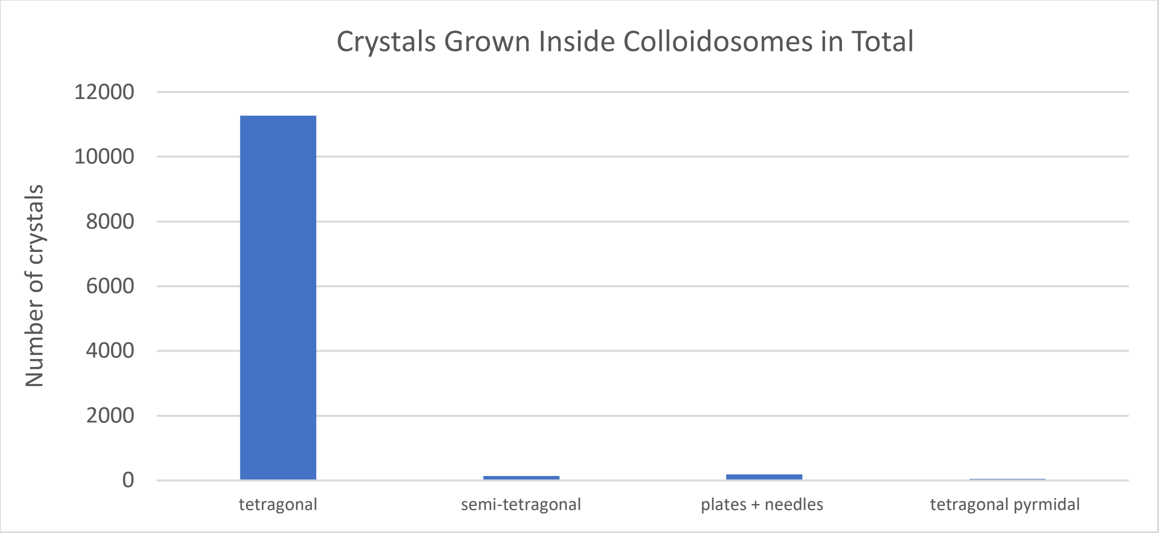

Figure 2.25: Number of crystals of classified shapes in total.

The location of crystals grown inside the colloidosomes was investigated using optical microscopy. Images were taken at room temperature and the location of the crystals was defined in reference to their proximity to the silica membrane. Locations were characterised as ‘edge’ if the crystal was close to or in contact with the silica membrane, ‘centre’ if the crystal was located in the centre of the colloidosome and ‘floating’ if the crystal was located neither at the edge nor the centre of the colloidosome. An example of this classification is demonstrated in Figure 2.26. The crystal shapes were included in the classification as described in the previous section. The location of crystals within the colloidosomes for different shapes of crystals was plotted as shown in Figure 2.26. This investigation was carried out to determine the localisation of crystals within colloidosomes as a potential indicator of the role served by the silica membrane during the nucleation stage of crystallisation and to gain an insight into the potential diffusion mass transport taking place across the membrane and within the encapsulated droplet. The majority of crystals were observed to be located at the ‘edge’, followed by ‘floating’ with very few, only tetragonal crystals, found in the ‘centre’ of the colloidosome. This may suggest that the silica membrane provides a heterogeneous nucleation site for crystallisation. However, as the microscope images were taken with the colloidosome dispersion deposited onto a glass slide, and with their spherical three-dimensional shape taken into account, it may also be due to the sedimentation of the crystals to the bottom at random. Diffusion mass transport effects cannot be conclusively evaluated due to the microscope images taken without disruption of the colloidosome dispersion to observe how the crystals might move under convection flow. Further investigations into the growth and movement of crystals inside the colloidosomes is required. This would involve the standardisation of the process and the development of a device that allows the crystallisation process inside colloidosomes to be observed *in situ*. This could involve the design of a microfluidic chamber, which standardises the production of colloidosomes and contains a chamber in which the crystallisation process can be monitored *in situ*.

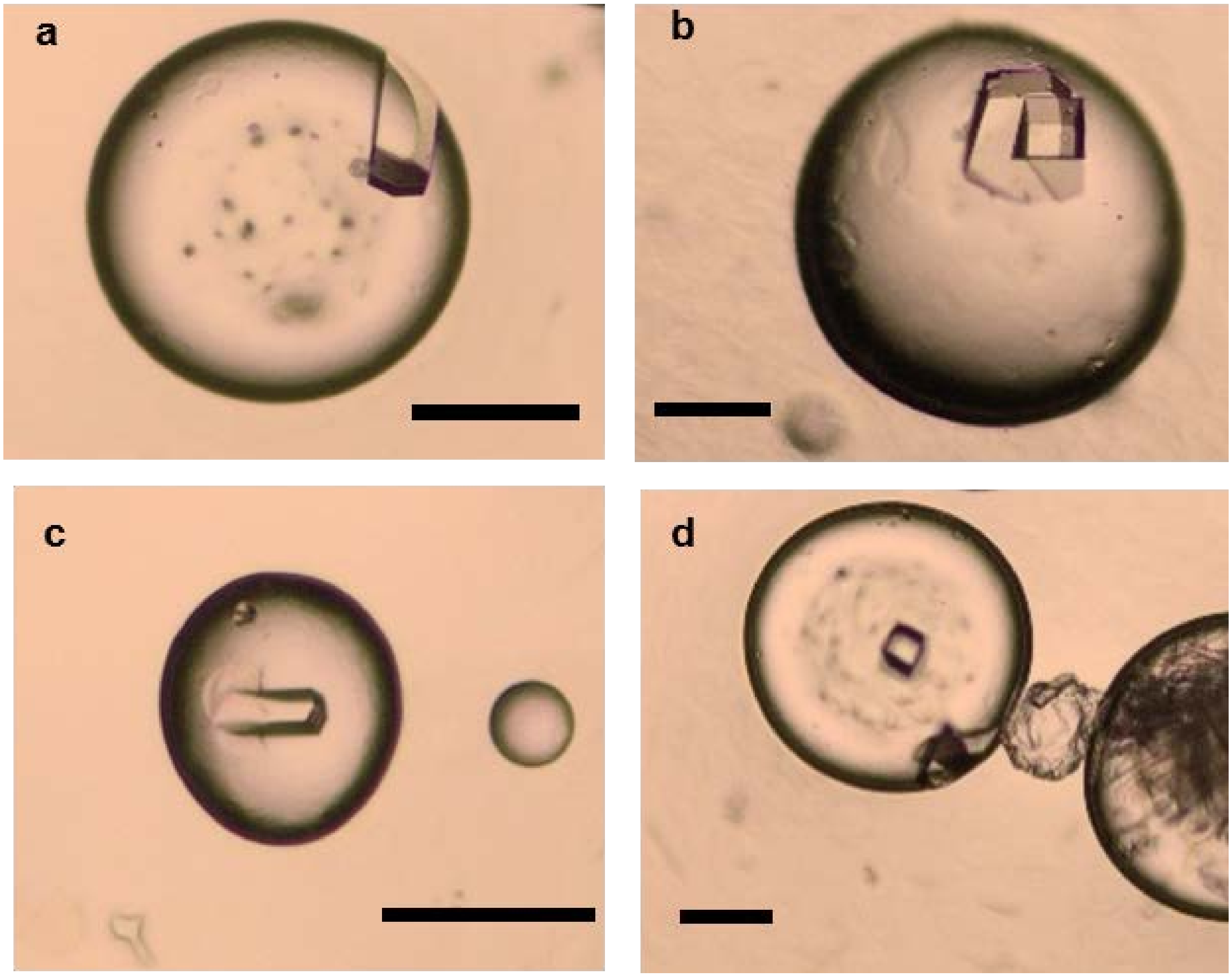

Figure 2.26: Examples of how the location characterisation of crystals grown inside colloidosomes was carried out: a) ’Edge’, b) ‘Floating’, c) ’Centre’, d) ’Edge’ and ‘Centre’. Scale bar = 100 µm.

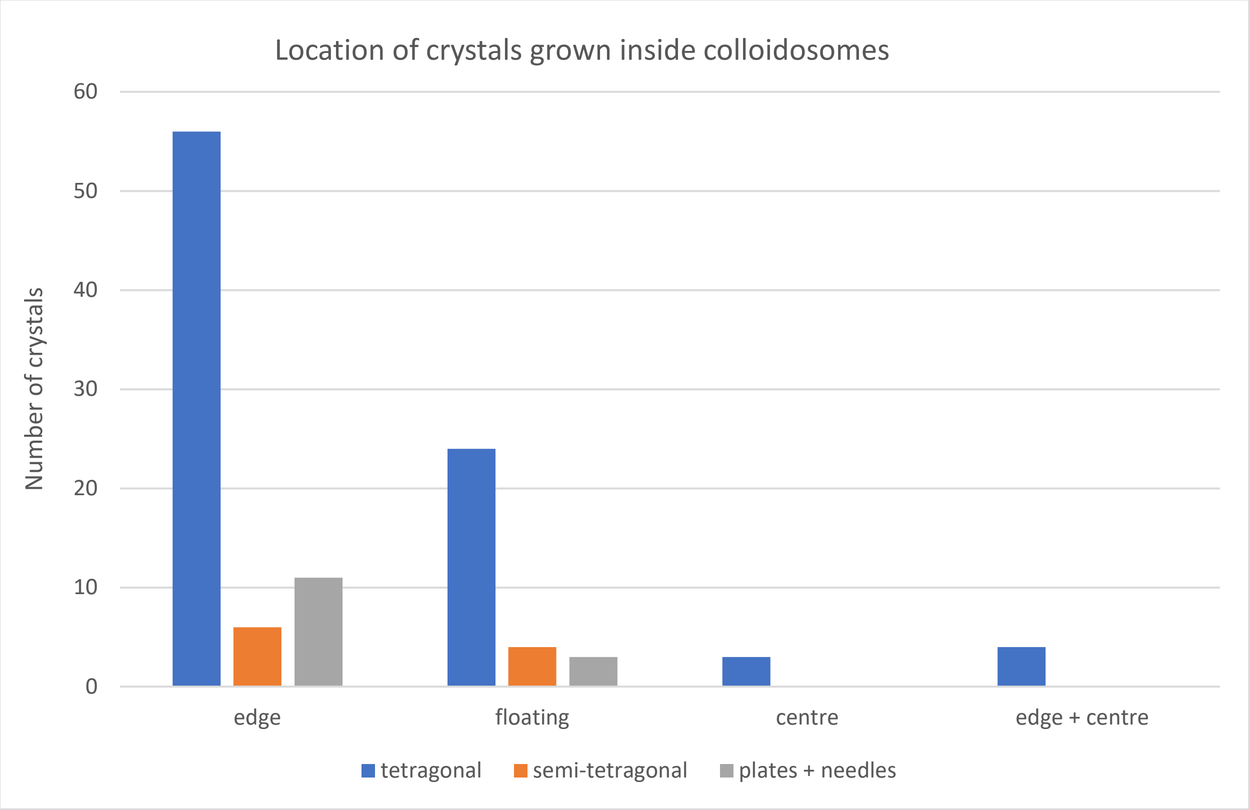

Figure 2.27: Location of crystals inside colloidosomes of different shapes.

2.4.2. Ferritin

Ferritin crystallisation was carried out inside the colloidosomes as described in the ‘Materials and Methods’ section, using vapour diffusion hanging drop (VDHD) method as a control. Two ferritin crystallisation systems were used, S1 and S2. Batch crystallisation of ferritin with S1 and S2 was attempted to provide a control, however, no crystal growth was observed. Two ferritin crystallisation systems were compared: S1 (Figure 2.28) and S2 (Figure 2.29), and temperatures of 4˚C and room temperature were compared for both the control and crystal growth inside colloidosomes. Crystal growth was not observed at room temperature for any of the experiments listed. Crystal growth was examined under optical microscopy once a day since the start if the incubation period. The first onset of crystal growth was observed at 13–14 days of incubation for S1 and S2 controls. This is in line with literature reports of expected crystal formation after 7–14 days of incubation by VDHD method. Crystal growth was observed inside the colloidosomes after 4 days of incubation in S1 and S2 systems. Crystals grown inside colloidosomes were 10–20 times smaller than those in the control. Figure 2.30 shows optical micrographs of the ferritin crystals grown inside colloidosomes at higher magnification which shows the diamond crystalline structure more clearly. Ferritin crystal shapes observed were consistent with diamond-like shapes observed in the literature, however further investigation into the crystallographic structure is required through XRD and/or 3D reconstruction.

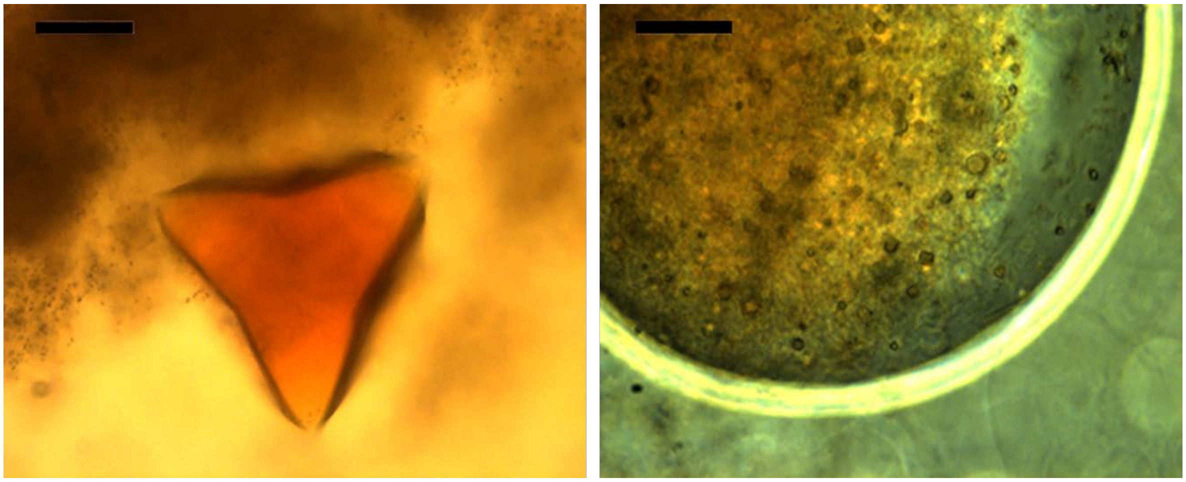

Figure 2.28: Ferritin crystallisation of S1 by VDHD method (left) and inside colloidosomes (right). Scale bar = 100 µm.

Ferritin crystals grown of S1 by VDHD method had an average crystal length (measured across the diagonal axis) of (232.6 ± 12.7 µm) and compared to those grown in colloidosomes which had an average crystal length of (12.8 ± 3.3 µm). The ferritin crystals grown in colloidosomes were approximately 20 times smaller than those grown by the VDHD method. Both methods produced crystals with the ‘diamond’ shape structure common for ferritin crystals, however as mentioned further investigation into the crystal structure is required to confirm this.

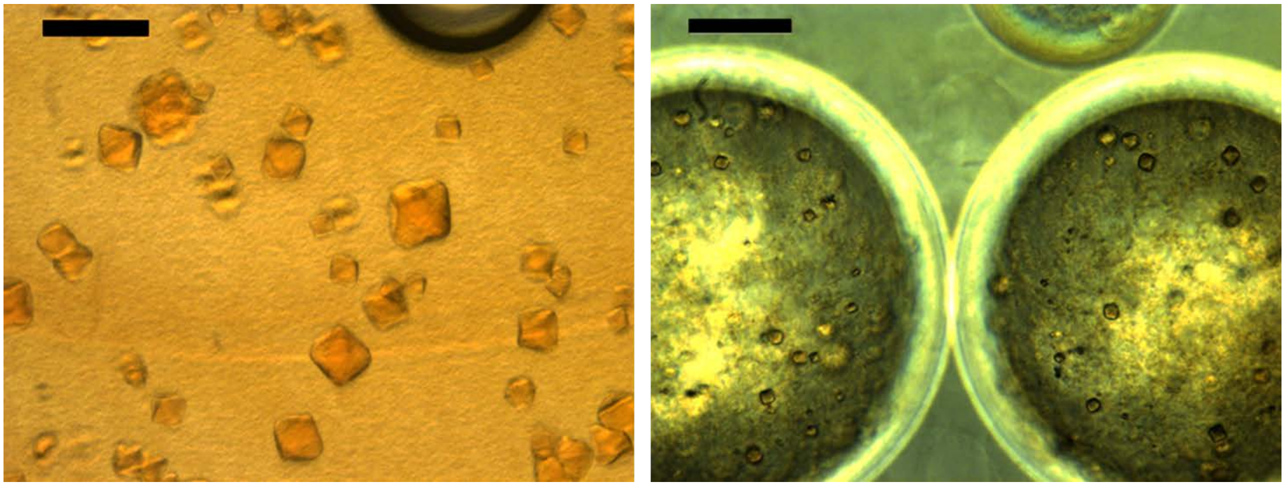

Figure 2.29: Ferritin crystallisation of S2 by VDHD method (left) and inside colloidosomes (right). Scale bar = 100 µm.

Ferritin crystals grown of S2 by VDHD method had an average crystal length (measured across the diagonal axis) of (36.8 ± 12.5 µm) and compared to those grown in colloidosomes which had an average crystal length of (12.6 ± 2.7 µm). The ferritin crystals grown in colloidosomes were approximately 3 x smaller than those grown by the VDHD method. Both methods produced crystals with the ‘diamond’ shape structure common for ferritin crystals, however as mentioned further investigation into the crystal structure is required to confirm this. Ferritin crystals grown inside colloidosomes with S1 and S2 have comparable crystal sizes of (12.8 ± 3.3 µm) and (12.6 ± 2.7 µm), despite the increase in ferritin concentration from 20 mg/mL to 50 mg/mL. This would indicate that the crystal growth of ferritin inside colloidosomes is less sensitive to concentration than the HDVD method (S1 = 232.6 ± 12.7 µm, and S2 = 36.8 ± 12.5 µm). This is contrary to lysozyme crystals which demonstrated higher sensitivity to protein concentration inside the colloidosomes than in batch crystallisation. These results are very interesting and could be expanded towards using minimal concentrations of ferritin crystals to achieve high quality crystallisation within colloidosomes. This is particularly promising for high value protein crystallisation where the protein supply is limited.

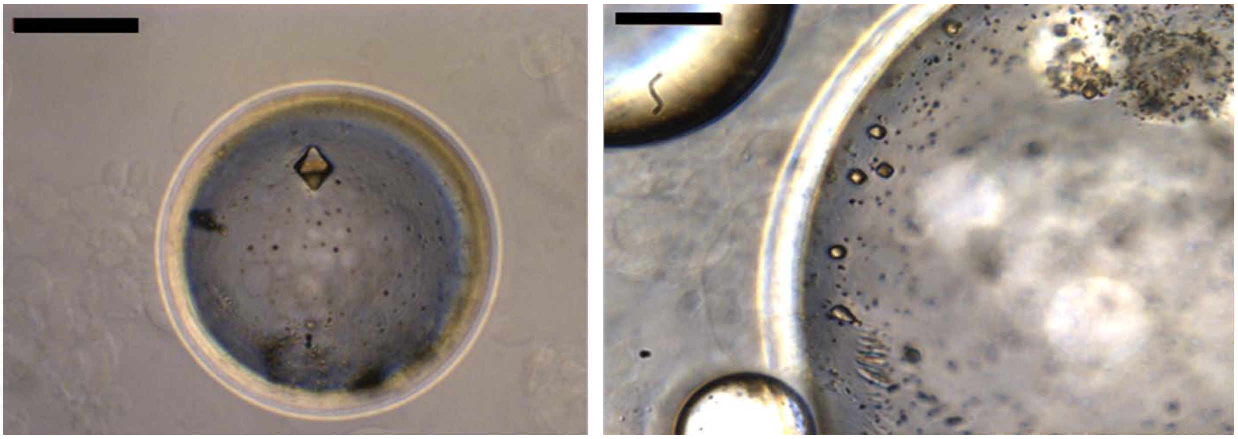

Figure 2.30: Crystallisation of ferritin inside colloidosomes in S1 (left) and S2 (right) at a higher magnification which shows the diamond crystal structure more clearly. Scale bar = 50 µm.

2.4.3. Extraction into Water

As mentioned, native protein crystals are very fragile and require chemical cross-linking to enhance their mechanical stability and resistance to dissolution in different solvents. Protein crystals grown inside colloidosomes were shown to be stable up for up to 6 months of incubation. These crystals were much easier to handle and image than those grown by batch crystallisation or by VDHD methods. Extraction of the protein crystals from the colloidosomes may be necessary to expand their application into areas which require the diffusion of species through the crystal lattice, particularly if they are insoluble in dodecane, such as catalysis or host-guest complexation for storage, drug delivery or template-directed synthesis.[3,36,43,49–51]

Glutaraldehyde used to chemically cross-link protein crystals in batch could not be used to cross-link proteins inside colloidosomes due to significant aggregation of the chemical in dodecane.

Colloidosomes were cross-linked with TMOS and extracted into water as described in the ‘Materials and Methods’ section. TMOS cross-linking was carried out after the successful growth of crystals inside the colloidosomes as the addition of TMOS to the initial protein crystallisation solution was seen to interfere with protein crystallisation. Lysozyme-containing colloidosomes disassembled upon extraction into water, indicating that complete cross-linking of the colloidosome membrane was not successful, despite it exhibiting considerable roughening of the surface and shrinkage of the water which would indicate cross-linking (Figure 2.31). This is consistent with the presence of a cross-linked silica matrix (surface roughening) and corrugated membrane surface (droplet shrinkage).[30] The presence of evidence of the cross-linking did not necessarily guarantee the successful extraction of the colloidosomes into water. For instance, cross-linking of colloidosomes containing mCherry was carried out under the same conditions and demonstrated similar results but was not successfully transferred to water (Figure 2.32).

Ferritin-containing colloidosomes were successfully cross-linked with TMOS in dodecane and transferred to water. Figures 2.33 and 2.34 show ferritin-colloidosomes cross-linked with TMOS for 42 hours at room temperature and at 4˚C for four days, after one week of being extracted into water. The c olloidosomes cross-linked at 4˚C for four days demonstrated a near-completely cross-linked shell, and the ferritin crystals appeared to be intact after transfer into water for up to one week (Figure 2.35).

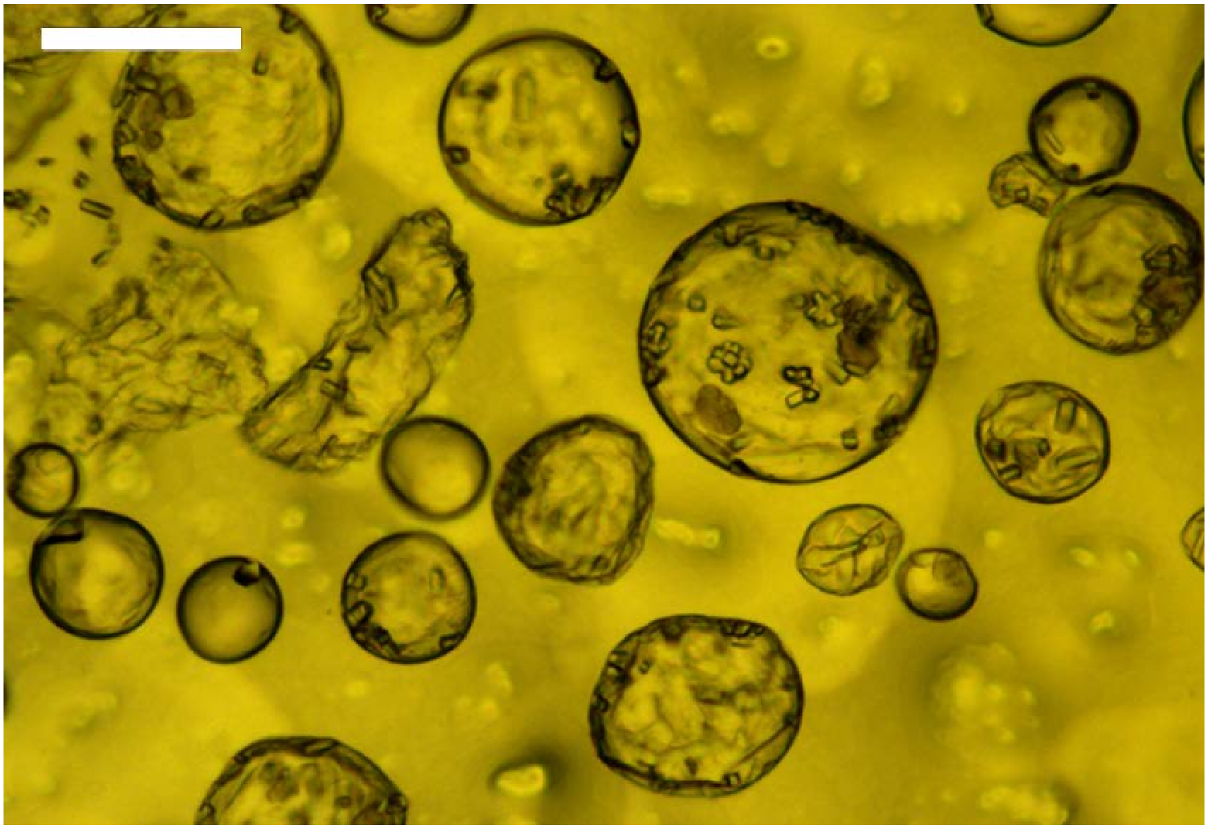

Figure 2.31: Optical microscopy images of lysozyme colloidosome cross-linked with TMOS. Lysozyme crystals are visible within colloidosomes. Roughening of the colloidosome membrane and contraction of the spherical shape and volume indicate that the cross-linking reaction has taken place. Scale bar = 200 µm.

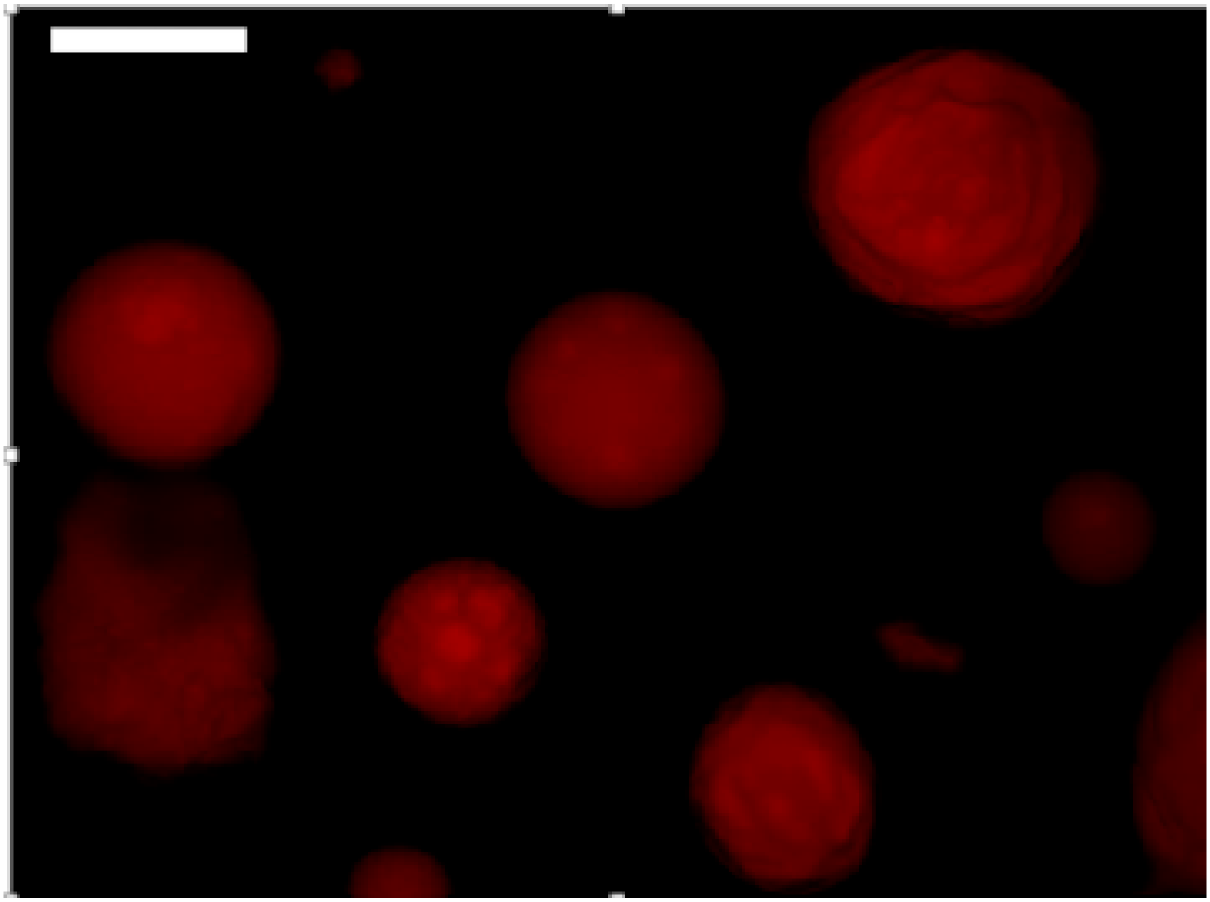

Figure 2.32: Fluorescence microscopy image of mCherry colloidosomes cross-linked with TMOS. mCherry protein crystallisation solution was successfully incorporated into discrete colloidosome membranes although no protein crystals were visible. Roughening of the colloidosome membrane and contraction of the spherical shape and volume indicate that the cross-linking reaction has taken place. Scale bar = 200 µm.

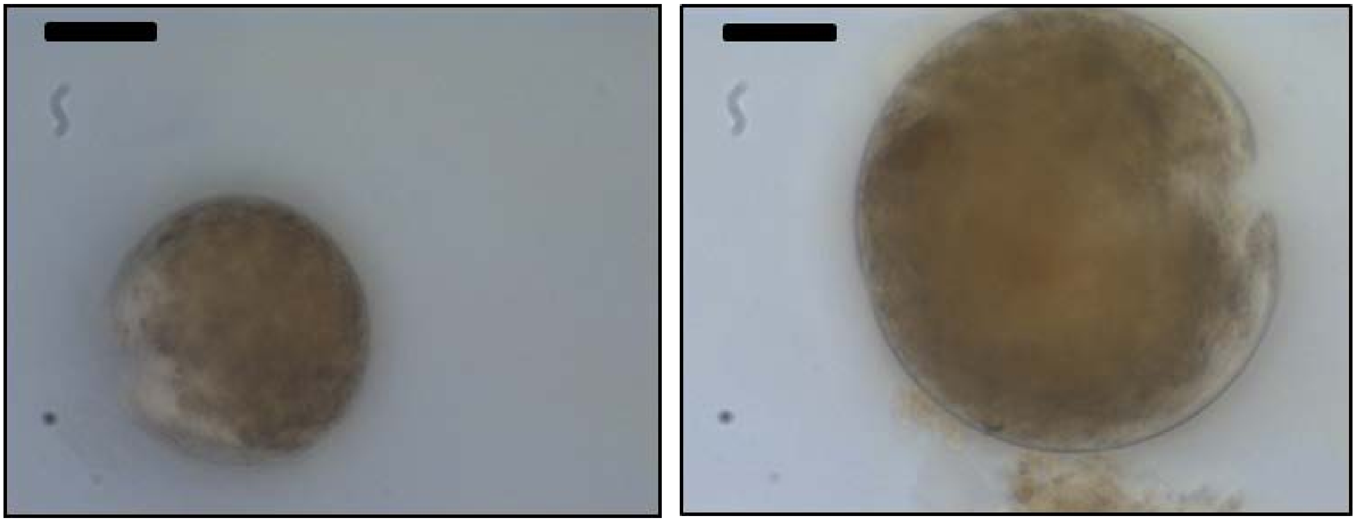

Figure 2.33: Ferritin-colloidosomes cross-linked with TMOS at room temperature for 42 hours and extracted into water. Scale bar = 50 µm.

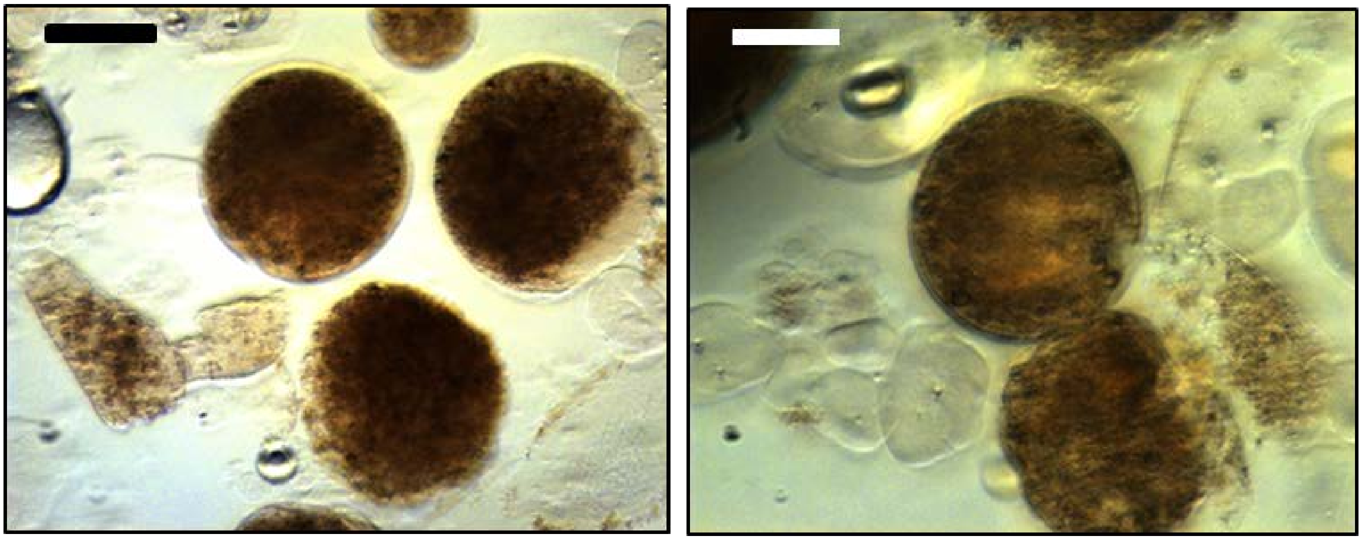

Figure 2.34: Ferritin-colloidosomes cross-linked at 4˚C for four days and extracted into water. Images taken one week after extraction into water. Scale bar = 100µm.

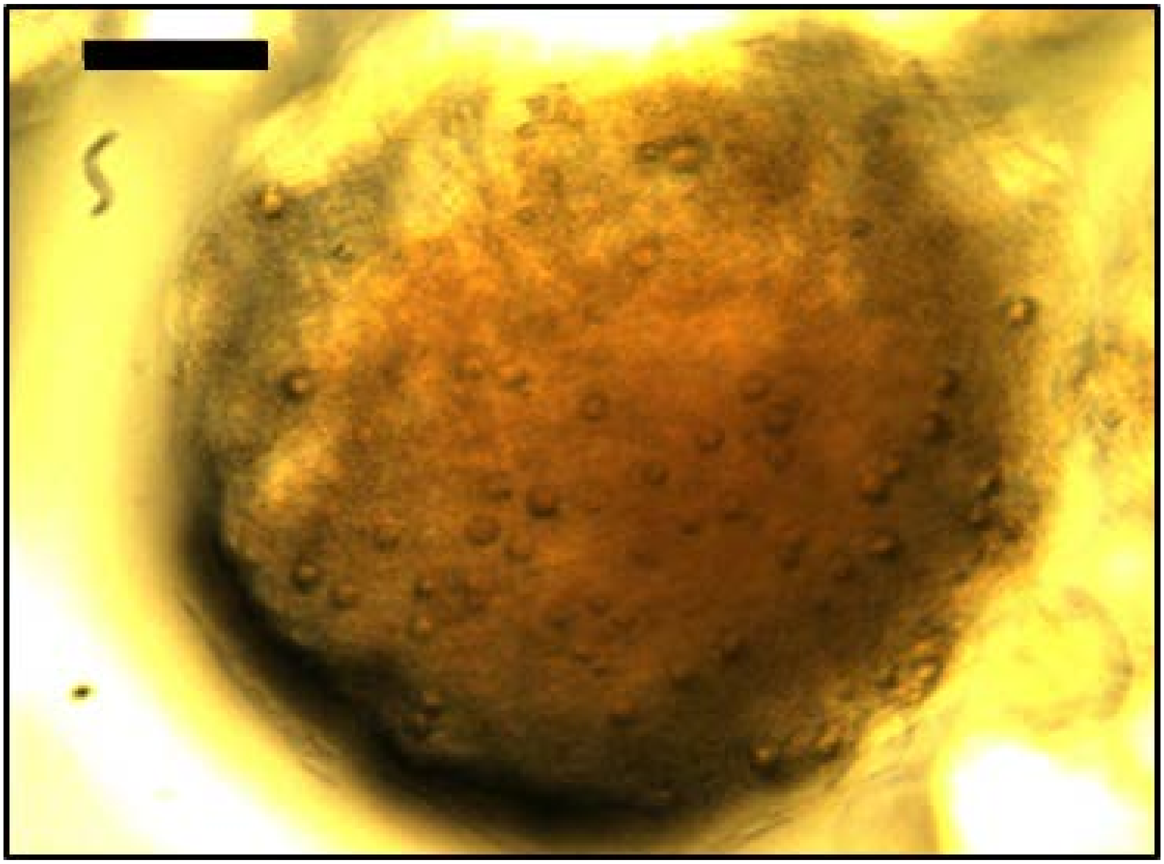

Figure 2.35: Ferritin-colloidosomes cross-linked at 4˚C for four days and extracted into water, at high magnification showing crystals intact one week after extraction into water. Scale bar = 100 µm.

2.4.4. Other Proteins

In addition to the successful crystallisation of lysozyme and ferritin inside colloidosomes, several attempts with other proteins were carried out such as mCherry, bacterioferritin, myoglobin, catalase and bovine liver catalase (BLC). Some of these results are shown in Figure 2.36. It appears, after 4 days of incubation at room temperature, both mCherry and BLC show signs of precipitation within the colloidosomes, which is a promising indication that with appropriate adjustment of the pH, concentration of solutes and temperature that protein crystallisation could be carried out successfully inside the colloidosomes.

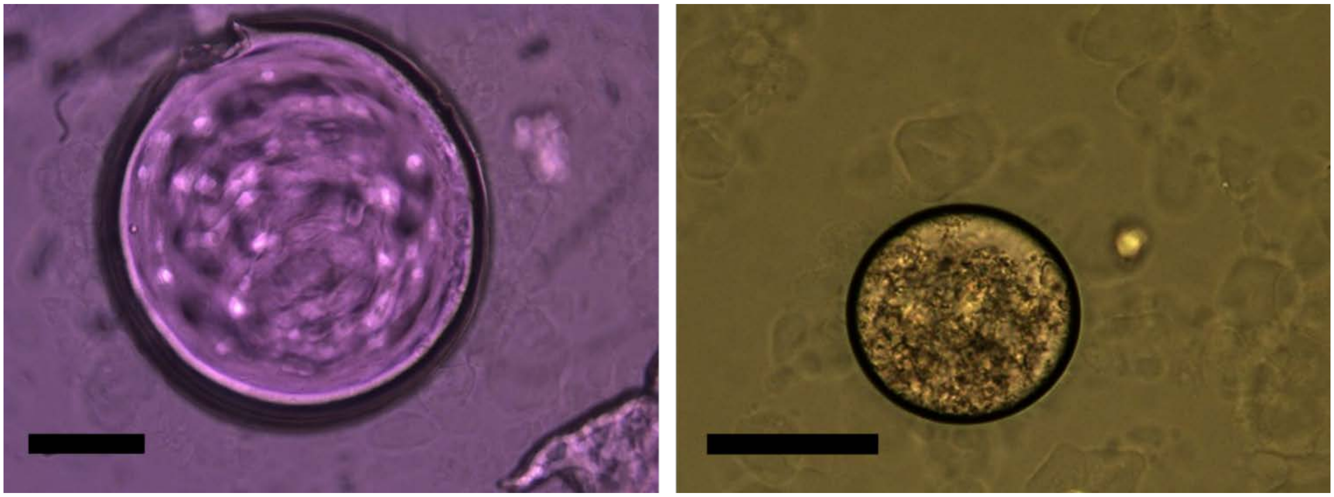

Figure 2.36: Optical microscopy image of mCherry with PEG 4000 inside colloidosomes (left) and BLC inside colloidosomes (right). Images taken 4 days after incubation at room temperature. Scale bar = 100 µm.

2.4.5. Confined Growth of Lysozyme Crystals in the Presence of Au NPs and CDs

In order to explore the scope for using colloidosomes as reaction vessels for protein crystallisation and expand its applications, investigations into the growth of lysozyme crystals within colloidosomes were carried out in the presence of metallic Au NPs and CDs. The presence of three-dimensional contaminants is known to modify the crystal growth process. This modification is dependent on the amount of contaminant, its structure and the crystal growth environment.[52] Au NPs were selected due to the ease of their synthesis, allowing a high degree of control over their size and surface properties, and due to their record of successful interaction with lysozyme crystals.[9,50,53] N CDs and NS CDs synthesised by the method described in 'Chapter 3' were also selected due to the cheap and facile synthesis which was carried out in house, as well as the ease of visualising these particles under optical fluorescence microscopy.

The literature surrounding the combination of gold nanoparticles (Au NPs) and protein crystallisation remains quite limited. Wei et al. (2011), utilised lysozyme crystals to monitor the time-dependent, protein directed growth of gold nanoparticles.[9] England et al. used single lysozyme crystals to synthesise isolated Au nanoclusters and investigated the plasmonic response of these composites.[50] Investigations into the use of Au NPs and ligand-functionalised Au NPs as nucleating agents to enhance crystal growth of hen egg white lysozyme have been carried out by Hodzhaoglu et al. (2008)[54] and Riberio et al. (2014),[53] respectively. Kertis et al. (2012) used nanoporous gold as heterogenous nucleants for the crystallisation of lysozyme, to determine the effect of porosity, surface area and surface chemistry on the entropic barrier to nucleation.[55] Ko et al. (2017) more recently carried out more extensive research into the use of Au NPs as nucleation-inducing agents for lysozyme crystallisation.[56]

As for the literature surrounding the interaction between lysozyme crystals and CDs, England et al. (2015)[57] used single crystal lysozyme for the confinement and *in situ* synthesis of citric acid-based CDs, however their use as nucleating agents for protein crystallisation and/or functionalisation beyond that has not been reported.

This work aims to investigate the capability of using colloidosomes as micro-reactors for the *in-situ* growth of functionalised lysozyme crystals by the incorporation of guest species of Au NPs and CDs, as well as investigating the effect of Au NPs and CDs on lysozyme crystal growth.

Lysozyme crystallisation samples were prepared as described in the ‘Materials and Methods’ section of this chapter. Different volumes of Au NPs and CDs solution were added to the lysozyme crystallisation solution during the assembly of colloidosomes to investigate the effect of Au NPs and CDs on the growth, shape and morphology of the lysozyme crystals. Lysozyme grown in the presence of Au NPs and CDs grown by batch crystallisation on water/DCM interface were used as a control. Optical microscopy images of the samples were taken after 11 days of incubation at room temperature. Images are labelled with the sample name and number e.g. A1, A2, etc. Table 2.2 summarises the volumes of Au NPs and CDs solutions used and is re-iterated below.

Table 2.3: Preparation of functionalised lysozyme crystals inside colloidosomes.

Sample	***Sample name***	***Sample number***			
		1	2	3	4
		Volume of sample added (μL)			
Au NPs (Batch)	A	20	40	60	80
Au NPs (Colloidosomes)	B	10	20	30	40
N CDs (Batch)	C	20	40	60	80
N CDs (Colloidosomes)	D	10	20	30	40
N S CDs (Batch)	E	20	40	60	80
NS CDs (Colloidosomes)	F	10	20	30	40

2.4.5.5. Lysozyme crystal growth in the presence of Au NPs

Batch crystallisation of lysozyme at the interface of water/DCM with the addition of Au NPs as described was used as the control (Figure 2.37). The crystals appear slightly pink (due to the red colour of the Au NPs solution), but otherwise transparent with clear presence of dark aggregates throughout the crystals. This would indicate that Au NPs have been incorporated into the lysozyme crystals, however further analysis to confirm this, as well as to investigate the location of the NPs via HRTEM and High-angle annular dark-field scanning transmission electron microscopy (HAADDF-STEM)[9], is required. The presence of Au NPs causes polycrystalline growth of large crystal complexes in the batch. In the batch the critical crystallisation nuclei are more spread apart and able to cluster around the surface of the Au NPs. This results in the formation of stable critical nuclei around the surface of the Au NPs which are able to grow simultaneously in different directions. This appears to result in the formation of these polycrystalline agglomerates, and disruption of the isomorphism of the lysozyme crystals. The increase in the volume of Au NPs added to the crystallisation solution appears to increase the observed effect, supporting this theory. Lysozyme crystals grown in the presence of Au NPs display elongated tetragonal morphologies similar to those obtained in experiments where the protein crystal solution post-nucleation was used to assemble colloidosomes (Section 3.1.3 of this chapter). This provides further evidence that the confinement of the crystallisation solution in colloidosomes offers control over the nucleation and growth of crystals in the presence of impurities, thereby resulting in unique morphologies of the crystal not observed in bulk. This could be due to the adsorption of the Au NPs onto the silica membrane, aiding the heterogenous nucleation of lysozyme crystals at the membrane. Similarly, the Au NPs may be behaving as a site for heterogenous nucleation within the solution volume of the colloidosome sphere.

Further analysis into the surface chemistry and aggregation condition of the Au NPs in the protein crystallisation solution at the interface of water/DCM is required to gain a better understanding of the heterogenous nucleation process and how it is influenced by the size and surface chemistry of the Au NPS. Furthermore, structural determination of the resulting polycrystalline agglomerates is required.

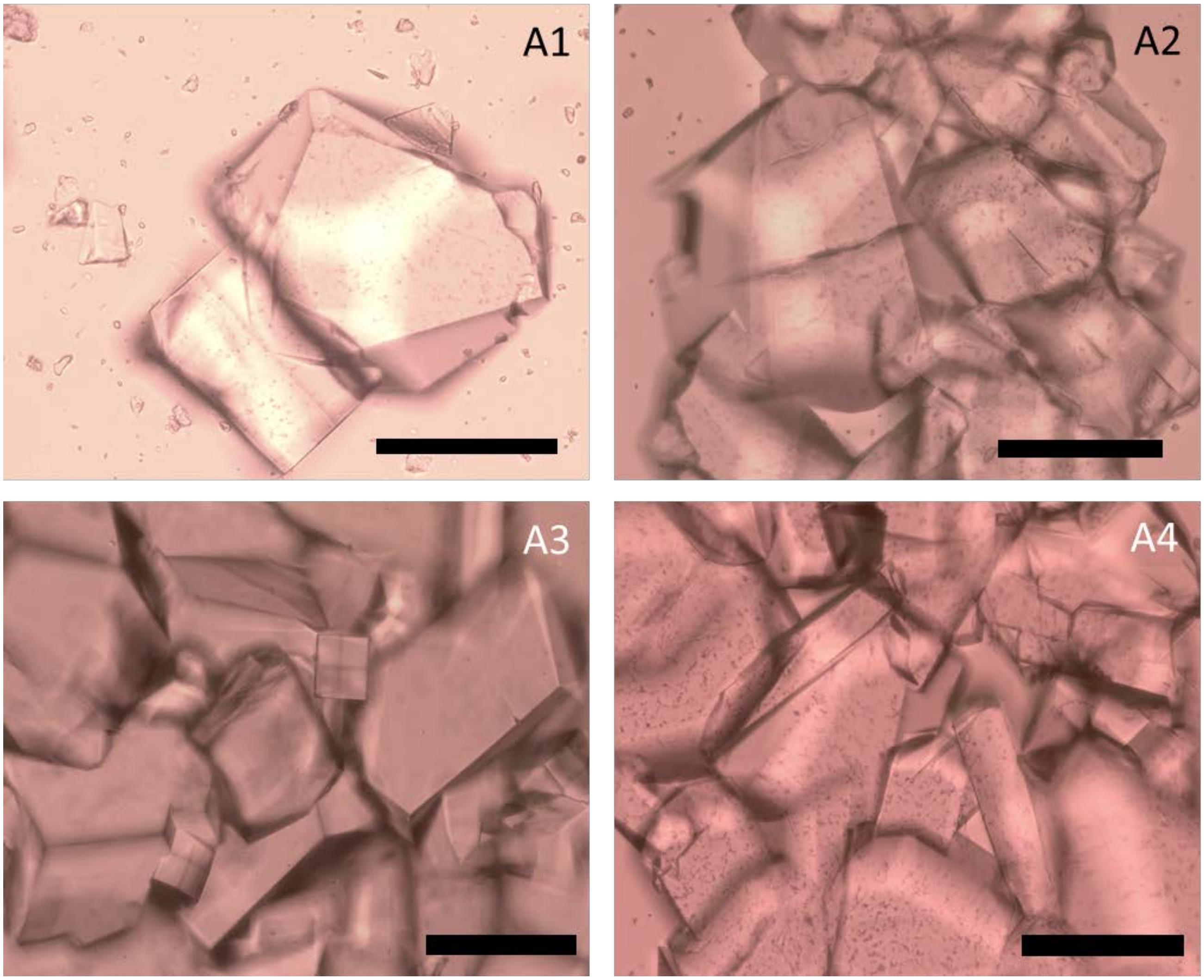

Figure 2.37: Optical Microscopy images of Au NPs functionalised lysozyme grown by batch crystallisation at the water/DCM interface at room temperature. Images taken after 11 days of incubation. Scale bar = 100 µm

Growth of Au NPs-functionalised lysozyme inside colloidosomes was carried out (Figure 2.38). In contrast to the results observed in batch, disruption of the lysozyme isomorphism appears to result in elongated tetragonal or monoclinic crystal structures as opposed to polycrystalline agglomerates. This may indicate once again that the Au NPs behave as heterogenous nucleation sites. However, the spatial and temporal control offered by the confined volume of the crystallisation solution in the colloidosome restricts the diffusion of critical nuclei and favours the preferential growth of one crystal face over another as opposed to the polycrystalline agglomerates observed in batch.[58] There does not appear to be a discernible trend between the increase in volume of Au NPs added and the change in crystal morphology. Once again this may be due to the higher degree of control over nucleation events in the colloidosomes compared to that in bulk. It has not been possible to isolate the nucleation events caused by the heterogenous nucleation sites offered by the silica nanoparticles and Au NPs. The only indication of Au NPs serving as additional nucleation sites has been the change in crystal morphologies observed.

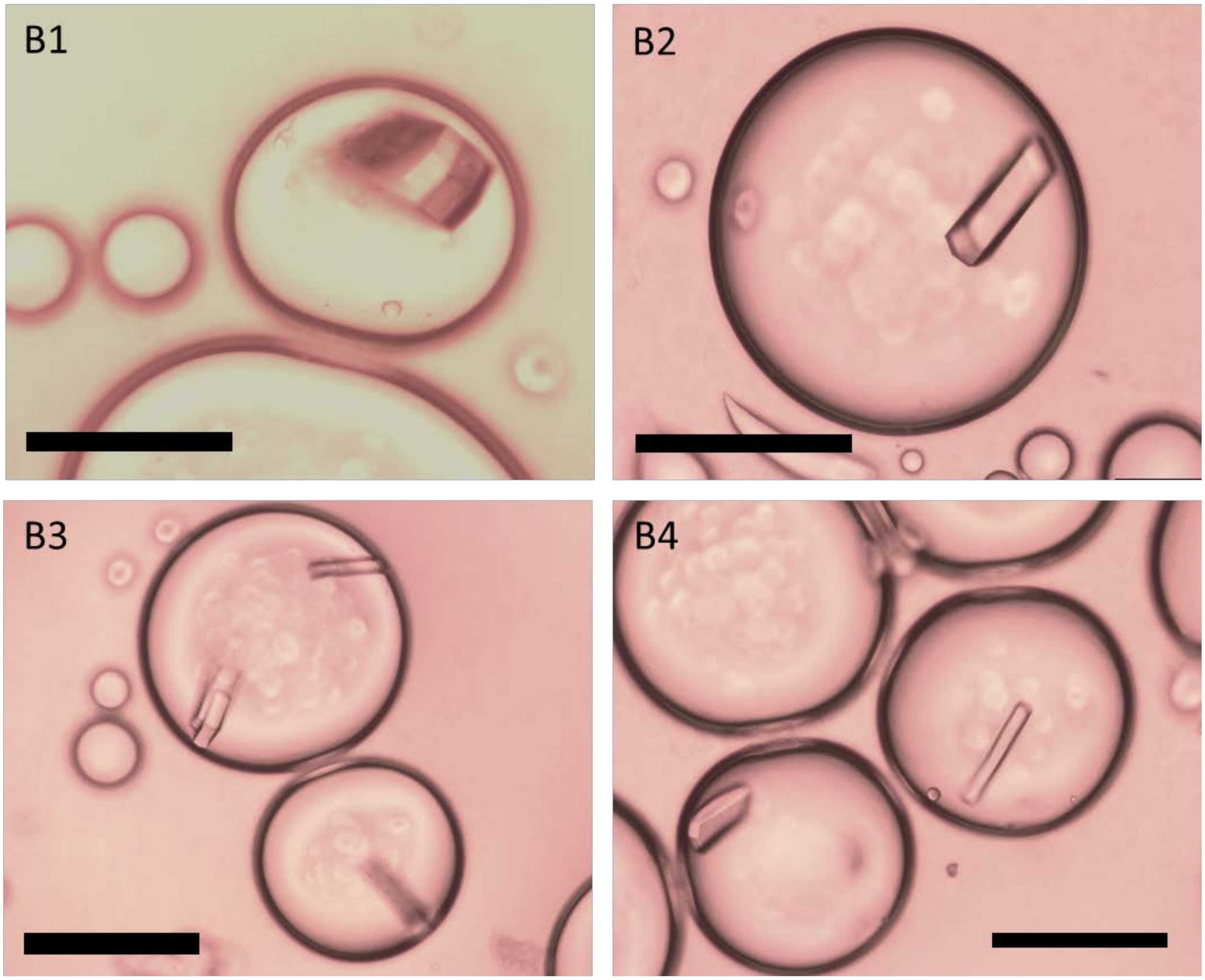

Figure 2.38: Optical Microscopy images of Au NPs-functionalised lysozyme grown inside colloidosomes at room temperature. Images taken after 11 days of incubation. Scale bar = 100 μm

2.4.5.6. Lysozyme crystal growth in the presence of CDs

The growth of lysozyme crystals functionalised with CDs was investigated as described in the 'Materials and Methods' section of this chapter. Lysozyme crystallisation was carried out in batch in the presence of N CDs (Figure 2.39 and 2.40) and NS CDs (Figure 2.43 and 2.44) at a water/DCM interface at room temperature. Similar to the results observed with Au NPs in batch the presence of CDs causes the growth of polycrystalline complexes with multiple direction, and loss of the expected tetragonal shape. This indicates that CDs may be serving as heterogenous nucleation sites, with nuclei clustering around the surface of the CDs causing nucleation and growth in multiple directions simultaneously. It is also possible that the CDs are adsorbed onto the surface of the silica membrane, aiding heterogenous nucleation of the lysozyme molecules at the silica membrane. As the volume of CDs solution added to the crystallisation solution increases, the polycrystalline nature observed increases, resulting in larger polycrystalline agglomerates. Optical fluorescence microscopy images of the crystals (Figure 2.40 and 2.44 for N CDs and NS CDs respectively) show the successful incorporation of the CDs into the lysozyme structure due to the fluorescence observed at excitation between 340 – 380 nm, which is characteristic of the CDs and not observed for native lysozyme grown under the same conditions.

The crystallisation of lysozyme inside colloidosomes in the presence of N CDs (Figure 2.41 and 2.42) and NS CDs (Figure 2.45 and 2.46) demonstrated slight disruptions to the isomorphism of the lysozyme crystals, resulting in elongated tetragonal structures. The polycrystalline agglomeration observed in the batch was not observed inside colloidosomes, which would indicate that using colloidosomes is advantageous for growing individual functionalised crystals compared to batch crystallisation. There was no clear trend observed between increase in the volume of the CDs added and changes to the crystal morphology. T his may be due to the lack of uniformity in the CDs surface chemistry (namely the presence of carboxylic acid, amide and amine groups on the surface of the CDs) and size which is discussed in further detail in Chapter 3.

Further investigations into the effect of CDs on the nucleation events taking place during protein crystallisation are required, with analysis of the influence of particle size, surface charge and aggregation condition of the particles. Structural determination of the crystals in batch and in colloidosomes is also required to determine the precise crystalline structure and location of CDs in the crystalline lattice.

2.4.5.7. N doped CDs

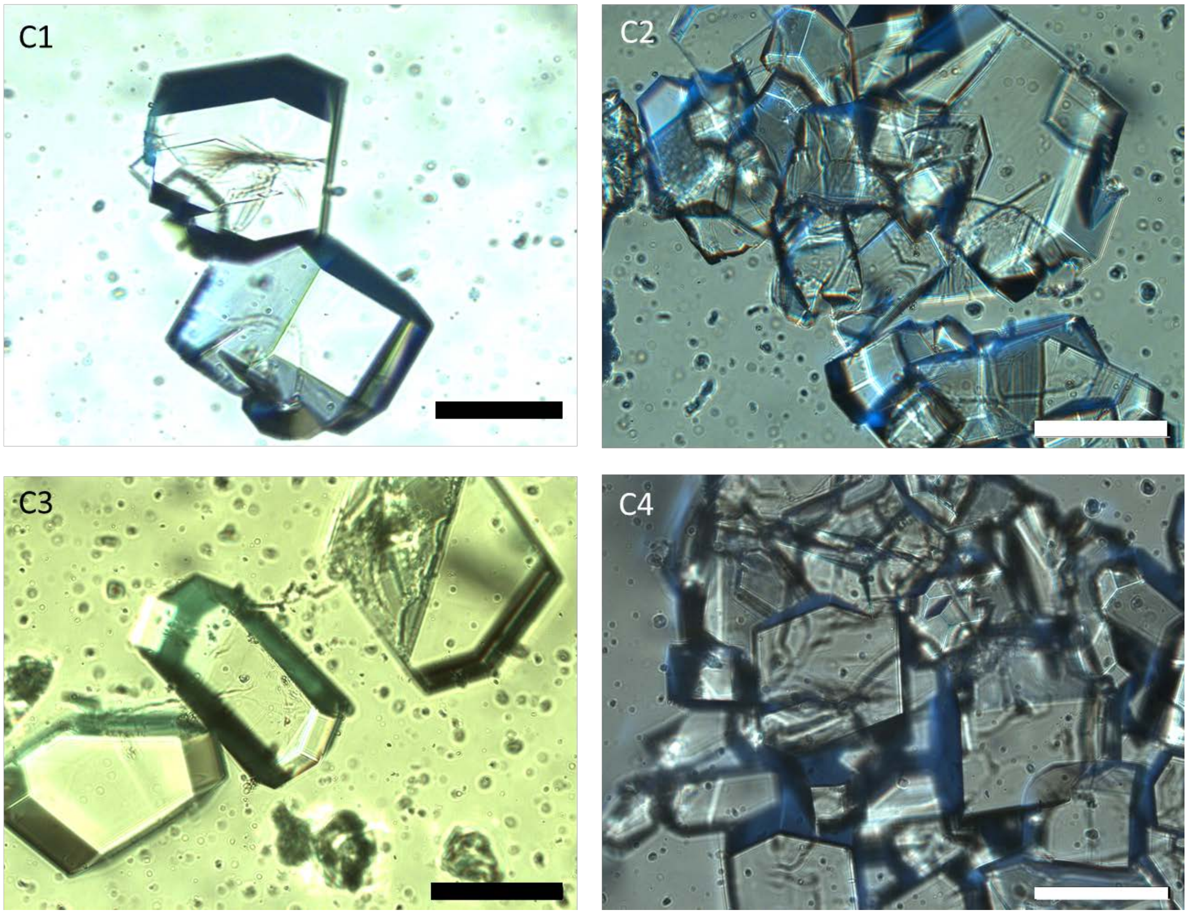

Figure 2.39: Optical Microscopy images of N CDs-functionalised lysozyme grown by batch crystallisation at the water/DCM interface at room temperature. Images taken after 12 days of incubation. Scale bar = 100 µm

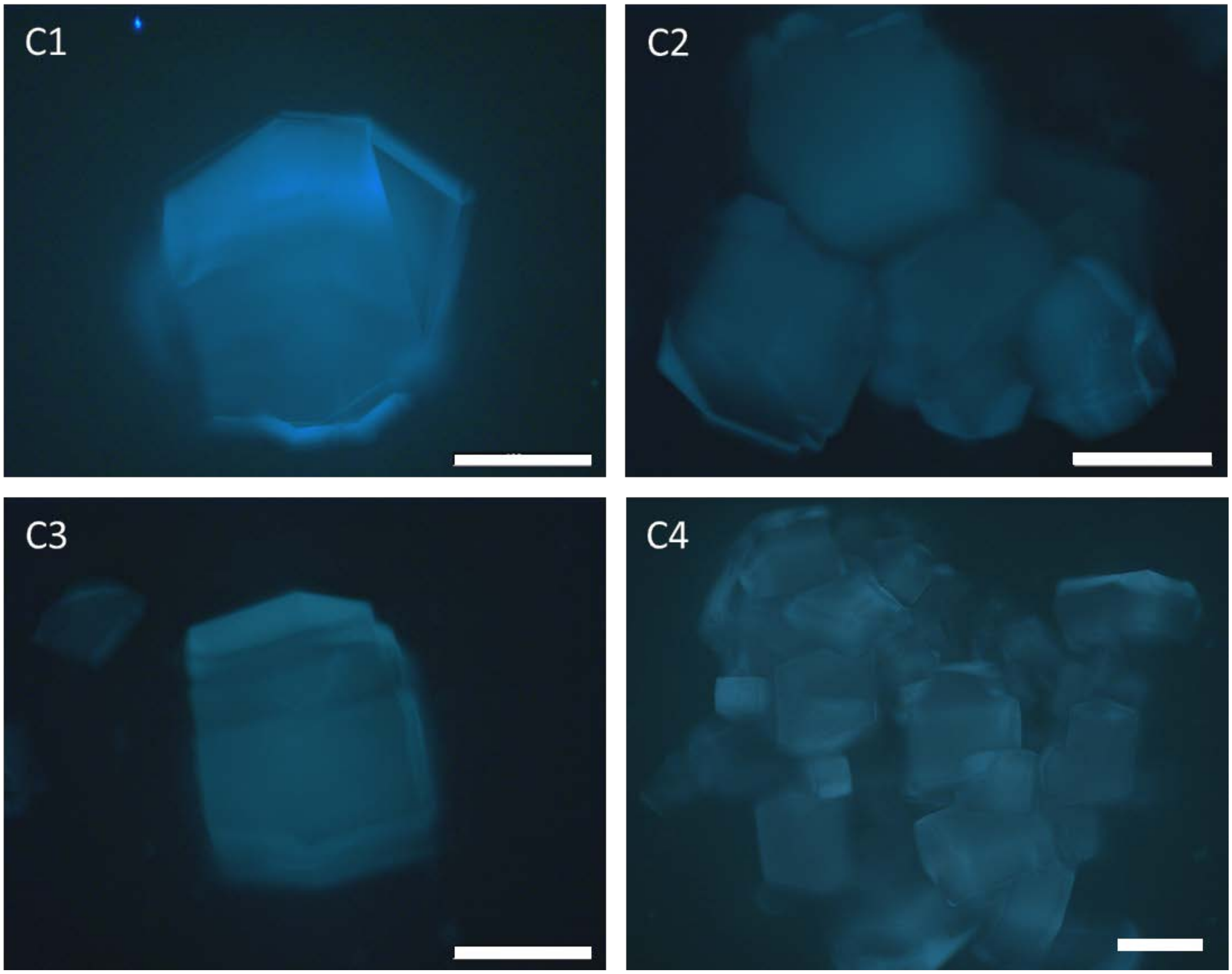

Figure 2.40: Fluorescence Optical Microscopy images of N CDs-functionalised lysozyme grown inside colloidosomes at room temperature. Images taken after 12 days of incubation using excitation laser of λ= 340 – 380 nm. Scale bar = 100 µm

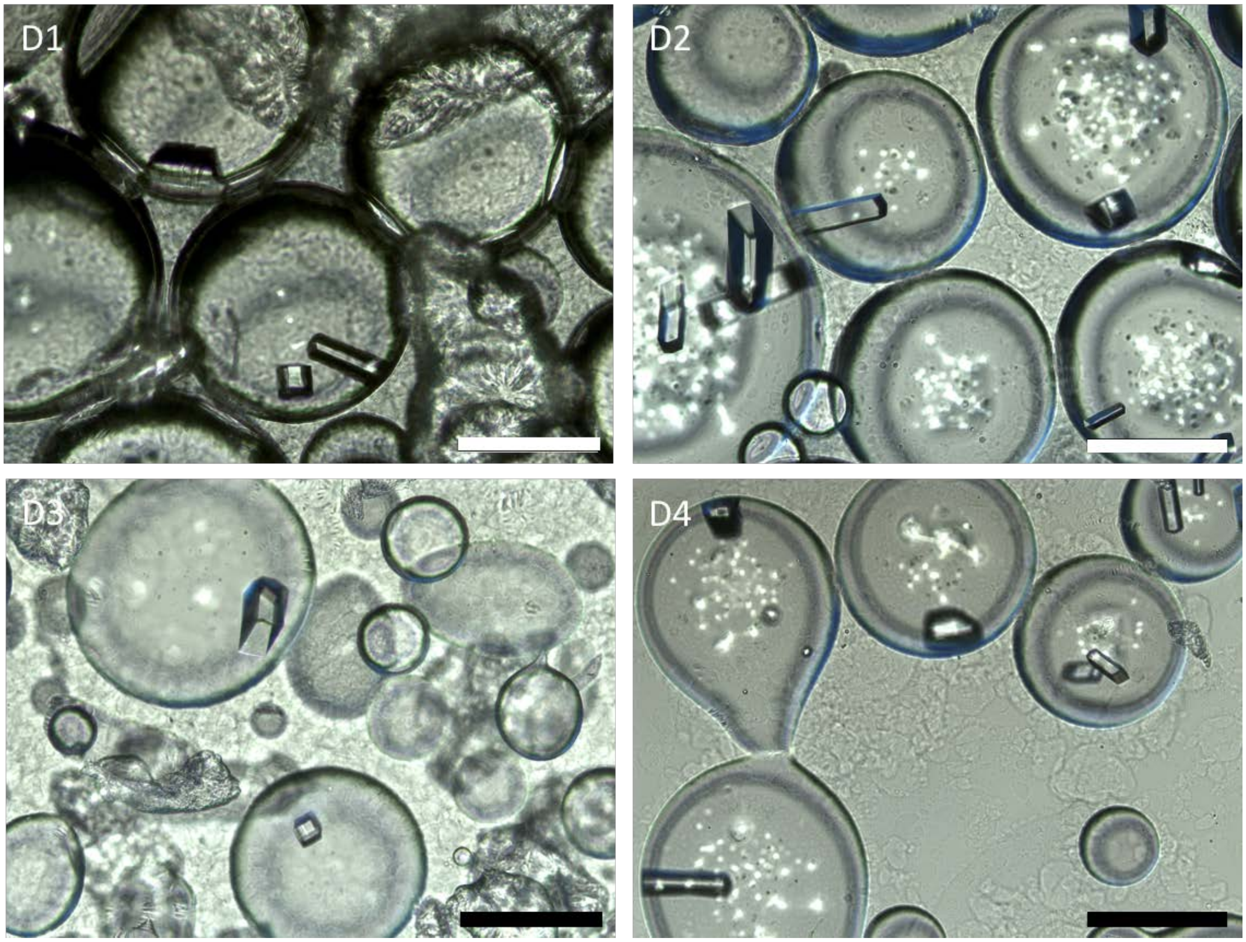

Figure 2.41: Optical Microscopy images of N CDs-functionalised lysozyme grown inside colloidosomes. Images taken 12 days after incubation at room temperature. Scale bar = 200 µm.

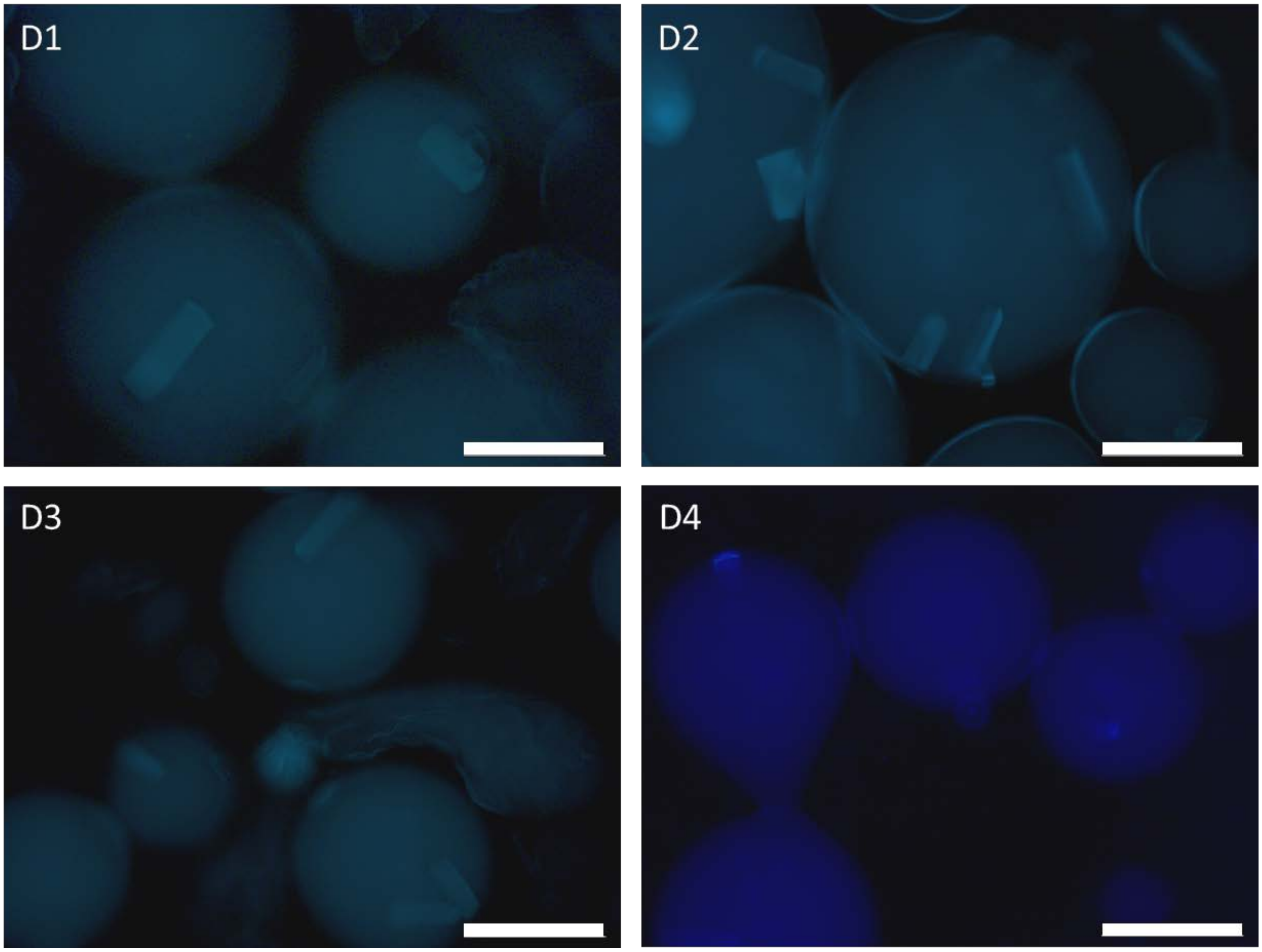

Figure 2.42: Fluorescence optical microscopy images of N CDs-functionalised lysozyme grown inside colloidosomes. Images taken 12 days after incubation at room temperature. Images taken after 12 days of incubation using excitation laser of λ= 340 – 380 nm. Scale bar = 200 µm.

3.5.2.2. N S doped CDs

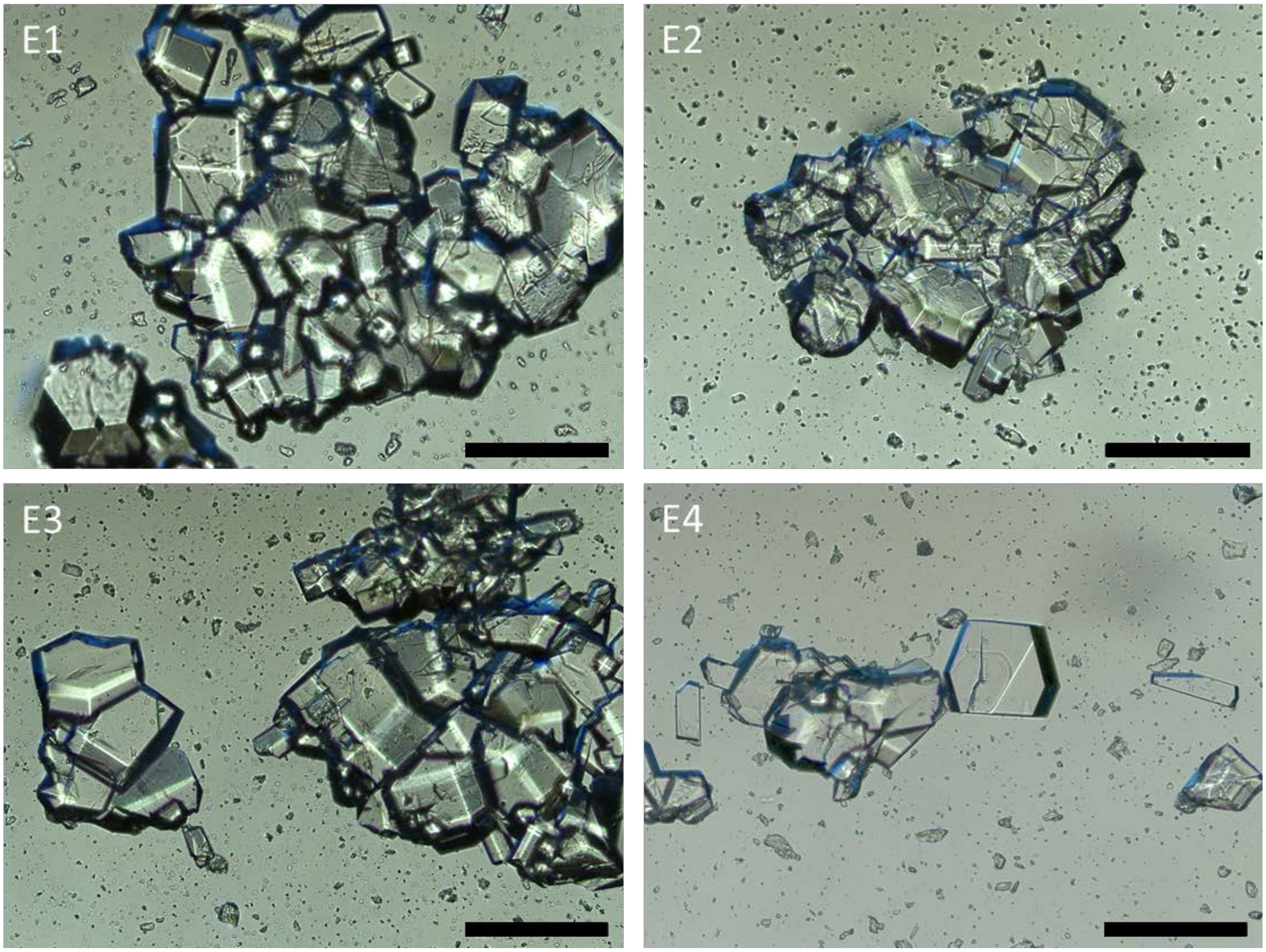

Figure 2.43: Optical microscopy images of N S CDs-functionalised lysozyme grown by batch crystallisation at the water/DCM interface at room temperature. Images taken after 12 days of incubation. Scale bar = 200 µm

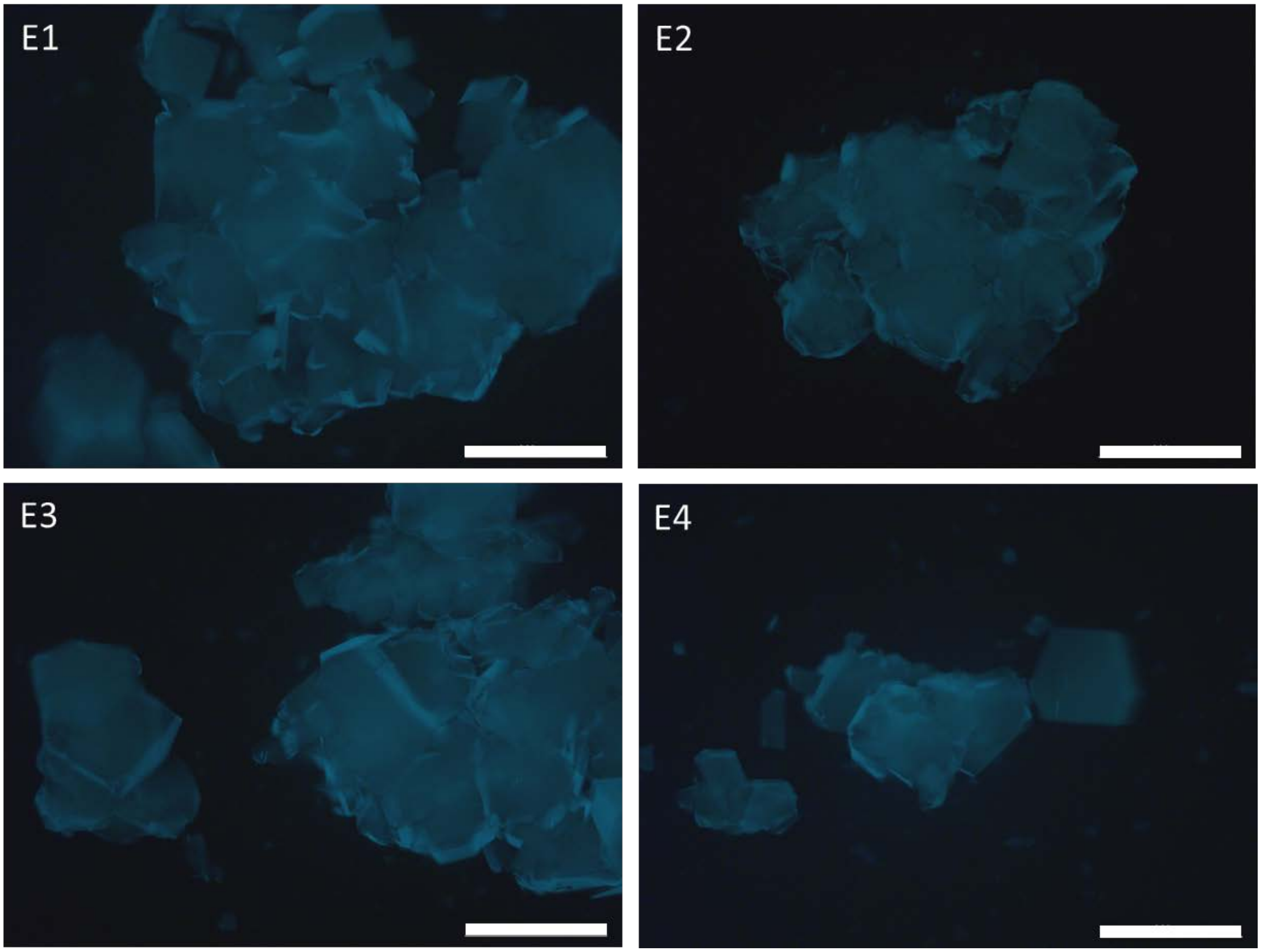

Figure 2.44: Fluorescence Optical Microscopy images of N S CDs-functionalised lysozyme grown inside colloidosomes at room temperature. Images taken after 12 days of incubation using excitation laser of λ= 340 – 380 nm. Scale bar = 200 μm

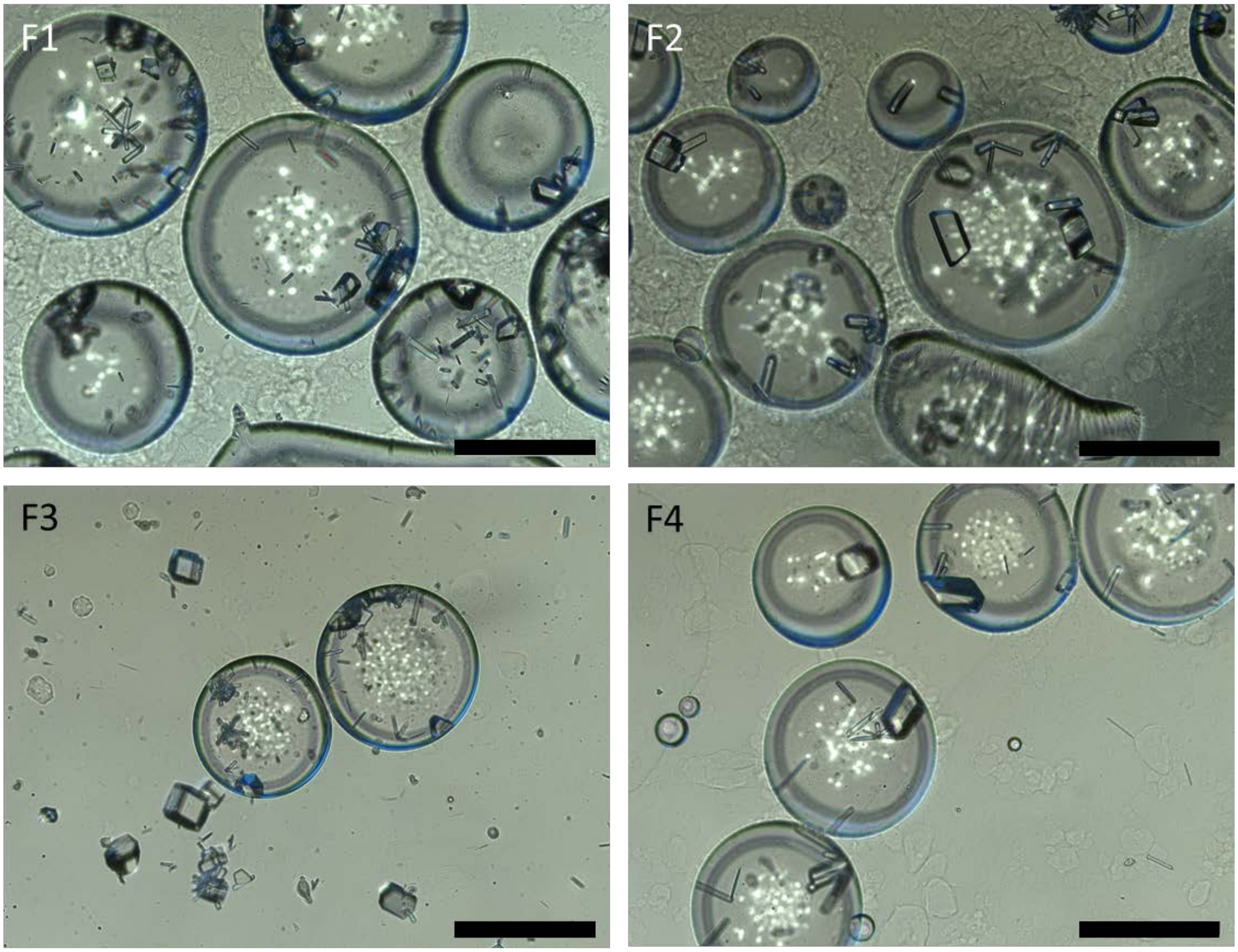

Figure 2.45: Optical Microscopy images of N S CDs-functionalised lysozyme grown inside colloidosomes. Images taken 12 days after incubation at room temperature. Scale bar = 200 µm.

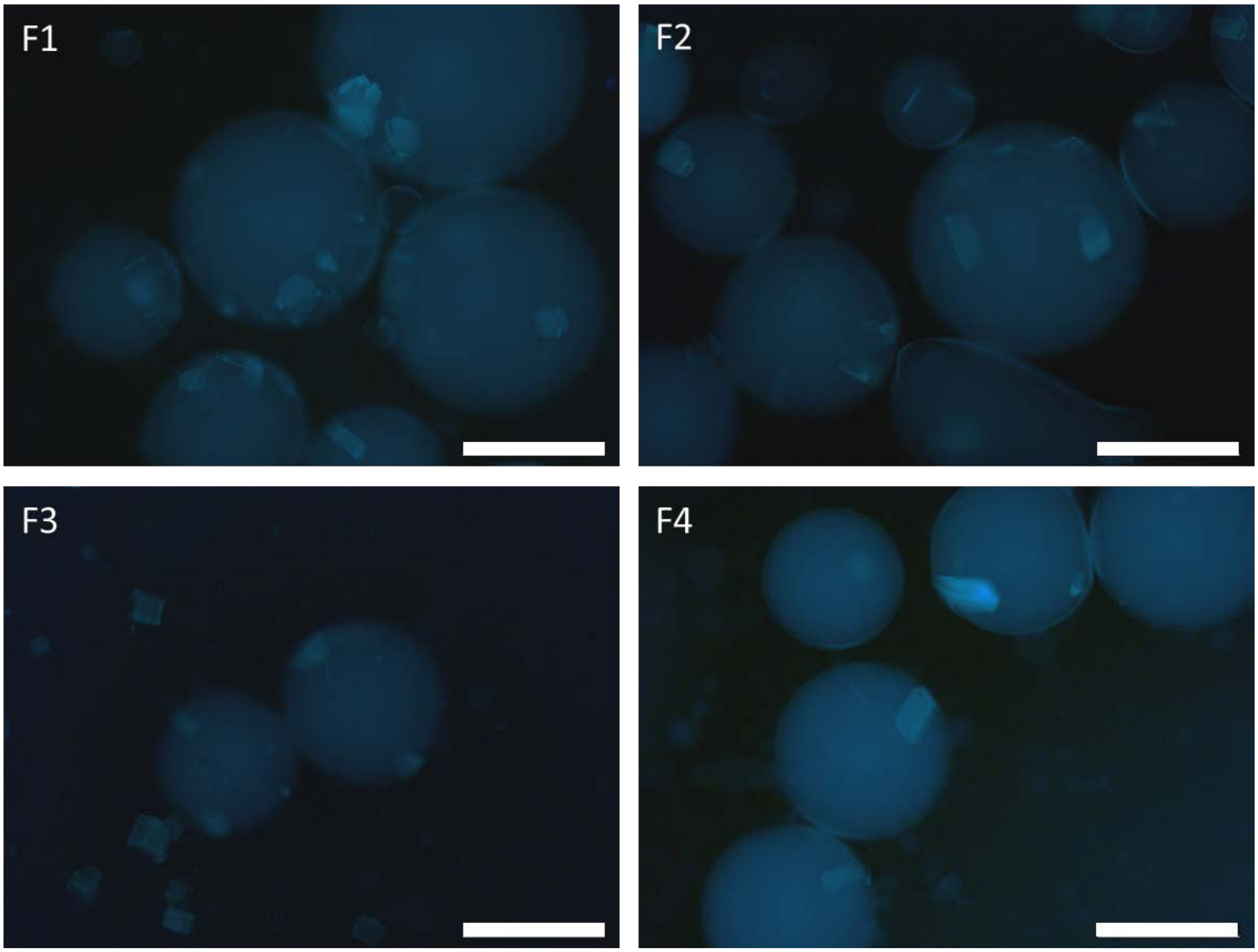

Figure 2.46: Fluorescence Optical Microscopy images of N S CDs-functionalised lysozyme grown inside colloidosomes. Images taken 12 days after incubation at room temperature. Images taken after 12 days of incubation using excitation laser of λ= 340 – 380 nm. Scale bar = 200 μm.

2.4.6. Theory of Protein Crystallisation Inside Colloidosomes

Protein crystallisation is a complex process, easily influenced by a variety of parameters which can both inhibit crystal growth as well as result in a variety of crystal sizes, shapes and morphologies. Identifying the optimum parameters for protein crystallisation remains a difficult and time-consuming process, despite the application of automation and miniaturisation of protein screening in recent years.[59] The use of colloidosomes as reaction vessels for the encapsulation and growth of protein crystals presents a novel technique for facile, cheap and time-effective growth of high-quality crystals with predictable sizes and morphologies. The exact mechanism by which colloidosome encapsulation aids protein crystal growth is not entirely understood and would require a comprehensive investigation which lies beyond the scope of this project. However, based on the investigations and analysis detailed in this chapter, and utilising the existing literature surrounding protein crystallisation, it is suggested that protein crystallisation is aided by two main processes; heterogenous nucleation and spatial and temporal control over nucleation events due to the confined volume of the protein crystallisation solution within colloidosomes. [58]

Nucleation is the rate limiting step towards protein crystallisation. Higher levels of saturation are needed for nucleation than crystal growth, which occurs in the meta-stable phase of the crystal phase diagram. Reaching the region of supersaturation as well as reducing the energetic barrier to nucleation can be used to facilitate protein crystallisation. One such method to lowering the energetic barrier to nucleation is the incorporation of heterogenic nucleation agents. The exact mechanism of heterogenous nucleation is yet to be fully understood, however a variety of materials such as minerals, seeds of protein crystals, ionisable surfaces and lipid membranes have been used successfully as heterogenous nucleation sites to aid protein crystallisation[2,5,41,47,55,58,60]

The encapsulation of the protein crystallisation solution contributes to the reduction in the energetic barrier to nucleation by two main routes. The presence of silica nanoparticles presents a potential site for heterogenous nucleation. This theory is supported by the experimental evidence, such as the growth of sea-urchin crystalline needle morphologies at the silica membrane (Section 3.1.1) which would only be observed in the event of heterogenous nucleation and surface attachment of the critical nuclei to the silica nanoparticles.[47]

The presence of a water/oil interface which is stabilised by the silica nanoparticles generates a gradient for the evaporation of water and the decrease in solubility in the protein/ increase in supersaturation of the solution. This is further exacerbated by the small volume of the droplet inside the colloidosome (1.78 – 4.2 nL) compared to batch crystallisation and HDVD ((3 -5 µL).

It is therefore appropriate to consider that the aqueous droplet in the colloidosome is a confined supersaturated metastable solution, which is analogous to single phase batch crystallisation in a confined volume. [58] The spatial and temporal control over nucleation events offered by the confined volume of the droplet provides greater control over the nucleation events and lowers the energetic barrier to critical nuclei clustering by restricting their diffusion within the confined volume. Better understanding of nucleation events, as well as the ability to control them presents new opportunities in the field of crystallisation production, seeing applications in biomaterials such as bone mineralisation. [58]

2.5. Conclusions and Further Work

This chapter details the development of a novel protein crystallisation technique, which to our knowledge, is first in kind. Silica nanoparticle colloidosomes (Pickering emulsions of water in oil) were used to encapsulate droplets of protein crystallisation solution. This technique is most synonymous with the existing technique of batch crystallisation in droplets, whereby all necessary components for crystallisation are present under suitable conditions to create a supersaturated crystallisation solution. The complex nature of protein crystallisation, and the multiple parameters which influence the nucleation and growth of crystals, must be considered with each experimental set up, and with the novelty of this technique in mind, it is most likely to be achieved by means of repeated trial and error. Crystals of lysozyme and ferritin were successfully grown inside the silica colloidosomes over a range of crystallisation conditions and temperatures, with more promising results observed with mCherry and BLC. Crystals grown inside colloidosomes were 10-20 x smaller than those observed in the control (batch crystallization and HDVD for lysozyme and ferritin respectively). The crystals retained the morphology observed in control, as well as additional morphologies not observed in control, such as the 'sea-urchin' morphology observed in lysozyme encapsulated in colloidosomes at 4˚C. Crystals appeared within 12 hours of incubation for lysozyme and 4 days for ferritin crystals. The crystals remained stable and intact for up to 8 months of incubation.

Due to time constraints on this project it was not possible to continue the exploration of the crystallisation of other proteins to success, however the results are highly promising and would encourage further investigation into the ubiquitous nature of this technique by expanding its application for other proteins. In order to enhance the efficiency of the protein crystallisation within colloidosomes, a potential avenue for the expansion of this work would be the use of automation. This would involve using existing protein crystallisation screening techniques to identify the optimal parameters for protein crystallisation of proteins which have been successfully crystallised by other methods, and to identify their adjustment for encapsulation in silica colloidosomes. The screening technique could also be used to adjust protein crystallisation parameters which are successful in hanging drop vapour diffusion methods to batch crystallisation in droplets. Automation of the colloidosome assembly could be facilitated using microfluidics, which allows for enhanced control of the colloidosome size, composition and ultimately scale up of the procedure. This would aid in both the speed of colloidosome assembly and facilitate the investigation of different cross-linking agents for the extraction of the colloidosomes and/or crystals into water and other solvents. [6,8,10,11,23–25,61–63]

Polymorphism is a common phenomenon observed in protein crystals, which can be observed even under the same experimental conditions. This is due to the highly dynamic nature of the protein molecule and sensitivity of forces holding the crystalline lattice together. This results in a wide range of conformational possibilities.[47] The observation of different polymorphs of lysozyme in colloidosomes in response to changes in temperature and protein concentration were observed. Often the results observed within colloidosomes were not observed in batch or other control crystallisation techniques, which may elude to increased sensitivity to the protein crystallisation solutions confined in colloidosomes to crystallisation parameters. This may indicate a potential advantage of colloidosomes in protein crystallisation screening. In addition to native lysozyme, investigations into the growth of lysozyme functionalised or co-crystallised with Au NPs and CDs were carried out.

Gold nanoparticles have been demonstrated to provide heterogenous nucleation surfaces which aid crystallisation. The interaction of the Au NPs with the protein crystallisation solution and subsequent effects on the surface charge and aggregation of the Au NPs requires further investigation. However, in theory, this could present a variety of surfaces of different size, curvature and surface chemistry available for critical nuclei clustering for nucleation and crystal growth.[56] Previous investigations in the literature into the use of Au NPs as nucleating agents have demonstrated that the small volume of Au NPs added to the crystallisation solution in droplets and in batch alters the crystallisation conditions, without causing any changes to the protein morphology or structure.[55,56,64] The results from this investigation show that presence of Au NPs induces morphological changes to the protein crystals but does not inhibit protein crystallisation. These changes are more apparent in the batch crystallisation experiments than inside colloidosomes. This may be due to the restriction of critical nuclei diffusion in the colloidosomes as well as the spatial and temporal control over nucleating events in the confined crystallisation solution volume. It has not been possible to isolate the effects of heterogenous nucleation sites between the silica nanoparticles and Au NPs, but nonetheless the results sufficiently demonstrate the capability of colloidosomes to grow functionalised lysozyme crystals which readily incorporate guest species *in situ*. X-ray diffraction studies on the lysozyme crystals in the presence and absence of Au NPs would be needed to investigate any changes to the protein structure caused by the presence of the Au NPs. Results of growing lysozyme crystals in the presence of N CDs and NS CDs demonstrate more definitively the successful incorporation of CDs into the lysozyme crystal structure, indicated by the fluorescence of the CDs-lysozyme crystals in batch and in colloidosomes. The results observed are very similar to those obtained with Au NPs, with polycrystalline agglomerates forming in batch and changes to the lysozyme crystal morphology observed in colloidosomes. As with Au NPs, further investigations are required to determine the effect of using CDs as nucleating agents. Also required is structural determination of the nanoparticle incorporation and crystal morphology . However, the results are highly promising and indicate additives, such as metallic nanoparticles or ligands, can be successfully incorporated into colloidosome crystallisation solutions. The spatial and temporal control of nucleation events offered by colloidosomes as well as functionalisation of the silica colloidosomes, and the use of additives, could be used to improve the crystallisation of proteins which are traditionally very difficult to crystallise, and grow functionalised crystals which can be tailored to a diverse range of applications such as drug delivery and catalysis.[2,43,65]

2.5.1. Diamond Light Source

In order to determine the success of protein crystallisation inside colloidosomes it was necessary to investigate the crystal quality and structure of crystals grown inside colloidosomes. Previous diffraction experiments using the Single Crystal X-Ray Diffractometer (University of Bristol) did not yield sufficient diffraction data. This section describes an experiment carried out at Diamond Light Source (Diamond House, Harwell Science and Innovation Campus) using the Versatile Macromolecular X-tallography *in-situ*(VMXi) beamline. The VMXi was used to collect diffraction data *in situ* from crystals grown inside colloidosomes. This experiment was the first of its kind to be carried out and presented many notable advantages such as the semi-complete automation of the process that did not require handling or manipulation of individual crystals, thereby retaining their integrity. The experiment did not require the crystals to be extracted from the colloidosome, thereby removing the need for cross-linking and extraction into aqueous media. Data was collected directly from the crystallisation experiments *in situ* with immediate feedback on the diffraction crystal quality.

The experiment was carried out without further opportunity to optimise the experiment due to time constraints on this project. Preliminary results however proved to be very promising. The sample preparation, data collection and results obtained are summarised below.

2.5.1.1. Sample Preparation and Screening

Protein crystallisation solutions inside colloidosomes were prepared as described in the 'Materials and Methods' of this chapter and stored in sealed glass vials for transport to the Diamond facility. Samples were then transferred to 96 microwell plate. A TTP Mosquito LCP (Figure 2.47) at 20˚C (Diamond, Crystallisation facility) was used to prepare the crystallisation screens. The LCP model was suitable for the transport of the highly viscous colloidosome emulsion into Greiner CrystalQuick X plates (Figure 2.48). The resulting droplet image as observed on the VMXi is shown in Figure (2.49).

Figure 2.47: Mosquito LCP instrument. [66]

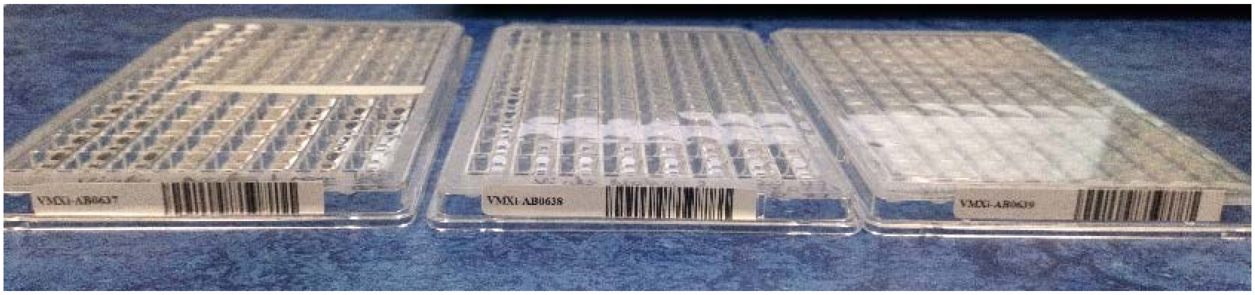

Figure 2.48: Greiner CrystalQuick X plates of crystal samples prepared using the Mosquito LCP instrument.

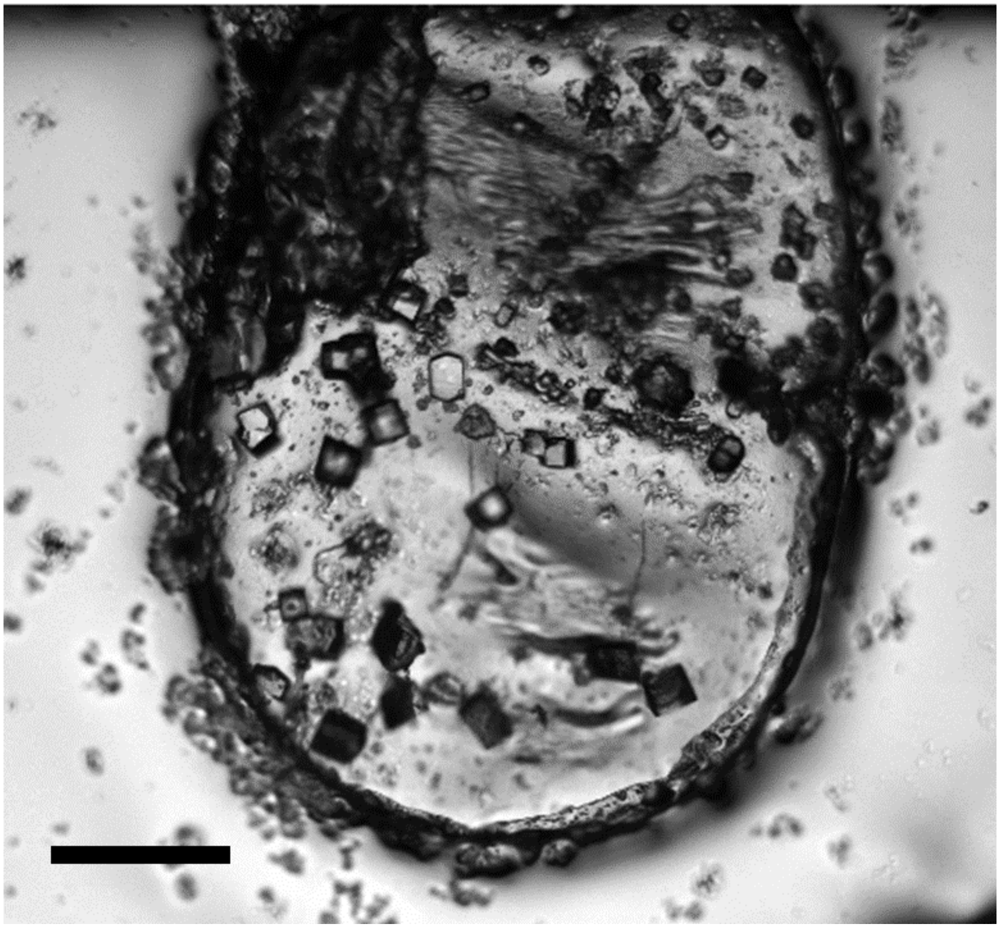

Figure 2.49: Image of screening droplet as observed on the VMXi

2.5.1.2. Data collection

The VMXi beamline set-up is demonstrated in Figure 2.50, highlighting all the major optical components of the instrument. Contrary to previous versions, the VMXi introduces new degrees of automation that do not require the user to operate the beamline directly, with data collection requests submitted via the web interface and crystallisation results evaluated via bespoke GUI in SynchWeb. The detector in use was an EigerX 4M detector (Dectris). Samples were prepared in SBS-format crystallisation plates (ANSI/SLAS 1-2004 to ANSI/SLAS 4-2004) with a drop size of 50 – 100 nL. The crystallisation plates were sealed with a plastic cover and stored in modified Rock Imager 1000 units (Formulatrix, ISA). The plates were transferred automatically between storage and imaging. The droplets were imaged through the bottom of the crystallisation plates.[67]

The parameters for data collection and summary data obtained are summarised in Table 2.3. Unfortunately, only one data set belonging to sample E4 (lysozyme crystallised at the Water/DCM interface in the presence of NS CDS, details in Results and Discussion section') was collected with sufficient data. However, the results of the data collection remain promising and could be easily improved towards a complete data set and diffraction pattern with more time and further optimization of the instrument and experimental set-up. [68]

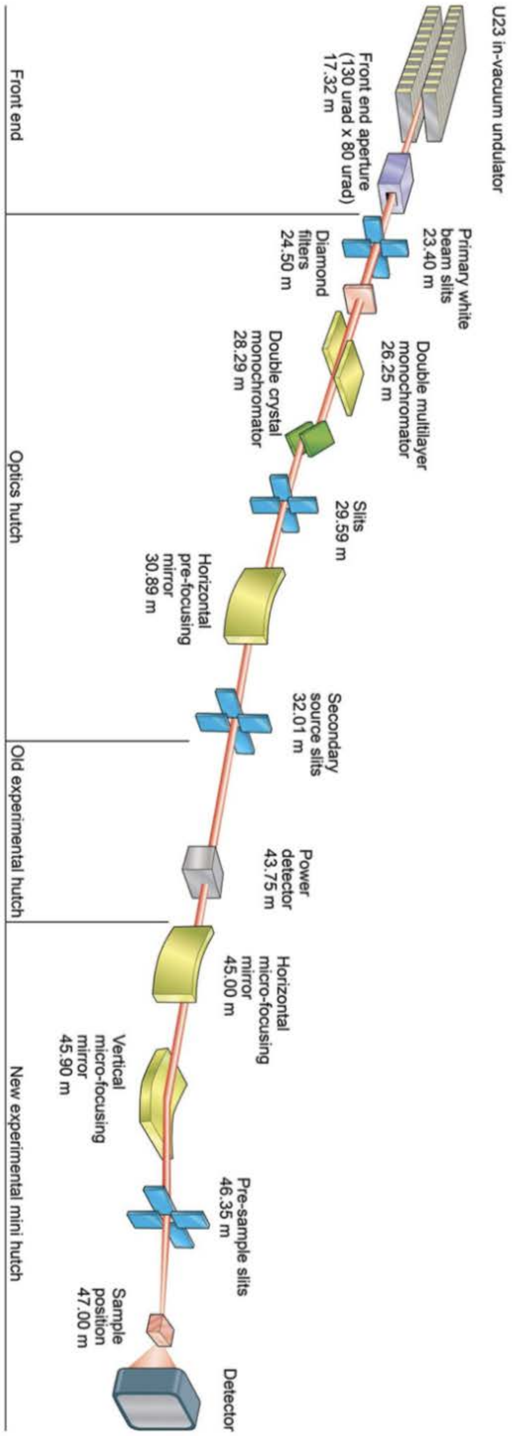

Figure 2.50: Schematic of the VMXi beamline set-up outlining the major optical components from sample to detector. Image adapted from Sanchez-Weatherby et al. (2019). Schematic is not to scale.[67]

Table 2.4: Data collection parameters and summary data for sample E4:

Parameter	**Overall**	**Inner shell**	**Outershell**
Images collected	1-600		
Resolution range (A)	56.42 – 2.5 (2.5 -11.8)		
Temperature (K)	293		
Goniometer position	4.33°		
Initial space group estimate	P4$_3$2$_1$2		
Unit cell parameters	a=79.8°, b= 79.8°, 37.5°. a=b=c=90°		
R$_{merge}$ (within I+/I-)	0.043	0.037	0.109
R$_{merge}$ (all I+ and I-)	0.046	0.038	0.126
R$_{meas}$ (all I+ and I-)	0.052	0.044	0.149
R$_{pim}$ (all I+ and I-)	0.024	0.022	0.078
Mean I/ ʃI	18.7	25.1	7.2
Mn(I) half-set correlation (CC1/2)	0.998	0.992	0.988
Completeness (%)	50.8	32.3	53.3
Multiplicity	4.1	3.6	3.1
Mean (|^2)	0.98	1.14	0.94
Total no. of reflections	8940	86	505
No. of unique reflections	2205	24	162
Solvent content (%)	41		
Point group	422		
Laue group	4/mmm		
PDB ID	3A3R		

A disadvantage of the data collection *in situ* is that the rotational axis is limited to the sample plate. a s a result, 60° is collected per crystal sample, and as multiple crystals are imaged, the data is merged and integrated to create a full data set. As only one sample was successfully imaged, the data set was limited to only 60° of sample E4. This was further reduced to 300 images in the data re-integration. Molecular replacement using a model with the same space group was used to overcome the issue of poor completion of the data set (50.8%). Diffraction data from 3A3R model (PDB ID) were used to solve the phase problem, molecular replacement was carried out in Phaser and a refinement run was done with refmac to generate an initial diffraction pattern (Figure 2.51) and initial model (Figure 2.52). The data sets were integrated using a combination of Xia2 and DIALS. The solvent content and number of molecules in the asymmetric unit were estimated to 41% solvent content and 1 molecule per asymmetric unit.

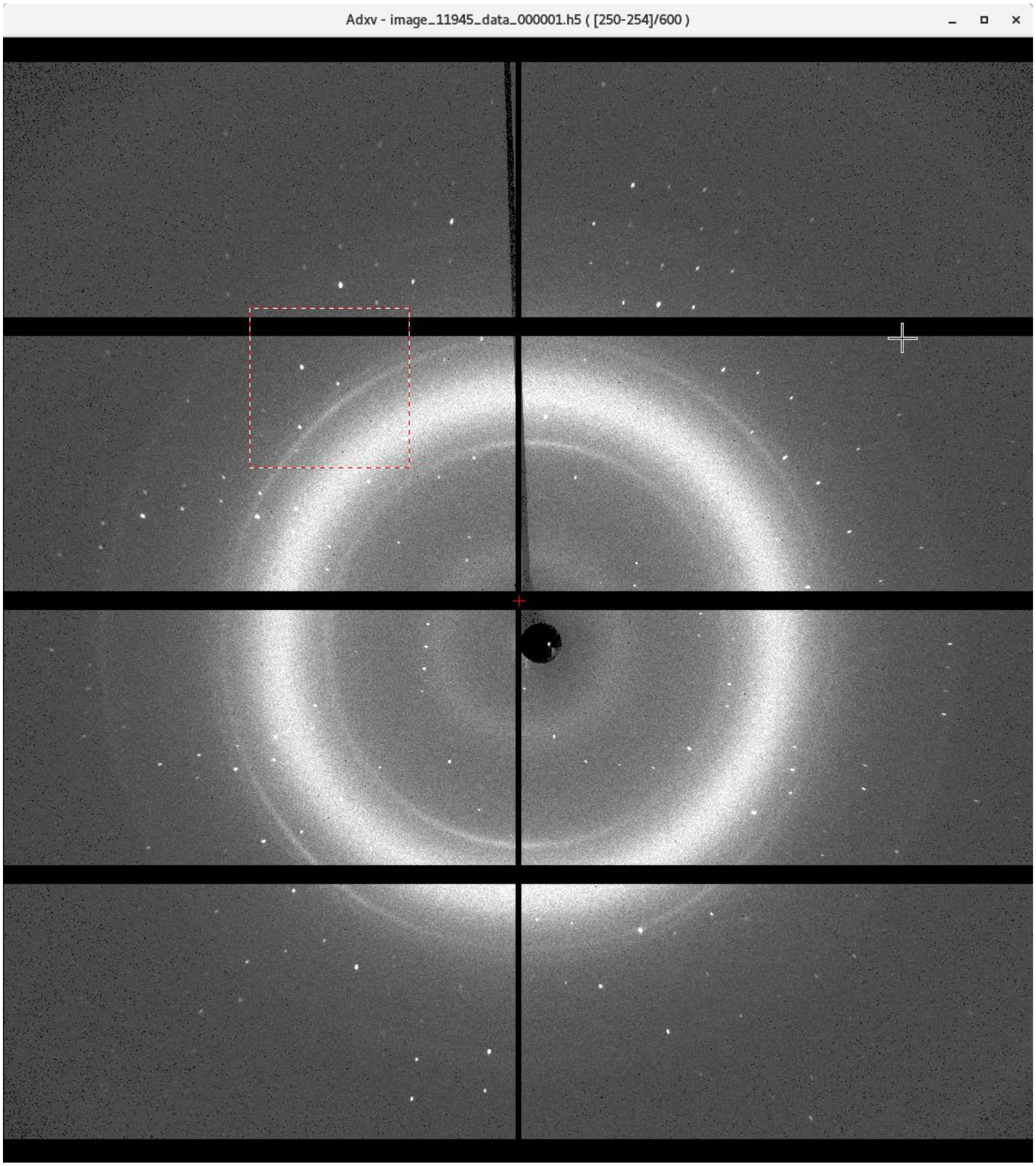

Figure 2.51: Initial diffraction pattern of lysozyme obtained from the E4 data set

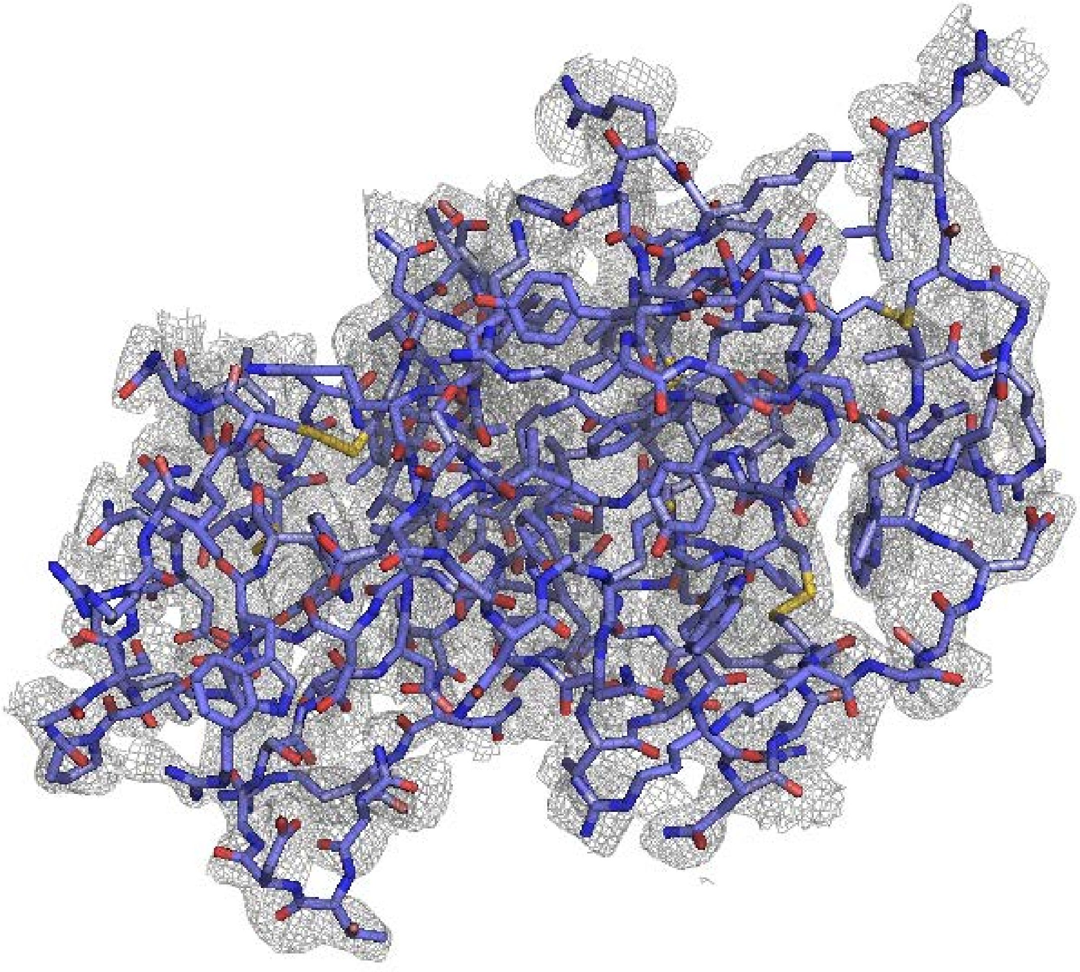

Figure 2.52: Initial model of lysozyme crystal generated from integration of E4 data set with phases from PDB ID model 3A3R for molecular replacement.

2.6. References

1. Yan, E.-K. *et al.* Cross-linked protein crystals by glutaraldehyde and their applications. *RSC Adv.* **5**, 26163–26174 (2015).
2. Abe, S. & Ueno, T. Design of protein crystals in the development of solid biomaterials. *RSC Adv.* **5**, 21366–21375 (2015).
3. Vilenchik, L. Z., Griffith, J. P., St. Clair, N., Navia, M. A. & Margolin, A. L. Protein crystals as novel microporous materials. *J. Am. Chem. Soc.* **120**, 4290–4294 (1998).
4. Lalonde, J. J. *et al.* Cross-Linked Crystals of Candida rugosa Lipase: Highly Efficient Catalysts for the Resolution of Chiral Esters. *J. Am. Chem. Soc.* **117**, 6845–6852 (1995).
5. Khurshid, S., Saridakis, E., Govada, L. & Chayen, N. E. Porous nucleating agents for protein crystallization. *Nat. Protoc.* **9**, 1621–33 (2014).
6. Chen, D. L., Li, L., Reyes, S., Adamson, D. N. & Ismagilov, R. F. Using Three-Phase Flow of Immiscible Liquids To Prevent Coalescence of Droplets in Microfluidic Channels : Criteria To Identify the Third Liquid and Validation with Protein Crystallization. 2255–2260 (2007).
7. Maeki, M. *et al.* Controlling protein crystal nucleation by droplet-based microfluidics. *Chemistry* **20**, 1049–56 (2014).
8. Zheng, B., Roach, L. S. & Ismagilov, R. F. Screening of protein crystallization conditions on a microfluidic chip using nanoliter-size droplets. *J. Am. Chem. Soc.* **125**, 11170–1 (2003).
9. Wei, H. *et al.* Time-dependent, protein-directed growth of gold nanoparticles within a single crystal of lysozyme. *Nat. Nanotechnol.* **6**, 93–97 (2011).
10. Chen, D. L., Gerdts, C. J. & Ismagilov, R. F. Using microfluidics to observe the effect of mixing on nucleation of protein crystals. *J. Am. Chem. Soc.* **127**, 9672–3 (2005).
11. Gerdts, C. J. *et al.* Time-controlled microfluidic seeding in nL-volume droplets to separate nucleation and growth stages of protein crystallization. *Angew. Chem. Int. Ed. Engl.* **45**, 8156–60 (2006).
12. Zhu, Y. *et al.* Nanoliter-scale protein crystallization and screening with a microfluidic droplet robot. *Sci. Rep.* **4**, 5046 (2014).
13. Ng, J. D., Gavira, J. A. & García-Ruíz, J. M. Protein crystallization by capillary counterdiffusion for applied crystallographic structure determination. *J. Struct. Biol.* **142**, 218–231 (2003).
14. Leunissen, M. Protein crystallization. *October* **383**, 7881–7887 (2011).
15. Yang, C.-G., Liu, Y.-H., Di, Y.-Q. & Xu, Z.-R. Generation of two-dimensional concentration-gradient droplet arrays on a two-layer chip for screening of protein crystallization conditions. *Microfluid. Nanofluidics* **18**, 493–501 (2014).
16. Yadav, M. K. *et al.* In situ data collection and structure refinement from microcapillary protein crystallization. *J. Appl. Crystallogr.* **38**, 900–905 (2005).
17. Dinsmore, a D. *et al.* Colloidosomes: selectively permeable capsules composed of colloidal particles. *Science* **298**, 1006–1009 (2002).
18. Thompson, K. L. *et al.* Covalently Cross-Linked Colloidosomes. *Macromolecules* **43**, 10466–10474 (2010).

19. Saraf, S., Rathi, R., Kaur, C. D. & Saraf, S. Colloidosomes an advanced vesicular system in drug delivery. *Asian J. Sci. Res.* **4**, 1–15 (2011).

20. Thompson, K. L., Armes, S. P. & York, D. W. Preparation of Pickering Emulsions and Colloidosomes with Relatively Narrow Size Distributions by Stirred Cell Membrane Emulsification. *Langmuir* **27**, 2357–2363 (2011).

21. Rossier-Miranda, F. J., Schroën, C. G. P. H. & Boom, R. M. Colloidosomes: Versatile microcapsules in perspective. *Colloids Surfaces A Physicochem. Eng. Asp.* **343**, 43–49 (2009).

22. Binks, B. P. Particles as surfactants—similarities and differences. *Curr. Opin. Colloid Interface Sci.* **7**, 21–41 (2002).

23. Sander, J. S. & Studart, A. R. Multiwalled functional colloidosomes made small and in large quantities via bulk emulsification. *Soft Matter* **10**, 60–68 (2014).

24. Shah, R. K., Kim, J. W. & Weitz, D. A. Monodisperse stimuli-responsive colloidosomes by self-assembly of microgels in droplets. *Langmuir* **26**, 1561–1565 (2010).

25. Sander, J. S. & Studart, A. R. Monodisperse functional colloidosomes with tailored nanoparticle shells. *Langmuir* **27**, 3301–3307 (2011).

26. Li, M., Huang, X. & Mann, S. Spontaneous Growth and Division in Self-Reproducing Inorganic Colloidosomes. *Small* **10**, 3291–3298 (2014).

27. Pera-Titus, M., Leclercq, L., Clacens, J.-M., De Campo, F. & Nardello-Rataj, V. Pickering interfacial catalysis for biphasic systems: from emulsion design to green reactions. *Angew. Chem. Int. Ed. Engl.* **54**, 2006–21 (2015).

28. Li, M., Huang, X., Tang, T.-Y. D. & Mann, S. Synthetic cellularity based on non-lipid micro-compartments and protocell models. *Curr. Opin. Chem. Biol.* **22**, 1–11 (2014).

29. Li, M., Green, D. C., Anderson, J. L. R., Binks, B. P. & Mann, S. In vitro gene expression and enzyme catalysis in bio-inorganic protocells. *Chem. Sci.* **2**, 1739 (2011).

30. Li, M., Harbron, R. L., Weaver, J. V. M., Binks, B. P. & Mann, S. Electrostatically gated membrane permeability in inorganic protocells. *Nat. Chem.* **5**, 529–536 (2013).

31. Tang, J., Quinlan, P. J. & Tam, K. C. Stimuli-responsive Pickering emulsions: recent advances and potential applications. *Soft Matter* **11**, 3512–3529 (2015).

32. Dinsmore, A., Hsu, M. & Nikolaides, M. Colloidosomes: selectively permeable capsules composed of colloidal particles. *Science (80-).* **298**, 1006–1009 (2002).

33. Gracias, D. H. Stimuli responsive self-folding using thin polymer films. *Curr. Opin. Chem. Eng.* **2**, 112–119 (2013).

34. Katepalli, H., John, V. T. & Bose, A. The response of carbon black stabilized oil-in-water emulsions to the addition of surfactant solutions. *Langmuir* **29**, 6790–6797 (2013).

35. Hoang, G. C. Pore-Size Control of Silica Gels in Acidic Water Conditions Using Sol-Gel Processing. *J. Korean Phys. Soc.* **31**, 227–230 (1997).

36. Ding, Y., Shi, L. & Wei, H. Protein-directed approaches to functional nanomaterials: a case study of lysozyme. *J. Mater. Chem. B* **2**, 8268–8291 (2014).

37. Guli, M., Lambert, E., Li, M. & Mann, S. Template-Directed Synthesis of Nanoplasmonic Arrays

by Intracrystalline Metalization of Cross-Linked Lysozyme Crystals. *Angew. Chemie* **122**, 530–533 (2010).

38. Mafune, F. *et al.* Microcrystal delivery by pulsed liquid droplet for serial femtosecond crystallography. *Acta Crystallogr.,Sect.D* **72**, 520–523 (2016).

39. Brinkley, M. A Brief Survey of Methods for Preparing Protein Conjugates with Dyes, Haptens and Crosslinking Reagents. *Bioconjug. Chem.* **3**, 2–13 (1992).

40. Kumar, V., Dost, S. & Durst, F. Numerical modeling of crystal growth under strong magnetic fields: An application to the travelling heater method. *Appl. Math. Model.* **31**, 589–605 (2007).

41. Heijna, M. C. R., Van Enckevort, W. J. P. & Vlieg, E. Growth inhibition of protein crystals: A study of lysozyme polymorphs. *Cryst. Growth Des.* **8**, 270–274 (2008).

42. Falkner, J. C. *et al.* Generation of Size-Controlled , Submicrometer Protein Crystals. **13**, 2679–2686 (2005).

43. England, M. W. *et al.* Fabrication of polypyrrole nano-arrays in lysozyme single crystals. *Nanoscale* **4**, 6710 (2012).

44. Granier, T., Gallois, B., Dautant, A., Langlois D'Estaintot, B., Precigoux, G. 1IER. (1997). Available at: http://www.rcsb.org/pdb/explore.do?structureId=1ier.

45. Georgieva, D. G., Kuil, M. E., Oosterkamp, T. H., Zandbergen, H. W. & Abrahams, J. P. Heterogeneous nucleation of three-dimensional protein nanocrystals. *Acta Crystallogr. Sect. D Biol. Crystallogr.* **63**, 564–570 (2007).

46. Lorber, B., Jenner, G. & Giegé, R. Effect of high hydrostatic pressure on nucleation and growth of protein crystals. *J. Cryst. Growth* **158**, 103–117 (1996).

47. McPherson, A. & Cudney, B. Optimization of crystallization conditions for biological macromolecules. *Acta Crystallogr. Sect. FStructural Biol. Commun.* **70**, 1445–1467 (2014).

48. Durbin, S. D. & Feher, G. Crystal growth studies of lysozyme as a model for protein crystallization. *J. Cryst. Growth* **76**, 583–592 (1986).

49. England, M. W., Patil, A. J. & Mann, S. Synthesis and confinement of carbon dots in lysozyme single crystals produces ordered hybrid materials with tuneable luminescence. *Chem. - A Eur. J.* **21**, 9008–9013 (2015).

50. Muskens, O. L., England, M. W., Danos, L., Li, M. & Mann, S. Plasmonic response of Ag- and Au-infiltrated cross-linked lysozyme crystals. *Adv. Funct. Mater.* **23**, 281–290 (2013).

51. Margolin, A. L. & Navia, M. a. Protein Crystals as Novel Catalytic Materials. *Angew. Chem. Int. Ed. Engl.* **40**, 2204–2222 (2001).

52. Wörle-Knirsch, J. M., Pulskamp, K. & Krug, H. F. Oops they did it again! Carbon nanotubes hoax scientists in viability assays. *Nano Lett.* **6**, 1261–1268 (2006).

53. Ribeiro, D. Using gold nanoparticles in protein crystallography: studies in crystal growth and derivatization. (2012).

54. Hodzhaoglu, F., Kurniawan, F., Mirsky, V. & Nanev, C. Gold nanoparticles induce protein crystallization. *Cryst. Res. Technol.* **43**, 588–593 (2008).

55. Kertis, F. *et al.* Heterogeneous nucleation of protein crystals using nanoporous gold nucleants. *J.*

Mater. Chem. **22**, 21928–21934 (2012).

56. Ko, S., Kim, H. Y., Choi, I. & Choe, J. Gold nanoparticles as nucleation-inducing reagents for protein crystallization. *Cryst. Growth Des.* **17**, 497–503 (2017).

57. England, M. W., Patil, A. J. & Mann, S. Synthesis and confinement of carbon dots in lysozyme single crystals produces ordered hybrid materials with tuneable luminescence. *Chemistry* **21**, 9008–13 (2015).

58. Grossier, R., Hammadi, Z., Morin, R. & Veesler, S. Predictive Nucleation of Crystals in Small Volumes and Its Consequences. *Phys. Rev. Lett.* **107**, 025504 (2011).

59. Dale, G. E., Oefner, C. & D'Arcy, A. The protein as a variable in protein crystallization. *J. Struct. Biol.* **142**, 88–97 (2003).

60. Ribeiro, D. *et al.* Use of gold nanoparticles as additives in protein crystallization. *Cryst. Growth Des.* **14**, 222–227 (2014).

61. Hu, Y. & Pérez-Mercader, J. Microfluidics-Assisted Synthesis of Cross-Linked Colloidosomes with Multisensitive Behaviors: A Potential Platform for Photo Memory Device and Blue-Light-Triggered Release Vehicle. *ACS Appl. Nano Mater.* acsanm.8b00554 (2018). doi:10.1021/acsanm.8b00554

62. Zheng, B., Tice, J. D., Roach, L. S. & Ismagilov, R. F. A droplet-based, composite PDMS/glass capillary microfluidic system for evaluating protein crystallization conditions by microbatch and vapor-diffusion methods with on-chip X-ray diffraction. *Angew. Chem. Int. Ed. Engl.* **43**, 2508–11 (2004).

63. Li, L. *et al.* Simple Host - Guest Chemistry To Modulate the Process of Concentration and Crystallization of Membrane Proteins by Detergent Capture in a Microfluidic Device. 14324–14328 (2008).

64. Shukla, S. *et al.* Porous gold nanospheres by controlled transmetalation reaction: A novel material for application in cell imaging. *Chem. Mater.* **17**, 5000–5005 (2005).

65. Horike, S., Shimomura, S. & Kitagawa, S. Soft porous crystals. *Nat. Chem.* **1**, 695–704 (2009).

66. ttplabtech. (2018).

67. Sanchez-Weatherby, J. *et al.* VMXi: a fully automated, fully remote, high-flux in situ macromolecular crystallography beamline. *J. Synchrotron Radiat.* **26**, 291–301 (2019).

68. Foadi, J. *et al.* Clustering procedures for the optimal selection of data sets from multiple crystals in macromolecular crystallography. *Acta Crystallogr. Sect. D Biol. Crystallogr.* **69**, 1617–1632 (2013).

Chapter 3: Novel Hybrid Synthesis of Fluorescent Nitrogen Doped and Nitrogen and Sulfur Doped Carbon Dots Derived from Nanocrystalline Cellulose

3.1. Aims of This Work

The aim of this work was to develop and optimise a novel synthetic mechanism for the synthesis of nitrogen doped carbon dots (N CDs) and nitrogen and sulfur doped carbon dots (NS CDs) using nanocrystalline cellulose (NCC) as a novel organic precursor. N CDs and NS CDs carbon were synthesised by the acid dehydration of cellulose pulp and microwave-assisted pyrolysis. This work therefore draws on two distinct synthetic approaches 'top-down' (acid hydrolysis) and 'bottom-up' (microwave pyrolysis) present in the literature to present a novel hybrid synthetic technique. The CDs were characterised to examine their size, morphology, optical properties, internal molecular structure, surface charge, quantum yield, and photostability. This characterisation served to elucidate a theory for the structure of the CDs, photoluminescence (PL) mechanism of the CDs and identify factors affecting and contributing to the PL behaviour.

3.2. Introduction

3.2.1. Quantum Dots vs Carbon Dots

Quantum dots (QDs) are fluorescent nanoparticles with size-dependant optical properties, broad excitation spectrums and high metabolic and photo stability. These properties are due to the quantum size effect in semiconductor nanocrystals that make up QDs, which possess dimensions smaller than that of the Bohr bulk exciton radius. This phenomenon thereby results in size-dependent optical properties. Despite these advantages, QDs are limited by their toxicity due to the presence of heavy metals in the semi-conductor crystals such as cadmium and arsenic and require functionalisation to make the particles bio-compatible.[1] In addition to their toxicity QDs are poorly soluble and their blinking (emitting light intermittently under constant illumination) properties make them difficult to track over time. Additionally, the size of QDs is often larger than the biomolecules they are conjugated with. This leads to complications when associating with multiple targets and the formation of artificial clusters, which impede normal cellular function and may lead to bioaccumulation of toxic materials in tissues and organs. These effects thereby limit their utility, particularly in biomedical applications.[2,3]

Carbon quantum dots or carbon dots (CDs) is a collective term used to describe discrete, quasi-spherical fluorescent nanoparticles, typically below 10 nm in diameter. These particles typically consist of a carbogenic core stabilised by oxidised surface groups, such as carboxylic acids and alcohols, which render them highly soluble in aqueous solutions.[4–6] CDs have received increasing attention as 'green' alternatives to QDs due to their simple and versatile synthesis, high stability, excellent biocompatibility and the abundance of renewable organic sources available as synthetic precursors.[1,7,8] They are chemically inert, highly photo-stable, easy to functionalise and possess highly tuneable photoluminescence owing to the diversity of available synthetic routes.[1] The unique electronic, chemical, optical and mechanical properties of CDs have made them attractive candidates for application in fields of photo-sensing, bio-imaging, catalysis and drug delivery.[1,2,9]

3.2.2. Carbon Dots

3.2.2.1. Types of carbon dots

Carbon dots can be divided into a classification developed by Valcarcel et al. into graphene quantum dots (GQDs), carbon quantum dots (CQDs), amorphous carbon dots or Carbon nanodots (CNDs) and polymeric carbon dots (PCs) depending on their structure and composition.[9] GQDs are two-dimensional spherical particles produced by the top-down exfoliation of graphitic structures to reveal a few layers of graphene sheets. CQDs are quasi-spherical particles comprising of a multi-layered crystalline graphitic core with a functionalised surface. The term 'quantum' is reserved for particles which exhibit a semi-conductor type delocalised band structure, where the

PL behaviour is attributed to the quantum confinement effect with some contributions from molecule-like surface states. CNDs are amorphous, quasi-spherical particles which do not display any quantum effects, whose PL behaviour is attributed exclusively to molecule-like excited states[6]. Due to the difficulty in determining whether the synthesised carbon nanoparticles exhibit quantum confinement effects, the CDs discussed in this work can be considered somewhere in the category of CQDs or CNDs and are referred to simply as CDs in this chapter.

3.2.2.2. Top Down vs. Bottom Up Synthesis of Carbon Dots

The synthesis of carbon dots (CDs) can be broadly categorised as top-down or bottom-up.[3] Top-down synthesis involves using a bulk carbon substrate as the starting material and the cleavage, miniaturisation, or breakdown of the substrate into nanoscale particles via physical, chemical or electrochemical techniques. This is often followed by chemical modification.[3] Laser ablation, arc-discharge, electrochemistry, and chemical oxidation are examples of top-down methods. This approach utilises carbohydrate sources with sp^2 enriched starting materials which lack the sufficient band gap to produce fluorescence,[10] such as multi-walled carbon nanotubes, graphene, candle soot, and graphite, etc. The advantage of this method is the retention of the sp^2 crystallinity and uniformity of synthesised product, at the expense of flexibility. [5]

Bottom-up synthesis involves the formation of CDs from organic starting materials and modification of their surface chemistry - also known as passivation - and hence functionality. The starting materials comprise of small molecules or polymers, such as amino acids[11], and carbohydrates, which undergo dehydration and carbonisation to form carbon dots. The presence of –OH, -C=O, $-NH_2$ and –COOH groups enable these molecules to be dehydrated at elevated temperatures. There are multiple approaches to the dehydration and carbonisation processes such as microwave pyrolysis, combustion, chemical and hydrothermal oxidation, acid-mediated reflux, and thermal decomposition.[5,12,21–25,13–20]

The chemical structure of the CDs varies according to the synthesis mechanism and is sensitive to synthesis parameters such as the ratio of reagents, temperature, pH, presence of additives or impurities (which can influence the nucleation and growth of CDs), solvents, type of reaction vessel, etc. CDs produced by bottom-up synthetic approaches possess less sp^2 crystallinity compared to those synthesised by the bottom-up approach and are much less uniform in nature. [10] This results in issues around the uniformity, purity, and consistency of surface chemistry of the synthesised CDs. These properties are crucial for uniform behaviour and mechanistic understanding of the PL behaviour.[9]

Where top-down synthesis is limited to using precursors with existing sp^2 characteristics, bottom-up synthesised CDs can be synthesised from a broad range of organic sources.[15] The use of carbohydrates as starting materials for the synthesis of CDs has been widely reported due to the multiple advantageous characteristics of these abundant biomolecules. The low cost, availability, heterogeneity, non-toxicity, low carbonisation temperatures, high water solubility and well-defined chirality has made them attractive agents for CD synthesis. Monosaccharides such as glucose and maltose, disaccharides such as sucrose and lactose as well as carbohydrate-based biopolymers such as chitosan, dextran, and hyaluronic acid, have been used as carbohydrate sources for the synthesis of fluorescent CDs. The diversity of their chemical structure, surface chemistry and physical properties coupled with the diversity of available synthesis mechanisms has been used to produce carbohydrate-based CDs of various morphologies, properties and structures.[5] Nanocrystalline cellulose (NCC) derived from the acid hydrolysis of cellulose pulp was used as the organic precursor for the synthesis of the CDs in this work.

Table 3.1 provides a broad overview of CDs synthesised using top-down and bottom up approaches as well as a variety of starting materials. The majority of the literature has categorised the synthetic technique as either ‘top-down’ or ‘bottom-up’, based on majority attributes of the CDs relating to the characterisation results such as the prevalence of sp^2/sp^3 in the carbogenic core. The possibility of a hybrid synthesis which combines the two techniques is not explicitly outlined in the literature.

Table 3.1: Provides a broad overview of different synthetic approaches, both top down and bottom up to synthesise CDs.[26,27] (td) denotes top down, (bu) denotes bottom up, (d) denotes doping, (sp) denotes surface passivating and (NR) denotes 'not recorded' in the literature.

Type of CD	Carbon Source	Doping /Surface passivating agent (if any)	Synthesis Method	Size (nm)	Quantum Yield (%)	Reference
Chlorin e6-conjugated CDs	Raw soot	-	Nitric acid oxidation (td)	1-2	NR	[28]
GQDs	Graphene Oxide	-	Hydrothermal (td)	5-13	5	[27]
GQDs	Graphene Oxide	-	Amino-hydrothermal	2.5	NR	[27]
GQDs	Graphene Oxide	-	Solvothermal	5.3	1.6	[27]
GQDs	Graphene Oxide	-	Photo-Fenton reaction	40	45	[27]
CDs	C_{60}	-	Calaysed cage-opening	2.7 -10	15-30	[27]
Boron doped CDs	Citric acid	Boric acid, urea (d)	Microwave heating (bu)	2-6	10-15%	[29]
CDs	Citric acid, ethylene diamine	-	Hydrothermal method (bu)	<5	80%	[30,31]
CDs	Citric acid	Tryptophan (d)	Microwave-assisted pyrolysis (td)	2-6	20.6%	[32]
Green emitting CDs	Citric acid, urea	-	Microwave assisted synthesis (bu)	2-6	36%	[33]
N, S-co doped CDs	Citric acid	Cystamine dihydrochloride(d)	Hydrothermal treatment	1.3 – 2.3	39.7%	[34]
N,S doped CDs	Citric acid, L-cysteine	L-cysteine (d)	Hydrothermal (bu)	NR	30-64%	[35]
PEI-CDs	Glycerol	PEI (d,sp)	Microwave pyrolysis (bu)	9 ± 1	NR	[36]
CDs	BSA + urea BSA + GuHCl Lipase + urea Lipase + GuHCl Pepsin + urea Pepsin + GuHCl	-	Microwave treatment (bu)	2-6	13.3% 14.4% 9.0% 12.8% 8.6% 13.1%	[37]
N-doped CDs	Grass	-	Hydrothermal treatment (bu)	3-5	4.2%	[38]
CDs	L-ascorbic acid	-	Hydrothermal treatment (bu)	2	6.79%	[39]
CDs	Glucose, monopotassium phosphate	-	Hydrothermal treatment (bu)	1.8 - 3.8	24%	[40]

CDs	Orange juice	-	Hydrothermal treatment (bu)	1.5 - 4.5	26%	[25]
N-doped CDs	Glucose	Ethylene Diamine(d), boronic acid (sp)	Carbonisation (bu)	1-7	NR	[41]
N-doped CDs	Glucose	Ammonia solution (d)	Ultrasonication (td)	2	NR	[42]
CDs	glucose	Glutathione (sp)	Hydrothermal synthesis (bu)	2.6 ± 0.2	7.2%	[43]
CD-Asp	d-glucose	L-aspartic acid (d)	Pyrolysis (bu)	2.28 ± 0.42	7.5%	[44]
®-amino alcohol functionalized CDs	L-phenylalaninol	-	Hydrothermal carbonisation (bu)	2.8	8.2%	[45]
Hydrophobic CDs	Pluronic F-68	PF-68 (partial sp)	Microwave pyrolysis (bu)	5-20	7%	[46]
CDs	Carbon nanopowder	2,2′-(ethylenedioxy)bis(ethylamine (sp)	Nitric acid oxidation (td)	5	NR	[47]
N-doped CQDs	Agarose	Ethylene diamine (d,sp)	Hydrothermal treatment (bu)	4.5	74.16%	[48]
CDs	MWCNTs, SWCNTs	Acetone (sp)	Acid oxidation (td)	3	10%	[49]
N-doped CDs	BSA	BSA(d)	Hydrothermal reaction (bu)	<6	44%	[50]
N-doped CDs	1, 3-bis(carboxymethyl)imidazolium chloride ([Im(AH)2]Cl aminoethylethanolamine (AEEA)	Reagents (d)	Autoclave pyrolysis (bu)	2.4	23.2	[51]
N-doped CDs	L-glutamic acid	-	Solid-phase microwave synthesis (bu)	1.64	41.2%	[52]
CQDs	Folic acid, Phosphoric acid	Folic acid, phosphoric acid (d)	Hydrothermal treatment (bu)	13.2 ± 1.6	NR	[53]
CDs	Milk	Milk (d)	Hydrothermal treatment (bu)	2.5 ± 1	5.7%	[54]

3.2.3. Novel Hybrid Synthesis of Carbon Dots

The synthesis mechanism has a decisive role in the structure of CDs and therefore the underlying PL mechanism. The existing literature surrounding CD synthesis definitively describes the synthesis mechanism as either ‘top-down’ or ‘bottom-up’. The categorisation depends on the synthetic mechanism and, as mentioned previously, the characteristics of the resulting CDs. Where top down synthetic routes produce crystalline CDs with a graphene-like core, excitation-dependent PL behaviour, low quantum yields and high photostability. Bottom up synthetic routes produce CDs that are quasi spherical particles with no crystal lattice, excitation-independent PL behaviour, high quantum yields and low photostability.[55]

The classification is often made using the properties of the CDs identified in the characterisation. To this effect there has not been much consideration in the literature for CDs which do not fit entirely into either category and demonstrate characteristics of both ‘top-down’ and ‘bottom-up’ CDs. Despite the breadth of literature introducing novel techniques, conditions and precursors to synthesise CDs, the mention or classification of ‘hybrid’ synthetic techniques which produce CDs with these features is not prevalent. This work presents a novel synthetic technique which combines top-down and bottom-up practices to produce CDs which demonstrate characteristics of both. The top-down acid hydrolysis of cellulose pulp into nanocrystalline cellulose (NCC), which retains the crystallinity of the precursor material, is combined with bottom-up synthesis of CDs by microwave assisted pyrolysis in the presence of doping and/or surface passivating agents. Microwave-assisted pyrolysis is simple, easy to use, low cost and very rapid compared to other synthesis techniques, such as hydrothermal synthesis.[56] This is a widely reported method that has been used on organic precursors including ascorbic acid, citric acid, glycerol, L-glutamic acid, and diethylene glycol-ammonium citrate.[3] Heteroatom doping of CDs has been widely reported as a means to improve the electronic and PL properties of CDs.[34,57] Numerous studies have been carried out into producing CDs containing nitrogen but less so into other co-doping or doping with other heteroatoms.[56]

3.2.4. Cellulose

Cellulose is the most abundant natural polymer and possesses many advantageous properties such as its low cost, low density, high strength, stability and biocompatibility. The cellulose polymer is a linear homo-polysaccharide polymer consisting of D-anyhdroglucopyranose (AGU) units held together by β-1,4-glycosidic bonds (Figure 3.1).[58]

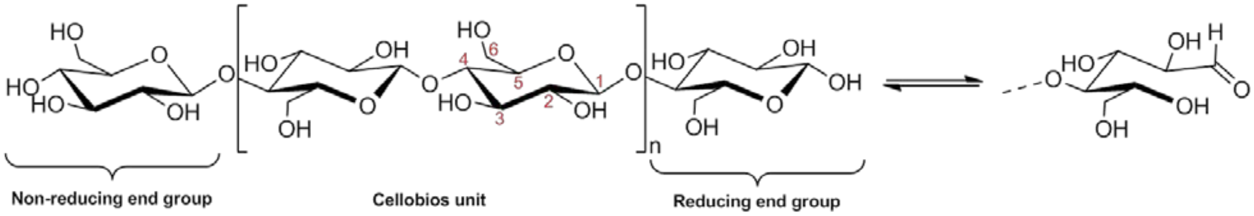

Figure 3.1: Molecular structure of cellulose[59]

These polymer chains are then ordered into microfibrils. The regular linear structure of cellulose and presence of hydroxyl groups in the molecules enables the polymers to form ordered crystalline structures held together by hydrogen bonds, producing microfibrils with crystalline and non-crystalline regions. These are illustrated in Figure 3.2. Several microfibrils assemble to form a macrofibre, which are arranged in different orientations to form the plant cell wall (Figure 3.3).[59]

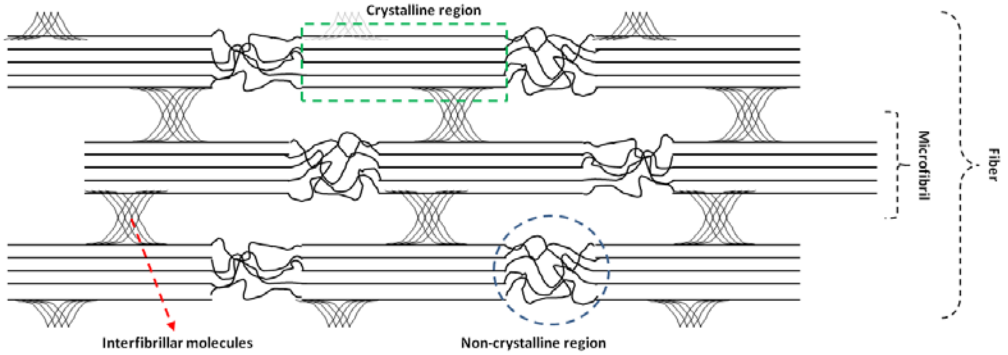

Figure 3.2: Crystalline and non-crystalline regions of the cellulose fibre.[59]

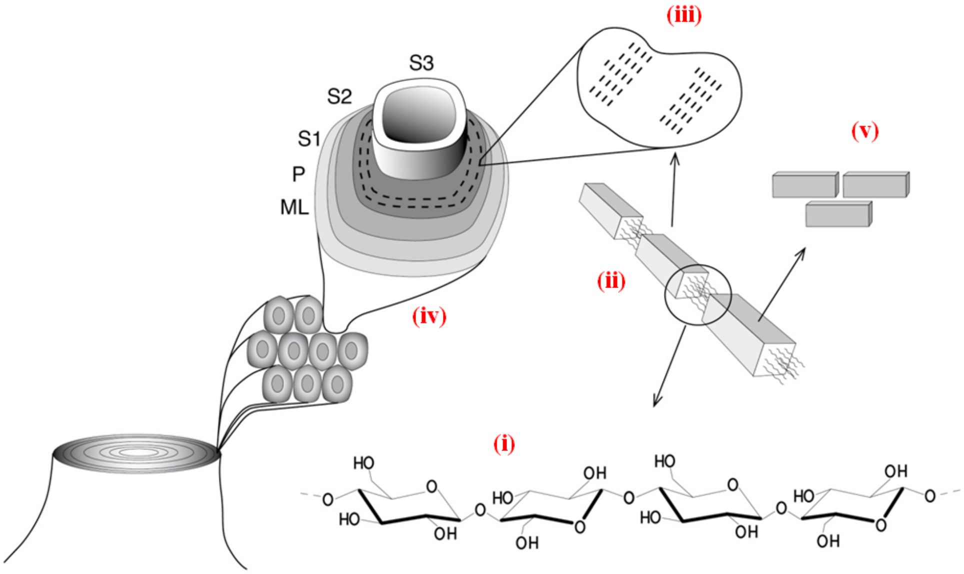

Figure 3.3: (i) Molecular structure of cellulose (ii) Cellulose polymers ordered into micro fibrils stabilised by hydrogen bonds with crystalline and non-crystalline regions (iii) Several micro fibrils assembled into macro fibrils (iv) macro fibrils are orientated in different directions to form fibrils in the cell wall.[59]

Mechanical treatments or chemical modifications of cellulose can be used to produce nanometre-scale cellulose such as cellulose nanofibrils (CNFs) or cellulose nanocrystals (CNCs). In this study, acid hydrolysis was used to break down the non-crystalline regions of the cellulose fibre, leaving behind crystalline regions in the nanometre size range in all dimensions, i.e nanocrystalline cellulose (NCC).[59]

As mentioned, NCC was used to synthesise N CDs and NS CDs by a novel hybrid synthesis technique. The literature contains two notable examples of similar synthetic approaches using cellulose as the organic precursor for the ‘hybrid’ synthesis of CDs, although it is not described as such. Wang et al (2015) synthesised water-soluble CDs by the ionothermal treatment of cellulose powder under catalysis of SO_3H-IL.[60] This involved the acid hydrolysis of the cellulose powder into sugars followed by the polymerisation, atomisation and growth of CDs from resulting carbogenic nuclei. Li et al (2017) used NCC obtained from the sulfuric acid hydrolysis of softwood pulp, followed by hydrothermal carbonisation to produced NCC/CDs hydrogels.[61] Table 3.2 provides an overview of different CD synthetic techniques which involve cellulose and its precursors.

Table 3.2: Summary of different CD synthetic techniques involving cellulose and its precursors.

Type of CD	**Carbon Source**	**Doping /Surface passivating agent (if any)**	**Synthesis Method**	**Size (nm)**	**Quantum Yield (%)**	**Reference**
N-doped carbon spheres	carboxymethylcellulose	Urea (d)	Hydrothermal carbonisation (bu)	200-800	18%	[62]
CDs	Bleached kraft eucalyptus pulp	PEG1500 N (sp)	Acid reflux with nitric and sulfuric acid (td)	1-3	1.2% (unmodified) (3.2% PEG modified)	[63]
CDs	Microcrystalline cellulose (average particle size 50 ⌠m)	-	Ionothermal treatment (td +bu)	8	4.7%	[60]
CDs	Cellulose powders (average particle size ~ 45 nm)	-	High pressure homogenization of cellulose powders (mechanochemical bu)	10-50 nm	1.3-1.7%	[64]
NCC/CDs hydrogels	Nanocrystalline cellulose obtained from sulfuric acid hydrolysis of Kraft softwood pulp	-	Hydrothermal carbonisation and dialysis to produce NCC/CDs hydrogels (bu)	Diameter = 2-8 nm, length = 40-60 nm	NR	[61]
CDs	〈-cellulose	-	Acid hydrolysis and carbonisation	10-20 nm	40-64%	[65]

(td) denotes top down, (bu) denotes bottom up, (d) denotes doping, (sp) denotes surface passivating and (NR) denotes ‘not recorded’ in the literature.

3.2.5. Synthesis Mechanism

This section outlines the synthesis mechanism used to produce CDs using acid hydrolysis and microwave assisted pyrolysis in the presence of doping and/or surface passivating agents. 1,2-ethylenediamine (EDA) and L-cysteine were used as doping/and or surface passivating agents to produce N-doped and N,S-doped CDs respectively. The synthesis mechanism is summarised as follows:

1. Acid Dehydration
2. Dehydration and carbonisation
3. Surface passivation

Acid Dehydration

Acid dehydration of cellulose powder takes place using concentrated sulfuric acid, which breaks down the non-crystalline regions of the cellulose microfibril to produce NCC.

Carbonisation

Carbonisation is the process whereby NCC is converted to its basic carbon-containing residues through microwave-assisted pyrolysis.[1] Microwave-assisted pyrolysis or carbonisation involves heating organic precursors above their melting point which leads to condensation, nucleation and growth of CDs under high temperature and pressure.[14,66] Small molecules or polymers which possess –C=O, O-H, -NH_2 and –COOH groups undergo dehydration at high temperatures and carbonisation to form CDs. [10]

Surface Passivation

Surface passivation involves the addition of dopants which introduce a surface layer - or shell - on the surface of the otherwise non-fluorescent carbon nanoparticles to enhance fluorescence, the effect and mechanism of which are described in more detail in the ‘surface passivation and doping’ section of this chapter.

Carbonisation and surface passivation occur simultaneously during microwave-assisted pyrolysis. To this effect, there are several considerations to be made, which include:

- High temperature is required for carbonisation of the precursor but temperatures which are too high can lead to the destruction of the capping reagent or dopants therefore resulting in poor surface passivation[7]
- During this synthesis, carbonisation and surface passivation occur simultaneously. Due to the intricate balance of these two processes, the effect of temperature, solvent, solvent convection and mixing is very important[67]
- The role of compounds acting as the carbon source relative to the role of compounds acting as the nitrogen source (or other dopant) is not well understood. However it is observed that for bottom up synthesised CDs the choice of dopant has a more pronounced effect on the properties of the as-synthesised CDs than the carbon source[67]
- Reaction temperature (microwave power), time, position and location of the vial in the microwave are all parameters that affect the formation of CDs
- The concentration, and type of dopant used (including the properties of the dopant such as boiling and evaporation point) influence the reaction
- Presence of impurities, amorphous cellulose and undigested polymer influence the reaction and affect the integrity of the organic precursor

- Volume and condition of the reaction vessel, for example whether it is sealed or not, how tight the air seal is, and so on influence the reaction conditions
- Convection currents through the reaction vessel, rate of evaporation of solvents in the mixture, density of reaction precursors and conduction of heat through the reaction vessel are additional considerations

3.2.6. Photoluminescence Behaviour

3.2.6.3. Photoluminescence Mechanism

In contrast to QDs, the exact mechanism of PL in CDs is not yet completely understood. Understanding the PL mechanism is important to underpin effective synthetic strategies and explore potential applications for the synthesised CDs.[10] The synthetic process to make CDs is very difficult to control and influenced by many parameters, resulting in inconsistencies amongst even identically-prepared CD samples which makes it very difficult to determine the PL mechanism experimentally.[3] Three plausible PL mechanisms for CDs which exist in the literature are summarised as follows:

- Quantum confinement effect (or conjugated π domains) determined by the carbon core, which has been observed to be size-dependent. Different sized CDs have different band gaps and hence exhibit diverse PL behaviour. This is also suggested to be responsible for excitation-dependent PL behaviour observed in CDs.
- Surface states are determined by the hybridisation of the carbon backbone and the connected chemical groups. Different functional groups possess different energy levels, which can result in a series of emissive traps. This influences radiative recombinations of electrons and holes confined to the surface. Oxygen-based groups on the carbon core are often the primary surface states of CDs. Surface states are considered the key factor in

tuning the luminescence of CDs. In addition to the choice of organic precursor and functional groups, different reaction conditions and reduction/oxidation of the CDs can also be used to tailor the PL behaviour.

- Molecule state – The molecule state is determined by organic fluorophore molecules connected on the interior or surface of the carbon backbone, which exhibit discrete PL behaviour. This is a PL centre commonly found in CDs prepared by bottom up synthesis using small molecules as the precursor, whereby small fluorophores are formed at low temperature carbonisation and eventually dehydrated and consumed to form the carbon core at higher temperatures.

It is widely suggested that CDs possess multiple fluorophores associated with the carbon core and oxygenated defect-related emissive traps on the surface. Based on this assumption, the overall optical properties of CDs are therefore determined by quantum confinement effects and competition between non-radiative trap sites and emissive states on the surface and can be tuned by controlling the size of sp^2 conjugated domains or the functional groups on the surface of CDs.[3,10,68,69]. A dual fluorescence band sometimes observed in CDs can be attributed to the intrinsic band gap associated with sp^2 conjugation in the core and extrinsic band associated with surface state emissions, which can be excited directly or through energy transfer from the intrinsic band. The presence of a single fluorescence band gap does not negate the possibility of these two bands existing but can mean the prevalence of one over another, which elucidates the composition, and thereby PL origin or mechanism of the CDs. (Figure 3.4)[10]

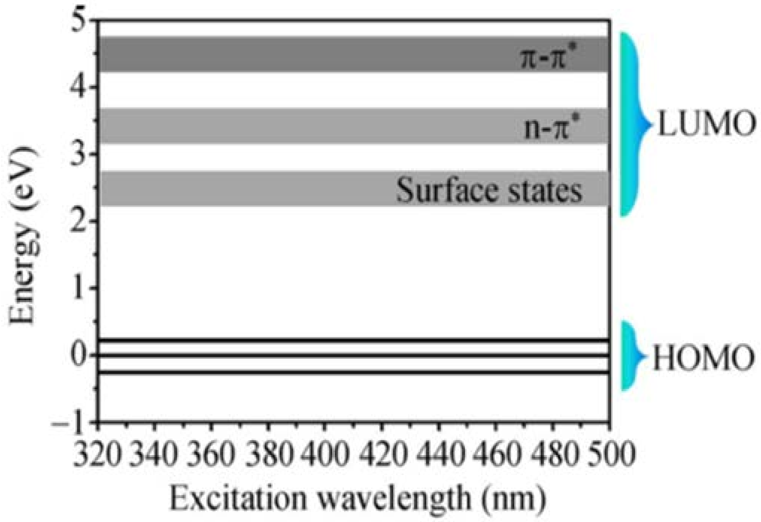

Figure 3.4:The dual fluorescence band in CDs associated with the core and surface state emissions [10]

3.2.6.4. Surface passivation and doping

Surface engineering of synthesised CDs can be used to enhance photoluminescence (PL), improve the quantum yield (QY) and tailor the CDs to specific targets and environments. The surface states greatly influence the PL behaviour and QY of CDs. Surface engineering by addition of functional groups, polymer passivation or changing the redox state of functional groups on the surface of CDs are examples of surface engineering which can take place during or after the synthesis of CDs.[3] Functionalisation of CDs by modifying the surface enables the particles to be tailored for specific functions and environments such as bio-sensing and targeted delivery. [1]

Heteroatom doping of CDs during or post-synthesis can be used to enhance the PL behaviour of CDs as well as their physicochemical properties.[3,70] In single component synthesis, heteroatom doping can be achieved by selecting a precursor in which the desired heteroatoms, such as N and S are present. These are then incorporated into the core of the synthesised CDs. Heteroatom doping in multicomponent synthesis of CDs can be achieved using additional precursors which contain the desired heteroatoms. As the organic precursor breaks down, the heteroatoms are incorporated into the core and at the surface of the CDs. The localisation of heteroatoms at the CD surface imparts surface functionalities such as amide/amine and carboxylic acid group functionalities which can be tailored to enhance solubility of CDs as well as introduce functions for catalysis and binding.[71] These CDs can then be referred to as 'doped' and/or 'surface passivated' CDs.[6] The most common heteroatoms used for doping are nitrogen and sulfur to produce N-doped CDs, S-doped CDs and N and S co-doped CDs. Other doping agents have been used to synthesise CDs for tailored applications such as Boron, used to produce CDs for detecting glucose, Magnesium doped CDs for cell imaging, and Manganate doped CDs as chemical sensors.[72]

As described previously, and in accordance with the established theories for PL of CDs, surface passivation is crucial to the PL behaviour and fluorescence performance of CDs.[2] Fluorescence emissions in CDs are associated with radiative recombination of surface trapped electrons and holes. Surface passivating agents stabilise the trapping sites on the carbon particle surface, and the large surface area to particle volume surface aids in enhancing the fluorescence emission.

There are three possible effects of doping which lead to enhanced PL behaviour and quantum yield (QY):

- Effective formation of emissive states – Doping results in increased diversity of surface sites, increasing the efficiency of trapping electrons and holes for recombination at the particle surface.
- Introduction of electron donating heteroatoms such as N or S as doping agents to enhance the PL behaviour.[5]
- Reduced quenching – suppression of processes competing with fluorescence emissions.[2]

The dominant mechanism can be elucidated by comparing the fluorescence decay and changes to QY with changes to the doping (type, concentration, etc.).[2] The process of CD formation and surface passivation occurs simultaneously and therefore surface passivating agents serve the dual role of passivating agent and dopant. For example, N-containing carbon sources such as 1,2-ethylenediamine (EDA) used as a passivating agent, causes simultaneous N-doping and formation of surface amide groups, which enhance the PL performance and increase the QY. There are multiple factors which can affect the fluorescence emission related to the surface doping including: amount of surface doping and degree of formation of a complete shell around the carbogenic core, degree of hybridisation with the carbon core and uniformity of surface doping. [7,57]

3.2.6.5. Quantum Yield

Fluorescence quantum yield (QY) describes the number of photons emitted relative to the number of photons absorbed by a fluorescent particle or material and is an important indicator the material's fluorescence performance. [10] The QY is described by equation 3.1.

$$\text{QY} = \frac{\#\, photons\ emitted}{\#\, photons\ absorbed} = \frac{k_f}{\sum\ k_i} \qquad (3.1)$$

where

- k_f is the fluorescence rate constant
- k_i donates the rate constants of all the decay processes from the first excited state of the fluorophore

The QY depends on both the synthetic route and surface state of the CD and is determined relative to a reference compound of known QY. QY is calculated using equation 3.2.

$$\mathrm{QY} = QY_{ref}\frac{\eta^2}{\eta_{ref}^2}\frac{I}{A}\frac{A_{ref}}{I_{ref}} \tag{3.2}$$

where

- I is the integrated fluorescence intensity
- A is the absorbance at the excitation wavelength
- η is the refractive index

3.2.6.6. Photobleaching and photostability

High photostability and predictable fluorescence decay of CDs is required for their use in applications of photo-sensing, bio-imaging, catalysis and energy applications.[55] Studies on the photostability of CDs remain limited and relative to the structure of the CDs investigated, which depends on the synthetic route employed. Analysis of the fluorescence decay alongside the quantum yield can be used to discern the origin of PL and identify the location of luminescent centres as being either surface-state or molecule-state or both. The surface state is formed by the hybridisation of chemical groups on the surface and the carbon core. Surface state CDs show weak PL behaviour with high photostability. Usually top-down synthesised CDs exhibit this behaviour. The molecule-state is formed by the consumption of small fluorophores formed in the carbonisation process as the temperature is increased. Molecule-state CDs show strong PL, high QY and low photostability. This behaviour is usually demonstrated by bottom-up synthesised CDs.[10,23,73,74]

Investigations into the photobleaching of CDs under UV excitation can be used to discern the mechanism of fluorescence decay and which PL centre it can be attributed to. This knowledge allows for strategies to be developed to enhance the photostability of the CDs under different conditions. Wang et al (2016)[55] identified the source of fluorescence decay in freshly prepared bottom-up synthesised CDs - or those stored continuously in the dark - as a photochemical process that occurs on the surface states of the CDs which is accelerated by the presence of oxygen-containing surface groups. Fluorescence decay was investigated in this work to model the photostability of CDs and contribute to the theory of PL mechanism.

3.3. Materials and Methods

3.3.1. Materials

Fibrous cellulose powder (CF11) purchased from Whatman was used as the carbohydrate source for CD synthesis. 48 wt.% of sulfuric acid diluted from 95% v/v sulfuric acid purchased from VWR chemicals was used for the acid hydrolysis. (99.5% purity) 1,2-ethylenediamine (EDA) solution purchased from Fluke Analytical and L-cysteine (97% purity) crystals obtained from Aldrich were used as surface passivating agents. MilliQ de-ionised water was used throughout.

3.3.2. Synthesis of Carbon Dots

Acid dehydration of cellulose powder was carried out using a variation of a a previously reported method by Takumi et al (2017)[75]. 17.2 mL of 48 wt.% sulphuric acid was added to 2g of cellulose powder and heated over an oil bath at 45°C for 3.5 hours and stirred with a magnetic stirrer. The mixture turned into a pale-yellow paste and was washed out with 175 mL of cold de-ionised water and transferred to a conical flask. The white dispersion was left to settle overnight, and the precipitant was collected. The precipitant (a white dispersion) was centrifuged several times at 1,500 g and equilibrated with de-ionised water until a clear supernatant of nanocrystalline cellulose (NCC) was obtained. The supernatant absorption was measured using UV-Vis spectroscopy, whereby a peak at 250 nm indicated the presence of NCC in solution.

The NCC was transferred to a 15 mL microwave digestion vessel. Ethylenediamine (EDA) and 0.025g/mL of L-cysteine in deionised water were used for N and S doping respectively. L-cysteine also served as a source for Nitrogen.[9] The microwave digestion vessel was placed in the centre of a Panasonic NNCF873S domestic microwave and heated for 8 minutes at medium power (600W). The formation of carbon dots was indicated by the formation of an orange/brown residue. The residue was dispersed in deionised water which resulted in the formation of a yellowish/brown solution. This was transferred to an Eppendorf tube and centrifuged for 10 minutes at 10,000 rpm to separate any large, non-fluorescent aggregates. The supernatant contained water-soluble fluorescent CDs and was stored in the fridge at 4°C in the dark to prevent photobleaching.

3.3.3. Characterisation of Carbon Dots

The chemical composition and surface groups of cellulose-based CDs were characterised by a range of physic-chemical characterisation techniques: Fourier-transform infrared spectroscopy (FTIR) (Perkin Elmer Spectrum One: FTIR spectrometer) and X-ray photoelectron spectroscopy (XPS) (Cardiff Catalysis Institute XPS instrument). UV-Vis spectroscopy (Perkin Elmer UV/Vis/NIR Spectrometer Lambda 750) and Fluorescence spectroscopy (Fluoromax 4) were carried out to investigate the PL properties and QY. Quinine sulfate was used as a reference to investigate the QY of the CDs. Zeta potential was measured using a Zetasizer NanoZS (Malvern). Powder x-ray diffraction (Bruker D8 Advanced with Cu Kα radiation, wavelength = 1.5406 Angstrom) and High-Resolution transmission electron microscopy (HRTEM, TEM2100) were used to analyse the crystalline structure of the CDs. This was carried out with technical assistance by JC. Eloi at the Electron Microscopy Unit, School of Chemistry, University of Bristol.

3.4. Results and Discussion

3.4.1. Synthesis Optimisation

The optimisation of the synthesis of CDs was carried out by a series of experiments to investigate the effect of different concentrations of surface passivating agents (EDA and L-cysteine) and microwave digestion times. As mentioned in the experimental section, UV-Vis spectroscopy was used to detect the presence of NCC in solution. Figure 3.5 shows a TEM micrograph of NCC used to synthesise CDs stained with uranyl acetate. The concentration of NCC used was within the range of (2.4-3.14 mg/mL). The NCC dispersion in water was stable for up to six weeks at room temperature, after which precipitation of cloudy aggregates appeared. Doping agents EDA and L-cysteine were added to the NCC solution and microwave digestion vessel was sealed and placed in the microwave. The synthesis resulted in the formation of a yellow-orange solution. To confirm the formation of CDs, the solution was illuminated under UV light at λ=365 nm, showing blue fluorescence which indicated the successful formation of CDs.

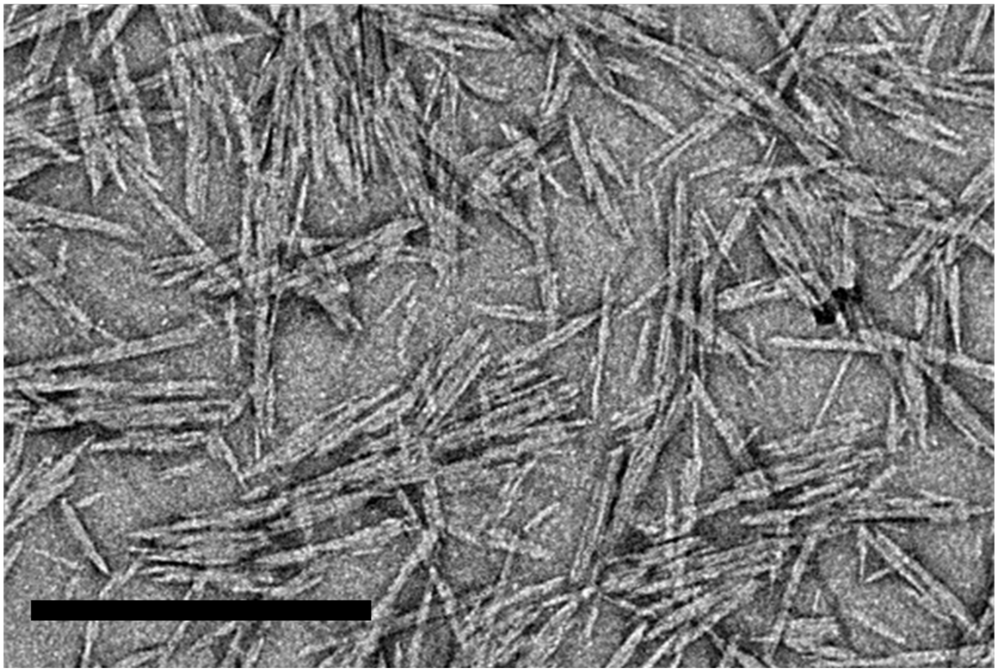

Figure 3.5: TEM image of uranyl acetate-stained NCC solution. The scale bar is = 500 nm. This image was obtained by Dr A.Patil

3.4.1.1. Microwave Digestion Time and Power

As mentioned previously, carbonisation, growth and surface passivation occur simultaneously during the microwave-assisted pyrolysis of the NCC to form CDs. This process, particularly the surface passivation, is highly sensitive to temperature, resulting in changes to the optical properties, PL behaviour and QY of the synthesised CDs.[76] The carbonisation temperature must be high enough to ensure the complete breakdown of NCC into its carbon-containing residues but not too high so as to destroy the heteroatom doping agents and affect the surface passivation.[1] CDs prepared at the same power and different reaction times resulted in different coloured CD solutions as shown in Figure 3.6.

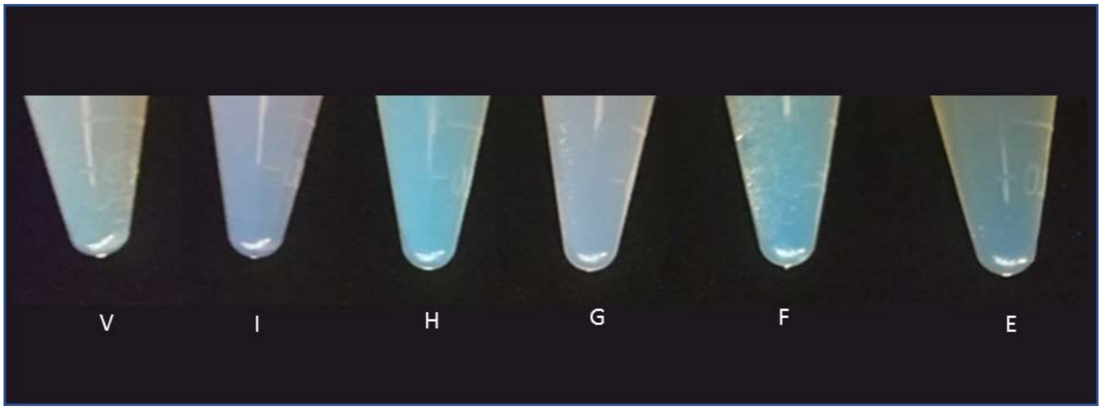

Figure 3.6: N CDs prepared at different reaction times in a hydrothermal reaction vessel at medium power. E: 5.5 mins, F: 6 mins, G: 8 mins, H: 9 mins, I: 10 mins, V: 11 mins.

Carbonaceous aggregation[9] post pyrolysis was minimised by the use of the sealed hydrothermal reaction vessel and centrifugation of the synthesised CD solution. The microwave power and time required was investigated by a series of experiments to determine the minimum microwave time and power, to achieve a facile, cheap and energetically efficient synthetic route. Low power (300 W) microwave setting did not form CDs after over 18 minutes of reaction. Reactions at high power (1000 W) resulted in the formation of a dark brown/black residue which did not fluoresce after 90 seconds of reaction. In contrast, reactions performed at medium power (600 W) for 8 minutes resulted in the formation of a dispersion of highly fluorescent CDs which was stable for up to 8 months.

3.4.1.2. Surface Passivating Agents

Surface passivation and/or heteroatom doping can be used to tailor the PL properties of CDs and enhance their QY. EDA and 0.025g/mL of L-cysteine were used as N and S dopants respectively. L-cysteine and NCC reacted together in the absence of EDA did not result in the formation of CDs as described previously. The fluorescence spectra and QY for CD samples prepared with varying dopant concentration (v/v%) diluted with de-ionised water were measured to investigate the relationship between dopant concentration and PL behaviour (Figure 3.7) and QY (Figure 3.8).

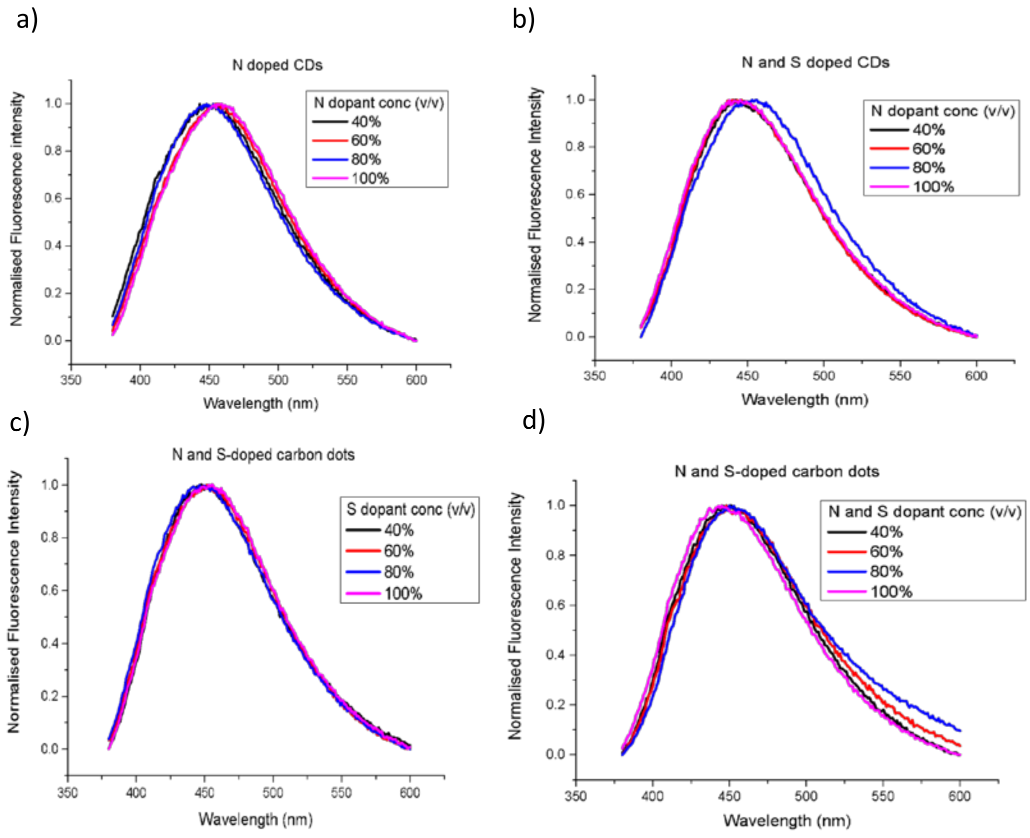

Figure 3.7: a) Normalised Fluorescence intensity of a) N-doped C dots synthesised with varying concentration (v/v%) of N dopant b) N,S-doped C dots synthesised with varying concentration (v/v%) of N dopant c) N,S-doped C dots synthesised with varying concentration (v/v%) of S dopant d) N,S-doped C dots synthesised with varying concentration (v/v%) of N and S dopant

The normalised fluorescence intensity t varying dopant concentrations for N-doped CDs and N,S-doped CDs is shown in Figure 3.7. Varying the dopant concentration of S dopant does not seem to have an effect on the position of the emission peak (Figure 3.7c), however there is a small shift in the emission peak to a longer wavelength by approximately 10-15 nm as the N dopant concentration is increased in N-doped CDs (Figure 3.7a) and a more pronounced shift to a shorter wavelength of approximately 20 nm in N,S-doped CDs. This may indicate that the S doping contributes to the enhancement of the N doping, producing higher sensitivity of fluorescence to the concentration of N dopant. This may elude to the mechanism of co-doping in which the S doping enhances the effect of N doping in a synergistic role.[77] However, in order to determine this, N-doped CDs and N,S-doped CDs prepared with the same N-dopant content would need to be compared as a control. There is no pronounced effect on varying both N and S dopant concentrations on the fluorescence intensity.

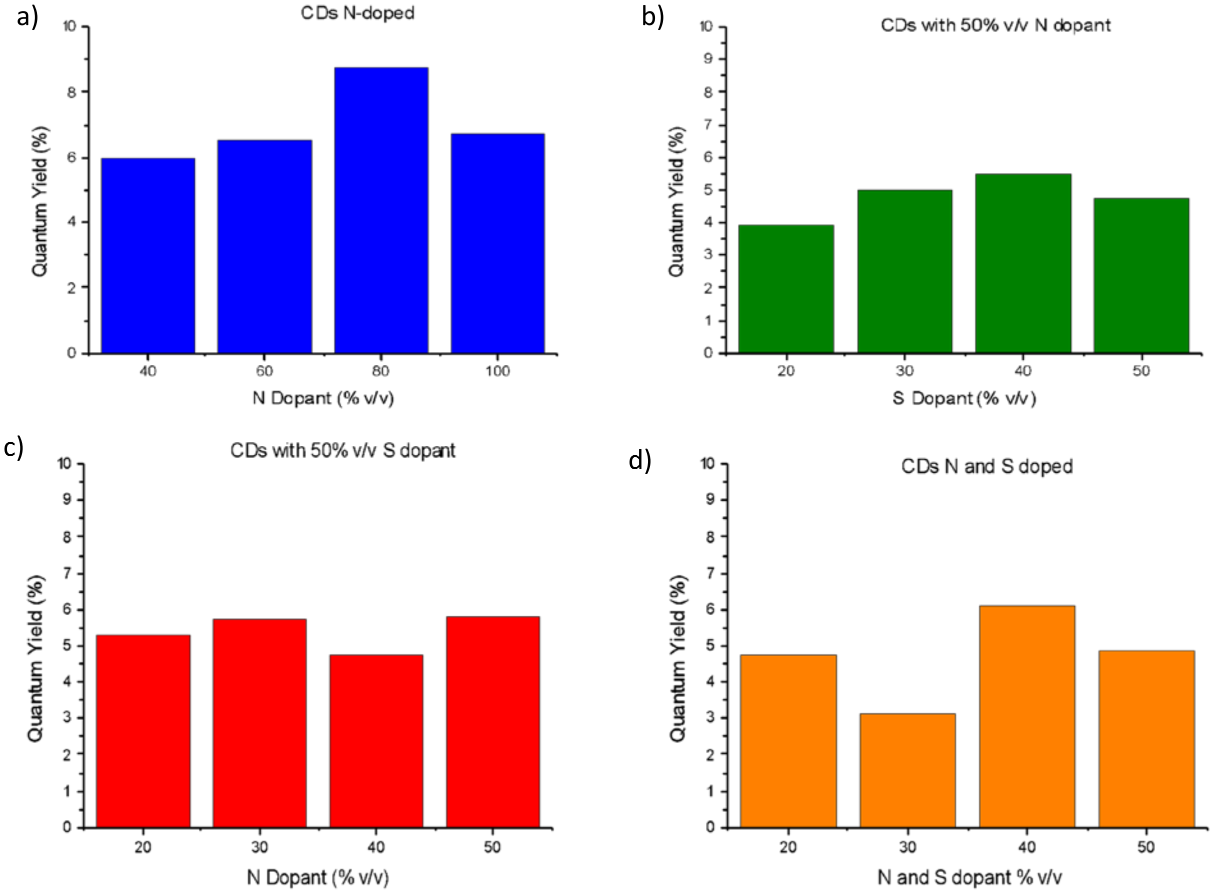

Figure 3.8: a)QY of N-doped CD samples with varying concentration (v/v %) of N dopant b) QY of N,S-doped CD samples with varying concentration (v/v %) of S dopant c)) QY of N,S-doped CD samples with varying concentration (v/v %) of N dopant d) QY of N,S-doped CD samples with varying concentration (v/v %) of N and S dopant

The QY for varying concentrations (v/v%) of N and S dopants is shown in Figure 3.8. There seems to be no consistent correlation between QY and dopant concentration, however the QY of N-doped CDs remains persistently higher than N,S-doped CDs. The variation of QY with varying N dopant concentration (Figure 3.8a) is more pronounced than with N,S-doped CDs whilst the S dopant concentration (v/v%) remains constant (Figure 3.8c), however both graphs lack a discernible trend. This would indicate that N doping has the greater contribution to quantum yield. However a comparison of N,S-doped CDs and N-doped CDs with equal composition of N dopant is required to confirm this and determine the effect of S and co-doping on the PL mechanism of the N,S-doped

CDs. It is however clear due to the lack of consistent trend amongst the variation of dopant concentration and associated QY that the dominant mechanism for enhancement of PL behaviour by surface passivation involves the formation of photoluminescent centres and emissive traps on the surface of the CDs rather than reduced quenching which would have a more pronounced concentration-dependent effect. [2,5] The precise concentrations and volumes used to synthesise CDs for the work carried out in this chapter are recorded in Table 3.3.

Table 3.3:

Type of CD	**Volume of NCC added/mL**	**Volume of EDA (100% v/v) added/µL**	**Volume of L-cysteine (0.025g/mL) added/µL**
N-doped	1	75	-
N,S-doped	1	37.5	37.5

3.4.2. Characterisation

3.4.2.3. Powder X-Ray Diffraction

XRD was used to monitor the CD synthesis and analyse the formation of CDs by measuring the XRD pattern of individual reagents and combinations of reagents used to synthesise the CDs. XRD pattern of the silicon holder shows a broad peak between 2θ= 5 – 15 ^{0}, which can be deducted from the XRD pattern of other samples (Appendix). The XRD pattern of the individual reagents was investigated before and after reaction in the microwave vessel at medium power for 8 minutes (Appendix). These were compared to the XRD pattern for N CDs and NS CDs (Figure 3.9 and Figure 3.10).

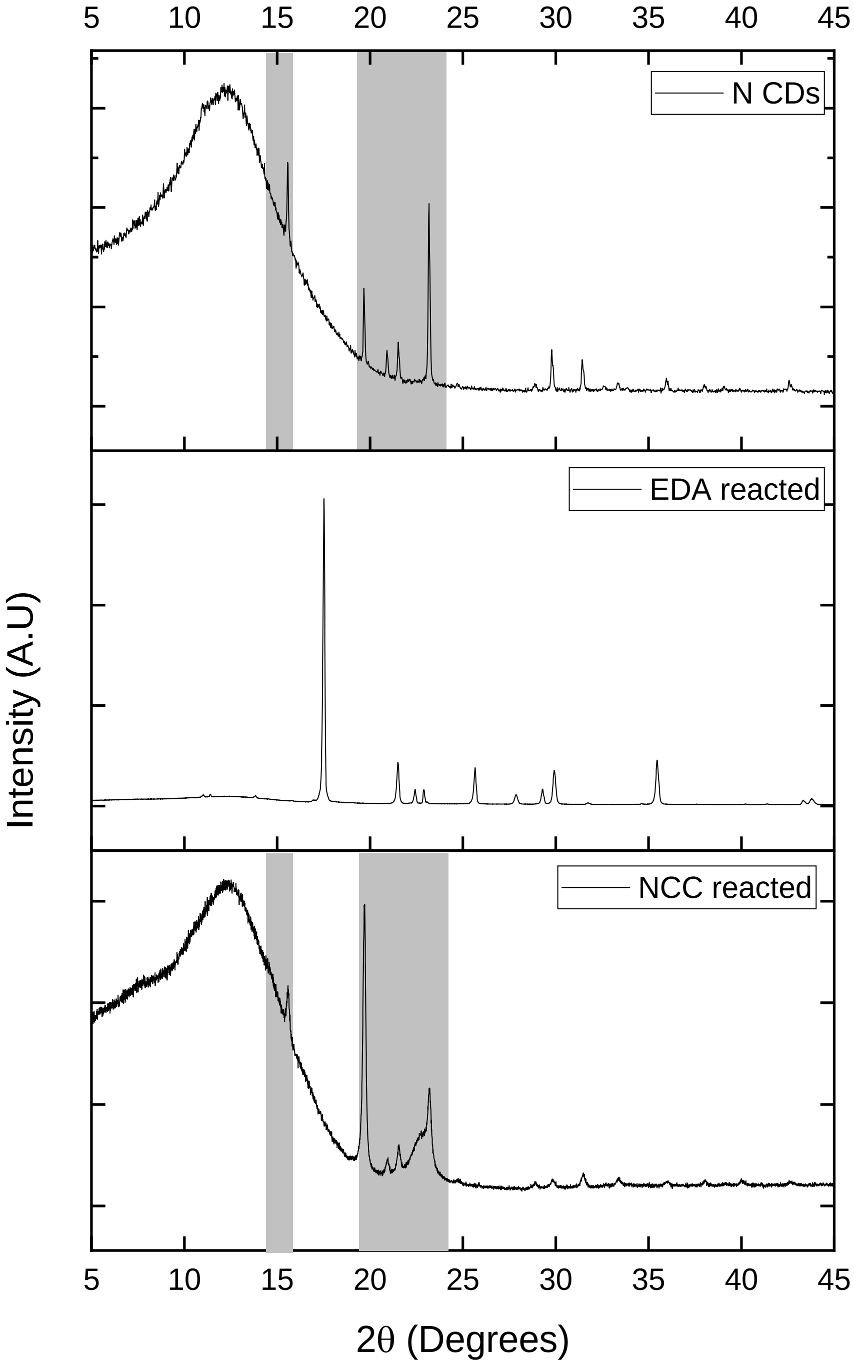

Figure 3.9: XRD pattern for N CDs, reacted NCC and reacted EDA reacted at medium power for 8 minutes in the microwave digestion vessel

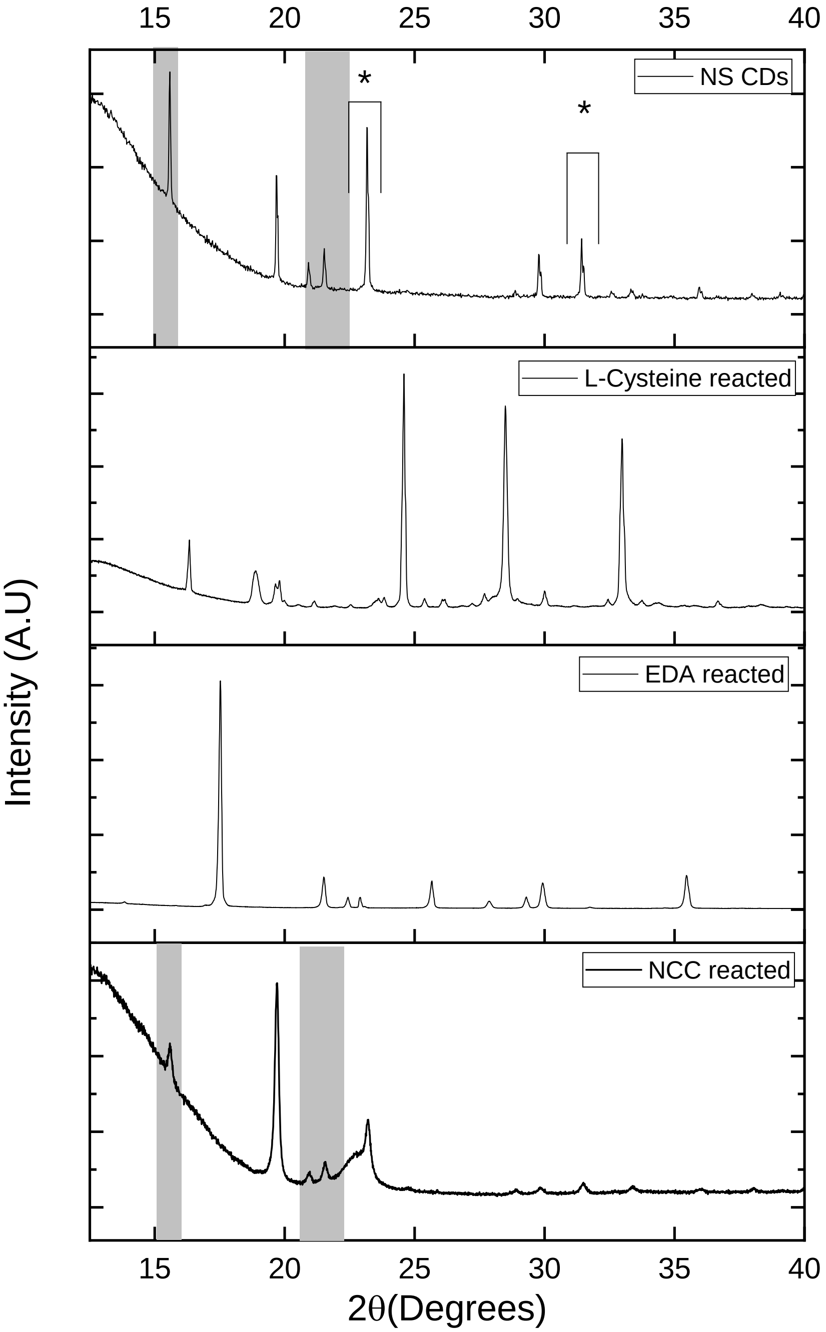

Figure 3.10: XRD pattern of NS CDs and individual reagents L-cysteine, EDA and NCC reacted at medium power for 8 minutes in the microwave digestion vessel

As discussed, NCC behaves as the primary precursor for the formation of N CDs and NS CDs, with EDA and L-cysteine behaving as doping agents and/or surface passivating agents.

The XRD pattern of synthesised N CDs and NS CDs (Figure 3.9 and 3.10) contain some of the crystalline peaks observed in NCC reacted in the microwave in the absence of any other reagents at $2\theta = 15.6°$ and 19.7° (highlighted in grey), which is not the case for EDA or L-cysteine. This would indicate that EDA and L-cysteine are used up in the reaction to form CDs whereas NCC is in surplus in the reaction. According to the literature, CDs are expected to demonstrate a broad peak between 2θ= 20- 30°. [8,14,46,68,70,78–81] It is not clear whether this peak is present in the XRD spectra of N CDs and NS CDs due to the low intensity of this peak compared to that of unreacted NCC and the background noise.[80] A range d-spacings are observed between 2.84 Å – 4.24 Å which is larger than expected. This may be due to nitrogen doping. [3,13,70,72,80–85,17,22,25,37,38,52,67,68]D-spacing larger than 3.3 Å of bulk graphite may be an indication of poor crystallisation. [81] the CDs therefore exhibit both crystalline and amorphous characteristics which are common for multicomponent bottom up synthesised CDs. [6,76,80,86]

The XRD spectra for N CDs and N,S CDs (Figure 13.0 and 14.0) demonstrated sharp crystalline peaks unique to that of any of the synthesis reagents at $2\theta = 20.9°$ and 31.42°, corresponding to d-spacings of 4.24 Å and 2.84 Å respectively, which were not possible to index. A range of graphitic d-spacing were observed between 2.84 Å – 4.24 Å which is larger than expected. This may be due to nitrogen doping.[3,13,70,72,80–85,17,22,25,37,38,52,67,68] D-spacing larger than 3.4 Å of bulk graphite may be an indication of poor crystallisation[37], turbostratic carbon structure[17] or the introduction of functional groups during the synthesis.[51] The CDs therefore exhibit both crystalline and amorphous characteristics which are common for multicomponent bottom-up synthesised CDs.[6]

3.4.2.4. High Resolution Transmission Electron Microscopy (HRTEM)

CD samples were diluted and pipetted onto copper-coated TEM grids and left to dry in air overnight. HRTEM was used to characterise the size, morphology and internal lattice structure of N CDs and N S CDs (Figure 3.11). The CDs appear to be discrete, monodisperse quasi-spherical particles with a narrow size distribution and no visible aggregation. N S CDs appeared to have a broader size distribution (2 – 16 nm) and a larger diameter on average than N CDs (2-10 nm). It is reported that the size of the CDs prepared depends on the carbon source (in this case unchanged) and the surface passivating agents.[3] The observed increase in size of the N S CDs is therefore in accordance with the presence of increased surface passivating agents, and the larger L-cysteine molecule. These hybridise with the carbon core during synthesis, followed by the nucleation and growth of the CD particles. Thus, larger CDs are produced as carbonisation and surface passivation occur simultaneously during microwave-assisted pyrolysis.

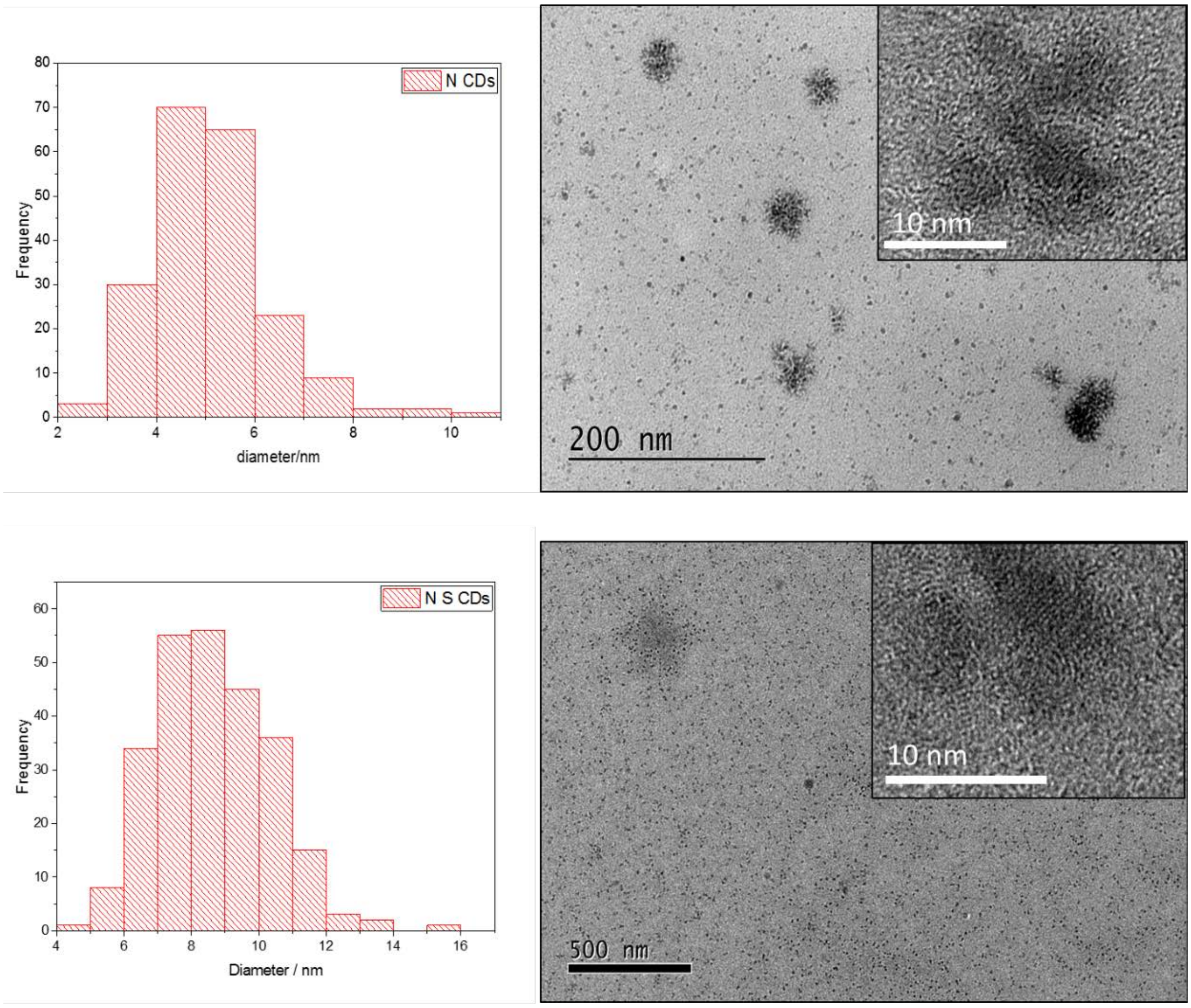

Figure 3.11: HRTEM micrographs of N CDs (insert: magnified HRTEM image of N CDs showing lattice fringes) and size distribution of N CDs (top) NS CDs (insert: magnified HRTEM image of NS CDs showing lattice fringes) and size distribution of NS CDs (bottom)

The XRD data agrees with the d-spacing measured via HRTEM. Interlayer spacing of 0.32 nm correspond to (002) lattice fringe [46,82] and 0.24-0.28 nm corresponding to (110) fringe of in-plane lattice spacing of graphene. Interlayer spacing depends on the degree of oxidation and the presence of carboxylic acid, hydroxyl and ether groups which can increase the interlayer spacing. [9] In which case, d-spacing observed larger than that of graphite (0.34 nm) may be due to these introduction of functional groups during the synthesis. [9,51]

3.4.2.5. FTIR

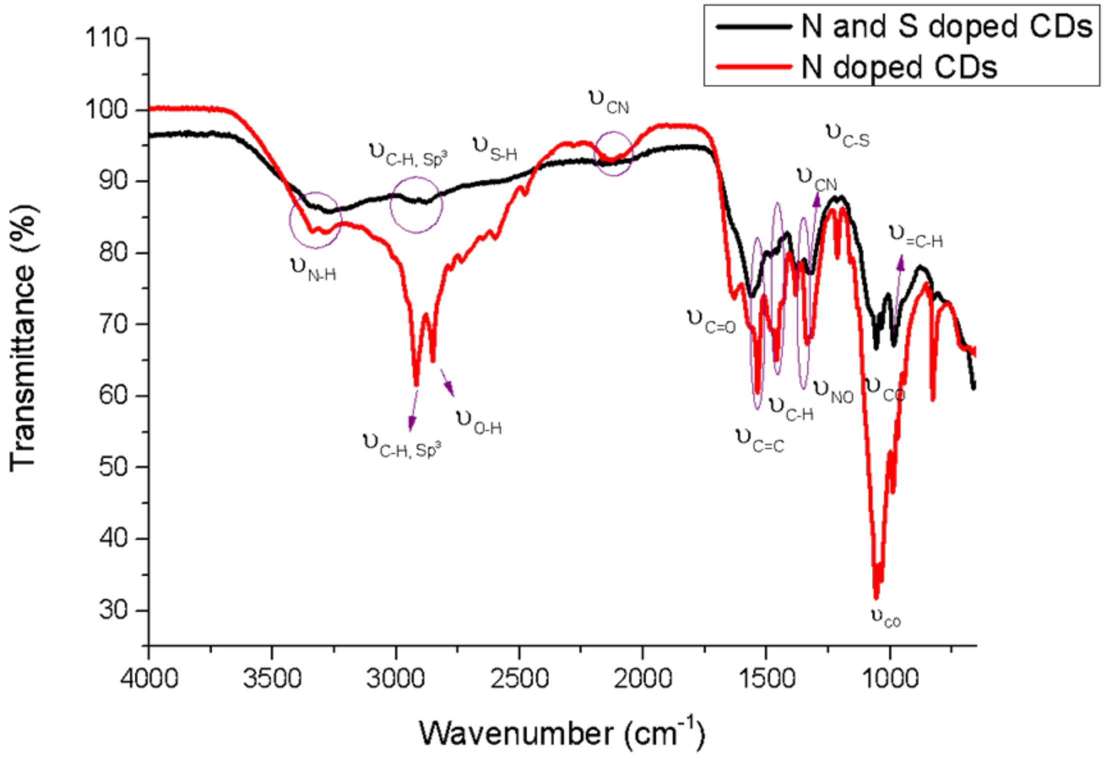

Figure 3.12: FTIR spectrum of N-CDs (red) and N,S CDs (black).

The FTIR spectra (Figure 3.12) confirmed the presence of oxygen-containing groups (OH, C=O, COO^{-},N-O, and C-O). FTIR spectra indicates that there is a large degree of similarity between the molecular structure of N CDs and N S CDs, with the exception of υ (S-H) s at ~2569 cm^{-1} and υ (C-S) at ~1211 cm^{-1} only observed in the FTIR spectra of N S CDs. This would imply that the process of CD formation during synthesis of the CDs by microwave-assisted pyrolysis follows a similar mechanism for both CD samples.

The FTIR spectrum for N CDs possesses υ(C=O) and υ(C-N) at ~1670 cm^{-1} and 1311 cm^{-1} respectively which indicates the formation of an amide bond (-CONR) at the carbon dot surface. υ(C=O) is observed at a lower wavenumber than expected, possibly due to conjugation. This confirms that EDA behaves as a passivating agent. υ(CN) nitrile stretch at 2137 cm^{-1} observed in N CDs and N S CDs may additionally indicate the presence of nitrogen atoms in the core as a polyaromatic structure.[34] As the formation of CDs and surface passivation occur simultaneously during microwave assisted-pyrolysis, the formation of amide groups at the surface and N-doping of the carbon core can coincide. The FTIR spectra for both CDs also indicated a range of oxygen containing functional groups, namely carboxylic acids, ethers and alcohols (Table 3.4). These functionalities facilitate the dispersion of CDs in aqueous medium and without further need for post-synthetic surface modification.[6]

Table 3.4: Summary of FTIR assignments from Figure 3.12.

Wavenumber/ cm^{-1}	**FTIR assignment**
3400-3200	N-H
3600-3200	O-H
3000-2876	C-H, Sp^3
2848	OH
2569	S-H
2137	CN nitrile
1649	C=O
1560	C=C aromatic
1490	COO^-
1459	C-H, sp^2
1383	N-O
1311	C-N amine
1211	C-S
1056	C-O ether
981	=C-H

3.4.2.6. X-ray Photoelectron Spectroscopy (XPS)

X-ray photoelectron spectroscopy was carried out to investigate the elemental composition, and surface chemistry (chemical and electronic state) of N CDs and NS CDs.

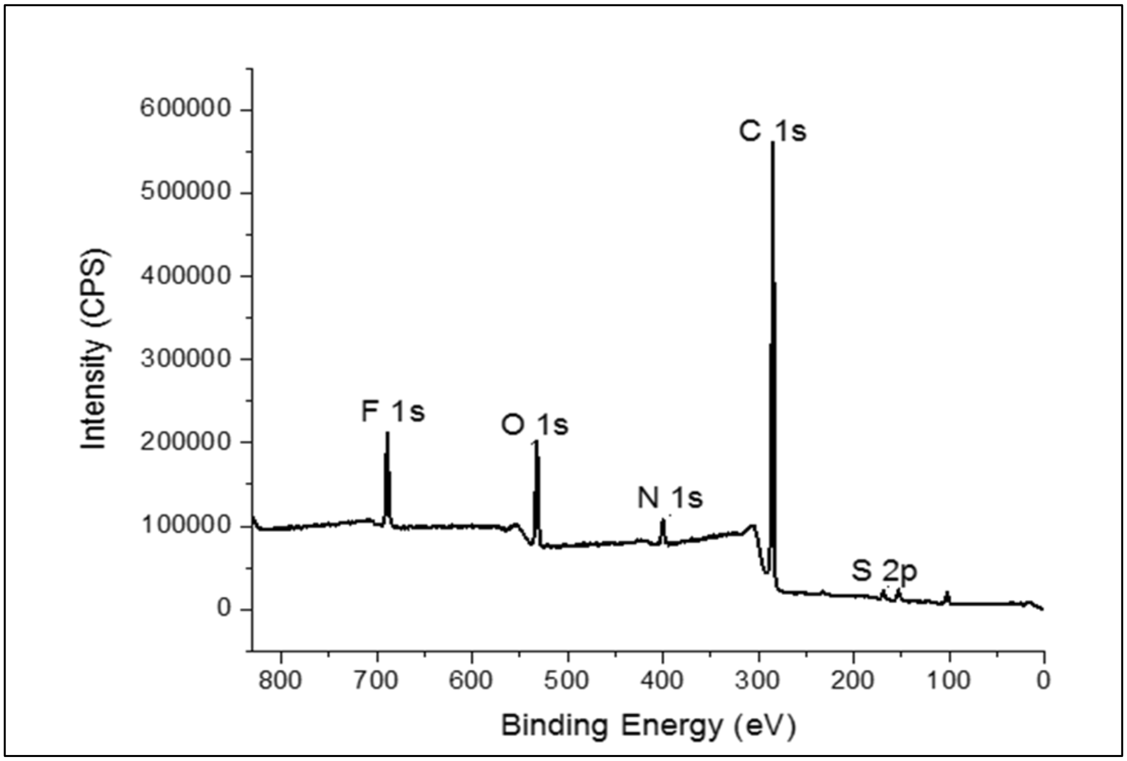

Figure 3.13: XPS spectrum of N CDs elemental scan

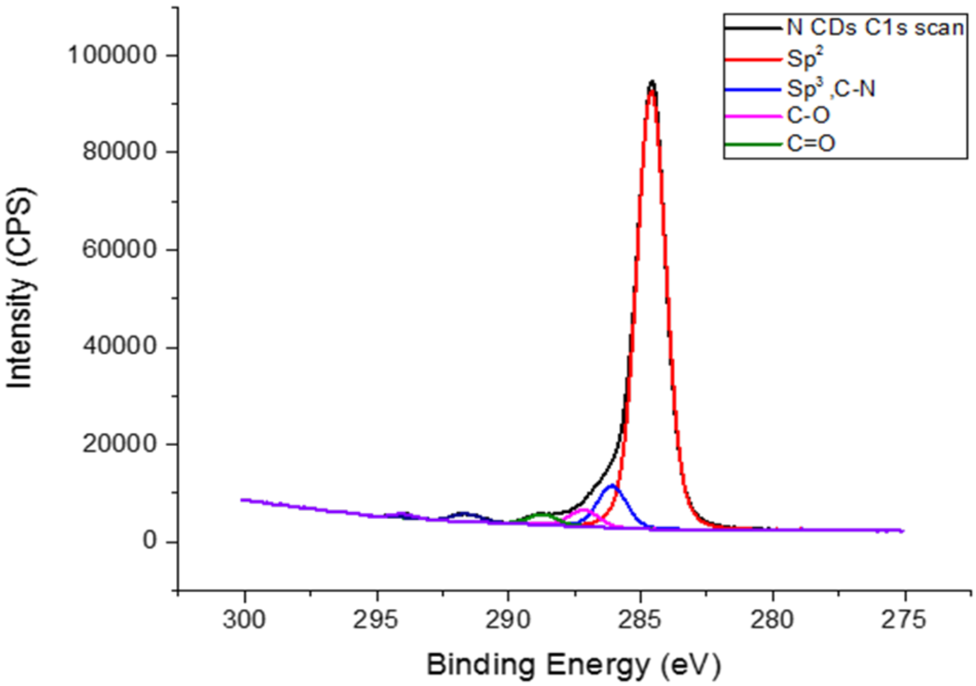

Figure 3.14: XPS spectrum of N CDs C1s scan

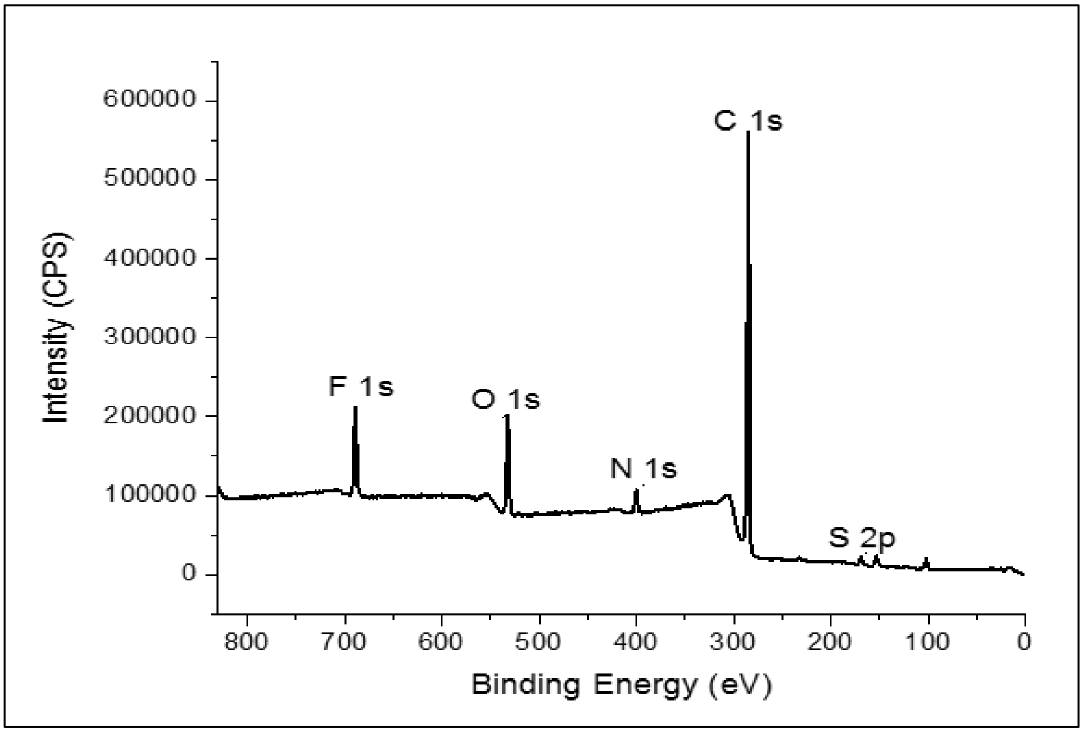

Figure 3.15: XPS spectrum of N S CDs elemental scan

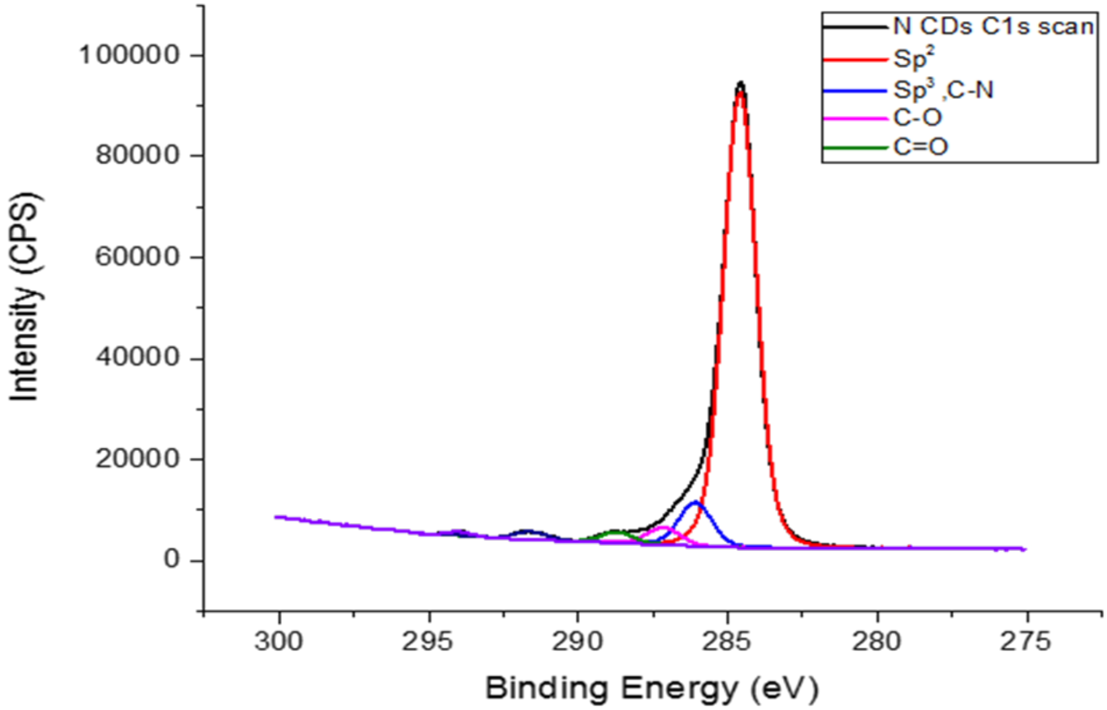

Figure 3.16: XPS spectrum of N S CDs C1s scan

Elemental analysis by X-ray photoelectron spectroscopy (XPS) was carried out on N-CDs and N,S CDs. The chemical composition of N-CDs was 78.85% C, 8.45 % O, 3.3 % N and <2% S and the chemical composition of N,S-CDs was 58.15% C, 17.69% N, 17.34 % O and 6.13% S. The difference observed between N CDs and NS CDs indicates the role of heteroatom doping plays on the composition and internal structure of CDs.[14,87] The high content of oxygen and nitrogen suggests the presence of amide, hydroxyl, carboxyl and carbonyl functional groups on the surface of carbon dots.[6,8]

The XPS spectra of N-CDs (Figure 3.13 and 3.14) exhibits five peaks at 169.08 eV, 258.08 eV, 400 eV, 533.08 eV and 689 eV which are attributed to S 2p, C 1s, N 1s, O 1s and F 1s respectively.

The F 1s peak is a potential contaminant from the water used to prepare the CDs sample or adsorbed onto the surface of CDs[88]. The corresponding high resolution XPS spectra of C1s shows four peaks centred at 284.5 eV, 285.88 eV, 286.98 eV, and 288.58 eV corresponding to graphitic Sp^2 carbons, Sp^3, C-OH/C-O/C-O-C and C=O respectively,[43,76] which indicates that the CD surface was functionalised with hydrophilic hydroxyl and carboxylate groups.[89] The XPS spectra of N,S-CDs (Figure 3.15 and 3.16) exhibits five peaks at 169.08 eV, 227 eV, 285.08 eV and 399.08 eV and 530.08 eV which are attributed to S 2p, S 2s, C 1s, N 1s, and O 1s respectively. The corresponding high resolution XPS spectra of C1s shows three peaks centred at 284.5 eV, 285.78 eV, 287.58 eV corresponding to graphitic Sp^2 carbons, Sp^3, and C-N/C=O respectively. The ratio of Sp^2:Sp^3 was 6.44:1 and 1.63:1 for N-CDs and N S CDs respectively. This would suggest that the dopants used in the synthesis procedure affect the molecular state of the synthesised CDs.[87]

3.4.2.7. Zeta Potential

N CDs and N,S CDs were found to be negatively charged and displayed a surface zeta potential of (-14.4 mV ±5.21) and (-1.64 mV±0.42) respectively at pH 12.6.The negative surface charge most likely results from the presence of high density of functional groups at the surface such as carboxylic acid and alcohol groups.[90] These results are in accordance with results obtained in the literature where carbohydrates were used as the organic precursor for the synthesis of CDs, producing CDs with a high negative charge. The charge of the CDs reflects their hydrophilicity and high solubility in aqueous solutions.[55,89,91,92] The relatively high standard deviation reflects the lack of uniformity between different CD samples, which is to be expected with multicomponent bottom-up synthesised CDs.[6]

3.4.2.8. Photoluminescence Behaviour: Absorption

UV-Vis spectroscopy and fluorescence spectroscopy were used to investigate the optical properties and photoluminescence behaviour of the as-synthesised CDs. The UV-Vis spectra of N-CDs (Figure 3.17) and NS CDs (Figure 3.18) were recorded and analysed to identify the possible origins of electronic transitions within the CDs samples.

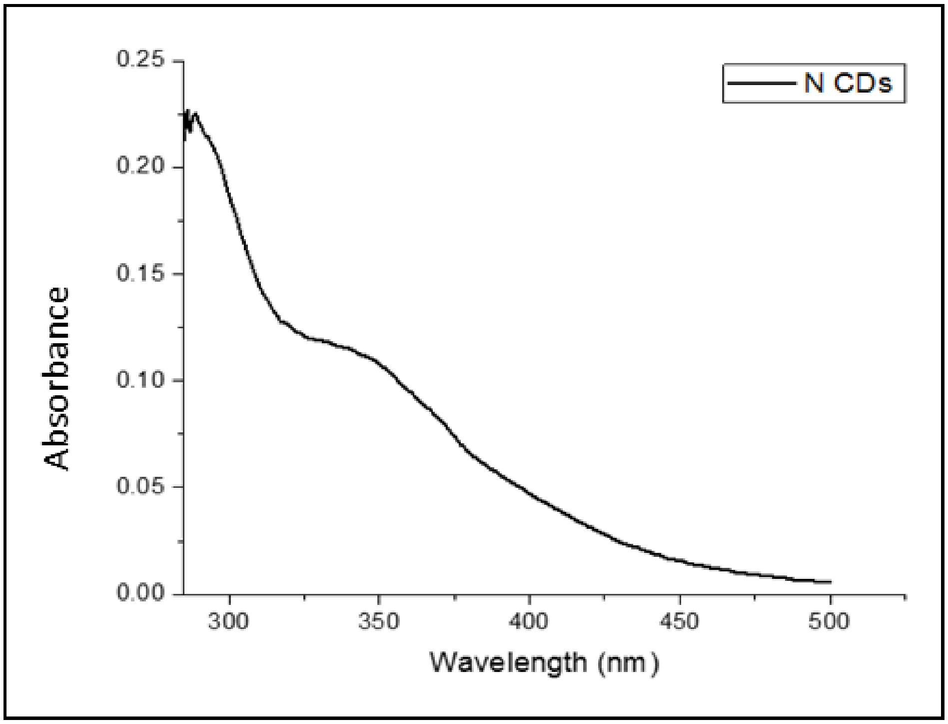

Figure 3.17: Absorption spectrum of N CDs

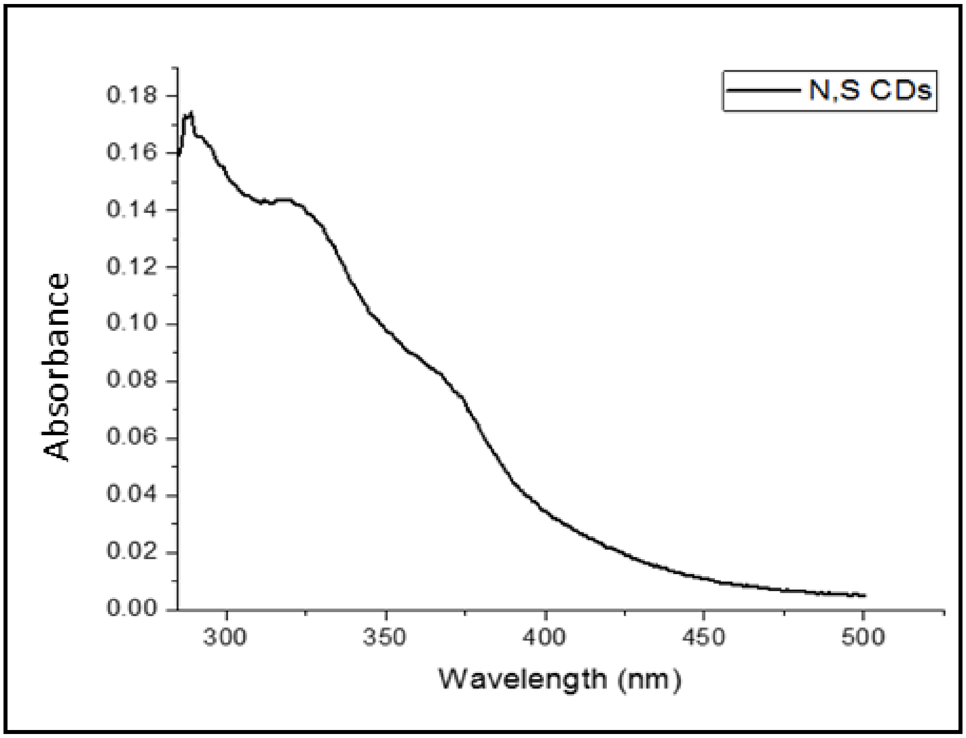

Figure 3.18: Absorption spectrum of NS CDs

The absorption peak at 290 nm is due to the π-π* transition of aromatic sp^2 domains (enhanced by graphitic lattice of the carbon core)[93. This peak] is attributed to the n- π* transitions of the C=O bonds at the core and other connected groups on the surface of the CDs. [34] The Broad peak observed > 340 nm is due to the formation of excited defect surface states induced by the N,S heteroatoms.[3,14,94] Peak observed at approximately 355 nm is due to n- π^* (amide) transition.[6]

3.4.2.9. Photoluminescence Behaviour: Fluorescence

Fluorescence spectroscopy on aqueous dispersions of the CDs samples was carried out to investigate the fluorescence behaviour of the N CDs and NS CDs at different excitation and emission wavelengths, and solution pH.

3.4.2.10. 3D Fluorescence

3D fluorescence spectroscopy was carried out (Figure 3.19 and 3.20) where the excitation and emission wavelengths were varied simultaneously to produce a contour plot of fluorescence intensity. This was used to identify the optimum excitation and emission wavelengths for N CDs and NS CDs.

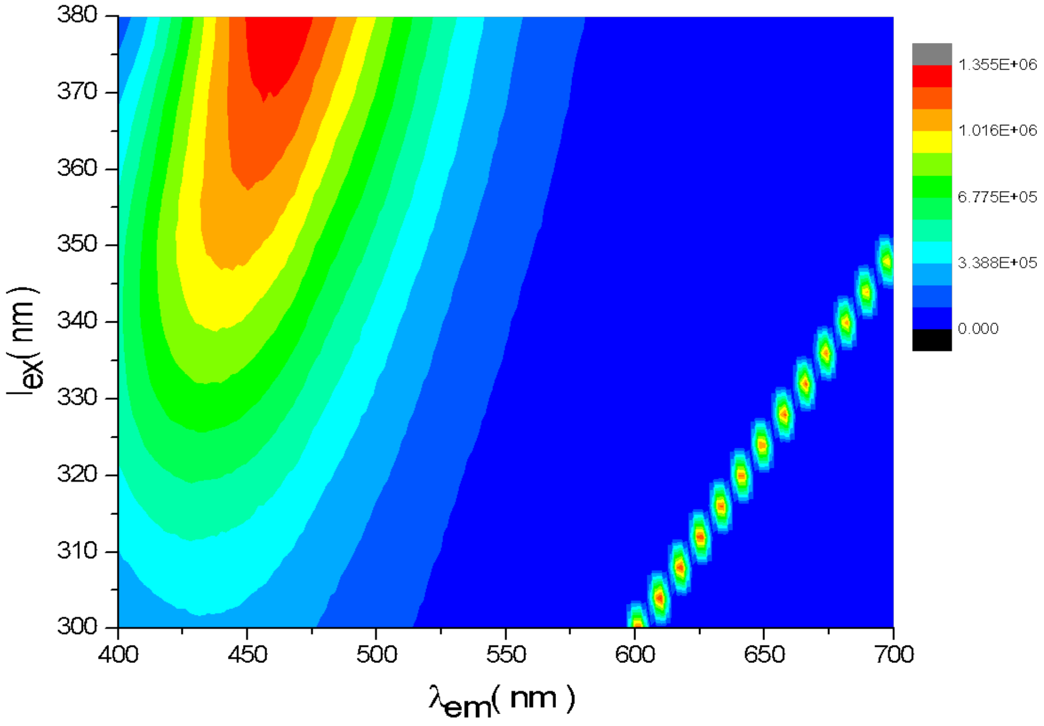

Figure 3.19: 3D Fluorescence spectra of N CDs at λ_{ex} =300 – 380 nm and λ_{em} =400 – 700 nm

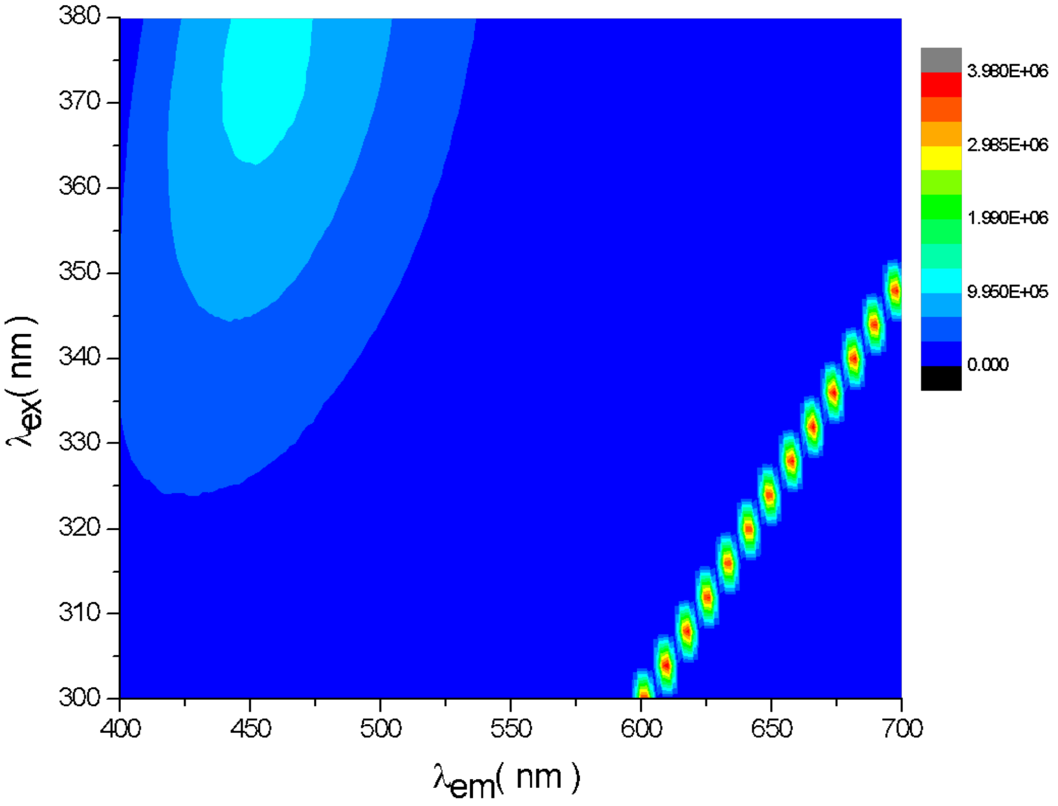

Figure 3.20: 3D Fluorescence Spectra of NS CDs at λ_{ex} =300 – 380 nm and λ_{em} =400 – 700 nm

The 3D fluorescence spectra for N CDs (Figure 3.19) and NS CDs (Figure 3.20) was investigated at excitation wavelengths λ=300- 380 nm and emission wavelengths of λ= 400 – 700 nm. Excitation topographs observed at 600 nm and beyond can be discounted as reflections from the excitation beam. The 3D fluorescence spectra were used to determine the peak excitation and emission wavelengths. N CDs exhibited peak excitation at were λ_{ex}=360- 380 nm and λ_{em}=450 - 475 nm. NS CDs exhibited peak excitation at λ_{ex}= 365 – 380 nm and λ_{em}= 445-475 nm. The N CDs showed significantly higher fluorescence intensity compared to NS CDs which agree with the QY results discussed later in this section.

3.4.2.11. Excitation Dependence

2D fluorescence spectroscopy was used to investigate the PL behaviour of N CDs and NS CDs. Excitation-dependent behaviour was investigated by varying the excitation wavelength (Figure 3.21 and 3.22).

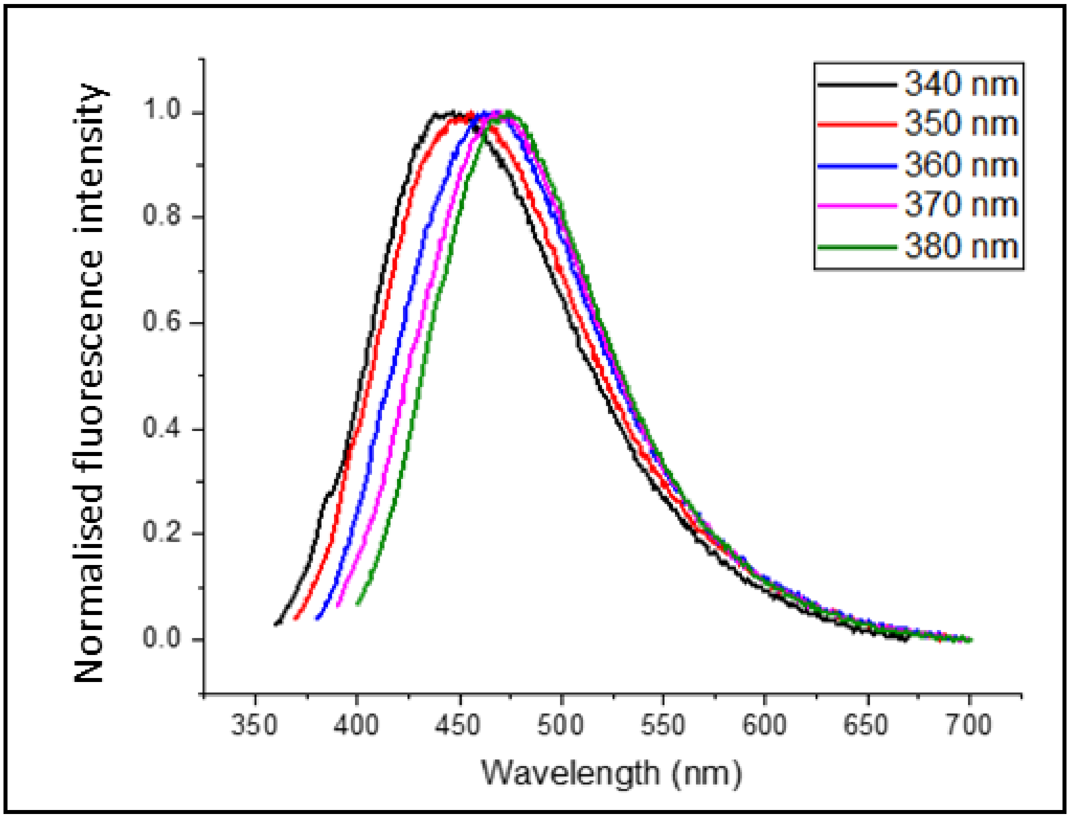

Figure 3.21: Excitation-dependent emission of N CDs (Normalised fluorescence intensity)

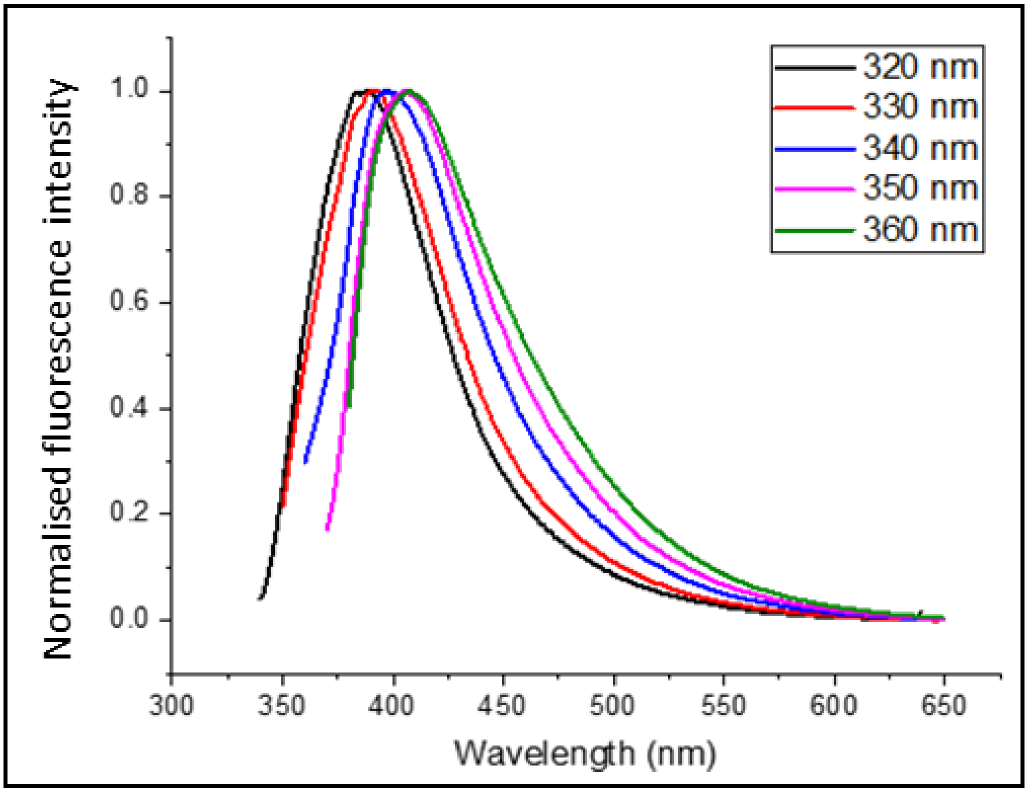

Figure 3.22: Excitation-dependent emission of NS CDs (Normalised fluorescence intensity)

N-CDs and N,S CDs demonstrated broad PL peaks, which is due to strong electron-electron interactions and weak phonon-phonon interactions. This may be due to the presence of multiple π-electron carriers as suggested by Yu et al. [15,59,83,84,95] The excitation-dependence of PL behaviour was investigated by excitation of the CDs at different wavelengths. The spectra were normalised to deduct the effect of concentration on fluorescence intensity and resolve the position of the PL peaks. N CDs (Figure 3.21) and N S CDs (Figure 3.22) displayed excitation-dependent emission with a red shift in the emission wavelength as the excitation wavelength was increased. Excitation-dependent PL behaviour has been extensively reported for carbon-based fluorescent nanomaterials[93] and may be attributed to the size distribution, resulting in a variation of the type and number of Sp^2 sites and presence of multiple functional surface moieties, which result in various emissive traps between the π and π* states. [25,72] The increase in the excitation wavelength causes a red shift in the emission, with a greater red shift observed for NS CDs than N CDs. This is due to a greater presence of functional groups or surface defects present at the surface of the NS CDs which would result in a higher sensitivity to this effect.[80]

3.4.2.12. pH Dependence

The pH dependent behaviour of N CDs and NS CDs was investigated by adjusting the pH of aqueous dispersions of the CDs. The spectra were normalised to deduct the effect of concentration on fluorescence intensity and resolve the position of the PL peaks (Figure 3.23 and 3.24).

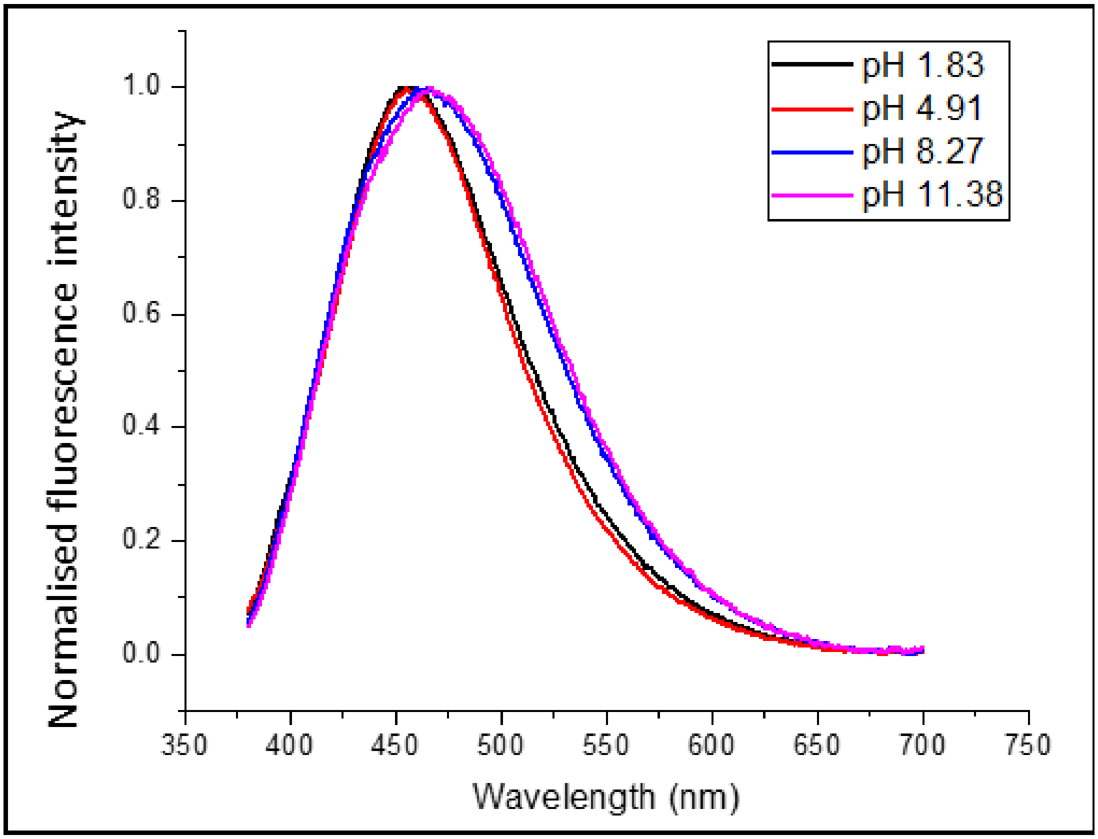

Figure 3.23: Normalised Fluorescence spectra of N CDs at different solution pH

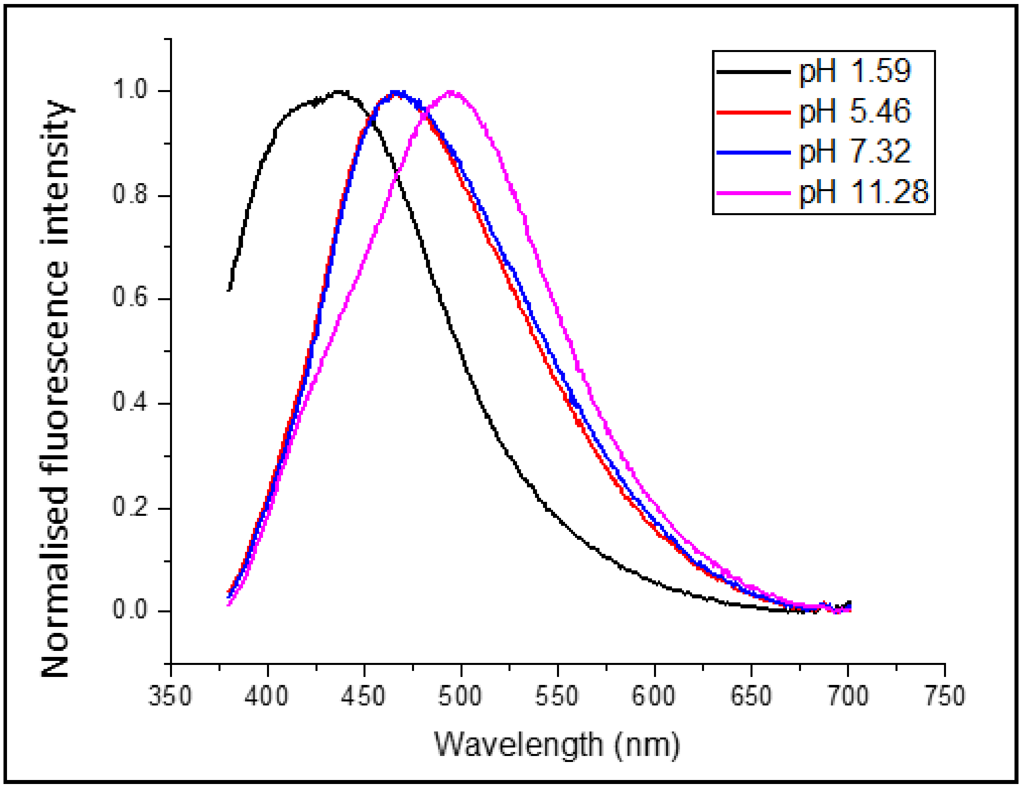

Figure 3.24: Normalised Fluorescence spectra of NS CDs at different solution pH

N-CDs (Figure 3.23) and N S CDs (Figure 3.24) exhibited pH-dependent fluorescence behaviour, with an increase in pH causing a red shift in the emission peak. This behaviour was more apparent in N S CDs than N-CDs. This implies that the molecular state of the CDs is affected by pH as described by Song et al[96], and confirms the dual role of N and S as dopants and surface passivating agents, whereby the use of N and S dopants introduces a higher sensitivity to pH due to the presence of surface passivating agents.

3.4.2.13. Quantum Yield

The quantum yield (QY) of the CDs was calculated using quinine sulfate as a reference. For calculation of quantum yield, five concentrations of each compound were made, all of which had absorbance less than 0.1 nm at the excitation wavelength, which was 340 nm for Quinine sulfate and 360 nm for the CD samples. Quinine sulfate (literature QY = 0.54) was dissolved in 0.1 M H_2SO_4 (refractive index (η) of 1.33) and CD samples were dispersed in ultrapure in water (η = 1.33). The fluorescence spectra were recorded at an excitation wavelength of 340 nm and 360 nm for quinine sulfate and the CDs, respectively. The absorbance value and integrated photoluminescence intensity were plotted. The gradients of the samples and the standards were determined. The data demonstrated good linearity and quantum yield was calculated using the Equation 3.2:

$$\mathrm{QY} = QY_{ref}\frac{\eta^2}{\eta_{ref}^2}\frac{I}{A}\frac{A_{ref}}{I_{ref}} \qquad (3.2)$$

where

- I is the integrated fluorescence intensity
- A is the absorbance at the excitation wavelength
- η is the refractive index
- Subscripts X and ST denote the samples and reference (quinine sulfate), respectively.

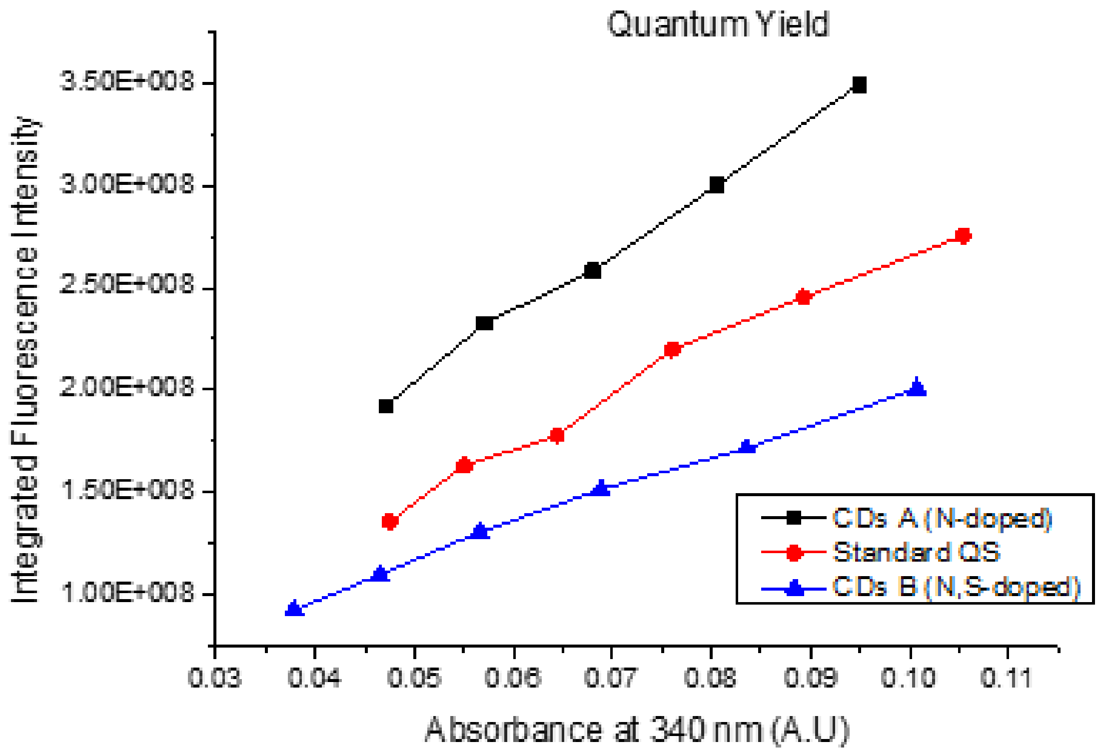

Figure 3.25: Calculation of QY using gradients from absorbance at λ_{ex} and integrated fluorescence intensity

Due to the high rate of photobleaching (discussed in the following section), the QY of the CDs varied depending on the condition under which it was measured. The QY results at different points are quoted in the 'Fluorescence decay' section of this chapter.

3.4.2.14. Fluorescence Decay

CDs were exposed to 365 nm UV light and the integrated fluorescence was measured over time to measure the rate of fluorescence decay and model the photostability of the CDs (Figure 3.26). The fluorescence decay was fit to an exponential decay function (Appendix). The fluorescence decay of N-CDs (0.0136 min^{-1}) was slower than that of NS CDs (0.0365 min^{-1}). The highest recorded QY value was 72% and 36% for N-CDs and NS CDs respectively. NS CDs rapidly photobleached with a half-life of t = 19 mins of exposure to UV light. N-CDs displayed higher photostability with a half-life of t = 51 mins. Both CDs retained fluorescence after 3 hours of exposure, reaching a plateau of fluorescence decay at 180 mins. The QY at this plateau was 5.13% and 4.05% for N-CDs and N,S CDs respectively. The CDs remained fluorescent after 6 months of storage at room temperature in optically opaque Eppendorf tubes.

The rapid fluorescence decay observed under UV excitation whilst retaining fluorescence indicates that there are two discrete PL centres present in the as-synthesised CDs; surface emissive states and the carbogenic core. The fluorescence decay in the presence of UV-light can be attributed to a photochemical process which is catalysed by the presence of oxygen containing groups, as described by Wang et al (2016).[97] XPS and FTIR analysis confirms the presence of these groups. These results are consistent with bottom-up synthesised CDs which possess PL centres in the surface emissive states of the CDs and demonstrate high QY and low photostability. The PL centre in the carbogenic core appears to retain fluorescence even after continuous UV excitation, with a much lower QY (5.13% and 4.05% for N-CDs and N,S CDs respectively). These results are consistent with top-down synthesised CDs which possess a PL centre in the carbogenic core and demonstrate high photostability and low QY.[55] The observation of both characteristics in the as-synthesised CDs provides evidence to demonstrate the ‘hybrid’ nature of the CDs which have been produced by this novel synthetic technique.

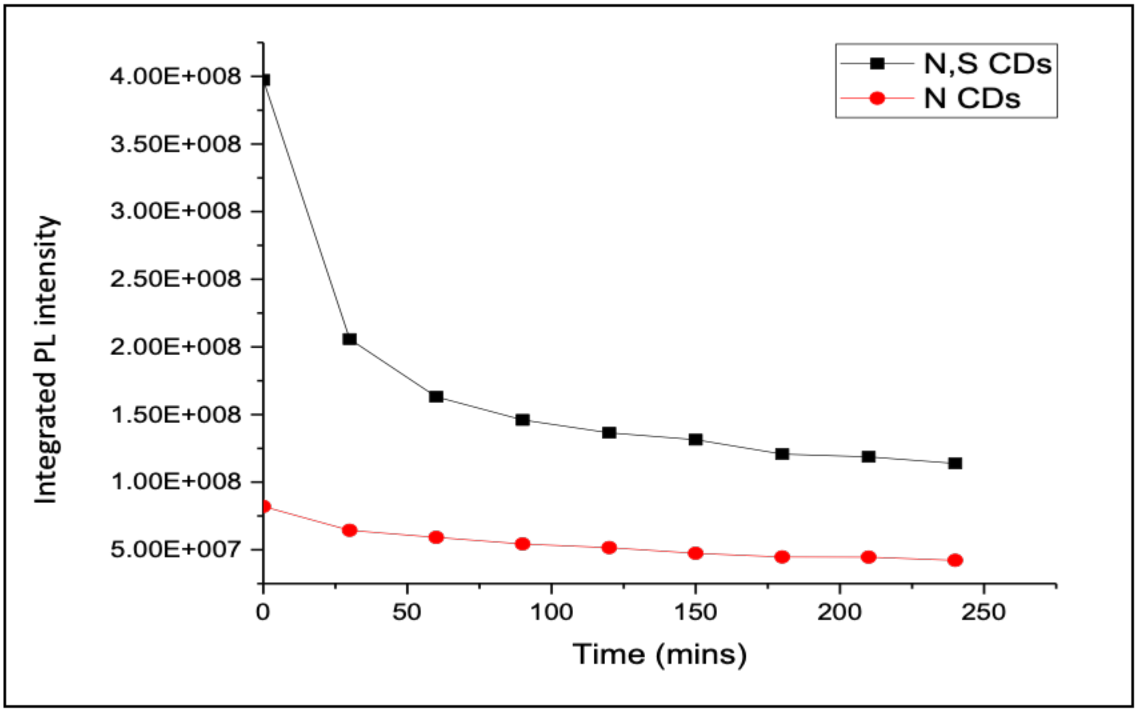

Figure 3.26: Fluorescence decay over time of N CDs (red) and NS CDs (black)

3.5. Conclusions and Further Work

This work presents a novel, cheap and facile hybrid synthesis technique for the synthesis of brightly fluorescent, water-soluble carbon dots (CDs) which draws on both ‘bottom-up’ and ‘top-down’ synthesis techniques. N CDs and NS CDs were prepared by the acid hydrolysis of cellulose pulp to produce NCC and microwave assisted pyrolysis of the NCC as the primary carbohydrate precursor and ethylenediamine and L-cysteine as N and S doping agents respectively. The CDs were characterised by HRTEM, XRD, FTIR, XPS, and their photoluminescence properties and QY were investigated. XRD was carried out to investigate the synthesis process and mechanism by analysing the crystalline structure of the synthesised CDs as well as the individual reagent components. To our knowledge, this type of investigation has not been carried out on CDs. XRD analysis indicated that NCC remains in surplus in the reaction whereas the N and S doping agents are completely used up in the formation of CDs. XRD analysis also confirmed the presence of both crystalline and amorphous regions within the CDs with d-spacing ranging from between 2.84 Å – 4.24 Å. HRTEM was used to investigate the size, morphology and lattice spacing of the CDs. The CDs were discrete, quasi-spherical particles with a narrow size distribution of 2-10 nm (N CDs) and 2-16 nm (N,S CDs). HRTEM confirmed the presence of graphitic interlayer spacing of 0.32 nm corresponding to (002) lattice fringe [46,82] and 0.24-0.28 nm corresponding to (110) fringe of in-plane lattice spacing. D-spacing larger than 3.3Å, observed in XRD, maybe a result of poor crystallisation, and/or the presence of functional groups introduced during the synthesis. The focus of synthesis optimisation centred around the use of minimal dopant amounts and concentrations as well as microwave time and power. The XRD data suggests that further optimisation of the amount and concentration of NCC used is required, as indicated by the presence of surplus NCC in the synthesised N CDs and N S CDs. Additionally, the use of XRD to examine the synthetic process at shorter intervals during the reaction process and determine the mechanism of CD formation could be carried out to aid this optimisation.

Characterisation by FTIR and XPS on the internal molecular structure of CDs indicates that there is a large degree of similarity between the molecular structure of N CDs and N S CDs, which indicates that the process of CD formation follows a similar mechanism, illustrating the validity of comparison between the two. The difference in elemental composition observed between N CDs and N S CDs confirms the role heteroatom doping plays on the composition and internal structure of CDs.[14,87] XPS and FTIR confirm the presence of Sp^2 and Sp^3 types of carbon and the presence of carboxylic, amide and nitric groups at the surface of the CDs. [6,8,90] N CDs and N,S CDs were found to be negatively charged, which is due to the presence of functional groups at the surface such as carboxylic acid and alcohol groups.[90] . The charge of the CDs reflects their hydrophilicity and high solubility in aqueous solutions.[55,89,91,92] This creates a potential avenue for the functionalisation of the surface of the CDs by electrostatic coating.[98]

The PL behaviour of the CDs was investigated. Both N CDs and N S CDs exhibited excitation-dependent emission, with a red shift in emission with higher excitation wavelengths. N CDs and N S CDs demonstrated emission sensitive to the pH of the dispersant solution, whereby an increase in pH resulted in a red shift of the emission peak. N S CDs demonstrated higher sensitivity to pH changes than N CDs. This effect has been attributed to the presence of functional groups and defects at the surface of the CDs, which is in turn related to the size distribution of CDs.[80] N S CDs have a wider size distribution than N CDs, which is in accordance with the higher degree of sensitivity of NS CDs to excitation wavelength and solution pH.

The highest QY observed for N CDs was 73% and N S CDs was 36%. N CDs displayed higher photostability and slower fluorescence decay (0.0136 min^{-1}) compared to N S CDs (0.0365 min^{-}

[1]). The lower QY overall and lower photostability exhibited by N S CDs compared to N CDs would indicate that the S dopant[1] hinders the growth of CDs as reported by Hu et al 2014,[24] as opposed to introducing new surface defects which further enhances the PL as reported by Xu et al 2015.[57] The lack of uniformity and predictability of the bottom-up synthesis procedure makes it difficult to determine the exact contribution of N and S doping to the PL behaviour mechanistically. In order to explore this further, CDs with the same level of N doping would have to be compared.

Although the exact mechanism of PL remains unclear, based on the extensive characterisation of CDs carried out in this work, we would suggest that the mechanism of PL is a combination of the quantum confinement effect at the core (indicated by the excitation-dependence of the PL behaviour), and radiative recombinations of electron-hole pairs at the surface of the CDs, which is influenced by the presence of functional groups and surface emissive traps. This provides great potential to tailor the PL behaviour of CDs synthesised by this method using different doping agents. Furthermore, a greater degree of control over the size of the CDs may be achieved using templating during the synthesis, such as the use of fluorsurfactants as templating agents as shown by Suzuki et al 2015[99], or by improving the post-synthesis purification and size sieving, perhaps through dialysis.

Analysis of the PL behaviour, and internal structure of the CDs suggested the presence of more than one PL centre: the carbogenic core and surface emissive traps. N CDs and NS CDs synthesised by this method exhibited characteristics commonly observed by both top down up synthesised CDs (such as excitation-dependent PL) top down synthesised CDs (such pH-dependent PL and low photostability). These results support the thesis that suggests this is a novel

---

hybrid synthetic technique, which to our knowledge has not been attempted anywhere else in the literature.

The focus of this chapter was the optimisation of the synthesis and characterisation of CDs, with this knowledge further work can be carried out to explore potential applications for these fluorescent particles. The tuneable and broad PL peak of the CDs coupled with their predicted fluorescence decay makes them excellent candidates for applications in bio-imaging and photocatalytic energy conversion.[4]

3.6. References

1. Milosavljevica, V.; Moulicka, A.; Kopela, P. Microwave Preparation of Carbon Quantum Dots with Different Surface Modification. *Web2.Mendelu.Cz* 16–22.
2. Anilkumar, P.; Wang, X.; Cao, L.; Sahu, S.; Liu, J.-H.; Wang, P.; Korch, K.; Tackett, K. N.; Parenzan, A.; Sun, Y.-P. Toward Quantitatively Fluorescent Carbon-Based "Quantum" Dots. *Nanoscale* **2011**, *3* (5), 2023–2027. https://doi.org/10.1039/c0nr00962h.
3. Zheng, X. T.; Ananthanarayanan, A.; Luo, K. Q.; Chen, P. Glowing Graphene Quantum Dots and Carbon Dots: Properties, Syntheses, and Biological Applications. *Small* **2015**, *11* (14), 1620–1636. https://doi.org/10.1002/smll.201402648.
4. Fernando, K. A. S.; Sahu, S.; Liu, Y.; Lewis, W. K.; Guliants, E. A.; Jafariyan, A.; Wang, P.; Bunker, C. E.; Sun, Y. P. Carbon Quantum Dots and Applications in Photocatalytic Energy Conversion. *ACS Appl. Mater. Interfaces* **2015**, *7* (16). https://doi.org/10.1021/acsami.5b00448.
5. Hill, S.; Galan, M. C. Fluorescent Carbon Dots from Mono- and Polysaccharides: Synthesis, Properties and Applications. *Beilstein J. Org. Chem.* **2017**, *13*, 675–693. https://doi.org/10.3762/bjoc.13.67.
6. Hutton, G. A. M.; Martindale, B. C. M.; Reisner, E. Carbon Dots as Photosensitisers for Solar-Driven Catalysis. *Chem. Soc. Rev.* **2017**, *46* (20), 6111–6123. https://doi.org/10.1039/c7cs00235a.
7. Zhai, X.; Zhang, P.; Liu, C.; Bai, T.; Li, W.; Dai, L.; Liu, W. Highly Luminescent Carbon Nanodots by Microwave-Assisted Pyrolysis. *Chem. Commun.* **2012**, *48* (64), 7955–7957. https://doi.org/10.1039/c2cc33869f.
8. Sharma, V.; Tiwari, P.; Mobin, S. M. Sustainable Carbon-Dots: Recent Advances in Green Carbon Dots for Sensing and Bioimaging. *J. Mater. Chem. B* **2017**, *5* (45), 8904–8924. https://doi.org/10.1039/c7tb02484c.
9. Gao, J.; Zhu, M.; Huang, H.; Liu, Y.; Kang, Z. Advances, Challenges and Promises of Carbon Dots. *Inorg. Chem. Front.* **2017**, *4* (12), 1963–1986. https://doi.org/10.1039/c7qi00614d.
10. Zhu, S.; Song, Y.; Zhao, X.; Shao, J.; Zhang, J.; Yang, B. The Photoluminescence Mechanism in Carbon Dots (Graphene Quantum Dots, Carbon Nanodots, and Polymer Dots): Current State and Future Perspective. *Nano Res.* **2015**, *8* (2), 355–381. https://doi.org/10.1007/s12274-014-0644-3.
11. Jiang, J.; He, Y.; Li, S.; Cui, H. Amino Acids as the Source for Producing Carbon Nanodots: Microwave Assisted One-Step Synthesis, Intrinsic Photoluminescence Property and Intense Chemiluminescence Enhancement. *Chem. Commun.* **2012**, *48* (77), 9634–9636. https://doi.org/10.1039/c2cc34612e.
12. Liu, R.; Wu, D.; Feng, X.; Müllen, K. Bottom-up Fabrication of Photoluminescent Graphene Quantum Dots with Uniform Morphology. *J. Am. Chem. Soc.* **2011**, *133* (39), 15221–15223. https://doi.org/10.1021/ja204953k.
13. Dong, Y.; Pang, H.; Yang, H. Bin; Guo, C.; Shao, J.; Chi, Y.; Li, C. M.; Yu, T. Carbon-Based Dots Co-Doped with Nitrogen and Sulfur for High Quantum Yield and Excitation-Independent Emission. *Angew. Chemie - Int. Ed.* **2013**, *52* (30), 7800–7804. https://doi.org/10.1002/anie.201301114.

14. Sun, C.; Zhang, Y.; Wang, P.; Yang, Y.; Wang, Y.; Xu, J.; Wang, Y.; Yu, W. W. Synthesis of Nitrogen and Sulfur Co-Doped Carbon Dots from Garlic for Selective Detection of Fe3+. *Nanoscale Res. Lett.* **2016**, *11* (1), 110. https://doi.org/10.1186/s11671-016-1326-8.

15. Bhunia, S. K.; Maity, A. R.; Nandi, S.; Stepensky, D.; Jelinek, R. Imaging Cancer Cells Expressing the Folate Receptor with Carbon Dots Produced from Folic Acid. *ChemBioChem* **2016**, *17* (7), 614–619. https://doi.org/10.1002/cbic.201500694.

16. Li, Q.; Ohulchanskyy, T. Y.; Liu, R.; Koynov, K.; Wu, D.; Best, A.; Kumar, R.; Bonoiu, A.; Prasad, P. N. Photoluminescent Carbon Dots as Biocompatible Nanoprobes for Targeting Cancer Cells. **2010**, No. ii, 12062–12068.

17. Puvvada, N.; Kumar, B. N. P.; Konar, S.; Kalita, H.; Mandal, M.; Pathak, A. Synthesis of Biocompatible Multicolor Luminescent Carbon Dots for Bioimaging Applications. *Sci. Technol. Adv. Mater.* **2012**, *13* (4), 045008. https://doi.org/10.1088/1468-6996/13/4/045008.

18. Fang, Y.; Guo, S.; Li, D.; Zhu, C.; Ren, W.; Dong, S.; Wang, E. Easy Synthesis and Imaging Applications of Cross-Linked Green Fluorescent Hollow Carbon Nanoparticles. *ACS Nano* **2012**, *6* (1), 400–409. https://doi.org/10.1021/nn2046373.

19. Yang, Z.; Li, Z.; Xu, M.; Xu, M.; Ma, Y.; Zhang, J.; Su, Y.; Su, Y.; Gao, F.; Wei, H.; et al. Controllable Synthesis of Fluorescent Carbon Dots and Their Detection Application as Nanoprobes. *Nano-Micro Lett.* **2013**, *5* (4), 247–259. https://doi.org/10.5101/nml.v5i4.p247-259.

20. Li, S.; Li, Y.; Cao, J.; Zhu, J.; Fan, L.; Li, X. Sulfur-Doped Graphene Quantum Dots as a Novel Fluorescent Probe for Highly Selective and Sensitive Detection of Fe(3+). *Anal Chem* **2014**, *86* (20), 10201–10207. https://doi.org/10.1021/ac503183y.

21. Wang, Y.; Hu, A. Carbon Quantum Dots: Synthesis, Properties and Applications. *J. Mater. Chem. C* **2014**, *2* (34), 6921. https://doi.org/10.1039/C4TC00988F.

22. Tang, L.; Ji, R.; Cao, X.; Lin, J.; Jiang, H.; Li, X.; Teng, K. S. Deep Ultraviolet Photoluminescence Graphene Quantum Dots. *ACS Nano* **2012**, *6* (6), 5102–5110. https://doi.org/10.1021/nn300760g.

23. Li, W.; Zhang, Z.; Kong, B.; Feng, S.; Wang, J.; Wang, L.; Yang, J.; Zhang, F.; Wu, P.; Zhao, D. Simple and Green Synthesis of Nitrogen-Doped Photoluminescent Carbonaceous Nanospheres for Bioimaging. *Angew. Chemie - Int. Ed.* **2013**, *52* (31), 8151–8155. https://doi.org/10.1002/anie.201303927.

24. Yang, S.; Wang, X.; Wang, H.; Lu, F.; Luo, P. G.; Cao, L.; Meziani, M. J.; Liu, J.; Liu, Y.; Chen, M.; et al. Carbon Dots as Nontoxic and High-Performance Fluorescence Imaging Agents. **2009**, 18110–18114.

25. Sahu, S.; Behera, B.; Maiti, T. K.; Mohapatra, S. Simple One-Step Synthesis of Highly Luminescent Carbon Dots from Orange Juice: Application as Excellent Bio-Imaging Agents. *Chem. Commun.* **2012**, *48* (70), 8835. https://doi.org/10.1039/c2cc33796g.

26. Jaleel, J. A.; Pramod, K. Artful and Multifaceted Applications of Carbon Dot in Biomedicine. *J. Control. Release* **2018**, *269* (August), 302–321. https://doi.org/10.1016/j.jconrel.2017.11.027.

27. Li, L.; Wu, G.; Yang, G.; Peng, J.; Zhao, J.; Zhu, J. J. Focusing on Luminescent Graphene Quantum Dots: Current Status and Future Perspectives. *Nanoscale* **2013**, *5* (10), 4015–4039. https://doi.org/10.1039/c3nr33849e.

28. Huang, P.; Lin, J.; Wang, X.; Wang, Z.; Zhang, C.; He, M.; Wang, K.; Chen, F.; Li, Z.; Shen, G.;

et al. Light-Triggered Theranostics Based on Photosensitizer-Conjugated Carbon Dots for Simultaneous Enhanced-Fluorescence Imaging and Photodynamic Therapy. *Adv. Mater.* **2012**, *24* (37), 5104–5110. https://doi.org/10.1002/adma.201200650.

29. Bourlinos, A. B.; Trivizas, G.; Karakassides, M. A.; Baikousi, M.; Kouloumpis, A.; Gournis, D.; Bakandritsos, A.; Hola, K.; Kozak, O.; Zboril, R.; et al. Green and Simple Route toward Boron Doped Carbon Dots with Significantly Enhanced Non-Linear Optical Properties. *Carbon N. Y.* **2015**, *83*, 173–179. https://doi.org/10.1016/j.carbon.2014.11.032.

30. Zhu, S.; Meng, Q.; Wang, L.; Zhang, J.; Song, Y.; Jin, H.; Zhang, K.; Sun, H.; Wang, H.; Yang, B. Highly Photoluminescent Carbon Dots for Multicolor Patterning, Sensors, and Bioimaging. *Angew. Chemie - Int. Ed.* **2013**, *52* (14), 3953–3957. https://doi.org/10.1002/anie.201300519.

31. Cai, Q.-Y.; Li, J.; Ge, J.; Zhang, L.; Hu, Y.-L.; Li, Z.-H.; Qu, L.-B. A Rapid Fluorescence “Switch-on” Assay for Glutathione Detection by Using Carbon Dots–MnO2 Nanocomposites. *Biosens. Bioelectron.* **2015**, *72* (5), 31–36. https://doi.org/10.1016/j.bios.2015.04.077.

32. Wang, L.; Wang, X.; Bhirde, A.; Cao, J.; Zeng, Y.; Huang, X.; Sun, Y.; Liu, G.; Chen, X. Carbon-Dot-Based Two-Photon Visible Nanocarriers for Safe and Highly Efficient Delivery of SiRNA and DNA. *Adv. Healthc. Mater.* **2014**, *3* (8), 1203–1209. https://doi.org/10.1002/adhm.201300611.

33. Zeng, Q.; Shao, D.; He, X.; Ren, Z.; Ji, W.; Shan, C.; Qu, S.; Li, J.; Chen, L.; Li, Q. Carbon Dots as a Trackable Drug Delivery Carrier for Localized Cancer Therapy: In Vivo. *J. Mater. Chem. B* **2016**, *4* (30), 5119–5126. https://doi.org/10.1039/c6tb01259k.

34. Chen, J.; Liu, J.; Li, J.; Xu, L.; Qiao, Y. One-Pot Synthesis of Nitrogen and Sulfur Co-Doped Carbon Dots and Its Application for Sensor and Multicolor Cellular Imaging. *J. Colloid Interface Sci.* **2017**, *485*, 167–174. https://doi.org/10.1016/j.jcis.2016.09.040.

35. Shi, L.; Yang, J. H.; Zeng, H. B.; Chen, Y. M.; Yang, S. C.; Wu, C.; Zeng, H.; Yoshihito, O.; Zhang, Q. Carbon Dots with High Fluorescence Quantum Yield: The Fluorescence Originates from Organic Fluorophores. *Nanoscale* **2016**, *8* (30), 14374–14378. https://doi.org/10.1039/c6nr00451b.

36. Wu, Y. F.; Wu, H. C.; Kuan, C. H.; Lin, C. J.; Wang, L. W.; Chang, C. W.; Wang, T. W. Multi-Functionalized Carbon Dots as Theranostic Nanoagent for Gene Delivery in Lung Cancer Therapy. *Sci. Rep.* **2016**, *6* (January), 1–12. https://doi.org/10.1038/srep21170.

37. Liu, X.; Li, T.; Hou, Y.; Wu, Q.; Yi, J.; Zhang, G. Microwave Synthesis of Carbon Dots with Multi-Response Using Denatured Proteins as Carbon Source. *RSC Adv.* **2016**, *6* (14), 11711–11718. https://doi.org/10.1039/C5RA23081K.

38. Liu, C.; Zhang, P.; Zhai, X.; Tian, F.; Li, W.; Yang, J.; Liu, Y.; Wang, H.; Wang, W.; Liu, W. Nano-Carrier for Gene Delivery and Bioimaging Based on Carbon Dots with PEI-Passivation Enhanced Fluorescence. *Biomaterials* **2012**, *33* (13), 3604–3613. https://doi.org/10.1016/j.biomaterials.2012.01.052.

39. Zhang, B.; Liu, C. Y.; Liu, Y. A Novel One-Step Approach to Synthesize Fluorescent Carbon Nanoparticles. *Eur. J. Inorg. Chem.* **2010**, No. 28, 4411–4414. https://doi.org/10.1002/ejic.201000622.

40. Yang, Z. C.; Wang, M.; Yong, A. M.; Wong, S. Y.; Zhang, X. H.; Tan, H.; Chang, A. Y.; Li, X.; Wang, J. Intrinsically Fluorescent Carbon Dots with Tunable Emission Derived from Hydrothermal Treatment of Glucose in the Presence of Monopotassium Phosphate. *Chem.*

Commun. **2011**, *47* (42), 11615–11617. https://doi.org/10.1039/c1cc14860e.

41. Wei, W.; Xu, C.; Wu, L.; Wang, J.; Ren, J.; Qu, X. Non-Enzymatic-Browning-Reaction: A Versatile Route for Production of Nitrogen-Doped Carbon Dots with Tunable Multicolor Luminescent Display. *Sci. Rep.* **2014**, *4* (SREP03564), 1–7. https://doi.org/10.1038/srep03564.

42. Zhang, H.; Dai, P.; Huang, L.; Huang, Y.; Huang, Q.; Zhang, W.; Wei, C.; Hu, S. A Nitrogen-Doped Carbon Dot/Ferroceneat??-Cyclodextrin Composite as an Enhanced Material for Sensitive and Selective Determination of Uric Acid. *Anal. Methods* **2014**, *6* (8), 2687–2691. https://doi.org/10.1039/c4ay00140k.

43. Wang, C.; Xu, Z.; Cheng, H.; Lin, H.; Humphrey, M. G.; Zhang, C. A Hydrothermal Route to Water-Stable Luminescent Carbon Dots as Nanosensors for PH and Temperature. *Carbon N. Y.* **2015**, *82* (C), 87–95. https://doi.org/10.1016/j.carbon.2014.10.035.

44. Zheng, M.; Ruan, S.; Liu, S.; Sun, T.; Qu, D.; Zhao, H.; Xie, Z.; Gao, H.; Jing, X.; Sun, Z. Self-Targeting Fluorescent Carbon Dots for Diagnosis of Brain Cancer Cells. *ACS Nano* **2015**, *9* (11), 11455–11461. https://doi.org/10.1021/acsnano.5b05575.

45. Wang, X.; Shen, X.; Li, B.; Jiang, G.; Zhou, X.; Jiang, H. One-Step Facile Synthesis of Novel β-Amino Alcohol Functionalized Carbon Dots for the Fabrication of a Selective Copper Ion Sensing Interface Based on the Biuret Reaction. *RSC Adv.* **2016**, *6* (22), 18326–18332. https://doi.org/10.1039/c5ra24348c.

46. Mitra, S.; Chandra, S.; Kundu, T.; Banerjee, R.; Pramanik, P.; Goswami, A. Rapid Microwave Synthesis of Fluorescent Hydrophobic Carbon Dots. *RSC Adv.* **2012**, *2* (32), 12129. https://doi.org/10.1039/c2ra21048g.

47. Meziani, M. J.; Dong, X.; Zhu, L.; Jones, L. P.; Lecroy, G. E.; Yang, F.; Wang, S.; Wang, P.; Zhao, Y.; Yang, L.; et al. Visible-Light-Activated Bactericidal Functions of Carbon “Quantum” Dots. *ACS Appl. Mater. Interfaces* **2016**, *8* (17), 10761–10766. https://doi.org/10.1021/acsami.6b01765.

48. Parvin, N.; Mandal, T. K. Synthesis of a Highly Fluorescence Nitrogen-Doped Carbon Quantum Dots Bioimaging Probe and Its in Vivo Clearance and Printing Applications. *RSC Adv.* **2016**, *6* (22), 18134–18140. https://doi.org/10.1039/c5ra25402g.

49. Cayuela, A.; Laura Soriano, M.; Valcárcel, M. Strong Luminescence of Carbon Dots Induced by Acetone Passivation: Efficient Sensor for a Rapid Analysis of Two Different Pollutants. *Anal. Chim. Acta* **2013**, *804*, 246–251. https://doi.org/10.1016/j.aca.2013.10.031.

50. Kumar, V. B.; Sheinberger, J.; Porat, Z.; Shav-Tal, Y.; Gedanken, A. A Hydrothermal Reaction of an Aqueous Solution of BSA Yields Highly Fluorescent N Doped C-Dots Used for Imaging of Live Mammalian Cells. *J. Mater. Chem. B* **2016**, *4* (17), 2913–2920. https://doi.org/10.1039/c6tb00519e.

51. Wang, C.; Wang, C.; Sun, D.; Li, A.; Chen, Y.; Zhuo, K. Facile Synthesis of Nitrogen-Doped Carbon Dots from COOHfunctional Ionic Liquid and Their Sensing Application in Selective Detection of Free Chlorine. *Mater. Res. Express* **2016**, *3* (9). https://doi.org/10.1088/2053-1591/3/9/095020.

52. He, G.; Xu, M.; Shu, M.; Li, X.; Yang, Z.; Zhang, L. Rapid Solid-Phase Microwave Synthesis of Highly Photoluminescent Nitrogen-Doped Carbon Dots for Fe 3 + Detection and Cellular Bioimaging. *Nanotechnology* **2016**, *27* (39). https://doi.org/10.1088/0957-4484/27/39/395706 Rapid.

53. Campos, B. B.; Oliva, M. M.; Contreras-Cáceres, R.; Rodriguez-Castellón, E.; Jiménez-Jiménez, J.; da Silva, J. C. G. E.; Algarra, M. Carbon Dots on Based Folic Acid Coated with PAMAM Dendrimer as Platform for Pt(IV) Detection. *J. Colloid Interface Sci.* **2016**, *465* (Iv), 165–173. https://doi.org/10.1016/j.jcis.2015.11.059.

54. Mehta, V. N.; Chettiar, S. S.; Bhamore, J. R.; Kailasa, S. K.; Patel, R. M. Green Synthetic Approach for Synthesis of Fluorescent Carbon Dots for Lisinopril Drug Delivery System and Their Confirmations in the Cells. *J. Fluoresc.* **2017**, *27* (1), 111–124. https://doi.org/10.1007/s10895-016-1939-4.

55. Wang, W.; Damm, C.; Walter, J.; Nacken, T. J.; Peukert, W. Photobleaching and Stabilization of Carbon Nanodots Produced by Solvothermal Synthesis. *Phys Chem Chem Phys* **2016**, *18* (1), 466–475. https://doi.org/10.1039/c5cp04942c.

56. Hu, Q.; Paau, M. C.; Zhang, Y.; Gong, X.; Zhang, L.; Lu, D.; Liu, Y.; Liu, Q.; Yao, J.; Choi, M. M. F. Green Synthesis of Fluorescent Nitrogen/Sulfur-Doped Carbon Dots and Investigation of Their Properties by HPLC Coupled with Mass Spectrometry. *RSC Adv.* **2014**, *4* (35), 18065. https://doi.org/10.1039/c4ra02170c.

57. Xu, Q.; Pu, P.; Zhao, J.; Dong, C.; Gao, C.; Chen, Y.; Chen, J.; Liu, Y.; Zhou, H. Preparation of Highly Photoluminescent Sulfur-Doped Carbon Dots for Fe(<scp>iii</Scp>) Detection. *J. Mater. Chem. A* **2015**, *3* (2), 542–546. https://doi.org/10.1039/C4TA05483K.

58. Tamilselvan Mohan, Silvo Hribernik, R. K. and K. S.-\r\nKleinschek. *Cellulose - Fundamental Aspects and Current Trends*; InTech, 2015. https://doi.org/10.5772/59889.

59. Tamilselvan Mohan, Silvo Hribernik, R. K. and K. S.-\r\nKleinschek. *Cellulose - Fundamental Aspects and Current Trends*; InTech, 2015. https://doi.org/10.5772/59889.

60. Wang, C.; Wang, C.; Xu, P.; Li, A.; Chen, Y.; Zhuo, K. Synthesis of Cellulose-Derived Carbon Dots Using Acidic Ionic Liquid as a Catalyst and Its Application for Detection of Hg2+. *J. Mater. Sci.* **2015**, *51* (2), 861–867. https://doi.org/10.1007/s10853-015-9410-5.

61. Li, W.; Wang, S.; Li, Y.; Ma, C.; Huang, Z.; Wang, C.; Li, J.; Chen, Z.; Liu, S. One-Step Hydrothermal Synthesis of Fluorescent Nanocrystalline Cellulose/Carbon Dot Hydrogels. *Carbohydr. Polym.* **2017**, *175*, 7–17. https://doi.org/10.1016/j.carbpol.2017.07.062.

62. Wu, Q.; Li, W.; Tan, J.; Wu, Y.; Liu, S. Hydrothermal Carbonization of Carboxymethylcellulose: One-Pot Preparation of Conductive Carbon Microspheres and Water-Soluble Fluorescent Carbon Nanodots. *Chem. Eng. J.* **2015**, *266*, 112–120. https://doi.org/10.1016/j.cej.2014.12.089.

63. da Silva Souza, D. R.; Caminhas, L. D.; de Mesquita, J. P.; Pereira, F. V. Luminescent Carbon Dots Obtained from Cellulose. *Mater. Chem. Phys.* **2018**, *203*, 148–155. https://doi.org/10.1016/j.matchemphys.2017.10.001.

64. Chae, A.; Choi, B. R.; Choi, Y.; Jo, S.; Kang, E. B.; Lee, H.; Park, S. Y.; In, I. Mechanochemical Synthesis of Fluorescent Carbon Dots from Cellulose Powders. *Nanotechnology* **2018**, *29* (16). https://doi.org/10.1088/1361-6528/aaad49.

65. Ng, Y. H.; Chin, S. F.; Pang, S. C.; Ng, S. M. The Luminescence Profile of Carbon Dots Synthesized from α-Cellulose under Different Acid Hydrolysis Conditions. *Opt. Mater. (Amst).* **2017**, *70*, 50–56. https://doi.org/10.1016/j.optmat.2017.05.014.

66. Zheng, B.; Gerdts, C. J.; Ismagilov, R. F. Using Nanoliter Plugs in Microfluidics to Facilitate and Understand Protein Crystallization. *Curr. Opin. Struct. Biol.* **2005**, *15* (5), 548–555. https://doi.org/10.1016/j.sbi.2005.08.009.

67. Peng, H.; Li, Y.; Jiang, C.; Luo, C.; Qi, R.; Huang, R.; Duan, C.-G.; Travas-Sejdic, J. Tuning the Properties of Luminescent Nitrogen-Doped Carbon Dots by Reaction Precursors. *Carbon N. Y.* **2016**, *100*, 386–394. https://doi.org/http://dx.doi.org/10.1016/j.carbon.2016.01.029.

68. Dhenadhayalan, N.; Lin, K.-C.; Suresh, R.; Ramamurthy, P. Unravelling the Multiple Emissive States in Citric Acid-Derived Carbon-Dots. *J. Phys. Chem. C* **2015**, acs.jpcc.5b08516. https://doi.org/10.1021/acs.jpcc.5b08516.

69. Niu, W. J.; Li, Y.; Zhu, R. H.; Shan, D.; Fan, Y. R.; Zhang, X. J. Ethylenediamine-Assisted Hydrothermal Synthesis of Nitrogen-Doped Carbon Quantum Dots as Fluorescent Probes for Sensitive Biosensing and Bioimaging. *Sensors Actuators, B Chem.* **2015**, *218*, 229–236. https://doi.org/10.1016/j.snb.2015.05.006.

70. Park, Y.; Yoo, J.; Lim, B.; Kwon, W.; Rhee, S.-W. Improving the Functionality of Carbon Nanodots: Doping and Surface Functionalization. *J. Mater. Chem. A* **2016**, *4* (30), 11582–11603. https://doi.org/10.1039/C6TA04813G.

71. Wang, C.-I.; Wu, W.-C.; Periasamy, A. P.; Chang, H.-T. Electrochemical Synthesis of Photoluminescent Carbon Nanodots from Glycine for Highly Sensitive Detection of Hemoglobin. *Green Chem.* **2014**, *16* (5), 2509–2514. https://doi.org/10.1039/C3GC42325E.

72. Wu, Z. L.; Liu, Z. X.; Yuan, Y. H. Carbon Dots: Materials, Synthesis, Properties and Approaches to Long-Wavelength and Multicolor Emission. *J. Mater. Chem. B* **2017**, *5* (21), 3794–3809. https://doi.org/10.1039/C7TB00363C.

73. Wang, L.; Zhu, S.; Wang, H.; Qu, S.; Zhang, Y.; Zhang, J.; Chen, Q.; Al, W. E. T. Common Origin of Green Luminescence in Carbon Nanodots and Graphene Quantum Dots. **2014**, No. 3, 2541–2547.

74. Loo, A. H.; Sofer, Z.; Bouša, D.; Ulbrich, P.; Bonanni, A.; Pumera, M. Carboxylic Carbon Quantum Dots as a Fluorescent Sensing Platform for DNA Detection. *ACS Appl. Mater. Interfaces* **2016**, *8* (3), 1951–1957. https://doi.org/10.1021/acsami.5b10160.

75. Okamoto, T.; Patil, A.; Nissinen, T.; Mann, S. Self-Assembly of Colloidal Nanocomposite Hydrogels Using 1D Cellulose Nanocrystals and 2D Exfoliated Organoclay Layers. *Gels* **2017**, *3* (1), 11. https://doi.org/10.3390/gels3010011.

76. Li, X.; Zhang, S.; Kulinich, S. A.; Liu, Y.; Zeng, H. Engineering Surface States of Carbon Dots to Achieve Controllable Luminescence for Solid-Luminescent Composites and Sensitive Be2+detection. *Sci. Rep.* **2014**, *4* (1), 4976. https://doi.org/10.1038/srep04976.

77. Ding, H.; Wei, J.-S.; Xiong, H.-M. Nitrogen and Sulfur Co-Doped Carbon Dots with Strong Blue Luminescence. *Nanoscale* **2014**, *6* (22), 13817–13823. https://doi.org/10.1039/C4NR04267K.

78. Baruah, U.; Gogoi, N.; Konwar, A.; Jyoti Deka, M.; Chowdhury, D.; Majumdar, G. Carbon Dot Based Sensing of Dopamine and Ascorbic Acid. *J. Nanoparticles* **2014**, *2014*, 1–8. https://doi.org/10.1155/2014/178518.

79. Tao, S.; Zhu, S.; Feng, T.; Xia, C.; Song, Y.; Yang, B. The Polymeric Characteristics and Photoluminescence Mechanism in Polymer Carbon Dots: A Review. *Mater. Today Chem.* **2017**, *6*, 13–25. https://doi.org/10.1016/j.mtchem.2017.09.001.

80. Bhaisare, M. L.; Talib, A.; Khan, M. S.; Pandey, S.; Wu, H. F. Synthesis of Fluorescent Carbon Dots via Microwave Carbonization of Citric Acid in Presence of Tetraoctylammonium Ion, and Their Application to Cellular Bioimaging. *Microchim. Acta* **2015**, *182* (13–14), 2173–2181. https://doi.org/10.1007/s00604-015-1541-5.

81. Li, H.; Kang, Z.; Liu, Y.; Lee, S.-T. Carbon Nanodots: Synthesis, Properties and Applications. *J. Mater. Chem.* **2012**, *22* (46), 24230. https://doi.org/10.1039/c2jm34690g.

82. Feng, T.; Ai, X.; An, G.; Yang, P.; Zhao, Y. Charge-Convertible Carbon Dots for Imaging-Guided Drug Delivery with Enhanced *in Vivo* Cancer Therapeutic Efficiency. *ACS Nano* **2016**, acsnano.6b00043. https://doi.org/10.1021/acsnano.6b00043.

83. Baker, S. N.; Baker, G. A. Luminescent Carbon Nanodots: Emergent Nanolights. *Angew. Chemie - Int. Ed.* **2010**, *49* (38), 6726–6744. https://doi.org/10.1002/anie.200906623.

84. Zhu, S.; Meng, Q.; Wang, L.; Zhang, J.; Song, Y.; Jin, H.; Zhang, K.; Sun, H.; Wang, H.; Yang, B. Highly Photoluminescent Carbon Dots for Multicolor Patterning, Sensors, and Bioimaging. *Angew. Chemie - Int. Ed.* **2013**, *52* (14), 3953–3957. https://doi.org/10.1002/anie.201300519.

85. Tang, L.; Ji, R.; Cao, X.; Lin, J.; Jiang, H.; Li, X.; Teng, K. S.; Luk, C. M.; Zeng, S.; Hao, J.; et al. Deep Ultraviolet Photoluminescence of Water-Soluble Self-Passivated Graphene Quantum Dots. *ACS Nano* **2012**, *6* (6), 5102–5110. https://doi.org/10.1021/nn300760g.

86. Kundu, A.; Lee, J.; Park, B.; Ray, C.; Sankar, K. V.; Kim, W. S.; Lee, S. H.; Cho, I. J.; Jun, S. C. Facile Approach to Synthesize Highly Fluorescent Multicolor Emissive Carbon Dots via Surface Functionalization for Cellular Imaging. *J. Colloid Interface Sci.* **2018**, *513*, 505–514. https://doi.org/10.1016/j.jcis.2017.10.095.

87. Zhou, W.; Zhuang, J.; Li, W.; Hu, C.; Lei, B.; Liu, Y. Towards Efficient Dual-Emissive Carbon Dots through Sulfur and Nitrogen Co-Doped. *J. Mater. Chem. C* **2017**, *5* (32), 8014–8021. https://doi.org/10.1039/c7tc01819c.

88. Liu, H.; He, Z.; Jiang, L. P.; Zhu, J. J. Microwave-Assisted Synthesis of Wavelength-Tunable Photoluminescent Carbon Nanodots and Their Potential Applications. *ACS Appl. Mater. Interfaces* **2015**, *7* (8), 4913–4920. https://doi.org/10.1021/am508994w.

89. Zhao, P.; Zhu, L. Dispersibility of Carbon Dots in Aqueous and/or Organic Solvents. *Chem. Commun.* **2018**, *54* (43), 5401–5406. https://doi.org/10.1039/c8cc02279h.

90. Havrdova, M.; Hola, K.; Skopalik, J.; Tomankova, K.; Petr, M.; Cepe, K.; Polakova, K.; Tucek, J.; Bourlinos, A. B.; Zboril, R. Toxicity of Carbon Dots – Effect of Surface Functionalization on the Cell Viability, Reactive Oxygen Species Generation and Cell Cycle. *Carbon N. Y.* **2016**, *99*, 238–248. https://doi.org/10.1016/j.carbon.2015.12.027.

91. López, C.; Zougagh, M.; Algarra, M.; Rodríguez-Castellón, E.; Campos, B. B.; Esteves Da Silva, J. C. G.; Jiménez-Jiménez, J.; Ríos, A. Microwave-Assisted Synthesis of Carbon Dots and Its Potential as Analysis of Four Heterocyclic Aromatic Amines. *Talanta* **2015**, *132*, 845–850. https://doi.org/10.1016/j.talanta.2014.10.008.

92. Zhai, X.; Gao, J.; Wang, X.; Mei, S.; Zhao, R.; Wu, Y.; Hao, C.; Yang, J.; Liu, Y. Inverse Pickering Emulsions Stabilized by Carbon Quantum Dots: Influencing Factors and Their Application as Templates. *Chem. Eng. J.* **2018**, *345* (March), 209–220. https://doi.org/10.1016/j.cej.2018.03.075.

93. Pei, S.; Zhang, J.; Gao, M.; Wu, D.; Yang, Y.; Liu, R. A Facile Hydrothermal Approach towards Photoluminescent Carbon Dots from Amino Acids. *J. Colloid Interface Sci.* **2015**, *439*, 129–133. https://doi.org/10.1016/j.jcis.2014.10.030.

94. Shamsipur, M.; Barati, A.; Karami, S. Long-Wavelength, Multicolor, and White-Light Emitting Carbon-Based Dots: Achievements Made, Challenges Remaining, and Applications. *Carbon N. Y.* **2017**, *124*, 429–472. https://doi.org/10.1016/j.carbon.2017.08.072.

95. Sun, D.; Ban, R.; Zhang, P. H.; Wu, G. H.; Zhang, J. R.; Zhu, J. J. Hair Fiber as a Precursor for Synthesizing of Sulfur- and Nitrogen-Co-Doped Carbon Dots with Tunable Luminescence Properties. *Carbon N. Y.* **2013**, *64*. https://doi.org/10.1016/j.carbon.2013.07.095.

96. Song, Y.; Zhu, S.; Xiang, S.; Zhao, X.; Zhang, J.; Zhang, H.; Fu, Y.; Yang, B. Investigation into the Fluorescence Quenching Behaviors and Applications of Carbon Dots. *Nanoscale* **2014**, *6* (9), 4676. https://doi.org/10.1039/c4nr00029c.

97. Wang, W.; Damm, C.; Walter, J.; Nacken, T. J.; Peukert, W. Photobleaching and Stabilization of Carbon Nanodots Produced by Solvothermal Synthesis. *Phys. Chem. Chem. Phys.* **2016**, *18* (1), 466–475. https://doi.org/10.1039/c5cp04942c.

98. Peng, Z.; Han, X.; Li, S.; Al-Youbi, A. O.; Bashammakh, A. S.; El-Shahawi, M. S.; Leblanc, R. M. Carbon Dots: Biomacromolecule Interaction, Bioimaging and Nanomedicine. *Coordination Chemistry Reviews*. 2017, pp 256–277. https://doi.org/10.1016/j.ccr.2017.06.001.

99. Suzuki, K.; Malfatti, L.; Carboni, D.; Loche, D.; Casula, M.; Moretto, A.; Maggini, M.; Takahashi, M.; Innocenzi, P. Energy Transfer Induced by Carbon Quantum Dots in Porous Zinc Oxide Nanocomposite Films. *J. Phys. Chem. C* **2015**, *119* (5), 2837–2843. https://doi.org/10.1021/jp510661d.

Chapter 4: Nano-Crystalline Cellulose Based-Carbon Dots; Cytotoxicity, Photostability and Encapsulation

4.1. Aims of the Work

The aims of this work were to investigate the cytotoxicity of N CDs and NS CDs (synthesised and characterised as described in Chapter 3) in HeLa cells to explore their potential for biological applications. Encapsulation of the CDs within silica colloidosomes and PDDA/ATP coacervates was carried out to investigate the effect of encapsulation on the PL behaviour and PS. Acoustic trapping using a standing acoustic and pressure field was used to pattern the coacervate-CD system into a two-dimensional array by a combination of in situ complex coacervation and an acoustic standing wave pressure field in order to facilitate investigations into the PL behaviour and PS of the coacervate-CDs.

4.2. Introduction

4.2.1. Carbon Dots as Bioimaging Agents

Carbon Dots (CDs) have attracted significant attention as the 'green' non-toxic alternative to semi-conductor quantum dots (QDs) with an abundance of organic precursors available for their cheap and facile synthesis. They possess unique and advantageous properties of high photostability, low cytotoxicity as well as tuneable surface chemistry and photoluminescence (PL) behaviour. This has made them attractive candidates for biomedical applications in theranostics, drug delivery and bio-imaging. [1] A review of the synthesis, properties, mechanism of PL and characteristics of CDs have been covered previously in Chapter 3. This Chapter will focus on the interaction of CDs with biomolecules and suitable considerations for their application as bioimaging agents.[23] These have been categorised into: biocompatibility and/or cytotoxicity, photoluminescence behaviour and photostability. Additionally, surface functionalisation and targeting and will be considered within the context of N CDs and NS CDs synthesised and characterised as described in Chapter 3.

4.2.2. Biocompatibility/cytotoxicity

As with other functional nanomaterials, the challenge for a holistic understanding of the cytotoxicity profile of CDs remains a challenge, however extensive studies into the cytotoxicity of CDs in vitro has repeatedly deemed them non-cytotoxic. The first investigations into CD cytotoxicity were carried out by Sun et al. (2006) They used PEGylated CDs (prepared by laser ablation and surface functionalisation using diamine-terminated PEG) to image human breast cancer cells (MCF-7). The CDs appeared to be non-blinking, highly photostable and most importantly non-cytotoxic. [4] Since then, many bioimaging investigations involving CDs using primarily fluorescence confocal microscopy have been carried out into different cell lines including: HeLa cells[5–12], Ehrlich ascites carcinoma cells (EAC)[13], adenocarcinomic human alveolar basal epithelial cells (A549)[14], Pancrea-1cells [15] and LLC-PK1 cells.[16] The exact mechanism of cellular uptake remains to be understood, however endocytosis is considered the major internalisation pathway. This is aided by surface functionalisation and can be used to target specific cells or cell organelles. [1]

In addition to in vitro characterisation, a crucial requirement for the use of CDs in bioapplications is the biocompatibility and cytotoxicity of these nanoparticles in vivo. The literature surrounding target-specific bioimaging and theranostics development for medical applications of CDs in vivo remains limited. In order to consider the potential success of CDs in these areas it is first imperative to understand their interactions with biomacromolecules such as lipids, proteins and nucleic acids within the cells. [1]However, this falls beyond the scope of this work and thus is not discussed in detail in this chapter. In vivo cytotoxicity CDs is also not discussed in detail in this chapter, however it has demonstrated promising results in investigations carried out by Yang et al. (2009) and Li et al. (2016) in mice and zebrafish respectively.[17,18]

4.2.3. Photoluminescence Behaviour and Photostability

The optical properties and photoluminescence behaviour of CDs can be tuned by a variety of techniques including: heteroatom doping, surface functionalisation and size control. CDs typically possess a strong absorption band within the UV-Vis range, with absorption at 260 – 320 nm attributed to the π-π* transition in the C=C at the carbon core, and 350-550 nm absorption in the visible range which is attributed to the surface functional groups. Excitation-dependent photoluminescence behaviour, a common feature of multi-component bottom-up fabricated CDs, is highly advantageous because it allows multi-colour imaging by simple adjustment of the excitation wavelength. Tuneable emission is widely considered to be due to the broad size distribution of the CDs as well as the variety of surface group functionalities present, with some CDs exhibiting charge-dependent, and pH dependent emission as well.[1,3]

As discussed in Chapter 3, the quantum yield (QY) and photostability (PS) of CDs are highly dependent on the synthesis mechanism and can be additionally enhanced by heteroatom doping, inorganic salt doping[19] and surface functionalisation. The observed trend is that QY and PS vary interchangeably, particularly in bottom-up synthesised CDs, and monitoring this behaviour can be used as a means to elude the underlying PL mechanism. High QY is an essential consideration for any utile fluorescent material, and high PS and resistance to photobleaching are very important properties for long-term imaging applications.[20] A limitation to their use as fluorescent labels is the susceptibility of CDs to photo-induced changes. These changes can vary with the degree of surface passivation and presence of encapsulation layers. It is therefore important to understand the mechanisms of these changes to reduce these effects, particularly photo-induced reduction or photobleaching. In semi-conductor quantum dots (QDs), photo-induced changes to fluorescence have been attributed to irreversible photo-oxidation of the quantum core (resulting in a blue shift of the fluorescence) or the formation of quenching states at the surface (marked by a decrease in the QY). The encapsulation of QDs in silica layers has been used to address this issue. In contrast, limited investigations have been carried out into the improvement of CDs photostability as the majority of top-down synthesised graphitic CDs do not demonstrate issues of low PS. Bottom-up synthesised CDs however demonstrate vast inconsistencies of QY and PS.[6]

4.2.4. Surface Functionalisation and Targeting

Surface functional groups can be introduced to CDs covalently (by co-polymerisation, amide coupling, esterification) and non-covalently (by electrostatic interactions, π interactions, chelation etc) and have a significant effect on the PL behaviour, QY, biocompatibility and photostability. This can therefore be used to tailor CDs for specific functions such as drug delivery or cell targeting. [1,21]

Fluorescence imaging of CDs internalised into cells has shown that the CDs are mostly non-specifically taken up into the cytoplasm, cell-membrane or both, with some instances of nuclear internalisation[1,22] Surface functionalisation, such as ligand conjugation, has been used for site-specific targeting of specific cell types and cellular organelles. CDs functionalised with folic acid and transferrin have been used to target cancer cells (which over express receptors for these ligands), differentiate between cancer cells and normal cells, and differentiate between different cancer cells.[1,15] Yang et al. synthesised PEGylated CDs functionalised with a nuclear localization signal peptide (NLS) for excitation-dependent nucleus imaging.[23] In 2016, they expanded this work for the targeted delivery of Doxorubicin for cancer therapy.[24] Chen et al used goat antimouse

IgG conjugated-CDs to image microtubules in A549 cells[25], and several groups have reported the use of triphosphonium for targeted bioimaging of mitochondria.[26–29]

4.2.5. Encapsulation

Although CDs have been used as delivery agents for a variety of biomolecules including drugs[24,30], nucleic acids[31,32], and metallic nanoparticles[33], there has been less focus on the encapsulation of CDs within compartments and/or organic frameworks to enhance their biocompatibility and/or photostability. In contrast, studies into QDs encapsulation have been carried out in a variety of molecules such viral capsids[34], block co-polymers[35] and surfactant/lipid micelles[36,37] to address the issue of biocompatibility, as well as encapsulation within layers of silica to enhance their PS.[38,39]

Where CDs are concerned, the issue of biocompatibility is somewhat less notable due to their low-cytotoxicity and much of the focus of encapsulation has been to combine the PL properties of CDs with an encapsulating material to tailor and/or aid its function for a specific application. Host-guest complexation of CDs inside porous materials such as metal organic frameworks (MOFs) and porous protein crystals has been carried out to develop a new class of bio-hybrid luminescent materials. England et al. (2015) utilised the crystallographic array of solvent channels within lysozyme single crystals as macroscopic templates for the in-situ synthesis of CDs. This resulted in the formation of tuneable, multi-colour, luminescent host-guest crystal-CDs composites. [40] Lin et al. (2014) encapsulated PEG-capped CDs into zeolitic imidazolate framework (ZIF-8) materials. The combination of the selective sensing and PL of the CDs with the selective adsorption of the MOFs was used to generate highly luminescent MOFs capable of acute sensing and targeting of analytes for chemical sensing applications.[39] Encapsulation has also been used to enhance the properties of CDs, namely their photostability, and resistance to thermal degradation.

Vassilakopoulou et al. (2017) encapsulated hydrophilic CDs into spherical MCM-41 nanoparticles to synthesise a hybrid material via directed sol-gel synthesis. The hybrid mcm-CD matrix retains the PL of the CDs and is protected by the porous matrix from thermal degradation up to temperatures of 550ºC.[41] This work describes the encapsulation of of N CDs and NS CDs into silica colloidosomes (previously discussed in Chapter 2.0 of this thesis) and coacervates, to investigate the sequestration of CDs and effects on their PS for potential applications in bio-imaging and targeted delivery.

4.2.6. Coacervates

Coacervates are membrane-free, spherical liquid-liquid assemblies, resembling an emulsion without a stabilising agent. These particles can possess nanoscale and microscale dimensions. The coacervate micro-droplets self-assemble by liquid-liquid phase separation from precise stochiometric mixtures of oppositely charged polyelectrolytes in aqueous media to form molecularly dense membrane-free droplets. They can be prepared using a variety of highly charged small molecules, mixed with oppositely charged polymers, peptides or polypeptides. The coacervates are able to sequester components such as dyes, enzymes and nucleotides, and as a result have been developed for use as carriers for small molecules, proteins and drugs due to their high loading capacity, retention of the bioactivity of the encapsulated species and stability over a wide range of temperatures and pH.[42–44]

Complex coacervation is essential to the formation of coacervate droplets. It is generally agreed that this process takes place by two steps. F irst is the formation of coacervate droplets. This process is governeded by the associative interactions that take place when two oppositely charged polymers or macromolecules are mixed. The electrostatic interaction between opposite charges towards neutralisation must be strong enough to result in a liquid-liquid phase separation (second step of coacervate formation) but not too strong such as to cause precipitation into a solid-liquid phase. The formation of coacervate droplets occurs as a result of multiple force interaction and balance. These forces are influenced by the solubility of the free polyelectrolyte molecular species compared to that of the molecular species bound to the coacervate microdroplet complex, the interaction potential between the polyelectrolyte molecular species, the hydrophobic effect and the change in solubility of the complex as a function of its size. [42,44–46]

The second step is of phase separation into a liquid-liquid phase that exists in thermodynamic equilibrium with the solvent. The two liquid phases which exist are the polymer rich, viscous and dense coacervate microdroplet phase and the polymer-sparse supernatant phase. The formation of coacervate microdroplets occurs first by the formation of the coacervates followed by liquid-liquid phase separation. The liquid-liquid phase separation results in an increase in entropy, as counter-ions are released into the solvent during the formation of the coacervate microdroplet complex. [42,44–46]. The enthalpic and entropic contribution can be described by Gibbs' free energy equation. (4.1)

$$\Delta G = \Delta Hm - T\Delta Sm \qquad (4.1)$$

In this work, a mixture of cationic poly diallyldimethyl ammonium chloride (PDDA) with anionic ATP was used to prepare coacervate microdroplets in water and encapsulate N CDs and NS CDs, which were synthesised by the mechanism described in Chapter 3. The Coacervate-CDs were assembled into a two-dimensional array by a combination of in situ complex coacervation and an acoustic standing wave pressure field.[47] Complex coacervation is the process of droplet formation by liquid-liquid phase separation which is driven by the electrostatic attraction forces between oppositely charged polyelectrolytes and the increase in entropy following the release of small counter ions bound around the system and restructuring of surrounding water molecules. Figure 4.1 shows a schematic representation of the formation of the components of a coacervate microdroplet from two oppositely charged molecular species PDDA and ATP which were used in this work.

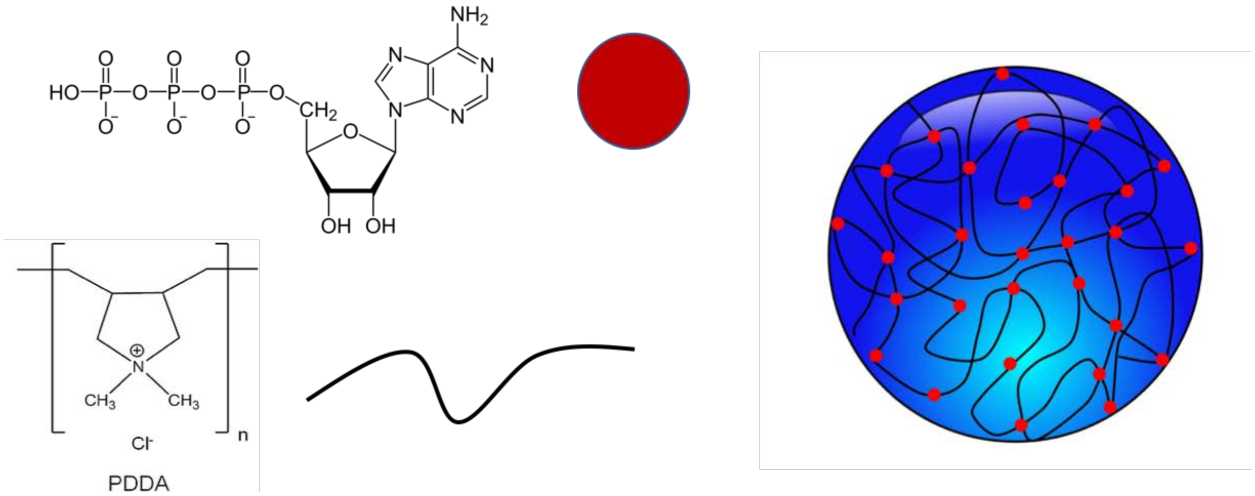

Figure 4.1: Components of ATTP/PDDA coacervate microdroplets (PDDA, positively charged, black line) (ATP, negatively charged, red sphere). [46]

4.2.7. Acoustic Trapping

Acoustic trapping devices, commonly referred to as ‘sonic tweezers’, offer a non-invasive, non-contact method for immobilising particles in fluid systems with a high degree of control and flexibility.[48] This has enabled acoustic trapping to be applied across a broad range of biotechnology studies.

Acoustic trapping has been used in particle studies to investigate the stability and morphology of microparticle agglomerates.[49] Particle and cell manipulation using acoustic trapping is being investigated for self-assembly and segregation in tissue engineering[50], particle trapping in microfluidics systems to construct non-contact bio-assays[51], as well as the control of nucleation and growth of colloidal crystals.[52] The ability to trap a fixed pattern of cells is being investigated for lab-on-a-chip applications with foreseen prospects in electronics and biosciences. [48,53] The three-dimensional differential trapping of cells and particles has been used to facilitate cell-particle interaction and cell-culture studies,[54] and enhance bioassays by reducing the time needed for cell clustering and creating non-contact arrays.[6,7,48] Nichols et al. (2018) utilised acoustic trapping and stimuli-responsive complex coacervation to fabricate micropatterned dipeptide hydrogels, containing functional components (enzymes, molecular dyes and oligonucleotides) which were spatially organised within the hydrogel.[45]

Simpler devices based on the use of acoustic forces, such as the flow cytometer cell-characterization system developed by Applied Biosystems, have already been realised as commercial products.[50] Seeding particles have also been used to extend the use of acoustic trapping into nano-scale objects for applications involving bacteria and viruses.[48,55,56] Other applications include targeted drug screening and delivery of trapped therapeutic cargo, and the use of acoustic radiation forces to induce cell lysis for both treatment and cell analysis.[54,57]

The principle of operation of these devices is the use of an acoustic radiation force which arises when a standing wave is generated in a microfluidic channel. [58] The vibration of the piezo-electric transducers is used to produce an acoustic wave. Linear wave propagation, and the presence of the acoustic standing wave throughout the fluidic volume (in this case water), is assumed.[59] The magnitude of the radiation force is proportional to the acoustic frequency.[51] A standing wave is generated as the sum of two independent travelling waves produced by each transducer. In a standing wave field, areas of maximum and minimum acoustic pressure are generated, where the minimum acoustic pressure is found at the nodal position of the standing waves. The variation of pressure creates a grid of trapping nodal planes. Dense microparticles are driven towards the nodes[51] in water, where they are trapped between regions of higher acoustic pressure[50,48]. [T]this is shown in Figure 4.2. Pressure nodes are located at a distance equal to λ/2. (Equation 4.2)

$$\lambda = \frac{C\ (speed\ of\ sound\ in\ water)}{f\ (frequency)}$$

Equation 4.2

The trapping pattern is fixed, adjusting to changes in the voltage and frequency of the signal supplied to the transducers and dependent on the device geometry. The phase and amplitude of the counter propagating waves can be changed independently.[50] Changing the phase difference of the counter propagating waves, by changing the excitation signal frequency of the piezo-electric transducers, can alter the nodal position of the standing wave that results.[60] The device design takes into consideration reflections produced within the system, and therefore transducers selected are acoustically matched to the fluid in the trapping chamber, which in this case is water.[58]

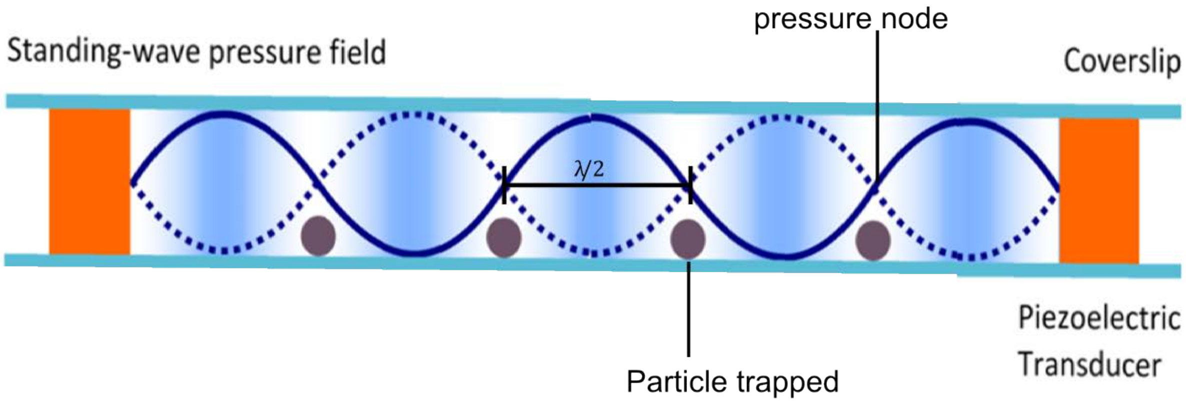

Figure 4.2: Schematic of device used with transducers (orange) aligned opposing each other. Transducers emit counter-propagating waves (solid and dashed blue lines). The sum of the two counter-propagating waves is a standing wave. Micro-sphere particles (grey spheres) are trapped in pressure nodes at distances equal to λ/2. Bottom and top cover slips make the device water tight. Image adapted from Bassindale et al. [61]

Acoustic trapping can be used for the spontaneous assembly of PDDA/ATP coacervates within a 2D array as demonstrated by Tian et al. (2016).[47] This is achieved by a combination of an acoustic standing wave and in situ complex coacervation. Primary coacervate droplets coalesce at the acoustic pressure node, which results in the formation of 2D micro-droplet arrays, whereby the droplet size and spacing can be adjusted by modulating the acoustic field and/or coacervate composition. Figure 4.3 shows a schematic representation of the acoustic trapping device and acoustic pressure distribution. The coacervate droplets are able to spontaneously sequester proteins, enzymes, and dye molecules etc. which can be achieved during or after coacervate assembly.[47]

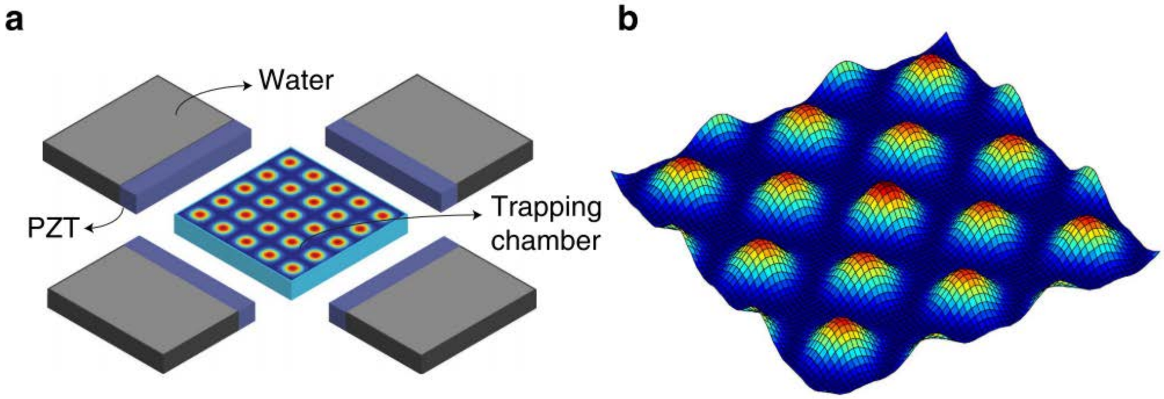

Figure 4.3: (a) schematic representation of the acoustic trapping device where four piezoelectric transducers (PZT) are arranged around a square chamber containing the colloidal particles. The four PZT elements are driven as 2 pairs. (b) Simulation of the acoustic pressure distribution generated in the chamber, high pressure (red), low pressure (blue). The acoustic pressure gradient causes the coacervate microdroplets to settle at the acoustic wave pressure nodes (blue). Figure Adapted from Tian et al. (2016)[47]

4.3. Materials and Methods

4.3.1. Imaging Cells with CDs

Imaging CDs within HeLa (Human cervical carcinoma cell line) cells was carried out in collaboration with Dr Monika Jakimowicz (BCFN). 30,000 HeLa cells were seeded in a confocal dish for 24 hours and changed to a basal MEM before the imaging experiment. 2 ⌠L of N CDs solution was added to the cells. These were incubated for 2, 5 and 7 hours. Images were taken using Confocal Widefield 6 microscope (Leica DMI6000 inverted epifluorescence microscope, Wolfson bioimaging suite, University of Bristol). Images were recorded following incubation. Samples were only illuminated during imaging.

4.3.2. Cytotoxicity Experiments

The cytotoxicity experiments were carried out in collaboration with Diego Hernandez Garcia (BCFN). HeLa were grown in Dulbecco's Minimal Essential Medium (DMEM) with low glucose (1 g/L). All growth media were supplemented with antibiotic-antimycotic (Anti-Anti) agents and 10% fetal bovine serum (FBS). Confluent cultures (80% or less) were detached from the surface using trypsin (Tryp LE Express) and plated at 5×10^3 cells/well in 96-well plates. Cell culture media and additives were purchased from Invitrogen, Life Technologies.

The influence of N CDs and NS CDs on HeLa cells was evaluated after 24 h of exposure and analysed with calcein and AlamarBlue assays. Cell survival was quantified by measuring calcein fluorescence. The fluorescence retained within live cells only. Changes in cell metabolism were assessed using AlamarBlue (AB, Life Technologies). HeLa cells were incubated with 0-1 mg/mL of NCDs for 24 h. Each experiment was repeated at least in triplicate in medium with reduced FBS (5%). Starosporine (1 µM/mL, Enzo Life Sciences) was used as a positive control. After 24 h, the plates were washed with PBS, and AB (5 % solution) and calcein (3 µM) were added in medium without FBS. After 1 h of incubation, the fluorescence of both dyes was read using a plate reader (BMG Labtech CLARIOstar) (AB λ_{ex} = 545 nm, λ_{em} = 590 nm, calcein λ_{ex} = 494 nm, λ_{em} = 517 nm). Results were expressed as percentages of the control and plotted against analyte concentration (in mg/mL).

4.3.3. Colloidosome CDs

N CDs and NS CDs were encapsulated into colloidosomes. The synthesis of CDs solution was carried out as described in Chapter 3.0 and the pH of the CDs solution was adjusted to pH 7.69 (to increase the cross-linking efficiency). Colloidosome-CDs were prepared by adding 100 µL of CDs solution to 2mL of (10mg/mL) silica-dodecane suspension. The suspension was then shaken by hand for 30 – 60s. The colloidosome-CDs were cross-linked using TMOS and extracted into water as described in Chapter 2.0, with the adjustment of the volume of TMOS added, whereby 20 µL and 100µL of TMOS were added to the colloidosome-CD emulsion in separate experiments. Samples were imaged using a Fluorescence Optical Microscope (Leica DMI3000B Fluorescence Optical Microscope). A photobleaching experiment was designed to model the PS of N CDs encapsulated in colloidosomes. N CDs were chosen over NS CDs due to their superior PS as observed in Chapter 3.0. The photobleaching experiment was carried out by illuminating the N CDs colloidosomes cross-linked with TMOS and extracted into water, under the fluorescence microscope laser at 100% power at λ_{ex}= 340-380 nm, for a period of 130 minutes. Images were taken every 10 minutes to investigate the fluorescence intensity of the CDs colloidosomes and observe any changes to their structure or morphology over time.

4.3.4. Acoustic Trapping of Coacervate-CDs

4.3.4.1. Acoustic Trapping Device

The acoustic trapping device used was designed and fabricated by Dr Liangfei Tian. The device was made form polyethylene terephthalate (PET), and consisted of a single square sample chamber, surrounded by four piezoelectric transducers (PZT) arranged as two orthogonal pairs. The PZT (Noliac, NCE 51, L15 x W2 x T1 mm) were attached to the back of the square sample chamber by an adhesive (Marabo Fixogum). A glass coverslip was attached by an adhesive to the bottom of the device, the top half was left open for sample injection. Opposing transducers were wired in parallel to a signal transducer (Agilent 33220a-001) and each connected to an oscilloscope (Agilent DSOX2014A). A schematic of the device is shown in Figure 4.4.[47]

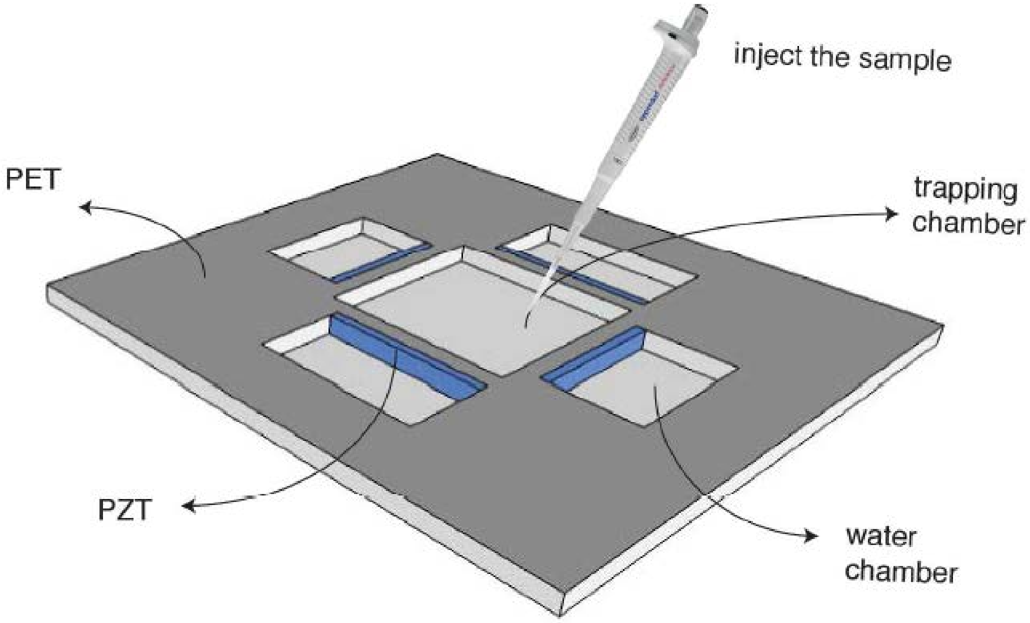

Figure 4.4: Schematic of the acoustic trapping device, designed and fabricated by Dr Liangfei Tian, showing the location of the square sample chamber, PZT and water chambers. Not to scale. Image adapted from supplementary information of Tian et al. 2016.[47]

4.3.4.2. Preparation of Coacervate-CDs Microdroplet Arrays

The CD-containing PDDA/ATP coacervate micro-droplet arrays were prepared by the addition of an aqueous solution of ATP (100 μL, 50 mM, pH 7) to a mixture of PDDA and CDs (1 mL, 5 mM monomer, 100-200 kDa, pH 7) in the presence of the two orthogonal acoustic standing waves generated from opposing transducer pairs operating at 6.76/6.78 MHz (10 V). The mixtures were stirred to ensure homogeneous formation of the coacervate droplets in the square chamber. After continuous coalescence of primary coacervate droplets over a period of 30 mins, a periodic 2D array of the CD-containing PDDA/ATP coacervate micro-droplet array was formed. The coacervate-CDs retained their position and structural integrity throughout the experiment.

The device was placed under the fluorescence optical microscope (Leica DMI3000B Fluorescence Optical Microscope). The acoustically trapped coacervate-CDs were excited using the fluorescence optical microscope laser at λ= 355- 425 nm under continuous illumination over a period of one hour. The mean fluorescence intensity was measured every ten seconds and the data was fit to an exponential decay function to determine the rate of fluorescence decay.

4.4. Results and Discussion

4.4.1. Imaging Cells with N CDs

HeLa cells incubated with N CDs for 2, 5 and 7 hours were imaged by Monika Jakimowicz (Figure 4.5). Blue fluorescence observed in the cells is due to the presence of CDs. This is evident from the contrast with the control experiment in which cells incubated under the same conditions in the absence of N CDs do not fluoresce. N CDs solution appears to have been taken up within the cytoplasm of the cell, with a relatively homogenous distribution throughout the cell volume. However further cellular trafficking and internalisation studies are required to identify the exact location and cellular fate of the CDs. Calceine dye staining of the cells confirms cell viability (indicated by the green fluorescence) and cells appear to be healthy, however AlamarBlue assay (to investigate changes to cellular metabolism) is required to confirm this. The cells were only illuminated at the time of imaging and therefore there is no indication of the photostability of CDs inside cells, and whether or not they photobleach under illumination. Further studies into the photostability of CDs incubated into cells are required to investigate this.

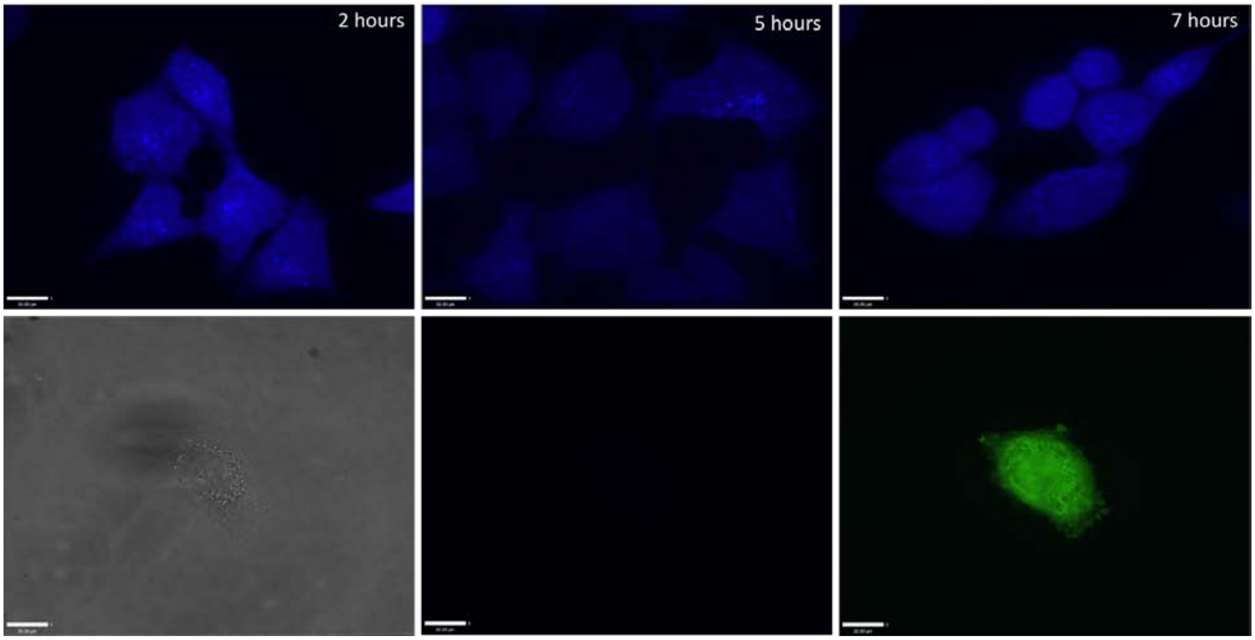

Figure 4.5: Widefield confocal images of HeLa cells incubated with N CDs after 2, 5 and 7 hours of incubation (top). Control samples not incubated with N CDs (bottom) from left to right: Brightfield image, widefield image, cells stained with calcein dye. Scale bar = 22 µm.

4.4.2. Cytotoxicity Experiments

Preliminary cytotoxicity experiments were carried out with N CDs and NS CDs using a HeLa cell line, and the influence of NCDs (Figure 4.6) and NS CDs (Figure 4.7) on HeLa cells was evaluated after 24 h of exposure and analysed with calcein AM (cell survival) and AlamarBlue (changes in cell metabolism) assays as described in the 'Materials and Methods' section of this chapter. The normalised fluorescence was plotted against the concentration of CDs in mg/mL.

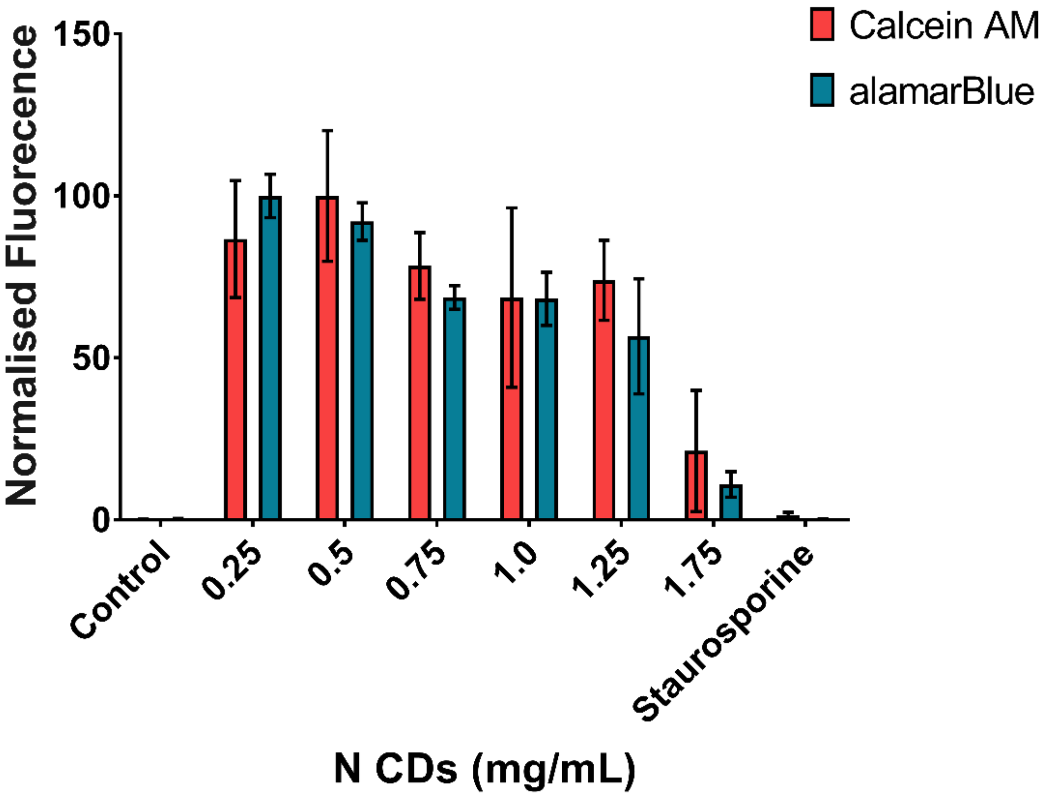

Figure 4.6: Cytotoxicity of N CDs introduced to HeLa cells after 24 hours of exposure. Normalised fluorescence plotted against the concentration of N CDs. Calcein AM assay (pink), alamarBlue (blue).

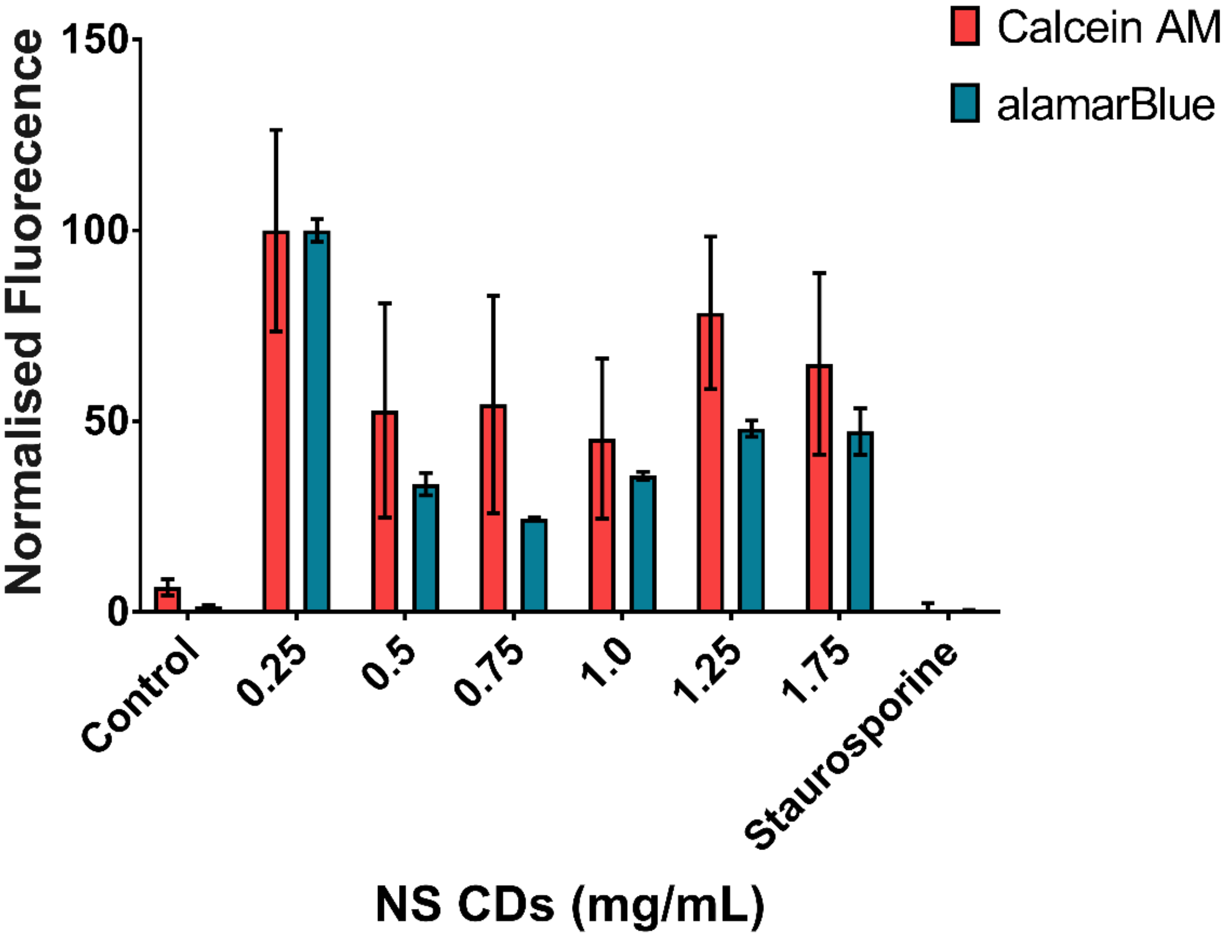

Figure 4.7: Cytotoxicity of NS CDs introduced to HeLa cells after 24 hours of exposure. Normalised fluorescence plotted against the concentration of N CDs. Calcein AM assay (pink), alamarBlue (blue).

N CDs had an overall less cytotoxic effect on the HeLa cells than NS CDs. N CDs demonstrated higher cell viability (normalised fluorescence of calcein AM) and cell metabolism (normalised fluorescence intensity of alamar Blue). Less standard deviation (represented by the margins of error) was observed for N CDs than NS CDs. N CDs demonstrated a consistent trend of reduced cell viability and cell metabolism as the concentration of CDs was increased. T here was no discernible trend observed for N S CDs.

The results from the preliminary cytotoxicity studies of N CDs and NS CDs were not considered reliable in isolation due to several issues with the results. Firstly, the issue with the control experiment whereby the survival rate was even lower than that of the CD-incubated cells. Secondly, the high margin of error observed particularly in the investigation with NS CDs and lack of discernible correlation between cell survival and CD concentration made the results much less reliable. Thirdly, the cell internalisation and trafficking studies would be required to determine if the CDs the internalisation pathway of the cells. These results were therefore analysed and used as a guide for the design of more extensive cytotoxicity experiments. It was decided therefore to proceed with more extensive cytotoxicity investigations with N CDs only (Figure 4.8) as they yielded much better preliminary results.

Cytotoxicity results were repeated with N CDs (Figure 4.8). HeLa cells were incubated with up to 1 mg/mL of NCDs for 24 h, each concentration including the control was tested in HeLa 1, HeLa 2, HeLa 3 and HeLa 4. Calcein AM and alamarBlue assays were used as described. Staurosporine was used as a positive control, which ensures cell death via intrinsic apoptotic pathways.[62]

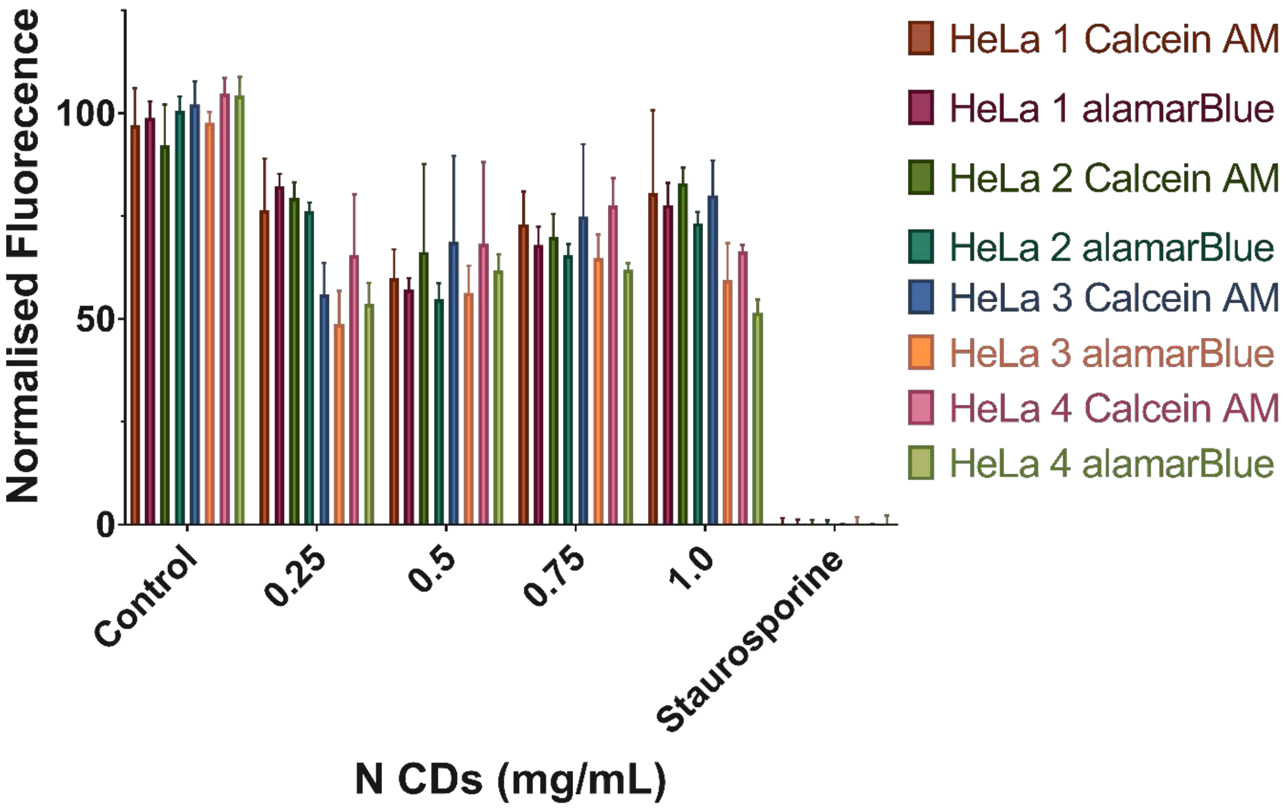

Figure 4.8: Cytotoxicity of N CDs introduced to HeLa cells after 24 hours of exposure Normalised fluorescence intensity plotted against concentration of N CDs (mg/mL)

The HeLa cells were incubated with N CDs between 0.25 – 1.0 mg/mL. The cells appear to survive and maintain metabolic function with up to 1.0 mg/mL of N CDs. The cell survival and metabolism appeared lower than that of the control, which is to be expected. There is no discernible trend between an increase in the concentration of CDs and a change in cell survival and/or metabolism as there is significant variation between different HeLa samples (samples 1 – 4), which precludes any definitive conclusions regarding the upper cytotoxicity limit of N CDs. Overall, it appears that the HeLa cells retain their viability and cellular metabolic activity after 24 hours of exposure to N CDs up to a 1.0 mg/mL of N CDs. These results are highly promising and would indicate that the N CDs are effectively non-cytotoxic and could potentially be used for bioimaging applications.

Further investigations into the cellular-uptake pathway and fate of the N CDs inside the cells is required to provide a full picture of the N CDs' cytotoxicity.

As previously mentioned, CDs are generally reported to be non-toxic in vitro.[3] The photostability of CDs in solution has been discussed in Chapter 3, and photostability of CDs encapsulated is discussed later in this chapter. A plethora of literature investigating the cytotoxicity of various types of CDs on a variety of cell lines, and the observed effect of surface passivating agents on the degree of cytotoxicity is available. [17,63,64]. Therefore, investigations using CDs of a similar nature to those synthesised (N-doped bottom-up synthesised CDs) on the same cell line (HeLa cells) have been selected in order to form a relevant comparison of these results with the literature. Additionally, as N CDs were incubated without further passivation or surface modification post-synthesis, only 'raw' (i.e CDs with no surface passivating agents) or N-doped CDs are quoted. Table 1.0 summarises the literature review.

Table 4.1: Summary of literature review of cytotoxicity studies of CDs incubated with HeLa cells

Type of CDs	Highest CD concentration used	Incubation Time /hrs	Assay	Changes to cell viability	Reference
Single component CDs made from potatoes by hydrothermal synthesis	75µg/mL	24	MTT	No significant cell viability decrease below 20%	[65]
Microwave synthesised Cl/N doped CDs using xylitol in the presence of HCL and EDA	1000 µg/mL	24	MTT	No cytotoxicity observed up to 100 µg/mL Slight cytotoxicity observed up to 1000 µg/mL	[66]
Oatmeal-derived CDs synthesised by hydrothermal treatment	2 mg/mL	48	CCK	Up to 90% cell viability retained	[67]
Hydrothermal CDs derived from potato	500 µg/mL	24	MTT	Survival rates > 95%	[68]
N CDs obtained from a one-step solvothermal method using graphene oxide and dimethylamine as a nitrogen source	400 µg/mL	24		~80% viability at 400 µg/mL	[69]
CDs derived from the microwave irradiation of different amounts of glutaraldehyde and poly(ethylenimine)	400 µg/mL	24	MTT	>90% viability at 400 µg/mL	[70]
N CDs obtained from the oxidised heating of N-containing amino acids (L-DOPA, L-arginine and L-histidine)	200 µg/mL	48	MTT	No decrease in cell viability observed	[71]
CDs obtained from the hydrothermal treatment of urea and p-phenylenediamine	200 µg/mL	52	MTT	No decrease in cell viability <10% observed	[72]
N CDs prepared by hydrothermal treatment of cocoon silk	80 µg/mL	24	MTT	Cell viability declined by <10%	[73]
CDs obtained from microwave pyrolysis of citric acid in the presence of tetraoctylammonium bromide	5 mg/mL	24	Tryphan Blue	Cell viability of >95% retained	[74]

Our investigation into cell viability utilised calcein AM and AlamarBlue assays to quantify the cell survival and changes in cell metabolism respectively. The concentrations of N CDs used were between 0-1 mg/mL which is considerably high compared to the concentrations used by other groups conducting similar investigations (Table 1.0). Cell viability and changes to the metabolism observed are not entirely consistent in trend as mentioned, however the HeLa cells retain a cell viability of over 50% after 24 hours of incubation with N CDs of concentrations up to 1 mg/mL. This is highly promising considering it surpasses the upper limit of the majority of cytotoxicity experiments. However as mentioned, further investigations are required in order to obtain a true picture of the cytotoxicity profile of these CDs. Further work may include: post-synthesis surface modification and/or functionalisation of the CDs, which could be investigated to reduce the cytotoxicity and enhance the biocompatibility of the CDs as well as ensure cell and/or organelle-specific targeting. Investigations of the CD cytotoxicity with other cell lines (both cancerous and healthy) and adjusting the synthetic process (particularly the amount of N doping agent used) to reduce the cytotoxic effects of the CDs as much as possible.

4.4.3. Carbon Dot Encapsulation

4.4.3.1. Colloidosome-CDs Encapsulation

N CDs and N S CDs encapsulated in colloidosomes (CDs – colloidosomes) were prepared, cross-linked with TMOS, and extracted into water, as described in the 'Materials and Methods' section. Optical fluorescence microscopy of N CDs colloidosomes and NS CDs colloidosomes (Figure 4.9) were taken at λ_{ex}=340-380 nm. N CDs colloidosomes appear brighter (higher fluorescence intensity) than NS colloidosome CDs under the same illumination conditions. This is in line with the characterisation of CDs outlined in Chapter 3.0, whereby N CDs demonstrated a higher QY and photostability than NS CDs. The CDs solution appeared to be retained well, with a homogenous distribution (appendix) within the cross-linked colloidosomes throughout the transfer and extraction into water. The NS CDs-colloidosomes demonstrated weak fluorescence intensity compared to N CDs-colloidosomes and completely photobleached within 10 minutes of illumination. The investigations were therefore carried forward using N CDs-colloidosomes only.

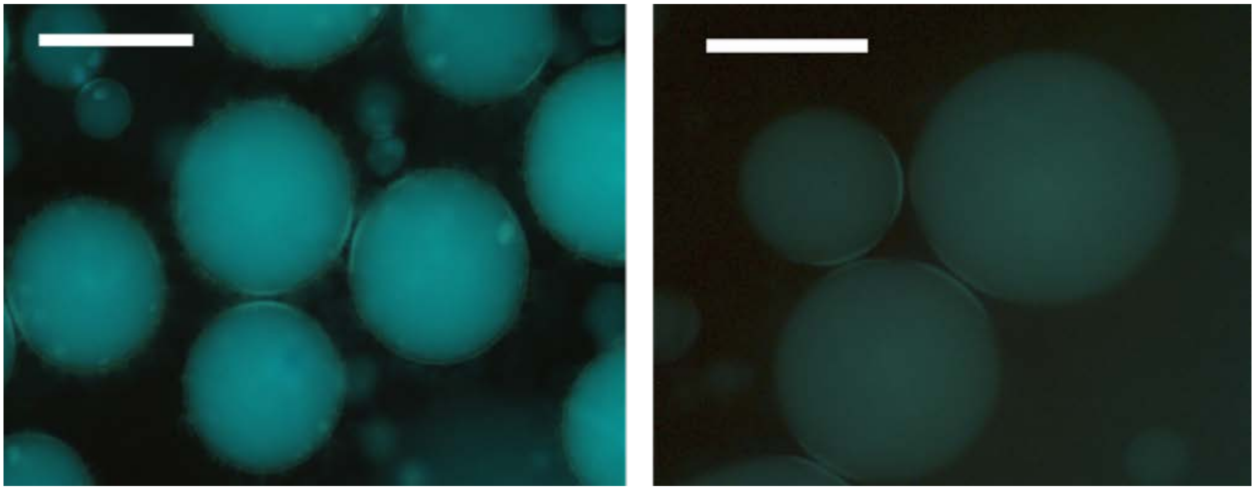

Figure 4.9: Fluorescence optical microscopy images of N CDs colloidosomes (left) NS CDs-colloidosomes (right) in water excited using the fluorescence microscope laser at λ_{ex}=340-380 nm. Scale bar = 200 µm

4.4.4. Fluorescence Decay Colloidosome- N CDs

4.4.4.2. Colloidosomes Cross-Linked with 20µL TMOS; Low Volume

A photobleaching experiment was carried out to investigate the fluorescence decay of the CDs colloidosomes and model their photostability. 50 µL of N CDS colloidosomes, previously cross-linked with 20 µLTMOS and extracted into water were pipetted onto a glass slide and illuminated under the fluorescence optical microscope for 130 minutes at λ_{ex} = 340 – 380 nm under continuous illumination at 100% laser power. Images were taken every in the same location in the sample every 10 minutes (Figures 4.10).

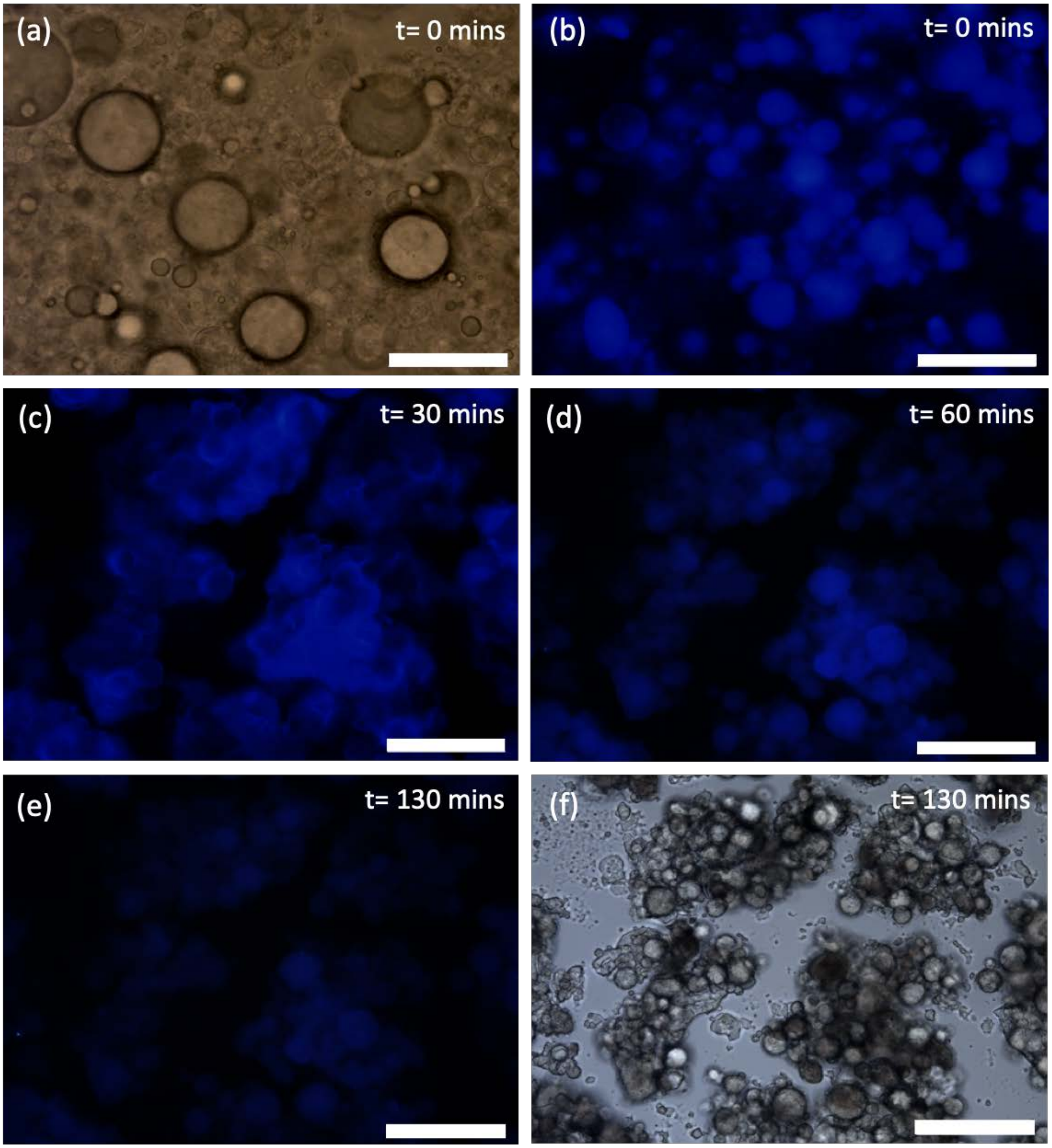

Figure 4.10: (a) fluorescence optical microscopy image of colloidosomes-N CDs illuminated at λ_{ex} = 340 – 380 nm a) Bright field image at t=0 mins, b) fluorescence image at t=0 mins, c) fluorescence image at t = 30 mins d) fluorescence image at t=60 mins e) fluorescence image at t= 130 mins, d) bright field image at t=130 mins. The scale bar = 100 µm.

The photobleaching experiment displayed some interesting results. The colloidosomes appeared to aggregate under illumination as well as dehydrate and collapse, with the silica membrane folding inwards. This type of dehydration under illumination has been observed before, where the aqueous solution inside the colloidosomes evaporates, causing the collapse of the colloidosome and inward folding of the ????. The aggregation or 'clumping' of colloidosomes however has not been observed. It appears that the colloidosomes clump together but retain distinct membranes as opposed to coalescing into larger structures. This aggregation or clumping made it very difficult to investigate the fluorescence decay of individual colloidosomes accurately and model the rate of decay and photostability of the CDs colloidosomes.

4.4.4.3. Colloidosomes Cross-Linked with 20µL TMOS; High Volume

In order to exclude the effect of dehydration - resulting in the collapse and aggregation of colloidosome-CDs - on the fluorescence decay, the experiment was repeated in a larger volume (250 µL) under the same conditions. The sample remained under constant illumination at λ= 340-380 nm and images were taken every minute for 1 hour (Figure 4.11) The increase in the volume of colloidosome-N CDs imaged reduced the dehydration effect observed in smaller volumes and significantly enhanced the rate of fluorescence decay observed. After 1 hour, the colloidosomes-N CDs remain intact which allowed for the rate of fluorescence decay to be quantified for individual colloidosomes. The rate of fluorescence decay was investigated by measuring the mean fluorescence intensity of individual colloidosome-CDs (Figure 4.11). The data was plotted against time and fit against an exponential decay function to model the fluorescence decay and photostability of the coacervate-CDs (Figure 4.12). The rate of fluorescence decay was measured between t = 8 mins and t = 50 mins, which was the time period identified where there was no movement of the colloidosomes between images taken. The N CDs-colloidosomes were shown to remain fluorescent after 1 hour of continuous illumination. The rate of fluorescence decay of colloidosome-CDs was 0.02541 ± 0.00246 min^{-1}, the exponential decay function is recorded in Table 2.0.

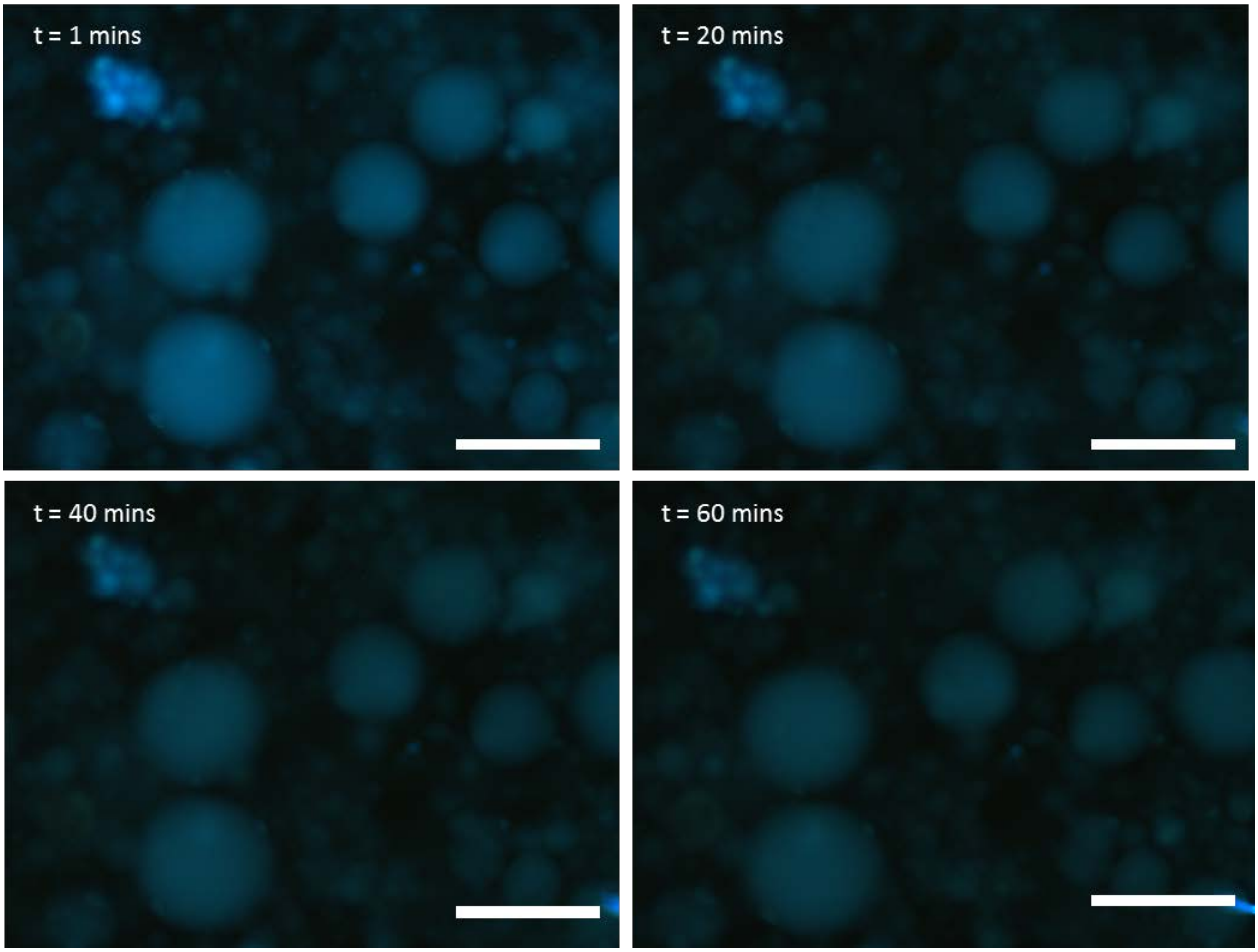

Figure 4.11: Fluorescence optical microscopy images of colloidosomes-N CDs illuminated at λ_{ex} = 340 – 380 nm at t= 1min, t=20 mins, t=40 mins and t=60 mins. Scale bar = 200 µm.

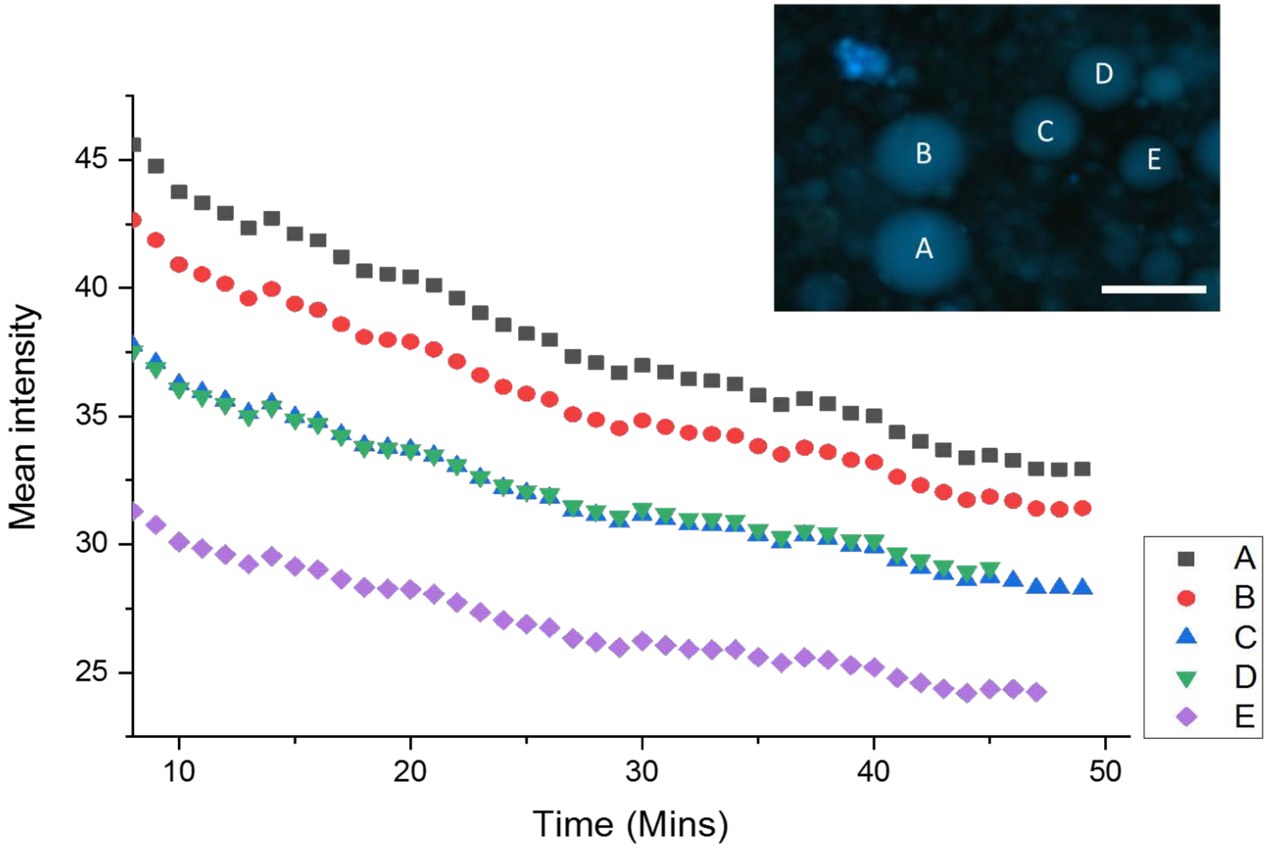

Figure 4.12: Fluorescence decay of colloidosomes-N CDs between t = 8 mins and t = 50 mins. Insert: Colloidosomes used to collect the fluorescence decay data labelled A to E. Scale bar = 200 µm

Table 4.2: Exponential decay function of colloidosome-N CDs

Model	ExpDec1
Equation	y = A1*exp(-x/t1) + y0
Plot	Mean intensity
y0	26.1991 ± 1.12746
A1	23.1105 ± 0.8399
t1	39.35554 ± 3.81137
Reduced Chi-Sqr	0.09076
R-Square (COD)	0.99348
Adj. R-Square	0.99314

4.4.4.4. Colloidosomes cross-linked with 100µL TMOS; High Volume

The fluorescence decay of N CDs-colloidosomes, previously cross-linked with 100 µL of TMOS and extracted into water was investigated. A large volume sample (250 µL) was pipetted onto a microscope slide which remained under constant illumination at λ = 340- 380 nm. Images were taken every minute for 1 hour (Figure 4.13). The N CDs-colloidosomes which were cross-linked with 100 µL of TMOS and extracted into water demonstrated considerable photobleaching compared to those cross-linked with only 20 µL under the same conditions. This effect is most likely caused by the encapsulated CDs rather than any change to the colloidosome membrane or dehydration of the encapsulated solution, as the colloidosomes appear to be intact without any collapse or aggregation observed. Using a higher volume of TMOS causes an increased production of methanol, which is a by-product of the TMOS cross-linking reaction, which can alter the composition of the encapsulated CD solution. Chapter 3 describes how the photostability CDs are sensitive to changes in the surface chemistry of the CDs, the increased production of methanol would therefore cause a change to the aqueous dispersion in which the CDs are suspended and affect the photostability of the CDs as observed.

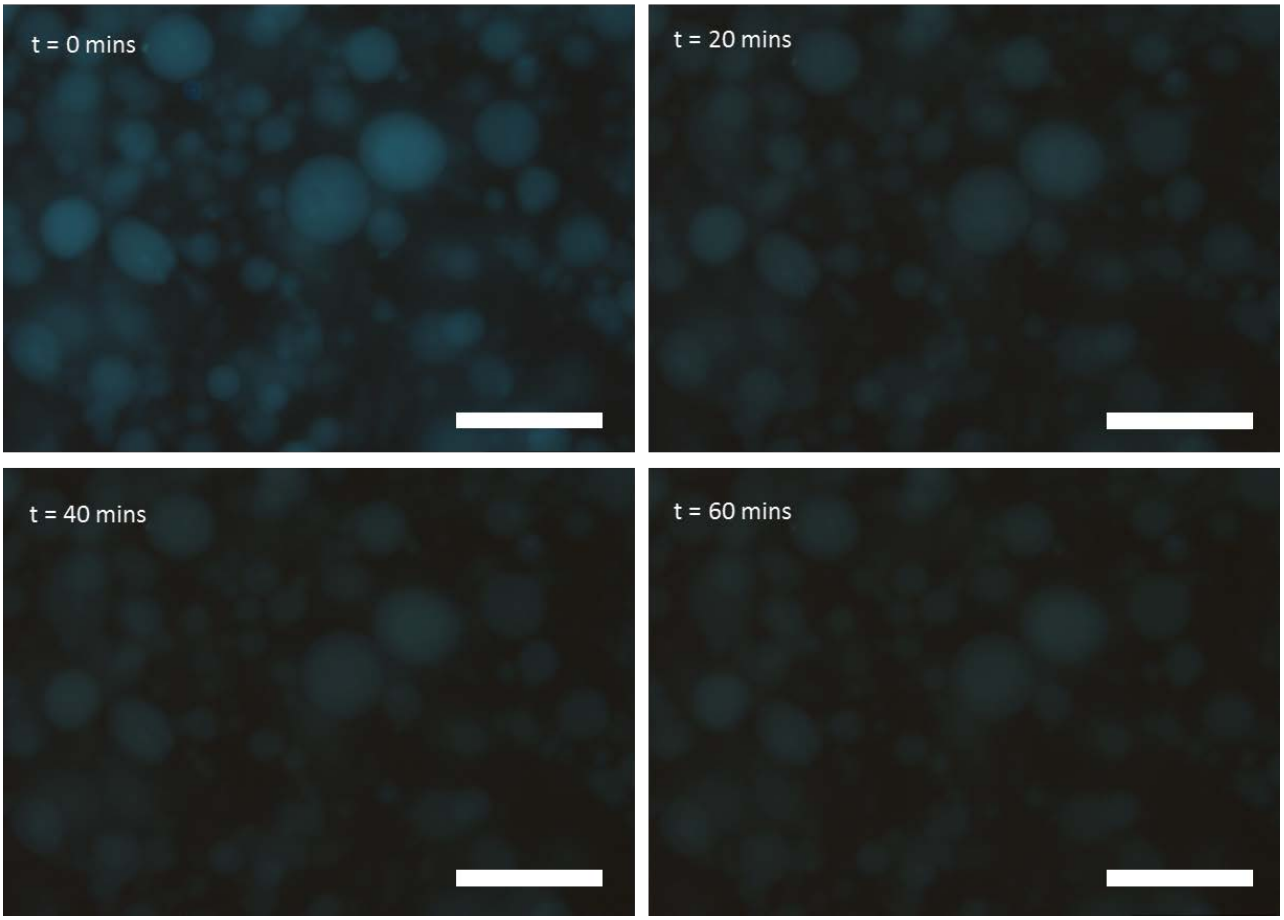

Figure 4.13: Fluorescence optical microscopy images of colloidosomes-N CDs illuminated at λ_{ex} = 340 – 380 nm at t= 1min, t=20 mins, t=40 mins and t=60 mins. Scale bar = 200 μm.

The results obtained from this investigation are very interesting and suggest that CDs can be successfully encapsulated within colloidosomes. These microcompartments may not be ideal for bioimaging applications due to the need for cross-linking to allow transfer into aqueous environments, which makes them highly non-biocompatible. They could however be explored for the construction of photocatalytic micro-reactors encapsulating CDs for spatially organised charge transfer reactions.[43,75,76]

Further investigations in to the encapsulation of CDs using coacervates was carried out. Acoustic trapping was used to immobilise the coacervates to prevent coalescence during investigations of the PS and fluorescence decay.

4.4.5. Acoustically-Trapped Coacervate-CDs

N CDs and NS CDs were encapsulated in coacervates and acoustically trapped by the mechanism described in section 2.3: ‘Acoustic trapping of coacervate-CDs’. Optical fluorescence microscopy was used to image the acoustically-trapped coacervate-CDs (Figure 4.14). The CDs solution was encapsulated within the coacervates with a homogenous distribution throughout (Appendix). N CDs coacervates had an average diameter of (39.2 μm ± 5.6), with a horizontal distance of (78.8 μm ± 7.2) and vertical distance of (78.2 μm ± 3.7) measured form the centre of each coacervate. NS CDs coacervates had an average diameter of (44.7 μm ± 5.8), with a horizontal distance of (78.9 μm ± 9.6) and vertical distance of (78.5 μm ± 4.4) measured form the centre of each coacervate.

The coacervate-CDs were continuously illuminated under the optical fluorescence microscope at λ_{ex}= 340 – 380 nm at 100% laser power. Images were taken at 10 second intervals over a period of 60 minutes. Figure 4.15 (N CDs-coacervates) and Figure 4.16 (NS CDs-coacervates) show images of a selected area of acoustically trapped coacervate-CDs over a period of 60 minutes under continuous illumination at λ_{ex}= 340 – 380 nm at 100% laser power, at 10-minute intervals. The rate of fluorescence decay was investigated by measuring the mean fluorescence intensity of individual CDs-coacervates. The data was plotted against time and fit against an exponential decay function to model the fluorescence decay and photostability of the CDs-coacervates.

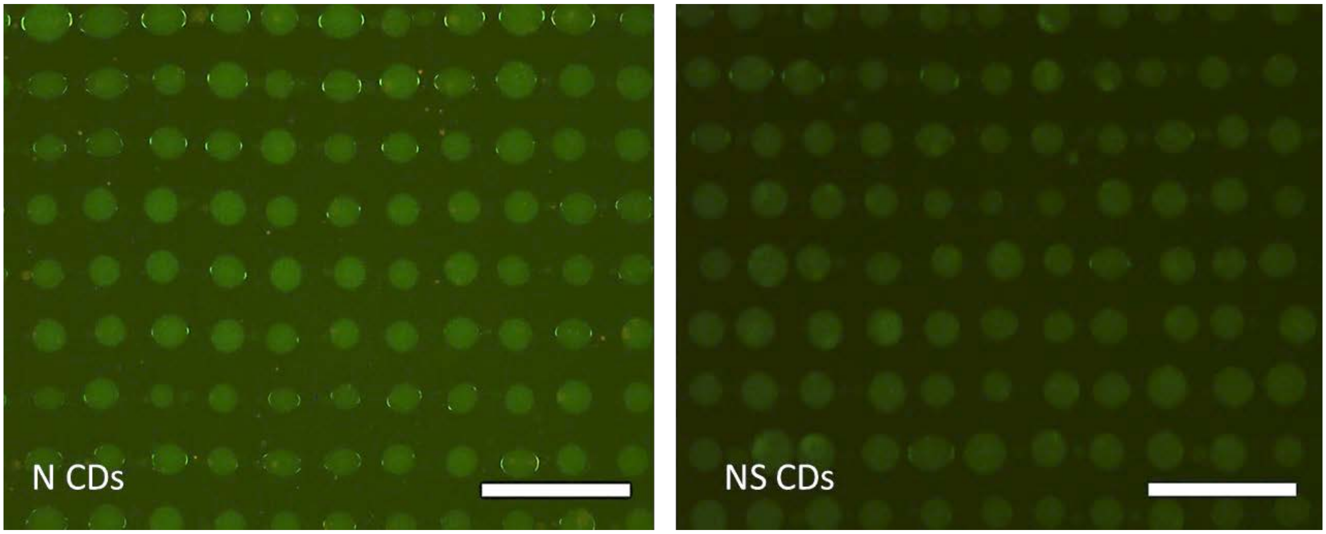

Figure 4.14: Fluorescence optical microscopy images of N CDs-coacervates (left) and NS CDs-coacervates (right) illuminated at λ_{ex}= 340 – 380 nm at 100% laser power. Scale bar = 200 µm

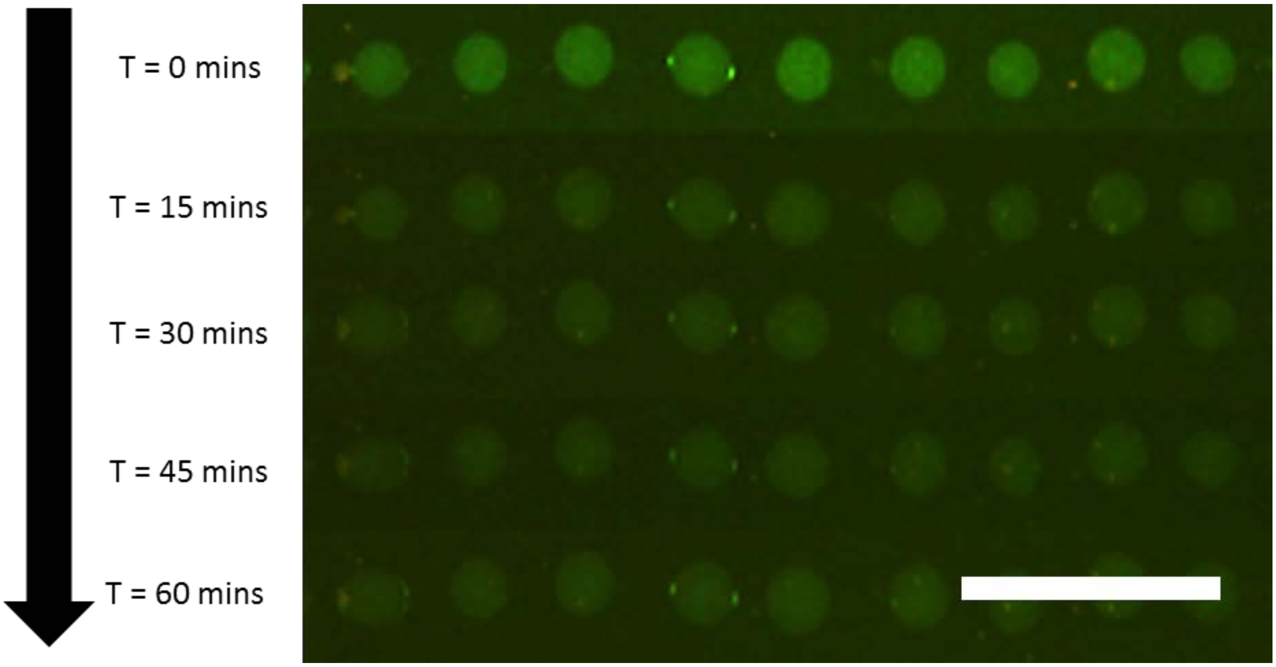

Figure 4.15: Fluorescence optical microscope images of a single row of acoustically-trapped N CDs-coacervates under continuous illumination at λ_{ex}= 340 – 380 nm at 100% laser power over a period of 60 minutes. Each row represents an interval of 15 mins. Scale bar = 200 µm.

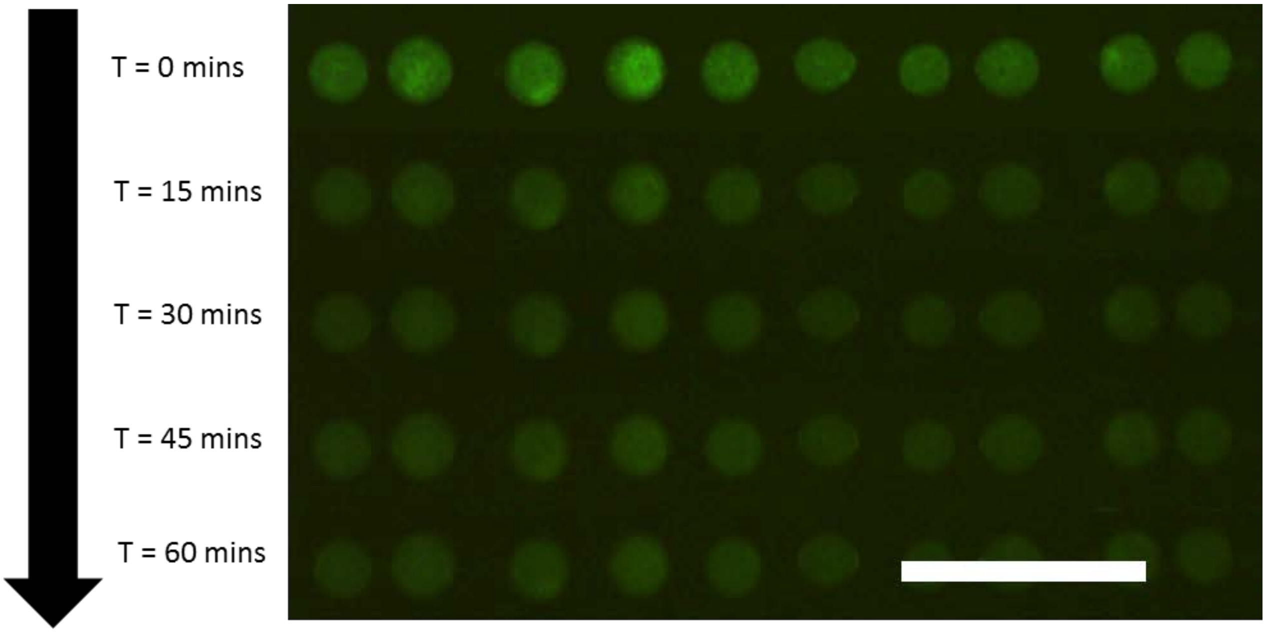

Figure 4.16: Fluorescence optical microscope images of a single row of acoustically-trapped NS CDs coacervates under continuous illumination at λ_{ex}= 340 – 380 nm at 100% laser power over a period of 60 minutes. Each row represents an interval of 15 mins. Scale bar = 200 µm.

Time lapse images taken of the selected area of coacervate CDs (Figure 4.15 and 4.16) show that that the coacervate-CDs retain their position within the pressure nodes of the acoustic trap. The coacervates retain their shape and structural integrity and there is no significant leakage of the sequestered CDs solution over time.

Acoustically trapped NS CDs-coacervates demonstrated a faster rate of fluorescence decay (0.00275 s^{-1}) than N CDs-coacervates (0.00195 s^{-1}), which is in accordance with results observed in Chapter 3. These describe the rate of fluorescence decay of the NS CDs in solution to be much faster than that of N CDs in solution. Both N CDs and NS CDs encapsulated in coacervates are not entirely photobleached after 1 hour of continuous illumination and can be seen to fluoresce despite the very small volume of CDs used.

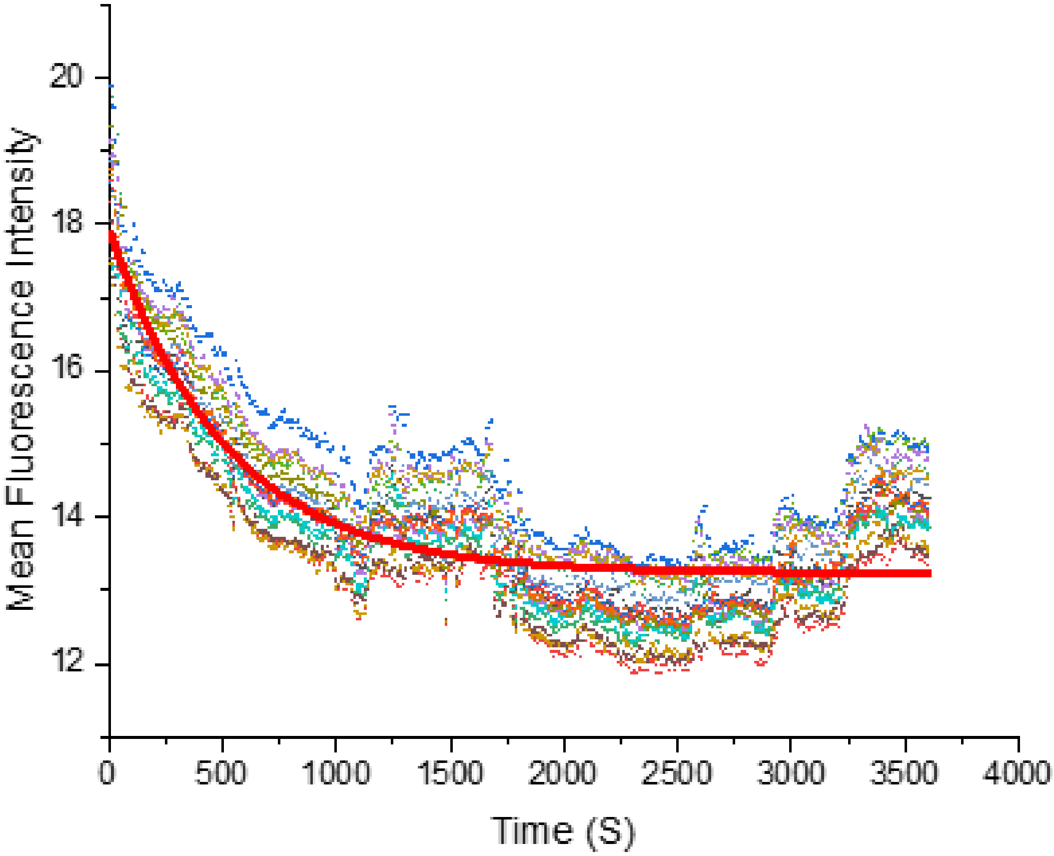

Figure 4.17: Fluorescence decay of acoustically-trapped coacervate N CDs with exponential decay fit

Table 4.3: Exponential decay function of acoustically trapped N CDs

Model	ExpDec1
Equation	y = A1*exp(-x/t1) + y0
Plot	Mean Fluorescence Intensity
y0	13.23857 ± 0.03834
A1	4.72229 ± 0.13706
t1	513.14911 ± 26.65975
Reduced Chi-Sqr	0.23169
R-Square (COD)	0.82915
Adj. R-Square	0.82819

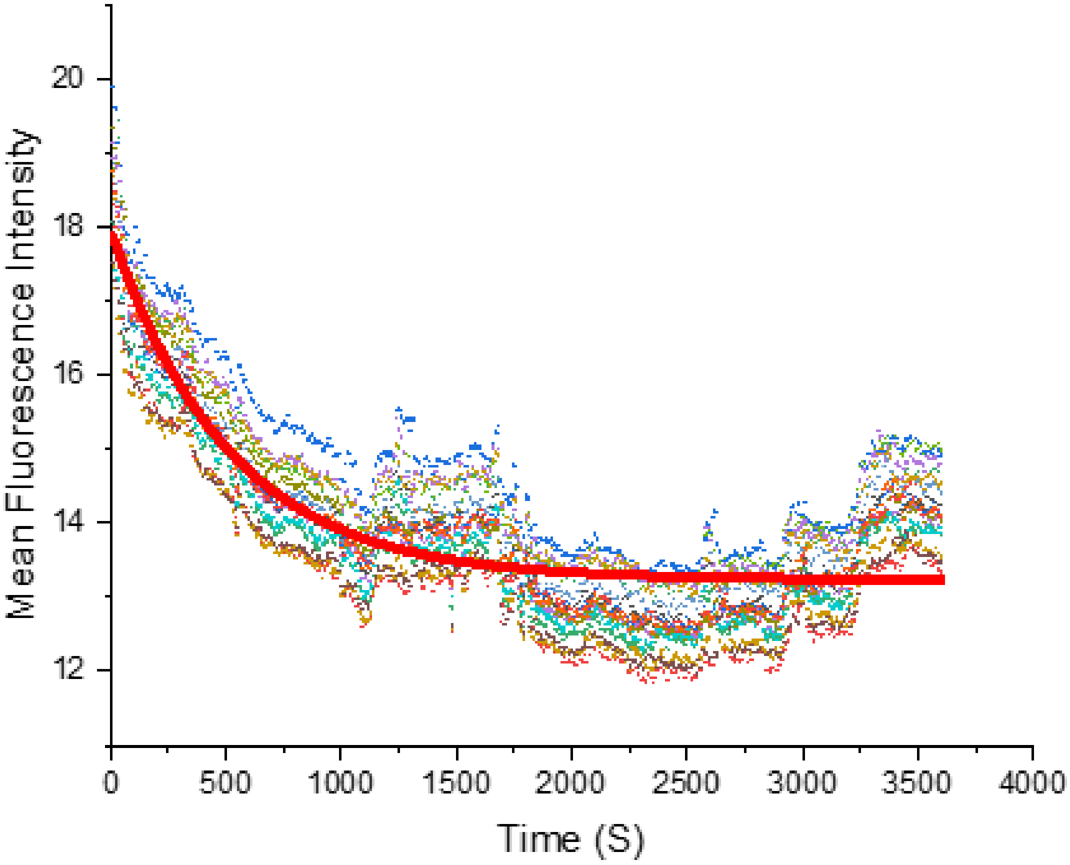

Figure 4.18: Fluorescence decay of acoustically trapped coacervate NS CDs with exponential decay fit

Table 4.4: Exponential decay function of acoustically trapped NS CDs

Model	ExpDec1
Equation	y = A1*exp(-x/t1) + y0
Plot	Mean Fluorescence Intensity
y0	13.23857 ± 0.03834
A1	4.72229 ± 0.13706
t1	513.14911 ± 26.65975
Reduced Chi-Sqr	0.23169
R-Square (COD)	0.82915
Adj. R-Square	0.82819

4.5. Conclusions and Further Work

Imaging of the cells with N CDs indicates that the cells can be successfully ‘dyed’ with N CDs. The CDs appear to be taken up into the cytoplasm of the cells. However, further investigation into the cellular uptake, trafficking and fate of the CDs after internalisation is required.

Preliminary cytotoxicity investigations of the CDs with HeLa cells demonstrated that the exposure of HeLa cells to N CDs resulted in higher overall cell viability and metabolism than NS CDs. HeLa cells retain a cell viability and cellular metabolism of over 50% after 24 hours of incubation with N CDs of concentrations up to 1 mg/mL. This concentration is significantly high compared to the concentrations of CDs used in bioimaging studies in the literature, as previously described. The lack of discernible correlation observed between an increase in the concentrations of N CDs used, and changes in cell viability or cellular metabolism across different HeLa cultures, can perhaps be attributed to the variation in the surface chemistry and size of CDs which can affect the internalisation and cellular trafficking of the CDs by HeLa cells.

Although variations in the results obtained from different HeLa samples prevent conclusions being drawn about the upper cytotoxicity limit, the N CDs are sufficiently non-cytotoxic to encourage further investigations into their use as bioimaging agents. Further work to expand on this work’s findings includes carrying out cytotoxicity experiments and intracellular trafficking studies on CDs solutions of different pH and zeta potential. Exploring different surface functionalising agents to enhance their biocompatibility and cellular uptake. Additionally, the PS and rate of fluorescence decay of CDs within cells remains to be considered. Surface functionalisation and adjustment of the dopants used in the synthesis process can be used to enhance their PS.

N CDs and NS CDs were successfully encapsulated into colloidosomes, with homogenous distribution throughout and retained their fluorescence activity throughout cross-linking and transfer into water. The Fluorescence decay of N CDs within colloidosomes was investigated. A high volume of the colloidosome-CDs dispersion was required to discount the effect of dehydration, which results in the collapse of the colloidosomes and loss of fluorescence. At low sample volumes, the CD-colloidosomes were observed to collapse and aggregate over time. This may be due to the in situ generation of methanol during the hydrolysis and condensation of TMOS which is used to cross-link the silica colloidosome membrane (as described in Chapter 2). The cause of aggregation of colloidosomes remains unclear, however it may be due to the generation of the alcohol.[77]

Using higher volumes of the colloidosome-CDs dispersions to evaluate the fluorescence decay demonstrated that the amount of TMOS used to cross-link colloidosomes has a significant effect on the PS of the sequestered CDs solution. This is likely due to the presence of methanol which is a by-product of the cross-linking reaction, and affects the surface chemistry of the CDs and therefore their PL behaviour. This would encourage further investigation into functionalising the silica nanoparticles to tune the PL behaviour of the encapsulated CDs solution, or use of different cross-linking agents which would enable the design of stimuli-responsive colloidosome-CDs such as light or changes to pH or temperature. CDs were successfully sequestered into coacervates and acoustically trapped in a 2D droplet array. The coacervate-CDs demonstrated slow fluorescence decay and retained their fluorescence after 1 hour of continuous illumination. Colloidosomes could not be manipulated by acoustic trapping due to the high density of these particles. Additionally, complex coacervation to sequester the CDs is required to take place in situ with the acoustic field in order to successfully pattern the CDs-coacervates. CDs solution behaves as the aqueous phase to assemble the water-in-oil colloidosomes which requires mechanical shaking to generate the spherical microcompartments which are dispersed in dodecane before they are cross-linked by TMOS and transferred to water. Dodecane is too viscous a solvent for the acoustic field to take effect.

As with colloidosomes, it is difficult to establish to what extent the PS of the CDs is improved by encapsulation. This is due to the absence of a valid control that can be used to compare the PS of the CDs as a function of encapsulation only. The encapsulation of the CDs solution within colloidosomes (and extraction into water) or coacervates alters the environment of the CDs dispersion, the surface chemistry of the CDs and therefore PL behaviour. It is therefore very difficult to identify the precise effect of encapsulation on PS and the mechanism by which it occurs.

Nevertheless, the ability to successfully sequester CDs within coacervates and manipulate them using an acoustic trap serves as an incredibly useful characterisation tool. The use of coacervates to encapsulate CDs is advantageous, not only to improve the photostability of CDs but also as a targeted delivery vehicle for CDs. Coacervates have already been used as vehicles for drug delivery,[44,45] and their use as encapsulating agents for CDs could be used to enhance their cellular uptake and considerably advance their application in the field of bioimaging and diagnostics.[20,27,30,46–48] In addition to bio-applications, acoustically trapped coacervate-CDs could be used to generate a photocatalytic array for light harvesting applications.[43,75,76]

4.6. References

1. Peng, Z. *et al.* Carbon dots: Biomacromolecule interaction, bioimaging and nanomedicine. *Coordination Chemistry Reviews* **343**, 256–277 (2017).
2. Wang, L. & Zhou, H. S. Green synthesis of luminescent nitrogen-doped carbon dots from milk and its imaging application. *Anal. Chem.* **86**, 8902–8905 (2014).
3. Wang, J. & Qiu, J. A review of carbon dots in biological applications. *J. Mater. Sci.* **51**, 4728–4738 (2016).
4. Sun, Y. *et al.* Quantum-Sized Carbon Dots for Bright and Colorful Photoluminescence. 7756–7757 (2006).
5. Wang, Y. & Hu, A. Carbon quantum dots: synthesis, properties and applications. *J. Mater. Chem. C* **2**, 6921 (2014).
6. Rakovich, A. & Rakovich, T. Semiconductor: Versus graphene quantum dots as fluorescent probes for cancer diagnosis and therapy applications. *J. Mater. Chem. B* **6**, 2690–2712 (2018).
7. Park, Y., Yoo, J., Lim, B., Kwon, W. & Rhee, S.-W. Improving the functionality of carbon nanodots: doping and surface functionalization. *J. Mater. Chem. A* **4**, 11582–11603 (2016).
8. Hill, S. A. *et al.* Three-minute synthesis of sp3nanocrystalline carbon dots as non-toxic fluorescent platforms for intracellular delivery. *Nanoscale* **8**, 18630–18634 (2016).
9. Kundu, A. *et al.* Facile approach to synthesize highly fluorescent multicolor emissive carbon dots via surface functionalization for cellular imaging. *J. Colloid Interface Sci.* **513**, 505–514 (2018).
10. Sharma, V., Tiwari, P. & Mobin, S. M. Sustainable carbon-dots: Recent advances in green carbon dots for sensing and bioimaging. *J. Mater. Chem. B* **5**, 8904–8924 (2017).
11. Wang, C. *et al.* Facile synthesis of nitrogen-doped carbon dots from COOHfunctional ionic liquid and their sensing application in selective detection of free chlorine. *Mater. Res. Express* **3**, (2016).
12. Feng, T., Ai, X., An, G., Yang, P. & Zhao, Y. Charge-Convertible Carbon Dots for Imaging-Guided Drug Delivery with Enhanced *in Vivo* Cancer Therapeutic Efficiency. *ACS Nano* acsnano.6b00043 (2016). doi:10.1021/acsnano.6b00043
13. Ray, S. C., Saha, A., Jana, N. R. & Sarkar, R. Fluorescent Carbon Nanoparticles : Synthesis , Characterization , and Bioimaging Application. 18546–18551 (2009).
14. Wu, Z. L. *et al.* One-pot hydrothermal synthesis of highly luminescent nitrogen-doped amphoteric carbon dots for bioimaging from Bombyx mori silk-natural proteins. *J. Mater. Chem. B* **1**, 2868–2873 (2013).
15. Li, Q. *et al.* Photoluminescent Carbon Dots as Biocompatible Nanoprobes for Targeting Cancer Cells. 12062–12068 (2010).
16. Hsu, P. C., Shih, Z. Y., Lee, C. H. & Chang, H. T. Synthesis and analytical applications of photoluminescent carbon nanodots. *Green Chem.* **14**, 917–920 (2012).
17. Yang, S. *et al.* Carbon Dots for Optical Imaging in Vivo. 11308–11309 (2009).
18. Li, S. *et al.* Crossing the blood-brain-barrier with transferrin conjugated carbon dots: A zebrafish model study. *Colloids Surfaces B Biointerfaces* **145**, 251–256 (2016).

19. Sun, Y.-P. *et al.* Doped Carbon Nanoparticles as a New Platform for Highly Photoluminescent Dots. *J. Phys. Chem. C* **112**, 18295–18298 (2008).

20. Wei, W. *et al.* Non-enzymatic-browning-reaction: A versatile route for production of nitrogen-doped carbon dots with tunable multicolor luminescent display. *Sci. Rep.* **4**, 1–7 (2014).

21. Yan, F. *et al.* Surface modification and chemical functionalization of carbon dots: a review. *Microchim. Acta* **185**, 424 (2018).

22. Song, Y. *et al.* Investigation into the fluorescence quenching behaviors and applications of carbon dots. *Nanoscale* **6**, (2014).

23. Yang, L. *et al.* One pot synthesis of highly luminescent polyethylene glycol anchored carbon dots functionalized with a nuclear localization signal peptide for cell nucleus imaging. *Nanoscale* **7**, 6104–6113 (2015).

24. Yang, L. *et al.* Doxorubicin conjugated functionalizable carbon dots for nucleus targeted delivery and enhanced therapeutic efficacy. *Nanoscale* **8**, 6801–6809 (2016).

25. Chen, M., Wang, W. & Wu, X. One-pot green synthesis of water-soluble carbon nanodots with multicolor photoluminescence from polyethylene glycol. *J. Mater. Chem. B* **2**, 3937–3945 (2014).

26. Du, F., Min, Y., Zeng, F., Yu, C. & Wu, S. A Targeted and FRET-Based Ratiometric Fluorescent Nanoprobe for Imaging Mitochondrial Hydrogen Peroxide in Living Cells. *Small* **10**, 964–972 (2014).

27. Xu, J. *et al.* Preparation of a Mitochondria-targeted and NO-Releasing Nanoplatform and its Enhanced Pro-Apoptotic Effect on Cancer Cells. *Small* **10**, 3750–3760 (2014).

28. Zhang, Y. *et al.* Mitochondria-Targeting Nanoplatform with Fluorescent Carbon Dots for Long Time Imaging and Magnetic Field-Enhanced Cellular Uptake. *ACS Appl. Mater. Interfaces* **7**, 10201–10212 (2015).

29. Wang, B. *et al.* A mitochondria-targeted fluorescent probe based on TPP-conjugated carbon dots for both one- and two-photon fluorescence cell imaging. *RSC Adv.* **4**, 49960–49963 (2014).

30. Arora, H. C. *et al.* Nanocarriers enhance doxorubicin uptake in drug-resistant ovarian cancer cells. *Cancer Res.* **72**, 769–778 (2012).

31. Wang, L. *et al.* Carbon-Dot-Based Two-Photon Visible Nanocarriers for Safe and Highly Efficient Delivery of siRNA and DNA. *Adv. Healthc. Mater.* **3**, 1203–1209 (2014).

32. Pierrat, P. *et al.* Efficient in vitro and in vivo pulmonary delivery of nucleic acid by carbon dot-based nanocarriers. *Biomaterials* **51**, 290–302 (2015).

33. Kim, J., Park, J., Kim, H., Singha, K. & Kim, W. J. Transfection and intracellular trafficking properties of carbon dot-gold nanoparticle molecular assembly conjugated with PEI-pDNA. *Biomaterials* **34**, 7168–7180 (2013).

34. Dixit, S. K. *et al.* Quantum dot encapsulation in viral capsids. *Nano Lett.* **6**, 1993–1999 (2006).

35. Gao, X. *et al.* In vivo molecular and cellular imaging with quantum dots. *Curr. Opin. Biotechnol.* **16**, 63–72 (2005).

36. Fan, H. *et al.* Surfactant-Assisted Synthesis of Water-Soluble and Biocompatible Semiconductor Quantum Dot Micelles. *Nano Lett.* **5**, 645–648 (2005).

37. Dubertret, B. In Vivo Imaging of Quantum Dots Encapsulated in Phospholipid Micelles. *Science (80-.).* **298**, 1759–1762 (2002).

38. Gerion, D. *et al.* Synthesis and Properties of Biocompatible Water-Soluble Silica-Coated CdSe/ZnS Semiconductor Quantum Dots †. *J. Phys. Chem. B* **105**, 8861–8871 (2001).

39. Lin, X., Gao, G., Zheng, L., Chi, Y. & Chen, G. Encapsulation of strongly fluorescent carbon quantum dots in metal-organic frameworks for enhancing chemical sensing. *Anal. Chem.* **86**, 1223–1228 (2014).

40. England, M. W., Patil, A. J. & Mann, S. Synthesis and confinement of carbon dots in lysozyme single crystals produces ordered hybrid materials with tuneable luminescence. *Chem. - A Eur. J.* **21**, 9008–9013 (2015).

41. Vassilakopoulou, A., Georgakilas, V. & Koutselas, I. Encapsulation and protection of carbon dots within MCM-41 material. *J. Sol-Gel Sci. Technol.* **82**, 795–800 (2017).

42. Johnson, N. R. & Wang, Y. Coacervate delivery systems for proteins and small molecule drugs HHS Public Access. *Expert Opin Drug Deliv* **11**, 1829–1832 (2014).

43. Lv, K., Perriman, A. W. & Mann, S. Photocatalytic multiphase micro-droplet reactors based on complex coacervation. *Chem. Commun.* **51**, 8600–8602 (2015).

44. Li, M., Huang, X., Tang, T.-Y. D. & Mann, S. Synthetic cellularity based on non-lipid micro-compartments and protocell models. *Curr. Opin. Chem. Biol.* **22**, 1–11 (2014).

45. Nichols, M. K. *et al.* Fabrication of Micropatterned Dipeptide Hydrogels by Acoustic Trapping of Stimulus-Responsive Coacervate Droplets. *Small* **14**, (2018).

46. Armstrong, J. P. K. *et al.* Cell paintballing using optically targeted coacervate microdroplets. *Chem. Sci.* **6**, 6106–6111 (2015).

47. Tian, L. *et al.* Spontaneous assembly of chemically encoded two-dimensional coacervate droplet arrays by acoustic wave patterning. *Nat. Commun.* **7**, 1–10 (2016).

48. Evander, M. & Nilsson, J. Acoustofluidics 20: applications in acoustic trapping. *Lab Chip* **12**, 4667–76 (2012).

49. J.F. Spengler, W. T. C. No Title. *Langmuir* **19**, 3635–3642 (2003).

50. Drinkwater, B. The real sonic screwdrivers. (2014).

51. Lilliehorn, T. *et al.* Trapping of microparticles in the near field of an ultrasonic transducer. *Ultrasonics* **43**, 293–303 (2005).

52. Hermes, M. *et al.* Nucleation of colloidal crystals on configurable seed structures. *Soft Matter* **7**, 4623 (2011).

53. Lee, J. W., Lee, C. Y., Teh, S. Y., Lee, A. & Shung, K. K. Acoustic particle trapping in a microfluidic device using frequency modulated signal. *2011 IEEE Int. Ultrason. Symp.* 1296–1299 (2011). doi:10.1109/ULTSYM.2011.0320

54. Nilsson, J., Evander, M., Hammarström, B. & Laurell, T. Review of cell and particle trapping in microfluidic systems. *Anal. Chim. Acta* **649**, 141–57 (2009).

55. Hammarström, B., Laurell, T. & Nilsson, J. ACOUSTIC TRAPPING OF BACTERIA AND NANOPARTICLES IN. 1707–1709 (2011).

56. Hammarström, B., Laurell, T. & Nilsson, J. Seed particle-enabled acoustic trapping of bacteria and nanoparticles in continuous flow systems. *Lab Chip* **12**, 4296–304 (2012).

57. Yi, C., Li, C.-W., Ji, S. & Yang, M. Microfluidics technology for manipulation and analysis of biological cells. *Anal. Chim. Acta* **560**, 1–23 (2006).

58. Courtney, C. R. P. *et al.* Manipulation of particles in two dimensions using phase controllable ultrasonic standing waves. *Proc. R. Soc. A Math. Phys. Eng. Sci.* **468**, 337–360 (2011).

59. Oberti, S. *et al.* Strategies for single particle manipulation using acoustic and flow fields. *Ultrasonics* **50**, 247–57 (2010).

60. Noguchi, Y. & Yamakoshi, Y. Micro particle trapping by opposite phases ultrasonic *,. **36**, 873–878 (1998).

61. Bassindale, P. G., Phillips, D. B., Barnes, a. C. & Drinkwater, B. W. Measurements of the force fields within an acoustic standing wave using holographic optical tweezers. *Appl. Phys. Lett.* **104**, 163504 (2014).

62. Antonsson, A. & Persson, J. L. Induction of apoptosis by staurosporine involves the inhibition of expression of the major cell cycle proteins at the G2/M checkpoint accompanied by alterations in Erk and Akt kinase activities. *Anticancer Res.* **29**, 2893–2898 (2009).

63. Yang, S. *et al.* Carbon Dots as Nontoxic and High-Performance Fluorescence Imaging Agents. 18110–18114 (2009).

64. Wang, Y. *et al.* Carbon dots of different composition and surface functionalization: cytotoxicity issues relevant to fluorescence cell imaging. *Exp. Biol. Med.* **236**, 1231–1238 (2011).

65. Xu, J. *et al.* Carbon dots as a luminescence sensor for ultrasensitive detection of phosphate and their bioimaging properties. *Luminescence* **30**, 411–415 (2015).

66. Kim, D., Choi, Y., Shin, E., Jung, Y. K. & Kim, B.-S. Sweet nanodot for biomedical imaging: carbon dot derived from xylitol. *RSC Adv.* **4**, 23210 (2014).

67. Yu, C. *et al.* A facile, green synthesis of highly fluorescent carbon nanoparticles from oatmeal for cell imaging. *J. Mater. Chem. C* **3**, 9514–9518 (2015).

68. Mehta, V. N., Jha, S., Singhal, R. K. & Kailasa, S. K. Preparation of multicolor emitting carbon dots for HeLa cell imaging. *New J. Chem.* **38**, 6152–6160 (2014).

69. Liu, Q., Guo, B., Rao, Z., Zhang, B. & Gong, J. R. Strong Two-Photon-Induced Fluorescence from Photostable, Biocompatible Nitrogen-Doped Graphene Quantum Dots for Cellular and Deep-Tissue Imaging. *Nano Lett.* **13**, 2436–2441 (2013).

70. Liu, H., He, Z., Jiang, L. P. & Zhu, J. J. Microwave-assisted synthesis of wavelength-tunable photoluminescent carbon nanodots and their potential applications. *ACS Appl. Mater. Interfaces* **7**, 4913–4920 (2015).

71. Xu, Y. *et al.* Nitrogen-doped carbon dots: A facile and general preparation method, photoluminescence investigation, and imaging applications. *Chem. - A Eur. J.* **19**, 2276–2283 (2013).

72. Ding, H., Yu, S.-B., Wei, J.-S. & Xiong, H.-M. Full-Color Light-Emitting Carbon Dots with a Surface-State-Controlled Luminescence Mechanism. *ACS Nano* **10**, 484–491 (2016).

73. Li, W. *et al.* Simple and green synthesis of nitrogen-doped photoluminescent carbonaceous

nanospheres for bioimaging. *Angew. Chemie - Int. Ed.* **52**, 8151–8155 (2013).

74. Bhaisare, M. L., Talib, A., Khan, M. S., Pandey, S. & Wu, H. F. Synthesis of fluorescent carbon dots via microwave carbonization of citric acid in presence of tetraoctylammonium ion, and their application to cellular bioimaging. *Microchim. Acta* **182**, 2173–2181 (2015).

75. Han, M. *et al.* Recent progress on the photocatalysis of carbon dots: Classification, mechanism and applications. *Nano Today* **19**, 201–218 (2018).

76. Lim, S. Y., Shen, W. & Gao, Z. Carbon quantum dots and their applications. *Chem. Soc. Rev.* **44**, 362–381 (2015).

77. Ogihara, H., Xie, J., Okagaki, J. & Saji, T. Simple method for preparing superhydrophobic paper: Spray-deposited hydrophobic silica nanoparticle coatings exhibit high water-repellency and transparency. *Langmuir* **28**, 4605–4608 (2012).

Chapter 5: Conclusions and Further Work

5.1. Conclusions and Further Work

The central theme of this thesis was to draw on the themes of biomimetic, biokleptic and bio-inspired research to develop novel functional materials, with the objectives of advancing the capability to tailor materials for specific functions and applications, enhance our knowledge of biological processes as a means to better understand and control them, and develop materials technology for a more sustainable future. Three experimental chapters were discussed which present novel developments in their own right as well as within the framework of biomimetic, biokleptic and bio-inspired research. Each experimental chapter utilised one or more of these themes in the experimental design, process and/or environment, synthesis technique and/or reagents used. This section concludes the outcomes of these chapters in line with the experimental aims of the work, the broader objectives of the research field and outlines potential future work to be carried out.

Chapter 2 discusses the development of a novel protein crystallisation technique, whereby colloidosomes were used to create confined micro-compartment reaction vessels for protein crystallisation and growth. The experimental design was bio-inspired in its use of compartmentalisation to control processes in a confined environment, biokleptic in its use of naturally abundant protein molecules, and biomimetic as the process of crystallisation within a semi-permeable membrane compartment is analogous to processes in nature such as that of biomineralisation of magnetosomes (lipid vesicles) by magnetotactic bacteria. This crystallisation technique was first in kind as far as we know: energy efficient, requiring minimal intervention and/or physical handling, and exhibiting very exciting results. Lysozyme crystals were successfully crystallised within colloidosomes and remained stable, retaining their crystalline shape and integrity for up to 8 months. Lysozyme crystals grown inside the colloidosome were 10-20x smaller than those grown in batch. The crystallisation process was investigated and found to be influenced by changes in temperature, protein concentration and time of incubation producing crystals of different shapes and morphologies which was not observed in batch. This would suggest that the confined environment plays some role in increasing the sensitivity of the crystallisation process to internal (protein concentration, osmotic pressure) and external parameters (temperature). Crystallisation of two crystallisation systems of ferritin were also successful with further promising results of successful precipitation of protein molecules of mCherry and bovine liver catalase. Au NPs, N CDs and NS CDS were incorporated into the crystallisation solution of lysozyme within colloidosomes to investigate the feasibility of *in situ* functionalisation of the protein crystals. The investigations were successful on both occasions, indicating the successful incorporation of Au NPs and CDs into the lysozyme crystal structure which was primarily observed through optical fluorescence microscopy but requires further investigation to be verified. The results from these investigations have indicated that the most likely theory on the mechanism of protein crystallisation within colloidosomes is that the silica nanoparticles (which form the membrane of the colloidosomes) provide a site for heterogenous nucleation which aids protein crystallisation.[1] Artefacts introduced into the crystallisation solution such as the Au NPs or CDs can additionally serve as heterogenous nucleation sites which allows them to be incorporated in the crystal structure *in situ*.[2–5] The majority of the investigations carried out on these systems have relied on optical fluorescence spectroscopy and further 3D reconstruction and crystalline diffraction studies are required to determine the precise crystallographic morphologies and crystal integrity. Preliminary structural characterisation of lysozyme protein crystals was carried out at the Diamond Light Source facility, using VMXi beamline to collect diffraction data from the protein crystals *in situ*. This was the first experiment of its kind to be carried out on the VMXi beamline, as the instrument is very new. Unfortunately only one (incomplete) data set was collected, but it is regardless very promising. Given the time restraints of this project it was not possible to improve these results, however with appropriate calibration and repetition, and perhaps introduction of automated assistance in the protein crystallisation screening, this work could be greatly advanced to establish a library of protein crystals. In addition to calibration of the diffraction instruments with the appropriate time and resources allocated - such as the incorporation of a microfluidic system to the assembly of protein crystallisation colloidosomes[6–8] - this technique could be of great benefit to the scientific community as a means to better understand protein crystallisation process, and as a rapid, facile, low energy protein crystallisation technique as well as a potential means for crystallising hard-to-crystallise proteins. Further work which could be considered is the use of protein crystals grown inside colloidosomes as catalytic centres, synthetic templates or storage and/or separation sites. This would involve combining the unique and confined reaction environment within colloidosomes with the availability of solvent channels within the protein crystal lattice. Taking lysozyme as an example, porous crystals of lysozyme (crystallised in bulk) have already been used to synthesise metallic nanoparticles, organic polymers and CDs. The Porous crystals have been used for catalysis, gas separation and storage of chemical moieties.[9–13] As the research is advanced, colloidosomes could, in theory be used to grow protein crystals of a particular size and/or morphology by adjustment of the crystallisation solution and external parameters such as temperature. This could be used to tailor protein crystals such that they are optimised for any of the applications mentioned.

Chapter 3 presents a novel hybrid synthesis mechanism for the fabrication of N CDs and NS CDs by acid hydrolysis of cellulose pulp into NCC and microwave-assisted pyrolysis of the NCC in the presence of EDA and L-cysteine as N and S dopants respectively. The mechanism is novel in that it incorporates elements of top-down and bottom-up synthesis to produce CDs that exhbit characteristics of both bottom-up and top-down synthesised CDs The CDs were characterised by a variety of techniques (HRTEM, XPS,FTIR, Fluorescence spectroscopy, and XRD.) to investigate their properties and elucidate a mechanism for the underlying PL behaviour.

In this way, a novel biokleptic precursor (NCC derived from the acid dehydration of cellulose pulp) was used to synthesis CDs using an entirely novel hybrid synthesis technique inspired by both top-down and bottom-up synthesis of CDs. The CDs were found to be quasi-spherical particles 2-12 nm in size with Sp^2 and Sp^3 characteristics in the carbon core and functional surface groups of carboxylic acid, alcohol and amide/amine groups. The CDs were found to exhibit tuneable, non-blinking, excitation-dependent PL behaviour, with high QY (73% and 32% for N CDs and NS CDs respectively). Although the PL mechanism is not entirely understood, the results of the investigations indicate that is most likely due to two PL centres, one in the carbon core and one at the passivated surface of the CDs. The non-blinking, high QY, tuneable PL, predic table fluorescence decay rate and hydrophilicity of the CDs make them excellent candidates for applications in bio-imaging and photo-sensing.

Chapter 4 builds on the work carried out in the previous two chapters and has a materials application focus. The cytotoxicity of CDs synthesised by the mechanism mentioned in Chapter 3 were investigated by incubation of HeLa cells with the CDs at different concentrations in aqueous dispersions. The CDs, particularly N CDs, were found to be relatively non-toxic with over 50% of cells retaining viability and metabolism after incubation for 24 hours with up to 1 mg/mL of CDs, however extensive cell internalisation and trafficking studies are required to determine the nature of the CDsb interaction with the cells. This is a very high concentration compared to other cytotoxicity experiments on similar CDs in the literature. It is therefore promising and would encourage further work in this area alongside functionalisation of the CDs surface to improve cytotoxicity and enable cellular (and potentially intracellular) targeting. Encapsulation of CDs in colloidosomes and coacervates were used to investigate the potential for enhancing the photostability of CDs as a function of encapsulation. Aqueous dispersions of CDs were successfully encapsulated in colloidosomes. The silica membranes were then cross-linked and extracted into water. The CDs remained fluorescent throughout and the fluorescence decay within colloidosomes was investigated. The inorganic nature of the colloidosome membrane limits its potential bio-applications. CDs were encapsulated in coacervates and an acoustic trap was used to pattern the CDs-coacervate into a 2D array. The ability to sequester CDs in coacervates to successfully manipulate them via non-contact acoustic trapping is highly advantageous as an investigative tool for the characteristics and potential behaviour for the CDs, as well as a platform for potential applications such as the spatial organisation of reactions, targeted delivery of CDs-coacervates, and lab-on-a-chip applications.

Herein, the themes of biomimetic, biokleptic and bio-inspired design have been implemented to generate exciting novel techniques and materials for a diverse range of technological and investigative applications. The work presented will hopefully be of valuable contribution to the scientific community in advancing our understanding and control of processes such as protein crystallisation, providing alternative materials and techniques to synthesise functional materials and pave the way for a more sustainable, interdisciplinary approach to materials design and fabrication.

5.2. References

1. Chayen, N. E., Saridakis, E., El-Bahar, R. & Nemirovsky, Y. Porous silicon: An effective nucleation-inducing material for protein crystallization. *J. Mol. Biol.* **312**, 591–595 (2001).

2. Hodzhaoglu, F., Kurniawan, F., Mirsky, V. & Nanev, C. Gold nanoparticles induce protein crystallization. *Cryst. Res. Technol.* **43**, 588–593 (2008).

3. Durbin, S. D. & Feher, G. Crystal growth studies of lysozyme as a model for protein crystallization. *J. Cryst. Growth* **76**, 583–592 (1986).

4. Khurshid, S., Saridakis, E., Govada, L. & Chayen, N. E. Porous nucleating agents for protein crystallization. *Nat. Protoc.* **9**, 1621–33 (2014).

5. Ko, S., Kim, H. Y., Choi, I. & Choe, J. Gold nanoparticles as nucleation-inducing reagents for protein crystallization. *Cryst. Growth Des.* **17**, 497–503 (2017).

6. Maeki, M. *et al.* Controlling protein crystal nucleation by droplet-based microfluidics. *Chemistry* **20**, 1049–56 (2014).

7. Yang, C.-G., Liu, Y.-H., Di, Y.-Q. & Xu, Z.-R. Generation of two-dimensional concentration-gradient droplet arrays on a two-layer chip for screening of protein crystallization conditions. *Microfluid. Nanofluidics* **18**, 493–501 (2014).

8. Chen, D. L., Gerdts, C. J. & Ismagilov, R. F. Using microfluidics to observe the effect of mixing on nucleation of protein crystals. *J. Am. Chem. Soc.* **127**, 9672–3 (2005).

9. Vilenchik, L. Z., Griffith, J. P., St. Clair, N., Navia, M. A. & Margolin, A. L. Protein crystals as novel microporous materials. *J. Am. Chem. Soc.* **120**, 4290–4294 (1998).

10. Abe, S. & Ueno, T. Design of protein crystals in the development of solid biomaterials. *RSC Adv.* **5**, 21366–21375 (2015).

11. England, M. W., Patil, A. J. & Mann, S. Synthesis and confinement of carbon dots in lysozyme single crystals produces ordered hybrid materials with tuneable luminescence. *Chemistry* **21**, 9008–13 (2015).

12. England, M. W. *et al.* Fabrication of polypyrrole nano-arrays in lysozyme single crystals. *Nanoscale* **4**, 6710 (2012).

13. Horike, S., Shimomura, S. & Kitagawa, S. Soft porous crystals. *Nat. Chem.* **1**, 695–704 (2009).

Chapter 6: Appendix

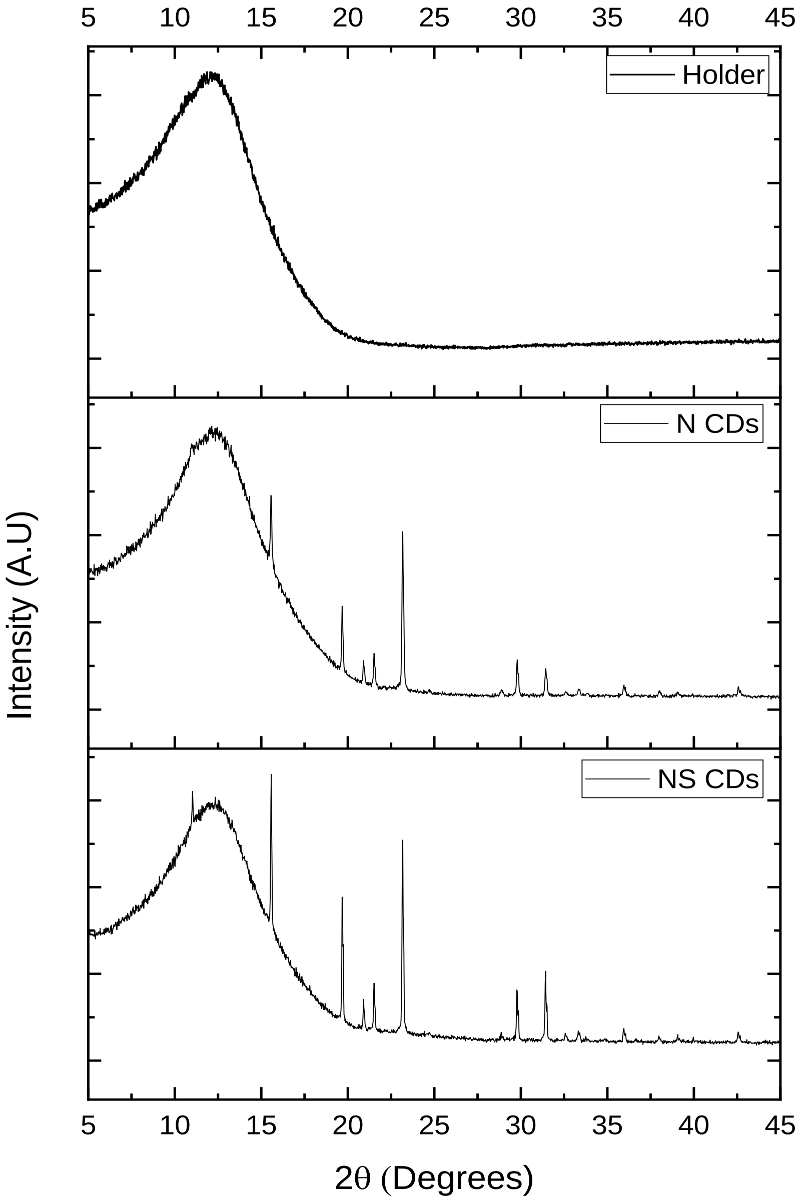

Figure A1: XRD pattern of the silicon holder, N CDS and NS CDs

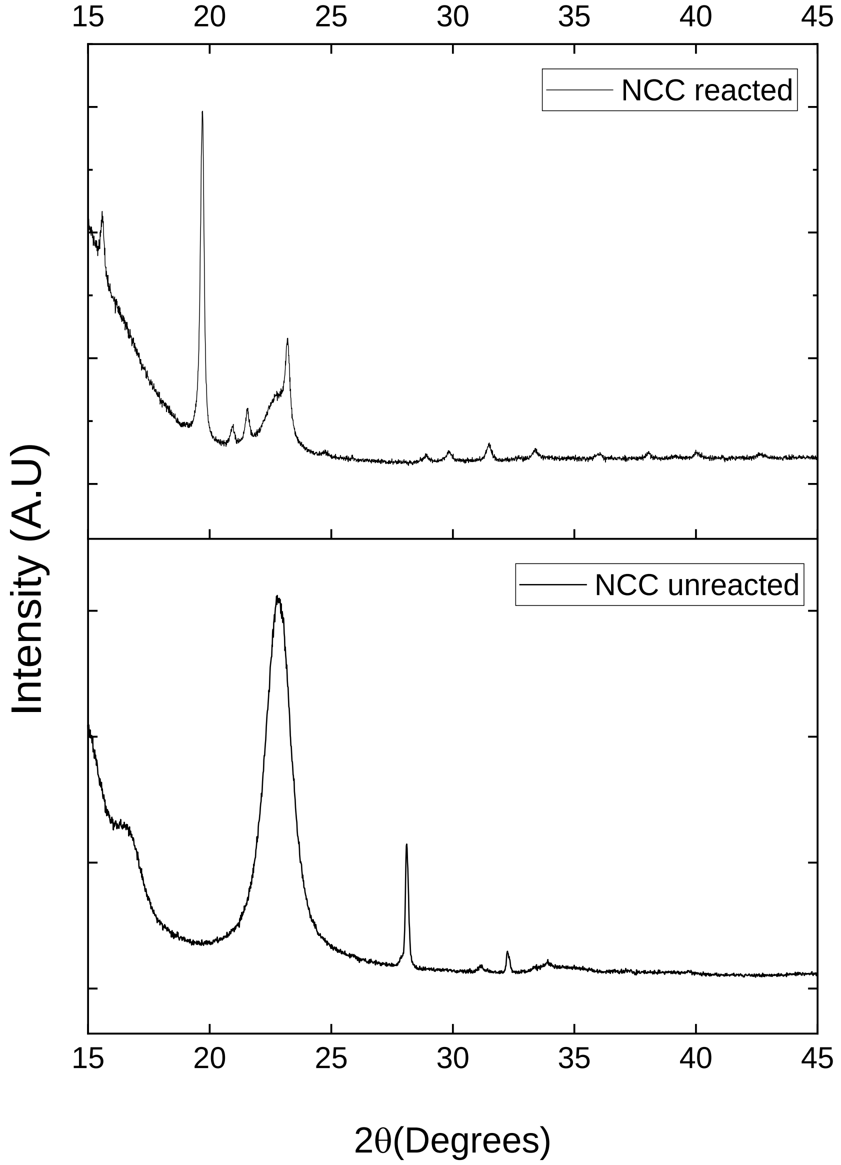

Figure A2: NCC reacted in the microwave digestion vessel for 8 minutes at medium power (top). NCC unreacted (bottom)

The XRD pattern of NCC before and after reaction in the microwave digestion vessel (Figure A2) shows a clear change in the structure of NCC as a result of the reaction. XRD spectra of NCC unreacted contains a broad peak at 2θ= 22.75^0 sharp crystalline peak at 28°, and small peak at 32.24°. XRD spectra of NCC reacted shows no broad peaks, and a sharp crystalline peak at 2θ = 19.712^0 followed by peaks at 2θ = 21.5^0, 23.2^0, 31.5^0.

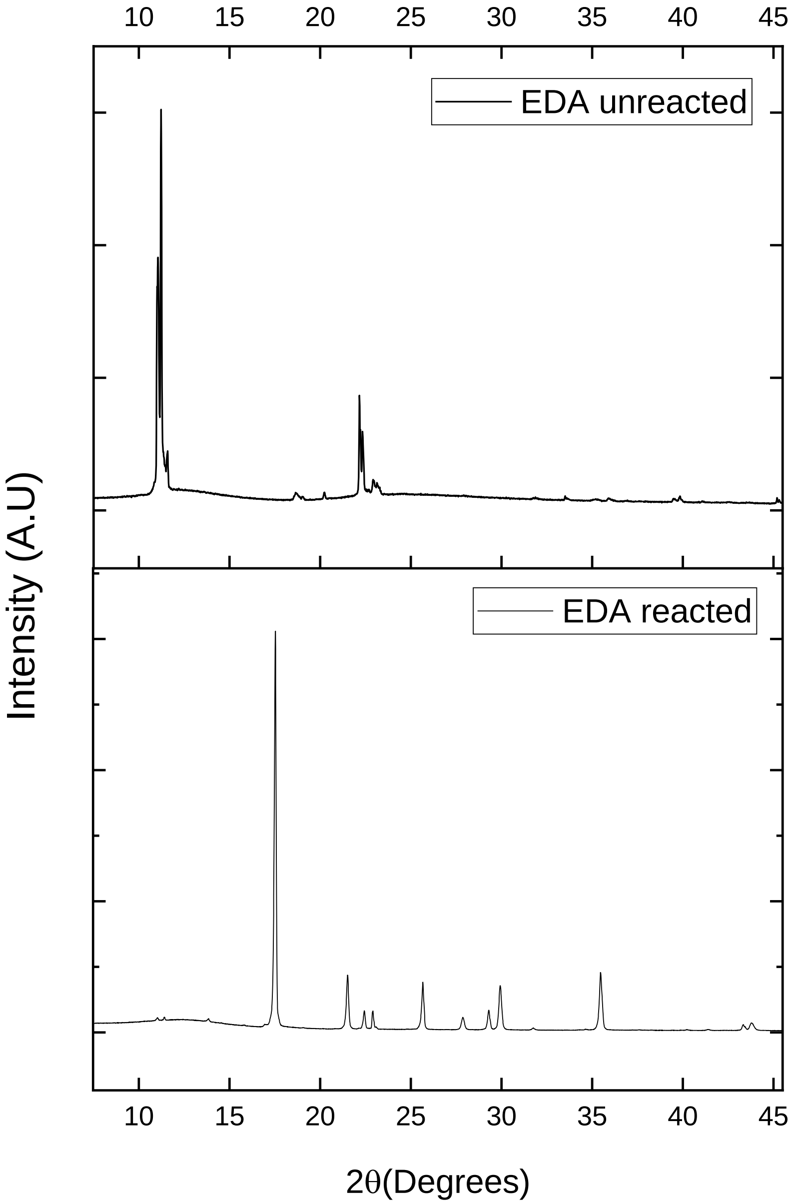

Figure A3: EDA unreacted (top), EDA reacted in the microwave digestion vessel for 8 minutes at medium power (bottom)

The XRD pattern of EDA before and after reaction in the microwave demonstrates a clear change in the structure of EDA. The XRD spectra of EDA unreacted contains crystalline peaks at 2θ= 11.2^0, and 22.7^0. The XRD spectra of EDA reacted shows sharp crystalline peaks at 2θ= 17.5^0, 21.5^0, 22.4^0, 22.9^0, 25.7^0, 27.9^0, 29.2^0, 35.4^0

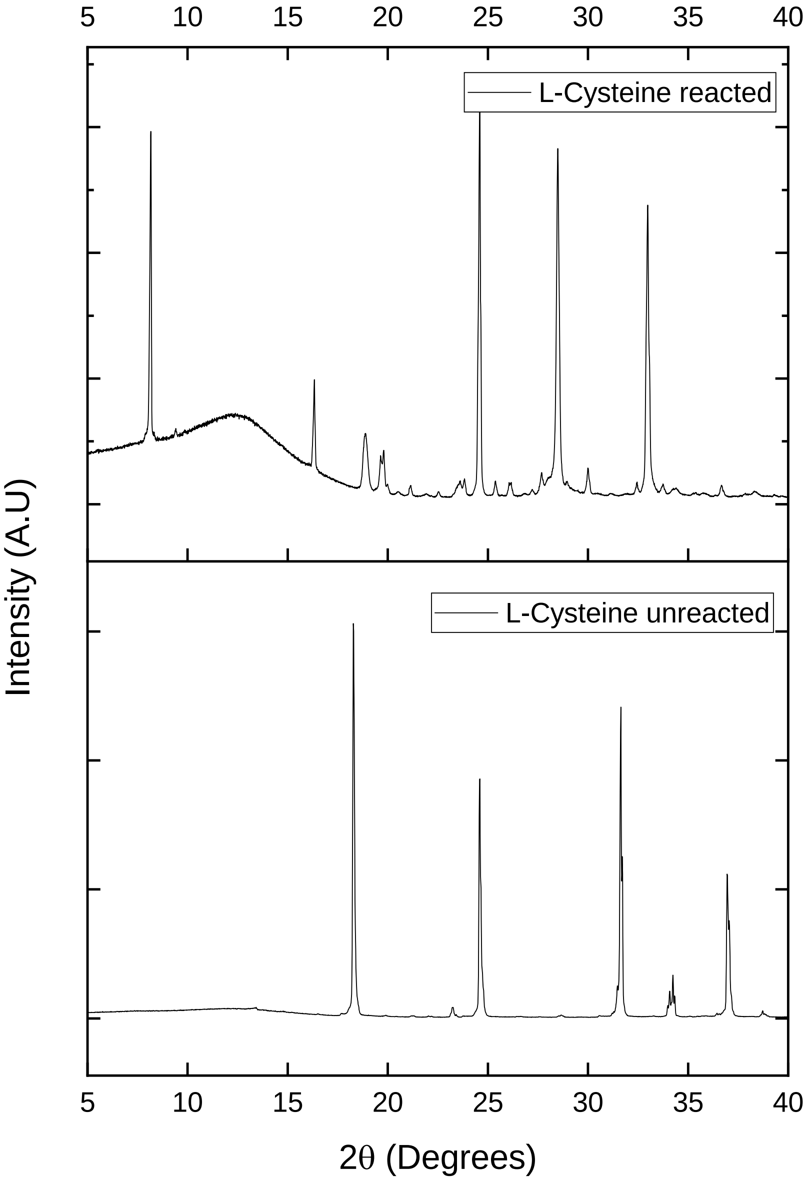

Figure A4: L-cysteine reacted in the microwave digestion vessel for 8 minutes at medium power (top) L-cysteine unreacted (bottom).

The reaction of L-cysteine introduces some changes to the structure of L-cysteine as demonstrated in Figure A4. L-cysteine unreacted contains crystalline peaks at 2θ= 18.3^0, 24.6^0, 31.6,34.3^0,36.9^0. L-cysteine reacted contains crystalline peaks at 2θ= 8.2^0, 16.3^0, 18.9^0, 19.8^0, 24.6^0, 28.5^0, 33^0 and a broad peak at 2θ= 12.4^0.

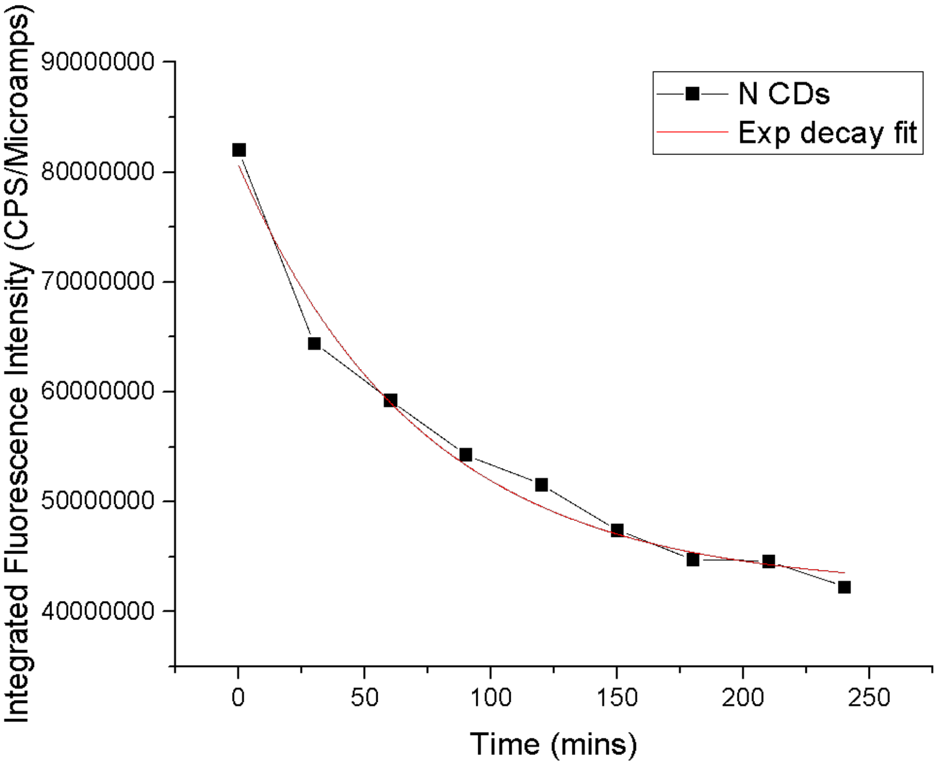

A5: Fluorescence decay of N CDs in solution with exponential decay fit

Table A1: Exponential decay function of N CDs in solution

Model	ExpDec1
Equation	y = A1*exp(-x/t1) + y0
Plot	Integrated Fluorescence Intensity
y0	4.21197E7 ± 1.73527E6
A1	3.84613E7 ± 2.06208E6
t1	73.08456 ± 10.71882
Reduced Chi-Sqr	3.29129E12
R-Square(COD)	0.98458
Adj. R-Square	0.97944

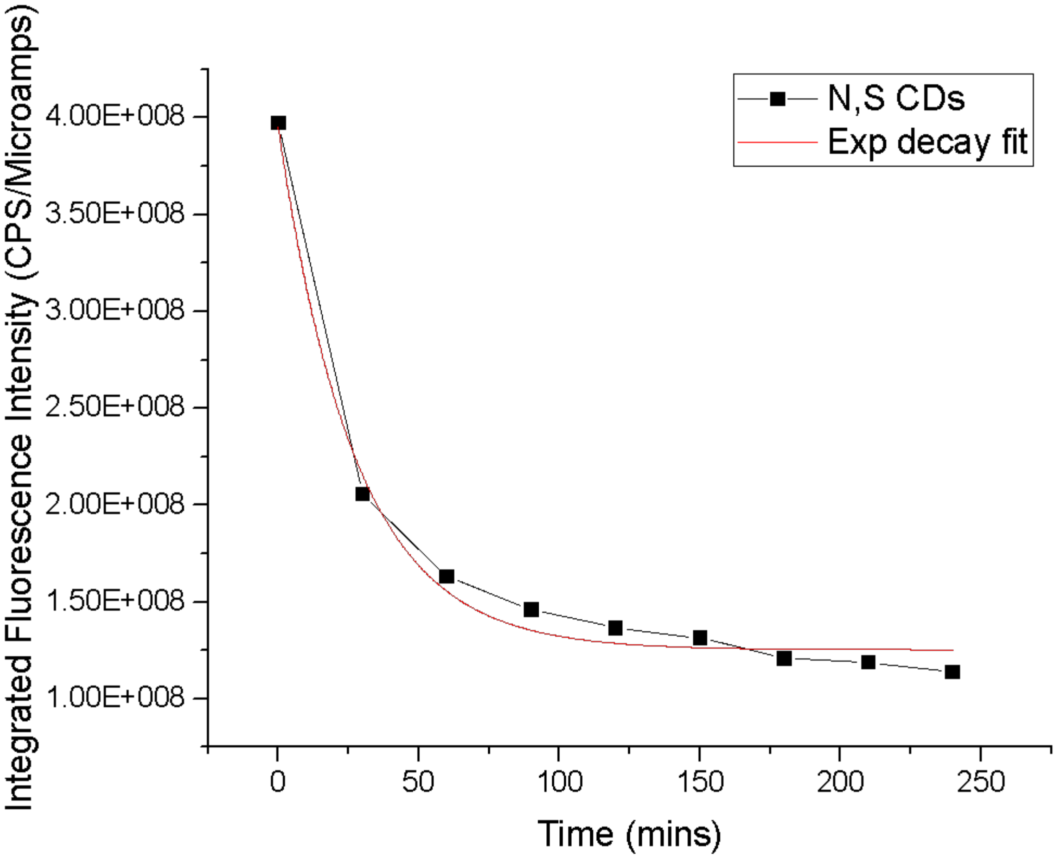

Figure A6: Fluorescence decay of NS CDs in solution with exponential decay fit

Table A2: Exponential decay function of N CDs in solution

Model	ExpDec1
Equation	y = A1*exp(-x/t1) + y0
Plot	Integrated Fluorescence Intensity
y0	1.25288E8 ± 4.31499E6
A1	2.70072E8 ± 1.03224E7
t1	27.38936 ± 2.64464
Reduced Chi-Sqr	9.30118E13
R-Square(COD)	0.99133
Adj. R-Square	0.98844

Fluorescence Intensity profiles across the diameter of colloidosomes shows the distribution of CDs solution inside colloidosomes

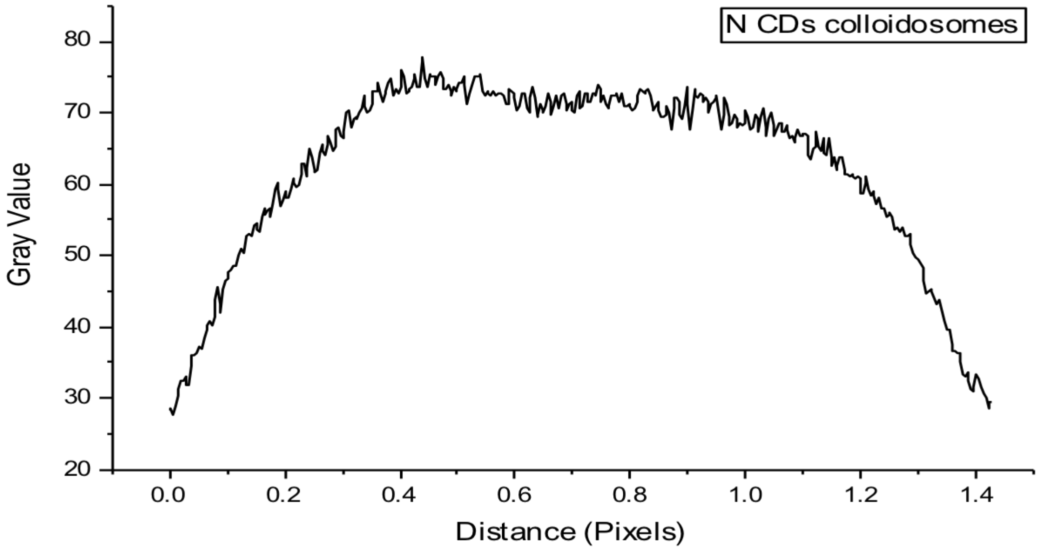

Figure A7: Plot profile of N CDs in colloidosomes. Standard deviation = 2.885392

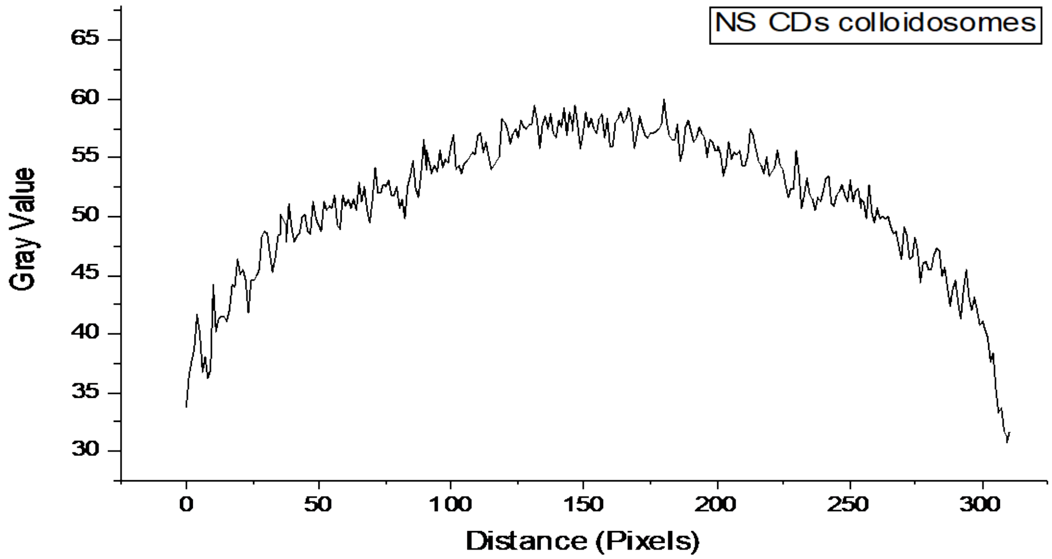

Figure A8: Plot profile of NS CDs in colloidosomes. Standard deviation = 2.64987

Fluorescence Intensity profiles across the diameter of coacervate droplets shows the distribution of CDs solution inside coacervates

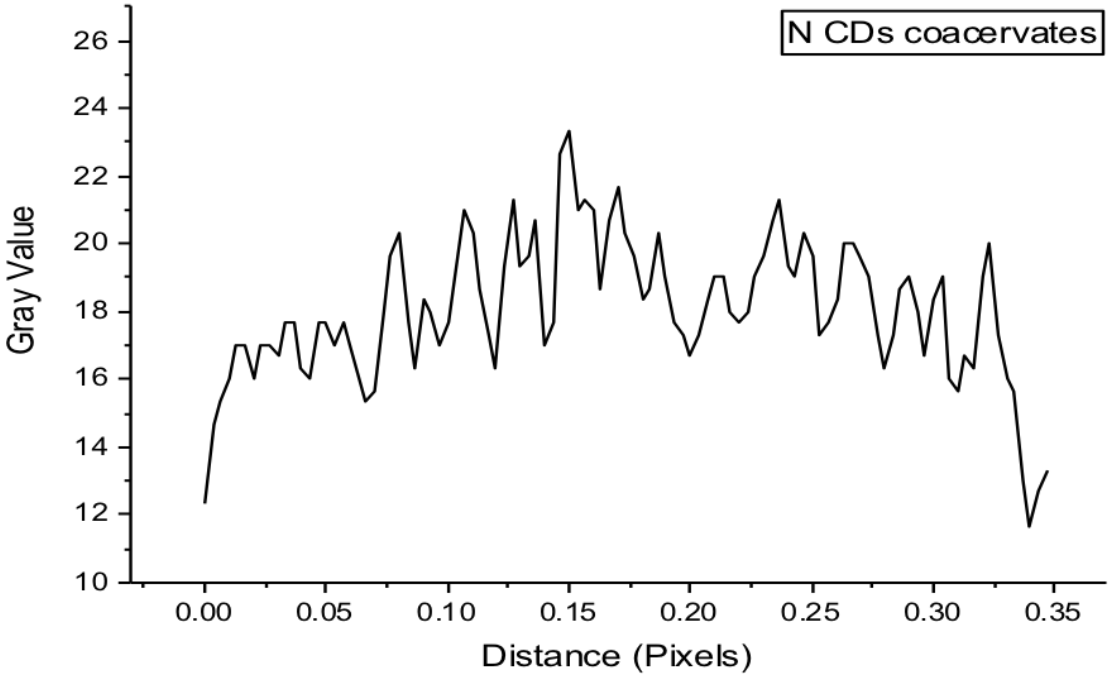

Figure A9: Plot profile of N CDs in coacervates. Standard deviation = 1.643458

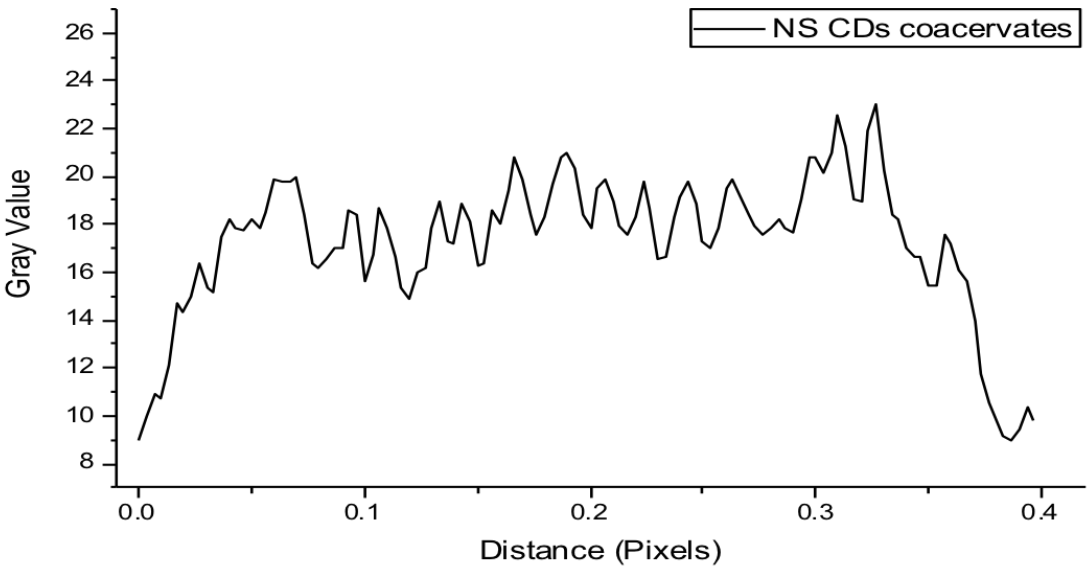

Figure A10: Profile of NS CDs in coacervates. Standard deviation = 1.620406